Techniques de Photoluminescence pour l'étude des Interfaces Photovoltaïques

Ming Xu

NNT : 2016SACLS053

THESE DE DOCTORAT
DE
L'UNIVERSITÉ PARIS-SACLAY
PRÉPARÉE À
L'UNIVERSITÉ PARIS SUD

ECOLE DOCTORALE N° 575
Electrical, optical, bio-physics and engineering

Spécialité de doctorat : Physique

Par

M. Ming XU

PHOTOLUMINESCENCE TECHNIQUES FOR THE CHARACTERIZATION OF PHOTOVOLTAIC INTERFACES

Thèse présentée et soutenue à Gif sur Yvette, le 8 avril 2016 :

Composition du Jury :

Mme KAMINSKI-CACHOPO Anne, Professeure, IMEP – LAHC – INP Grenoble, Rapporteur
M. ALCUBILLA GONZALEZ Ramon, Professeur, CRNE – UPC, Rapporteur
Mme ATKINSON Paola, Chargée de recherche CNRS, INSP – UPMC, Examinatrice
Mme MUNOZ Delfina, Ingénieure de recherche CEA – INES, Examinatrice
M. ETCHEBERRY Arnaud, Directeur de recherche CNRS, ILV – UVSQ, Examinateur
M. BOUTCHICH Mohamed, Maître de conférences UPMC – GeePs, Co-directeur de thèse
M. KLEIDER Jean-Paul, Directeur de recherche CNRS – GeePs, Directeur de thèse
M. BRÜGGEMANN Rudolf, Chercheur Université d'Oldenburg et CNRS, Invité

université PARIS-SACLAY
ÉCOLE DOCTORALE
Physique et ingénierie : électrons, photons, sciences du vivant (EOBE)

Titre : Techniques de luminescence pour l'étude des interfaces photovoltaïques

Mots clés : photoluminescence, photovoltaïques, interface, silicium cristallin

Résumé : Dans ce travail, nous avons appliqué des techniques de photoluminescence en régime stationnaire (PL) et photoluminescence en régime modulé (MPL) à l'étude d'hétérojonctions formées entre du silicium cristallin (c-Si) et du silicium amorphe hydrogéné (a-Si:H). Plus précisément, nous avons comparé des échantillons constitués de dépôts de (n)a-Si:H, (i)a-Si:H, (n)a-Si:H/(i)a-Si:H, et (p)a-Si:H/(i)a-Si:H sur des wafers de (n) c-Si de haute qualité électronique. Les mesures en fonction de la température montrent que la durée de vie des porteurs en excès diminue lorsque la température diminue, ce qui peut être qualitativement reproduit par la simulation dans un mécanisme de recombinaison de type Shockley-Read-Hall (SRH) en tenant compte du niveau d'énergie du dopant (phosphore) dans le substrat et de niveaux peu profonds électroniquement actifs à l'interface.

Nous avons également étudié des échantillons dopés par implantation d'ions puis passivés par AlOx, a-Si:H et SiC. Des signatures de dislocations sont révélées à basse température par des pics supplémentaires de PL.

Nous avons également comparé les résultats de cartographies de PL et de durée de vie obtenues par l'analyse de l'amplitude de MPL, et par l'analyse de son déphasage. Il est constaté que les propriétés optiques des échantillons ont un grand impact sur la cartographie PL, ce qui pourrait conduire à une conclusion erronée sur leur homogénéité. En revanche, les cartographies de durée de vie sont moins sujettes à des variations de paramètres optiques et au bruit provenant du processus de mesure, phénomènes qui ne sont pas intrinsèques à l'échantillon étudié.

La nature différentielle de la mesure MPL est étudiée. Nous démontrons la notion de durée de vie à l'état stationnaire et de durée de vie différentielle. Nous analysons différents types de recombinaisons avec la durée de vie MPL et avons mis en œuvre des simulations des hétérojonctions a-Si:H/c-Si. Nous constatons que dans le domaine d'excitation intéressant pour le photovoltaïque, la durée de vie différentielle est souvent inférieure à la durée de vie à l'état stationnaire. Nous faisons aussi des comparaisons entre les durées de vie obtenues par mesures dites QSSPC et MPL et montrons qu'elles sont en fait égales.

La combinaison des techniques de PL et de MPL nous a permis d'étudier le coefficient de recombinaison radiative en fonction de la température. Les résultats publiés jusqu'ici dans la littérature couvrent la plage de température de 300 K à 90 K. Dans cette plage, nos résultats sont en très bon accord avec ces résultats publiés précédemment. Mais, grâce à notre système de mesure et à la combinaison PL/MPL, nous avons obtenu des valeurs de ce coefficient jusqu'à 20 K et nous avons pu proposer une fonction polynômiale du cinquième degré qui permet de bien reproduire les variations en fonction de la température sur toute la plage de 20 K à 300 K.

Dans une dernière partie de la thèse, les propriétés de transport de porteurs et l'effet de couplages sont étudiés dans des empilements de quantum dots. Nous avons examiné les quantum dots de InAs qui croissent de manière ordonnée en formant des chaînes à partir d'une couche tampon en InGaAs (couche dite de "cross hatch pattern"). Nous avons caractérisé par PL des monocouches ainsi que des multicouches empilées de chaînes de quantum dots. L'effet de couplage entre dots dans le plan est observé sur des échantillons de monocouches, et nous remarquons une inhibition du couplage vertical entre couches qui est expliqué par l'effet du champ de déformation de la couche de cross hatch pattern.

Université Paris-Saclay
Espace Technologique / Immeuble Discovery
Route de l'Orme aux Merisiers RD 128 / 91190 Saint-Aubin, France

Title : Luminescence Techniques For The Characterization Of Photovoltaic Interfaces

Keywords : photoluminescence, photovoltaics, interface, crystal silicon

Abstract : Silicon solar cells remain the driving technology and dominate the photovoltaics market. Hydrogenated amorphous silicon/crystalline silicon (a-Si:H/c-Si) heterojunction cells achieve the best efficiency in silicon cells to date (25.6%). A great part of this achievement is assigned to the improvement of the passivation of the emitter/absorber interface. In that regard, luminescence techniques whether Photoluminescence (PL) or Modulated photoluminescence (MPL), are particularly appropriate to investigate surface defects and effective carrier lifetime.

In this work, we developed a PL/MPL setup coupled to a helium cooled cryostat to the study of a-Si:H/c-Si heterojunctions. Considering the modulated nature of the MPL, we introduced the concept of steady state lifetime and differential lifetime. Through simulations, we analyzed different types of recombination mechanisms and found that the differential lifetime is lower than the steady state lifetime. We also benchmarked the lifetime determined by photoconductance decay measurements and the MPL lifetime and demonstrated that they are actually equal.

We have analyzed various samples of a-Si:H/c-Si heterojunctions from multiple sources, particularly within the framework of the European project HERCULES (High Efficiency Rear Contact solar cells and Ultra powerful moduLES). The samples are composed of various doping and passivation layers such as AlOx, a-Si:H and a-SiC:H fabricated on high quality (n)c-Si wafers. The temperature dependent measurements show that the excess carrier lifetime decreases when the temperature decreases, which is explained by the Shockley-Read-Hall recombination model at the heterojunction interface. The combination of PL and MPL measurements have enabled us to determine the radiative recombination coefficient in crystal silicon as a function of temperature. Our measurements have extended the original data to 20 K. We propose a fifth order polynomial of the radiative recombination coefficient as a function of temperature in the range of 20 to 300 K and it agrees very well to others' work. We also investigated the possibility to extend the system to carry out PL and MPL mapping in order to extract the cell homogeneity and the lifetime distribution across the sample. We found that the optical property of sample has a significant impact on the PL mapping and could lead to incorrect conclusion with respect to the homogeneity. However the lifetime mapping from MPL produces imaging that is less prone to variation of optical properties.

At last, we utilized the temperature dependent micro PL to investigate the coupling of InAs quantum dot chains (QDC) stacks grown on InGaAs cross hatch patterns separated with a 10 nm GaAs layer. The PL spectra are dominated by the top-most stack, indicating that the QDC layers are nominally uncoupled. However, under the high excitation power densities achievable with the micro PL system, when the high-energy peaks of the top stack are saturated, low-energy PL peaks from the bottom stacks emerge as a result of the carrier transfer across the GaAs spacers. These unique PL signatures contrast with the state-filling effects in conventional, coupled QD stacks and serve as a means to quickly assess the presence of electronic coupling in stacks of dissimilar-sized nanostructures.

Université Paris-Saclay
Espace Technologique / Immeuble Discovery
Route de l'Orme aux Merisiers RD 128 / 91190 Saint-Aubin, France

Techniques de Photoluminescence pour l'étude des Interfaces Photovoltaïques

Ming XU

ECOLE D'OCTORALE N° 575
Electrical, optical, bio-physics and engineering
Directeur de thèse: Jean-Paul KLEIDER
Co-directeur de thèse: Mohamed BOUTCHICH

Laboratoire Génie électrique et électronique de Paris
Spécialité de doctorat: Physique

Université Paris-Saclay Date de soutenance: Le 8 avril 2016

Résumé

Dans ce travail, nous avons appliqué des techniques de photoluminescence en régime stationnaire (PL) et photoluminescence en régime modulé (MPL) à l'étude d'hétérojonctions formées entre du silicium cristallin (c-Si) et du silicium amorphe hydrogéné (a-Si:H). Plus précisément, nous avons comparé des échantillons constitués de dépôts de (n)a-Si:H, (i)a-Si:H, (n)a-Si:H/(i)a-Si:H, et (p)a-Si:H/(i)a-Si:H sur des wafers de (n) c-Si de haute qualité électronique. Les mesures en fonction de la température montrent que la durée de vie des porteurs en excès diminue lorsque la température diminue, ce qui peut être qualitativement reproduit par la simulation dans un mécanisme de recombinaison de type Shokley-Read-Hall (SRH) en tenant compte du niveau d'énergie du dopant (phosphore) dans le substrat et de niveaux peu profonds électroniquement actifs à l'interface.

Nous avons également étudié des échantillons dopés par implantation d'ions puis passivés par AlOx, a-Si:H et SiC. Des signatures de dislocations sont révélées à basse température par des pics supplémentaires de PL.

Nous avons également comparé les résultats de cartographies de PL et de durée de vie obtenues par l'analyse de l'amplitude de MPL, et par l'analyse de son déphasage. Il est constaté que les propriétés optiques des échantillons ont un grand impact sur la cartographie PL, ce qui pourrait conduire à une conclusion erronée sur leur homogénéité. En revanche, les cartographies de durée de vie sont moins sujettes à des variations de paramètres optiques et au bruit provenant du processus de mesure, phénomènes qui ne sont pas intrinsèques à l'échantillon étudié.

La nature différentielle de la mesure MPL est étudiée. Nous démontrons la notion de durée de vie à l'état stationnaire et de durée de vie différentielle. Nous analysons différents types de recombinaisons avec la durée de vie MPL et avons mis en œuvre des simulations des hétérojonctions a-Si:H/c-Si. Nous constatons que dans le domaine d'excitation intéressant pour le photovoltaïque, la durée de vie différentielle est souvent inférieure à la durée de vie à l'état stationnaire. Nous faisons aussi des comparaisons entre les durées de vie obtenues par mesures dites QSSPC et MPL et montrons qu'elles sont en fait égales.

La combinaison des techniques de PL et de MPL nous a permis d'étudier le coefficient de recombinaison radiative en fonction de la température. Les résultats publiés jusqu'ici dans la littérature couvrent la plage de température de 300 K à 90 K. Dans cette plage, nos résultats sont en très bon accord avec ces résultats publiés précédemment. Mais, grâce à notre système de mesure et à la combinaison PL/MPL, nous avons obtenu des valeurs de ce coefficient jusqu'à 20 K et nous avons pu proposer une fonction polynômiale du cinquième degré qui permet de bien reproduire les variations en fonction de la température sur toute la plage de 20 K à 300 K.

Dans une dernière partie de la thèse, les propriétés de transport de porteurs et l'effet de couplages sont étudiés dans des empilements de quantum dots. Nous avons examiné les quantum dots de InAs qui croissent de manière ordonnée en formant des chaînes à partir d'une couche tampon en InGaAs (couche dite de "cross hatch pattern"). Nous avons caractérisé par PL des monocouches ainsi que des multicouches empilées de chaînes de quantum dots. L'effet de couplage entre dots dans le plan est observé sur des échantillons de monocouches, et nous remarquons une inhibition du couplage vertical entre couches qui est expliqué par l'effet du champ de déformation de la couche de cross hatch pattern.

1. Les perspectives de l'énergie photovoltaïque

Depuis la révolution industrielle, l'industrie moderne est alimentée par les énergies fossiles telles que le pétrole, le charbon ou encore le gaz naturel. L'efficacité énergétique que ces énergies offraient a permis le développement de nos sociétés modernes et des biens de consommation et de confort. Néanmoins, force est de constater que ce développement irréversible produit des effets non négligeables sur l'environnement et sur l'homme. En effet, le changement climatique, la pollution de l'air et les conséquences sur la santé des personnes suscitent une prise de conscience auprès des gouvernements et des citoyens. Ces derniers sont de plus sensibles au développement des énergies renouvelables et l'ensemble des politiques publiques nationales et internationales intègrent des programmes de développement avec pour ambition la réduction de l'empreinte humaine sur l'environnement (Fig. 1).

Fig. 1 Vue de Pékin en janvier 2013.

Parmi les énergies renouvelables qui ont la faveur des preneurs de décision, on trouve la conversion photovoltaïque. A ce jour, plusieurs technologies photovoltaïques ont été établies ou sont à l'étude *e.g.* cellules solaires en couche mince (CIGS, CdTe, a-Si:H), cellules à base matériaux III-V (le plus souvent sous concentration) et les cellules à base de silicium cristallin (c-Si). Bien que les technologies récentes (jonctions multiples, CPV etc.) puissent présenter un meilleur rendement de conversion, leur coût de production demeure rédhibitoire et les modules à base de silicium dominent toujours le marché mondial (Fig. 2).

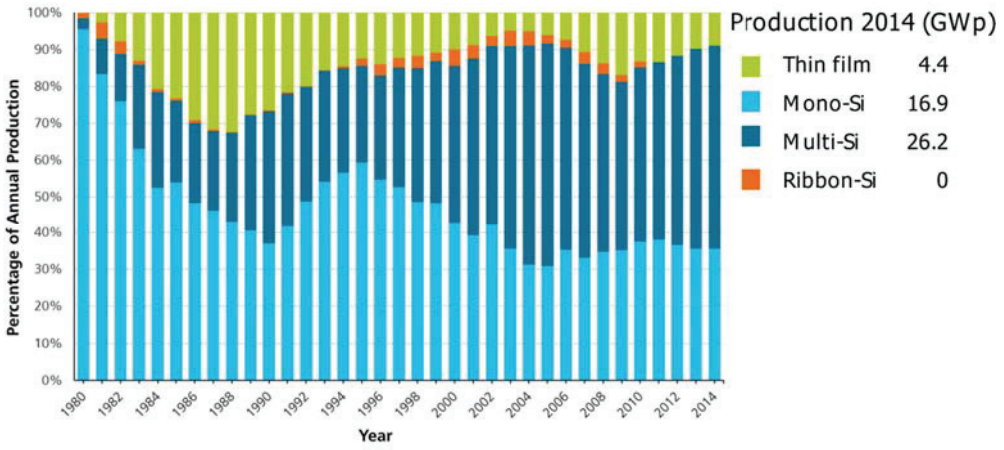

Fig. 2 Production photovoltaïque par technologie [1].

2. Cellules solaires à hétérojonction de silicium : amorphe/cristallin

Malgré leur bon rendement et leur faible coût, les cellules solaires à base de silicium présentent deux défauts : le budget thermique indispensable à la diffusion des dopants pour la fabrication des cellules solaires de la première génération est conséquent ; afin d'éviter les pertes par manipulation ou les contraintes thermiques, le substrat est bien plus épais que l'épaisseur nécessaire à l'absorption des photons. La deuxième génération de cellules solaires est basée sur les couches minces et donc consomme moins de matériau. Notamment, le dépôt de silicium amorphe hydrogéné (a-Si:H) peut être réalisé par PECVD (Plasma-enhanced chemical vapor deposition) à une température <250°C que pour le c-Si. Depuis quelques années, de nouvelles cellules solaires en silicium combinent les avantages des deux matériaux par le dépôt d'une couche très mince de a-Si:H pour passiver la surface du c-Si et pour former des hétérojonctions. La figure 3 représente le schéma d'une cellule SHJ (silicon heterojunction) et son diagramme des bandes d'énergie.

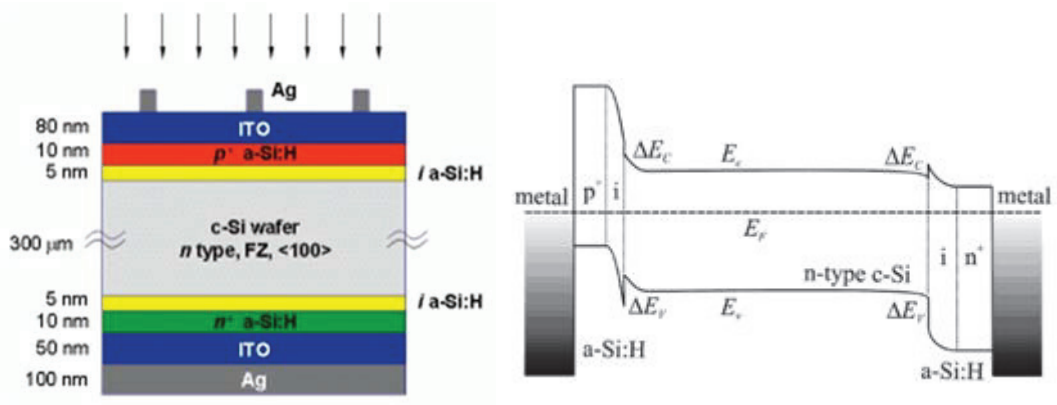

(a) (b)

Fig. 3 (a) Cellule à hétérojonction a-Si:H/c-Si et (b) le diagramme de bande.

3. Caractérisation de l'hétérojonction a-Si:H/c-Si par les techniques de photoluminescence en régime stationnaire et en régime modulé

La technique de photoluminescence modulée (MPL) a été développée à partir de la photoluminescence (PL) afin d'étudier la durée de vie des échantillons dans les SHJ [2]. Lorsqu'un matériau est illuminé par une excitation modulée, le taux de génération des paires électron-trou est soumis à la même modulation :

$$\tilde{G}(t) = G_{DC} + G_{AC}e^{i\omega t} \qquad \text{(Eq. 1)}$$

G_{DC} et G_{AC} sont les composantes continues et modulées du taux de génération des porteurs. ω est la fréquence angulaire de modulation. La variation de l'intensité de la PL mesurée en fonction du temps s'exprime avec un déphasage ϕ :

$$\tilde{I}(t) = I_{DC} + I_{AC}e^{i\omega t} \qquad \text{(Eq. 2)}$$

I_{DC} et I_{AC} sont respectivement la composante continue et l'amplitude de la composante du premier ordre de l'intensité de photoluminescence.

On montre que

$$\phi(\omega) = -\tan^{-1}(\tau_{eff}\omega) \qquad \text{(Eq. 3)}$$

et

$$I_{AC}(\omega) = \propto \frac{1}{\sqrt{1+(\omega\tau_{eff})^2}} \qquad \text{(Eq. 4)}$$

Ces expressions, nous permettent de déterminer la durée de vie effective τ_{eff} à partir du déphasage ou de l'amplitude de la luminescence en régime modulé.

Dans notre travail, nous avons défini les concepts de durée de vie stationnaire τ_{ss} et différentielle τ_{diff}. Le premier se réfère aux mesures effectuées en mode continu ou quasi stationnaire. Le

second est lié à la modulation inhérente à un éclairement dépendant du temps. On montre ainsi, que La mesure MPL représente la durée de vie différentielle.

$$\tau_{ss} = \frac{\Delta n_{DC}}{G_{DC}} \qquad \text{(Eq. 5)}$$

$$\tau_{diff} = \frac{d\Delta n_{DC}}{dG_{DC}} \qquad \text{(Eq. 6)}$$

4. Caractérisation expérimentale et simulation de SHJ

Cartographie de PL/MPL

Dans un premier temps, nous avons adapté le banc de mesure pour permettre d'une part des mesure à basse temperature jusqu'à 20K et une station de cartographie pour cartographie des substrats PV. Nous avons comparé des cartographies par les techniques de PL et MPL sur des précurseurs de cellules SHJ afin d'analyser leur homogénéité, figure 4. Bien que les deux techniques de cartographie produisent des résultats assez similaires, la cartographie de PL est très dépendante des paramètres optiques du système de mesure et du montage. Ainsi, le carré de plus forte intensité sur la figure 4 (a) est lié à une modification de la réflexion provenant du porte-substrat et non pas aux propriétés de l'échantillon. En revanche, la cartographie de MPL donne une image claire de l'échantillon et ne dépend pas des caractéristiques optiques du montage.

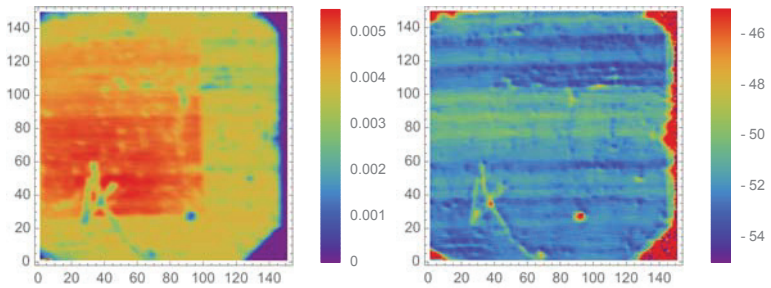

(a) (b)

Fig. 4 Cartographie de : (a) intensité de PL et (b) déphasage de MPL.

Caractérisation de durée de vie effective dans du c-Si avec différentes couches de passivation

Dans un second temps, nous avons mesuré à température ambiante des échantillons de différentes hétérojonctions de silicium formées entre un substrat de c-Si de haute qualité et des couches de passivation diverses. Sur les échantillons avec une passivation formée uniquement

d'une couche de silicium amorphe intrinsèque, nous observons que l'augmentation de l'épaisseur de la couche intrinsèque conduit à l'augmentation de la durée de vie. Les mesures de la durée de vie d'échantillons représentatifs de l'émetteur des cellules (passivation du silicium cristallin de type n par une bicouche formée de a-Si:H intrinsèque et de a-Si:H de type p) indiquent qu'un dopage plus important dans l'émetteur entraîne davantage de défauts d'interface et par conséquent augmente la recombinaison des porteurs. Nous avons aussi montré que la passivation par du a-Si:H de type n créait moins de défauts d'interface.

Caractérisation en fonction de la température

Nous avons mesuré la durée de vie des échantillons à SHJ en fonction de la température. Nous trouvons que les durées de vie de tous les échantillons diminuent quand la température diminue indépendamment du niveau d'injection. Ce comportement global ne dépend pas de la structure de SHJ ni du type de passivation (Fig. 5) [3].

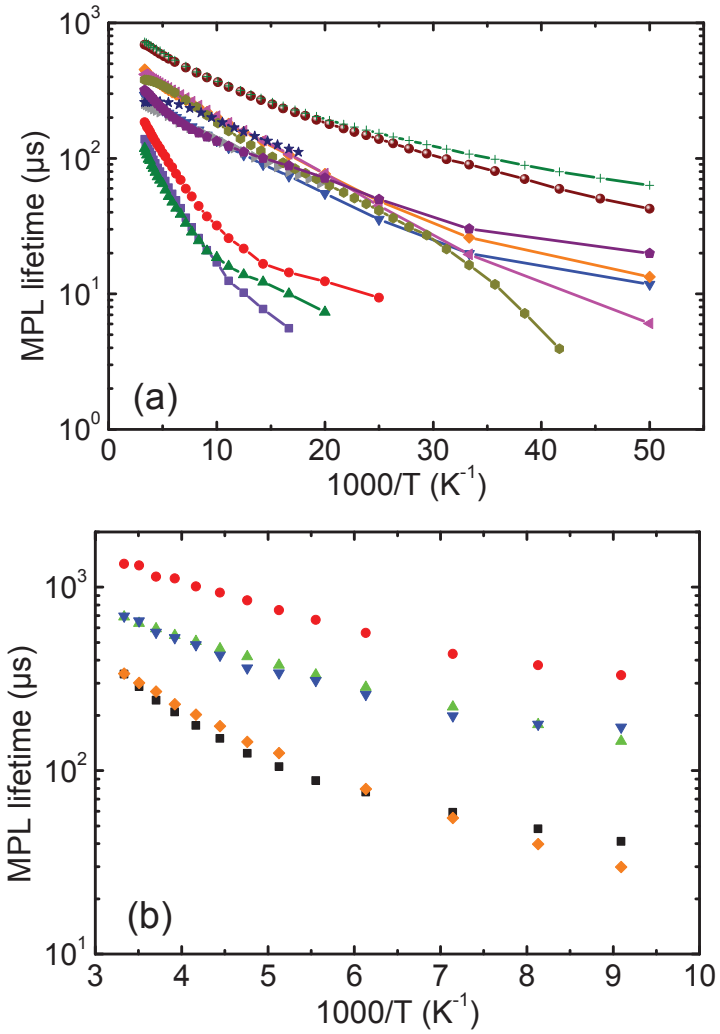

Fig. 5 Durée de vie mesurée par MPL sur différents échantillons à SHJ pour différentes couches de passivation (a) sous forte injection et (b) sous faible.

En régime de faible injection, en utilisant le modèle de recombinaison de Shockley-Read-Hall (SRH) il est possible d'analyser ces résultats en termes de niveaux d'énergie. Cependant, les écarts énergétiques observés par rapport au bord de bande sont très faibles, ce qui peut semer le doute quant à une analyse considérant des propriétés homogènes sur toute l'épaisseur de la structure. Afin de bien prendre en compte les courbures de bande aux interfaces, nous avons effectué des simulations par éléments finis.

Simulation

Des simulations numériques ont montré qu'il est nécessaire de tenir compte du niveau donneur du phosphore dans le substrat comme un centre de recombinaison SRH. En ajoutant des défauts à l'interface, il est possible d'obtenir des valeurs de durée de vie et une dépendance avec la température semblables à celles obtenues expérimentalement par MPL (cf. Fig. 6). Toutefois, la reproduction des résultats expérimentaux n'est pas parfaite et nécessitera des travaux de modélisation plus poussés.

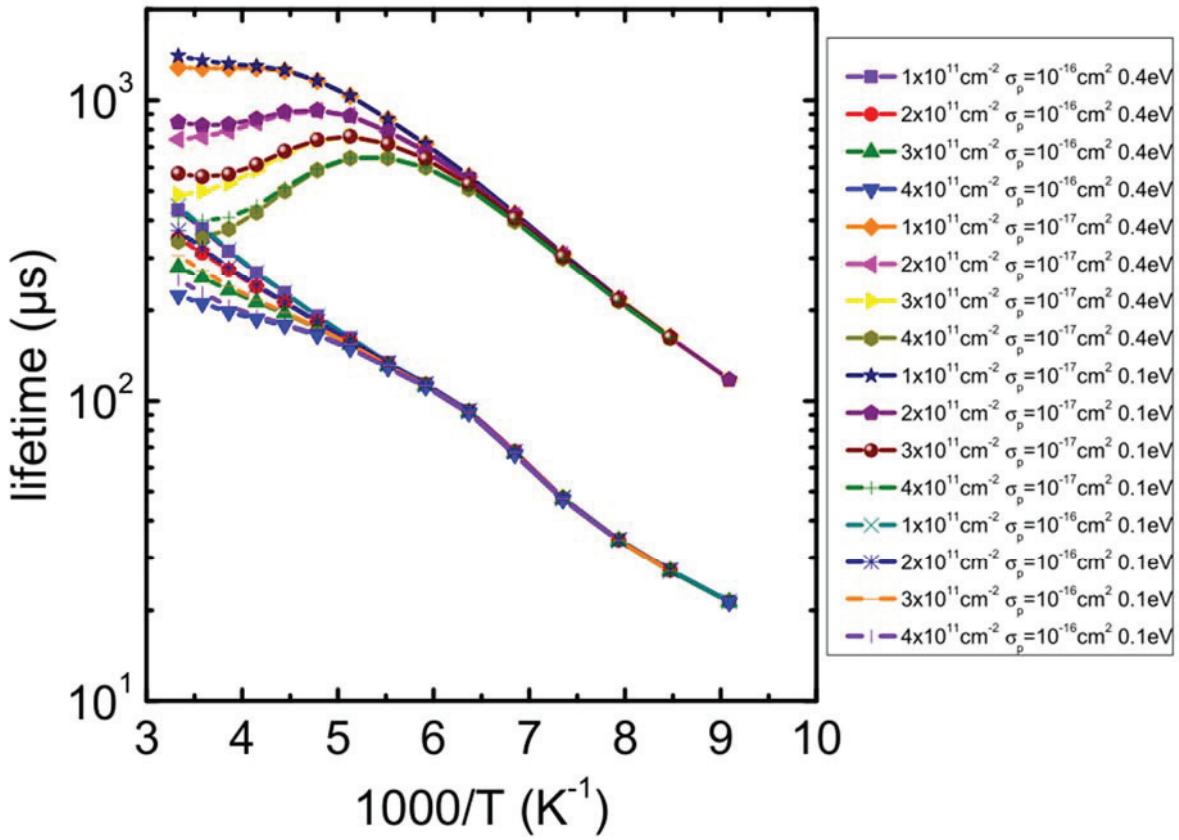

Fig. 6 Simulation de la durée de vie effective de cellules SHJ avec différents paramètres de la densité de défauts et de sections efficaces de capture, le niveau du phosphore est considéré comme centre de recombinaison

5. Comparaison PL/MPL : détermination de la dépendance avec la température du coefficient de recombinaison radiative

La combinaison des techniques de PL et de MPL nous a permis d'étudier le coefficient de recombinaison radiative *B* en fonction de la température. Les résultats publiés jusqu'ici dans la littérature couvrent la plage de température de 300 K à 90 K. Dans cette plage, nos résultats sont en très bon accord avec les résultats publiés précédemment. Mais, grâce à notre système de mesure et à la combinaison PL/MPL, nous avons pu étendre la plage de valeur du coefficient *B* jusqu'à 20 K (Fig. 7).

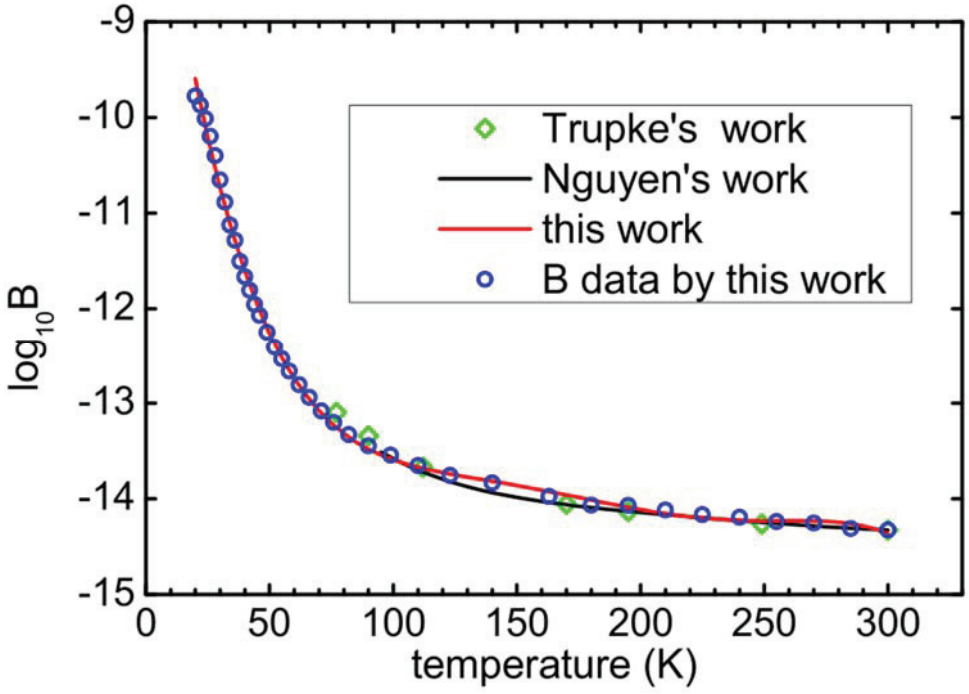

Fig. 7 Coefficient de recombinaison radiative B du silicium cristallin en fonction de la température, obtenu par les mesures de PL/MPL entre 20 et 300 K, et comparaison avec des résultats issus de la littérature [4][5].

Nous proposons une fonction polynômiale de $B(T)$ du cinquième degré qui permet de reproduire les variations en fonction de la température sur toute la plage de 20 K à 300 K :

$$log_{10} B(T) = -5.92914 - 0.230597\,T + 0.00271769\,T^2 - 1.57055 \times 10^5\,T^3 + 4.356627 \times 10^8\,T^4 - 4.6377 \times 10^{11}\,T^5 \quad \text{(Eq. 7)}$$

6. Observation du transfert de charge par PL et micro PL dans des empilements de chaines de boites quantiques en InAs

Dans le cadre d'une collaboration avec l'Université de Chulalongkorn (Thailande), nous avons étudié à l'aide de nos techniques de caractérisation micro PL le transfert de charge et couplage dans des empilements de chaines de boites quantiques en InAs. Ces boites quantiques croissent de manière ordonnée en formant des chaînes à partir d'une couche tampon en InGaAs (couche dite de "cross hatch pattern"). Nous avons caractérisé par PL des monocouches ainsi que des multicouches empilées (Fig. 8 (a)) [6].

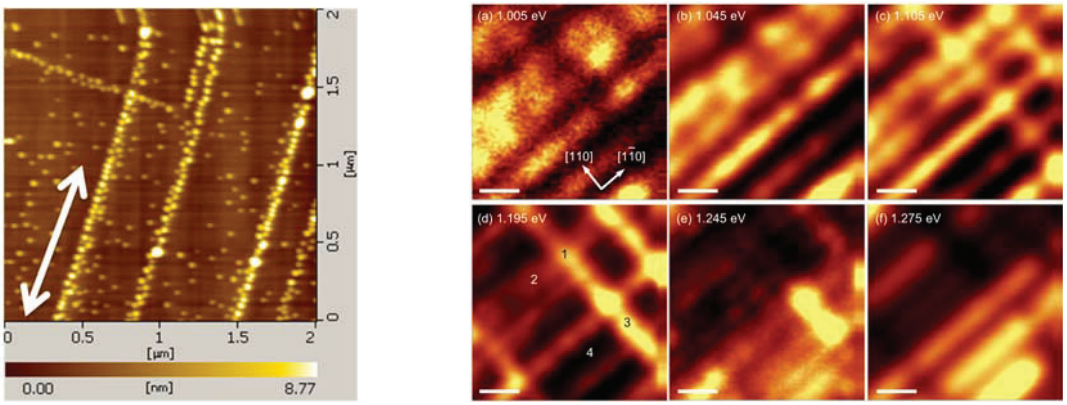

(a) (b)

Fig. 8 (a) Image AFM de l'échantillon avec 1-empilement et (b) la cartographie par micro-PL en fonction de l'énergie.

Les cartographies établies par microPL représentent les émissions des chaînes de boîtes quantiques le long des directions cristallographiques [110] (Fig. 8 (b)). Nous avons observé que lorsque les chaînes sont empilées et séparées par une couche de GaAs, la couche supérieure domine l'émission et les émissions de couches inférieures sont absentes. Cependant en augmentant la densité de puissance injectée nous avons observé que la couche supérieure sature et les pics d'émission des couches inférieures apparaissaient. Nous pouvons ainsi identifier et localiser les processus de transfert entre plusieurs couches empilées grâce à la cartographie micro PL [7].

7. Conclusion

Nous avons appliqué des techniques de photoluminescence en régime stationnaire (PL) et photoluminescence en régime modulé (MPL) à l'étude d'hétérojonctions formées entre du silicium cristallin (c-Si) et du silicium amorphe hydrogéné (a-Si:H). Nous avons comparé des échantillons constitués de dépôts de différentes couches de passivation sur des wafers de (n) c-Si

de haute qualité électronique. Les mesures en fonction de la température montrent que la durée de vie des porteurs en excès diminue lorsque la température diminue, ce qui peut être qualitativement reproduit par simulation en considérant un mécanisme de recombinaison de type Shokley-Read-Hall (SRH). Par ailleurs, nous montrons qu'il est nécessaire de tenir compte du niveau d'énergie du dopant (phosphore) dans le substrat et des niveaux peu profonds électroniquement actifs à l'interface. La comparaison de mesures de PL et MPL a permis de déterminer l'évolution avec la température du coefficient de recombinaison directe B(T) dans le silicium sur une large plage de température (de 300 K à 20 K). Ces mesures étendent la gamme de valeur disponible dans la littérature et nous proposons un modèle polynomial pour reproduire l'évolution de B(T). Enfin, nous avons aussi appliqué la technique de micro photoluminescence à l'étude de chaînes de boites quantiques d'InAs. Cette approche permet d'observer sur des cartographies micro PL l'effet du couplage entre des empilements de boîtes quantiques séparés par 10 nm de GaAs.

8. Références

[1] "Photovoltaics Report," Fraunhofer Institute for Solar Energy Systems, Mar. 2016.

[2] Ming Xu, Mohamed Boutchich, Alexandre Jaffre, Jose Alvarez, Marie-Estelle Gueunier-Farret, Jean-Paul Kleider, and Nazir P. Kherani, "Temperature dependent photoluminescence in silicon based heterojunction solar cell," in *EU PVSEC Conference Proceedings*, Amsterdam, Netherlands, 2014, pp. 1214 – 1217.

[3] M. Xu, "Characterization of a-Si:H/c-Si heterojunction by temperature dependent modulated photoluminescence," presented at the International Conference on Amorphous and Nanocrystalline Semiconductors, Aachen, Germany, Sep-2015.

[4] T. Trupke, M. A. Green, P. Würfel, P. P. Altermatt, A. Wang, J. Zhao, and R. Corkish, "Temperature dependence of the radiative recombination coefficient of intrinsic crystalline silicon," Journal of Applied Physics **94**, 4930 (2003).

[5] H. T. Nguyen, S. C. Baker-Finch, and D. Macdonald, "Temperature dependence of the radiative recombination coefficient in crystalline silicon from spectral photoluminescence," Applied Physics Letters **104**, 112105 (2014).

[6] M. Xu, A. Jaffré, J. Alvarez, J.-P. Kleider, A. Jittrong, T. Chokamnuai, S. Panyakeow, M. Boutchich, and S. Kanjanachuchai, "Temperature dependent photoluminescence and micromapping of multiple stacks InAs quantum dots," AIP Conference Proceedings 1649, 3 (2015).

[7] S. Kanjanachuchai, M. Xu, A. Jaffré, A. Jittrong, T. Chokamnuai, S. Panyakeow, and M. Boutchich, "Excitation transfer in stacked quantum dot chains," Semicond. Sci. Technol. **30**, 055005 (2015).

Acknowledgements

I would like to extend my sincerest thanks and appreciation to my supervisor Jean-Paul Kleider who is a knowledgeable scientist with great patience, to my co-supervisor Mohamed Boutchich for his kind help in life and impressive pursuit of career, also to my talented colleague José Alvarez whose enthusiasm impresses me a lot, and to Rudi Brüggemann for his mastery and meticulousness in the work. I would also like to thank Alexandre Jaffré for his experimental expertise, Marie-Estelle Gueunier-Farret for supporting me through the ANR-SMASH IBC² as well as Prof. Songphol Kanjanachuchai from Chulalongkorn University for his help to apply our luminescence techniques on a nanostructured system. This thesis would not have been possible without their support.

Thanks to the China Scholarship Council, who provided financial support during my graduate studies.

I would like to thank Prof. Anne Kaminski-Cachopo and Prof. Ramon Alcubilla González for having accepted to be the reviewers for my manuscript and getting along with the tight schedule. I also would like to thank the other members of the PhD defense committee, Dr. Delfina Muñoz, Dr. Arnaud Etcheberry and Dr. Paola Atkinson.

I thank all my colleagues of PHEMADIC division. I also would like to thank many other colleagues in the GeePs laboratory for their kindness and intuitive answer to my questions, which have helped advance this work. It has been a great time working with them.

Finally, many thanks to my family for their encouragements and confidence. And thanks to my dear friends for supporting and accompanying, although I do not list all your names, and Irene for her love.

Table of contents

1 Introduction **1**

1.1 Photovoltaics as a leading renewable energy . . . 1
1.2 Crystalline silicon based solar cells . . . 3
1.2.1 Structure of the c-Si solar cells . . . 3
1.2.2 Silicon heterojunction solar cell . . . 4
1.3 Hydrogenated amorphous material and amorphous/crystalline heterojunction 7
1.4 Project HERCULES . . . 10
1.5 Principle of photoluminescence . . . 11
1.6 Previous work . . . 13
1.6.1 Photoluminescence characterization . . . 13
1.6.2 Temperature dependent characterization . . . 18
1.7 Numerical simulation and guidelines . . . 20
1.8 Work in this thesis . . . 21

2 Experimental techniques **23**

2.1 Photoconductance measurement . . . 23
2.1.1 Transient mode . . . 25
2.1.2 QSSPC mode . . . 25
2.1.3 General mode . . . 25
2.2 Photoluminescence . . . 25
2.2.1 Macro-PL measurement . . . 26
2.2.1.1 Steady state PL . . . 28
Single point . . . 28
Mapping . . . 28
2.2.1.2 Modulated photoluminescence . . . 29
Theory . . . 29
System frequency response . . . 30
Measurement sensitivity . . . 30

Lifetime extraction 32
MPL mapping 32
2.2.2 Micro PL measurement 35

3 Theory and model **37**
3.1 Steady state vs. differential lifetime 37
3.2 Bulk recombination mechanism and related lifetime 41
3.2.1 Band to band radiative recombination 41
3.2.1.1 Steady state lifetime 41
3.2.1.2 Differential lifetime 41
3.2.1.3 Temperature dependence 42
3.2.2 Auger recombination 43
3.2.2.1 Steady state lifetime 43
3.2.2.2 Differential lifetime 44
3.2.2.3 Temperature dependence 46
3.2.3 Defect-mediated non-radiative recombination 47
3.2.3.1 Steady state lifetime 47
3.2.3.2 Differential lifetime 47
3.2.3.3 Temperature dependence 50
3.3 Comparison of steady state and differential lifetime 53
3.3.1 Auger and radiative recombination 53
3.3.2 Auger, radiative and SRH recombination 54
3.4 Simulation of the differential lifetime 56
3.4.1 Investigated structure 56
3.4.2 Simulation method of the MPL lifetime 59
3.4.3 Lifetime extraction from different regions 60
3.4.3.1 Without space charge layer 60
3.4.3.2 With inversion layer 63
3.5 Conclusion 67

4 Experimental results **69**
4.1 Samples: sources and description 69
4.2 Measurement of the lifetime at room temperature by PL and MPL 74
4.2.1 Comparison of the photoconductance decay QSSPC and transient modes 74
4.2.2 Comparison between the photoconductance decay and MPL 75
4.2.3 MPL lifetime measurements on SHJ 77

4.2.3.1 Impact of the intrinsic layer . . . 77
4.2.3.2 Impact of the emitter and the doping . . . 78
4.2.3.3 Emitters versus BSF . . . 79
4.2.3.4 Impact of the TCO . . . 80
4.2.4 PL and MPL mapping . . . 82
4.2.4.1 PL mapping . . . 82
4.2.4.2 MPL mapping . . . 84
4.3 Temperature dependent PL/MPL measurements . . . 86
4.3.1 Steady state photoluminescence . . . 87
4.3.1.1 Regular temperature dependence of the photoluminescence 87
4.3.1.2 Irregular temperature dependence of the Photoluminescence 88
Observation of the photoluminescence quenching . . . 90
4.3.2 Temperature dependence of the modulated photoluminescence . . . 92
4.3.2.1 High injection . . . 93
4.3.2.2 Low injection temperature dependent lifetime spectroscopy 93
Emitter with an intrinsic a-Si:H layer . . . 93
Emitter without the intrinsic a-Si:H layer . . . 96
Intrinsic a-Si:H layer only . . . 96
BSF . . . 96
AlOx . . . 96
Summary of the temperature dependence of the MPL lifeitme 96
4.3.2.3 Temperature dependence of the integrated PL spectrum . 99
4.4 Simulation . . . 103
4.4.1 Without SRH recombination from doping . . . 103
4.4.1.1 Low level illumination intensity . . . 103
4.4.1.2 High level illumination intensity . . . 104
4.4.2 With SRH recombination from doping . . . 105
4.4.2.1 Low level illumination intensity . . . 106
4.4.2.2 High level illumination intensity . . . 106
4.4.2.3 Surface defects and phosphorus defect at the same time . 107
4.4.2.4 Conclusion of the simulation . . . 108
4.5 Conclusion . . . 109

5 Observation of the Excitation transfer in stacked quantum dot chains by micro PL 111
5.1 Introduction . . . 111
5.2 Experimental . . . 113

5.3 QDCs stacks morphology . . . 114
5.4 Results and discussion . . . 116
5.4.1 Single QDC layer: basic emission peaks . . . 117
5.4.2 Multi-Stack QDCs: dominant emission from top-most layers . . . 120
5.4.3 Multi-Stack QDCs: excitation transfer . . . 122
5.5 Temperature dependent PL of QDs . . . 124
5.6 Conclusion . . . 128

6 Conclusions and perspectives **129**
6.1 The road so far . . . 129
6.2 A look into the future . . . 131
From the experimental point of view . . . 131
From the analysis and simulation point of view . . . 132

References **133**

Appendix A Derivation of MPL theory **145**
A.1 Modulated carrier concentration . . . 145
A.2 Modulated PL . . . 146

Appendix B Setup specifications **149**
B.1 Macro PL . . . 149
B.2 Micro PL . . . 150

Appendix C PL transient decay **151**

Appendix D Abbreviations table **155**

Appendix E Publications **157**

Chapter 1

Introduction

1.1 Photovoltaics as a leading renewable energy

Modern industry is powered by fossil fuels such as oil, coal and natural gas. the industrial revolution enabled higher energy conversion efficiency as well as the exploitation of new fossil resources that were not accessible to human consumption. in the 21st century, fossil fuel remain the leading energy supporting human activities. Although not sustainable, it is far away from exhaustion. However, the environmental impact is becoming increasingly critical : climate change and air pollution becoming global concerns government as well as citizen calling for renewable and clean energy to reduce human fingerprints upon the environment.

Requirements for cleaner environment and health care become stringent. In many cities around the world, people have to cope with days when PM2.5 (Particulate Matter up to 2.5 micrometers in size) level reach health and safety limit (see Fig. 1.1).

In that regard, both renewable energies and products running on clean energies take an increasing share in the daily life confronted with both the environmental pressure and climate change. Being aware of the irreversible damage in front of us, institutions and governments have invested worldwide in the research on renewable energies particularly solar energy, see Fig. 1.2. As it is reported by NREL, PV capacity has grown by a factor of 68 between 2000 and 2013, Germany leading the installed capacity with 35.9 GW [2].

To date, various PV technologies are established or under investigation: thin film solar cells (CIGS, CdTe), concentration solar cells based on III-V materials and silicon based solar cells. Although the recent technologies (multiple junction CPV etc.) could potentially achieve higher efficiency and lower cost per watt, as shown in Fig. 1.3, silicon based device still dominate the global market.

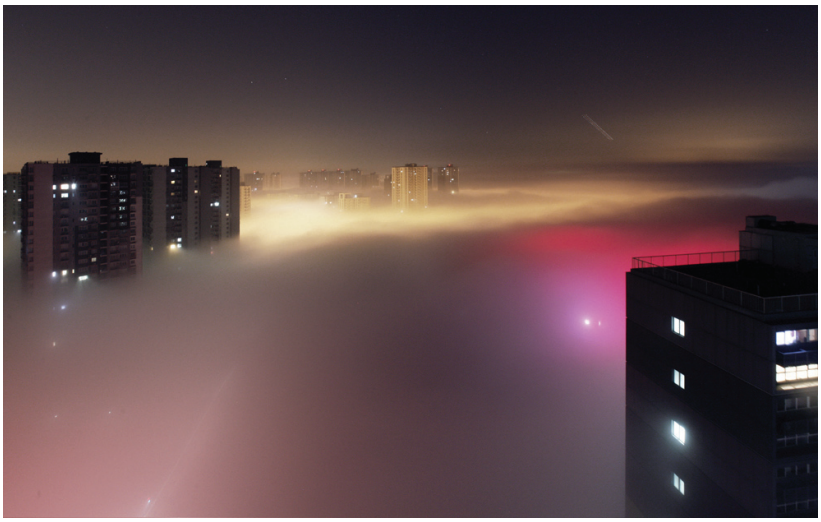

Fig. 1.1 Fantastic airpocalypse in Beijing January 2013 [1].

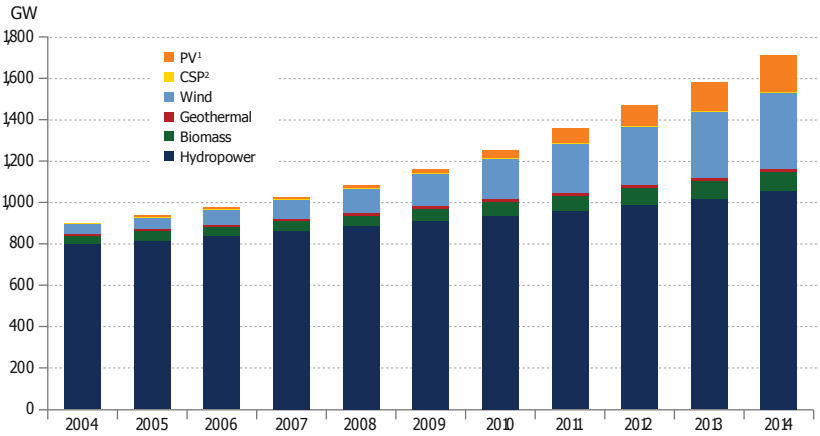

Fig. 1.2 PV capacity evolution among all renewable energy. (*PV, photovotaics **CSP, concentrated solar power)

As shown in Fig. 1.4, silicon solar cells contribute up to 90 percent of global shipment in 2014.

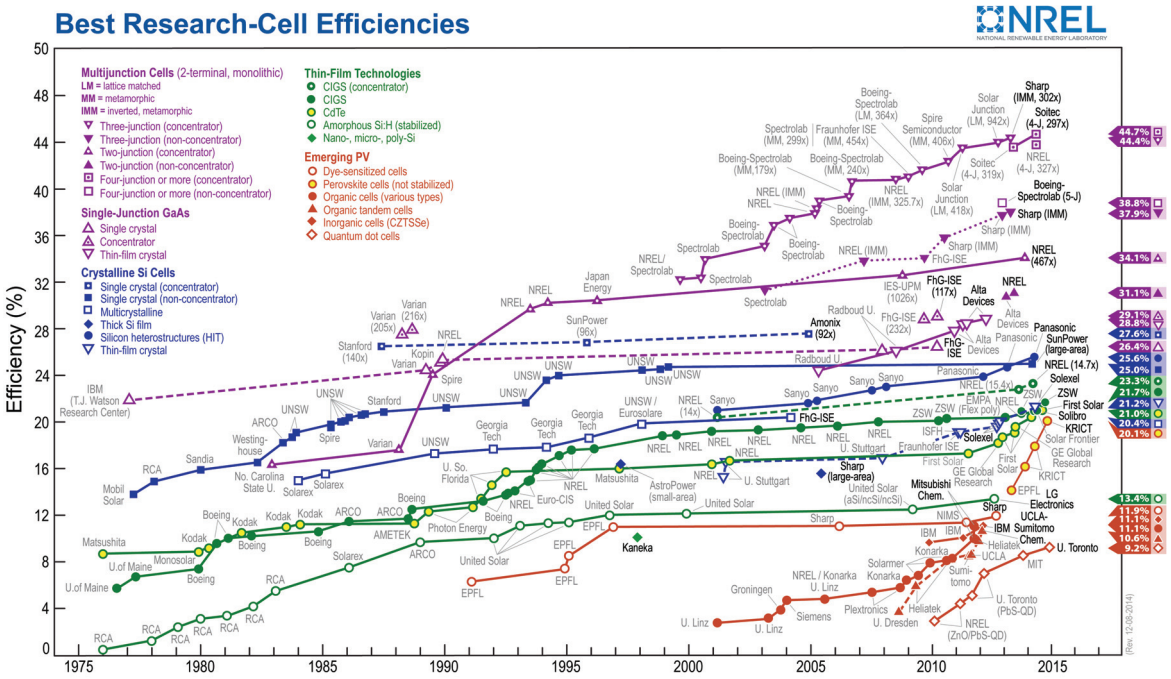

Fig. 1.3 PV efficiency of all existing technologies and their evolutions [2].

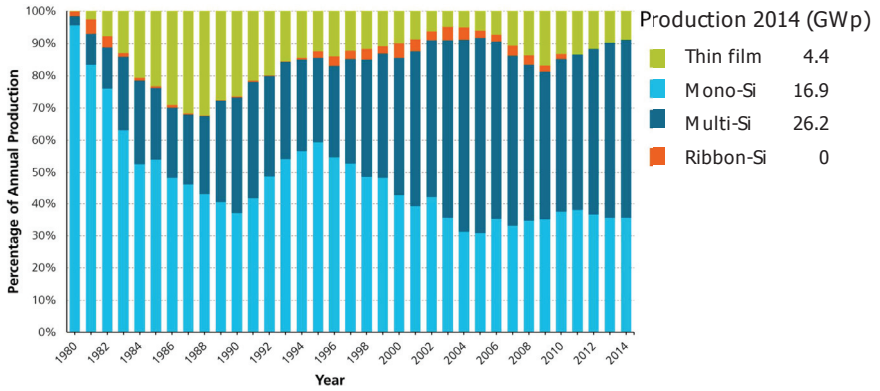

Fig. 1.4 PV production in year 2014 [3].

1.2 Crystalline silicon based solar cells

1.2.1 Structure of the c-Si solar cells

The classical and currently commercialized solar cell is composed of a p-type wafer as the absorber, an n+ layer as the emitter, an anti-reflection layer and Ag wirings on top as well as back side Al contact and back surface field (BSF) at the back interface [4], see Fig. 1.5 leftmost. In this configuration, the back side of the cell is in direct contact with the Al contact. After a firing process, this interface turns into an alloy and the Al gives rise to BSF

and band bending which repulses minority carriers from the back surface, thus decreasing recombination. The Al BSF does not passivate the interface defects as efficiently as a dielectric passivation. Moreover, the thermal expansion coefficients of Al and Si are different rendering the stack prone to fracture when thinner substrate are utilized.

This structure has been replaced by the PERC (Passivated Emitter, Rear Contact) structure [5], the PERL (Passivated Emitter, Rear Locally diffused) [6], and the PERT (Passivated Emitter, Rear Totally diffused) [7] proposed by UNSW as shown in Fig. 1.5. The PERC cell, consists of a back surface that is passivated with a dielectric where some holes are left open to permit the Al contacts to reach the heterojunctions. To further decrease the recombination at the Al/Si interface. The PERL cell, is an extension of the PERC where the contact region has been locally doped to form a BSF. The recombination can be even further reduced by combining the dielectric and BSF yielding to the PERT cell where the structure is composed of a BSF at the Si/dielectric interface.

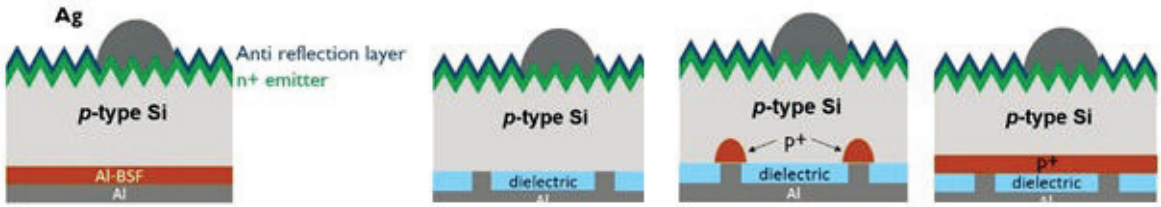

Fig. 1.5 BSF, PERC, PERL and PERT structure of solar cells [8].

Despite the dramatic increase of the efficiency, these structures present several drawbacks. The holes in the dielectric layer are drilled by laser ablation that causes damage to the wafer and create defects. In addition, the pathways for collecting carriers are limited to small areas, thus having a negative impact on the fill factor.

A promising solution would be to passivate the contact [9]. In this configuration, the whole interface between metal contact and silicon wafer is passivated and thus there is no direct contact, such as in hydrogenated amorphous/crystalline silicon heterojunction solar cells.

1.2.2 Silicon heterojunction solar cell

Despite their high efficiency and their relatively low cost, the classical silicon solar cells processes suffer from high thermal budget necessary to diffuse the dopants to form the PN junction or the BSF. A promising solution is provided by the silicon heterojunctiion (SHJ) solar cell where the PN and BSF junctions are founded by the deposition of hydrogenated amorphous silicon. Indeed, the deposition of a-Si:H thin films can be realized by PECVD

(Plasma-enhanced chemical vapor deposition) at much lower temperature than that of c-Si. Since then, silicon solar cells combine the advantages of the two materials by the deposition of a-Si:H onto c-Si wafers to form the silicon heterojunctions (SHJ). The stack and band diagram of a typical SHJ solar cell is shown in Fig. 1.6 and we will discuss it in the next section.

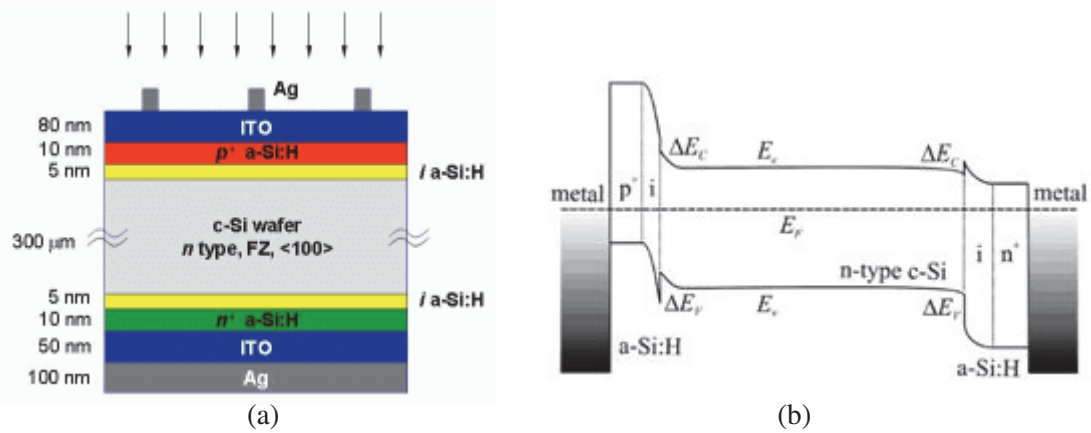

Fig. 1.6 (a) Structure of a-Si:H/c-Si heterojunction solar cell and (b) band diagram [10].

In 1983, Hamakawa and Okuda reported the first amorphous and polycrystalline heterojunction solar cell, with an efficiency of over 9% and 12%, respectively [11, 12]. The major breakthrough came in 1991, when SANYO Electric Cooperation introduced the advanced HIT structure (Heterojunction with Intrinsic Thin-layer) to reach an efficiency of 14.8% [13]. When the technology was further improved with texture on the surface, the efficiency reached 16.8% and later on 18.4% with the back surface field implemented at the rear of the cell. This configuration turned out to be then the most efficient concept in silicon wafer solar cell technology and the record was regularly improved over years. It is worth mentioning that in October 2015 Kaneka and New Energy and Industrial Technology Development Organization (NEDO) announced their SHJ solar cell with double-sided electrodes that reached a conversion efficiency of 25.18%.

The driving force to improve the efficiency of modern solar cells consists of adapting the cell structure to reduce further the interface recombination at the back surface. There are some other aspects in the structure such as the surface texturation to reduce the reflection and the interdigitated back contact (IBC) solar cells to reduce the shadow effect from the contacts leads.

As illustrated in Fig. 1.7, the metal contacts of IBC cells are located in the back as an alternative arrangement to avoid the shadow of incident light, which reduces by 60-70% the optical loss compared to the previous structure [15]. As a result more sunlight reaches the

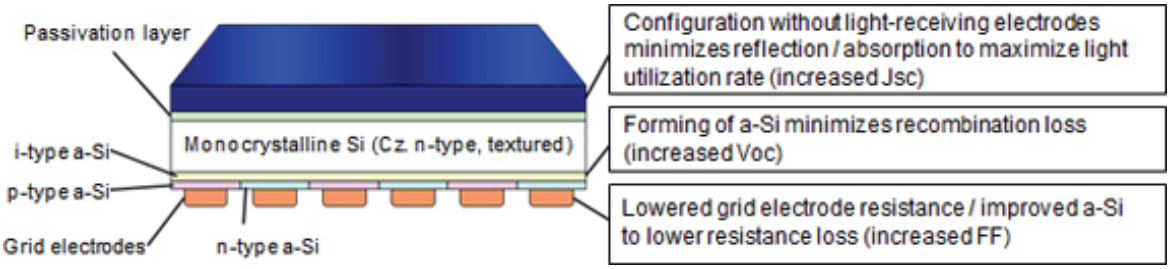

Fig. 1.7 Schematic of the IBC heterojunction solar cell [14].

absorption layer. Moreover, a thicker metal grid reduces the resistance loss when located on the back surface rather than at the front. However, the key to reduce the recombination loss significantly is to deposit high quality amorphous silicon on the crystalline wafer. The passivation layer on the front side is also crucial to the efficiency of the solar cell, although the details of this layer are not unveiled. In April 2014, Panasonic announced a HIT® solar cell of 25.6% efficiency [14, 16]. Details of the solar cell and the comparison with previous work are shown in Tab. 1.1.

Table 1.1 Progress of the efficiency [16].

Year	1991	2013	2014	Improvement 2013/2014
Area (cm^2)	1	101.8	143.7	
Thickness (µm)	N/A	98	150	
Voc (V)	0.614	0.750	0.740	-1.3%
Jsc (mA/cm^2)	37.9	39.5	41.8	+5.8%
F.F. (%)	0.776	83.2	82.7	-0.6%
Eff (%)	18.1	24.7	25.6	+3.6 %

The Voc is the open circuit voltage, Jsc the short circuit current, F.F. the fill factor and Eff the solar cell efficiency. Voc is an important factor that influences the solar cell efficiency, because it is directly related to the quasi-Fermi level splitting in the device and thus to the interface passivation. Since the quasi-Fermi level splitting is also related to the photoluminescence (PL) intensity emitted from the solar cell at the same time [17], the PL can be utilized to characterize the efficiency of solar cells and the quality of the interface passivation. Stronger PL intensity usually indicates higher Voc and efficiency.

1.3 Hydrogenated amorphous material and amorphous/crystalline heterojunction

The history of a-Si:H/c-Si silicon solar cells dawned with Grigorovici et al. [18] reporting the first a-Si:H/c-Si heterojunction in 1968. The a-Si:H was deposited by evaporation onto c-Si at room temperature to form a PN junction which exhibited rectification. At that time, the a-Si:H was so defective that the desirable electrical features were impossible to achieve. The first attempt of doping a-Si:H was carried out in 1969 by Chittick with phosphorus using PECVD [19]. Later, Brodsky conducted the characterization with IR and Raman spectroscopy on a-Si:H deposited at room temperature and 250 °C, respectively and concluded that the hydrogen bonds were responsible for the passivation effect [20]. Pankove found that the intrinsic amorphous silicon could serve as a good passivation for the crystalline silicon dangling bonds [21].

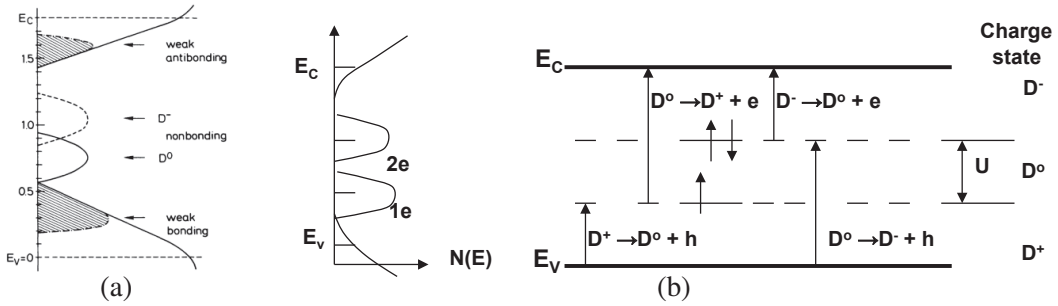

Fig. 1.8 (a) a-Si:H density of states in band gap. (b) Transition between band gap states [22].

The amorphous silicon is a disordered material which lacks the long-distance order in the lattice. There are a large number of silicon atoms with unpaired bonds which can be passivated with hydrogen. The hydrogen content can be as much as 10 atomic percent. Due to relaxation, it is a direct bandgap material. The density of the states differs greatly from that of the crystalline silicon [23] as shown in Fig. 1.8(a). The Si-Si weak bond in the material introduces band tails and the dangling bond of Si introduces deep defect states in the band gap.

Fig. 1.8(b) shows the amphoteric deep defect in the a-Si:H band gap. The defect is neutral when occupied by one electron (state D^0), positively charged when not occupied by any electron (state D^+) and negatively charged (state D^-) when occupied by two electrons. The defect can transit between these states. The transition between D^0 and D^- is often represented by a Gaussian distribution of acceptor states. The transition between D^+ and D^0 resembles donor and is often represented by a Gaussian distribution of donor states. D^+ and

D^0 are at the same energy level. However, more energy is needed for the second electron to induce the transition between D^0 and D^-. This energy is defined as the correlation energy.

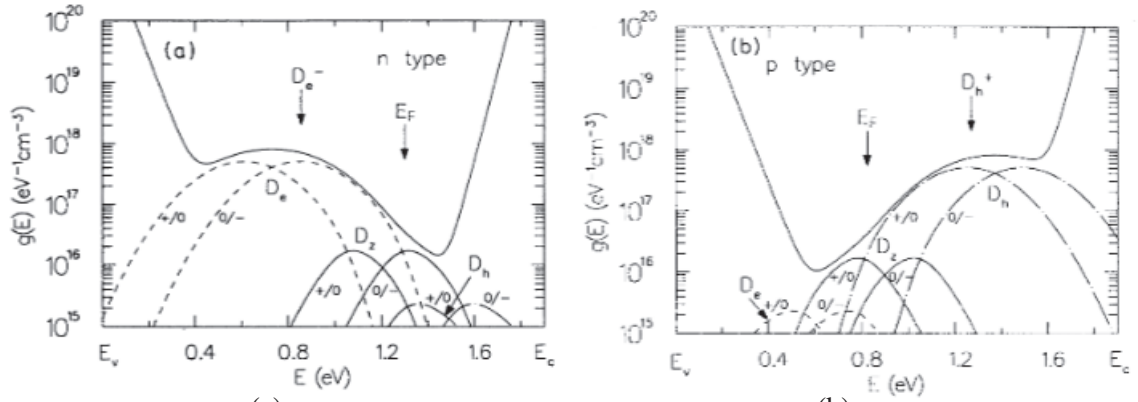

(a) (b)

Fig. 1.9 Different defect distribution in (a) n-type and (b) p-type a-Si:H bandgap according to the defect pool model [24].

There are several models to account for the defect distribution in amorphous silicon. The prevailing one would be the defect pool model [24, 25]. As shown in Fig. 1.9, the defect distribution is related to the Fermi level and changes with band bending. The position of Fermi level affects the balance of Si-Si weak bond.Thus when the Fermi level is close to the valence band, the defect state distribution is close to the conduction band and when the Fermi level is close to the conduction band, the defect state distribution is close to the valence band. In Fig. 1.10, at the SHJ interface, the distribution of defects in a-Si:H bandgap influences the interface with c-Si bandgap.

Let's take a detailed look at the structure of the a-Si:H/c-Si heterojunction solar cell and its band diagram [10]. As illustrated in Fig. 1.6(a), the wafer is typically 100 $\sim$ 300 µm thick, the intrinsic a-Si:H layer is under 10 nm and the doped a-Si:H layer around 10 nm. The band diagram of the heterojunction is shown in Fig. 1.6(b).

The band gap of a-Si:H is typically 1.75 eV. The alignment of the Fermi level at equilibrium results in a band bending. In Fig. 1.6(b), the intrinsic hydrogenated amorphous layer provides very effective passivation of the dangling bonds of crystal silicon interface, and at the same time isolates this interface from the defective doped a-Si:H or metal contact.

On the front side, the band bending between p-type a-Si:H and n-type c-Si prevents the transport of electrons. The bending forms a strong barrier against the electron transport from the wafer while the holes can either cross the barrier through thermionic emission or by tunneling. On the back side, the band bending formed by highly doped n-type a-Si:H and n-type c-Si prevents the transport of holes and the electrons cross to the n-type a-Si:H either

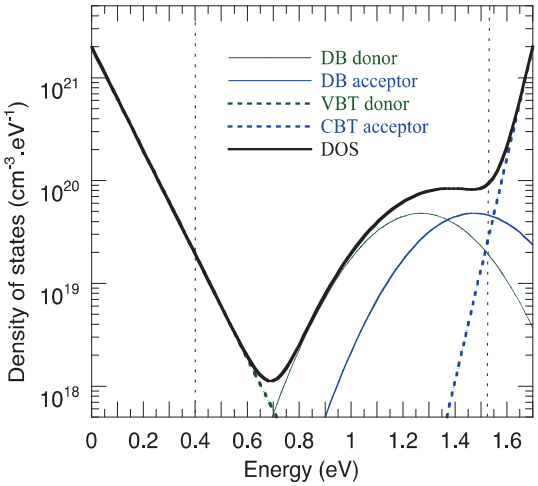

Fig. 1.10 The figure shows the density of states distribution in a-Si:H band gap. The distribution is calculated with defect pool model for p-doped a-Si:H. Two vertical dashed lines indicate the position of c-Si band edges with respect to the a-Si:H band edge of an SHJ. The defect state distribution in a-Si:H is projected into the c-Si. [26].

by thermionic emission or by tunneling through the intrinsic a-Si:H layer. The selective transport of carriers effectively reduces the interface recombination.

1.4 Project HERCULES

The abbreviation ”HERCULES” means ”High Efficiency Rear Contact solar cells and Ultra powerful moduLES”. It is a collaborative project within the framework of the European Union which aims at developing the innovative n-type c-Si device structures based on back-contact solar cells with alternative junction formation, as well as related structures including hybrid concepts (homo-heterojunction). 16 institutes* and industrial partners from 7 countries are involved as shown in Fig. 1.11.

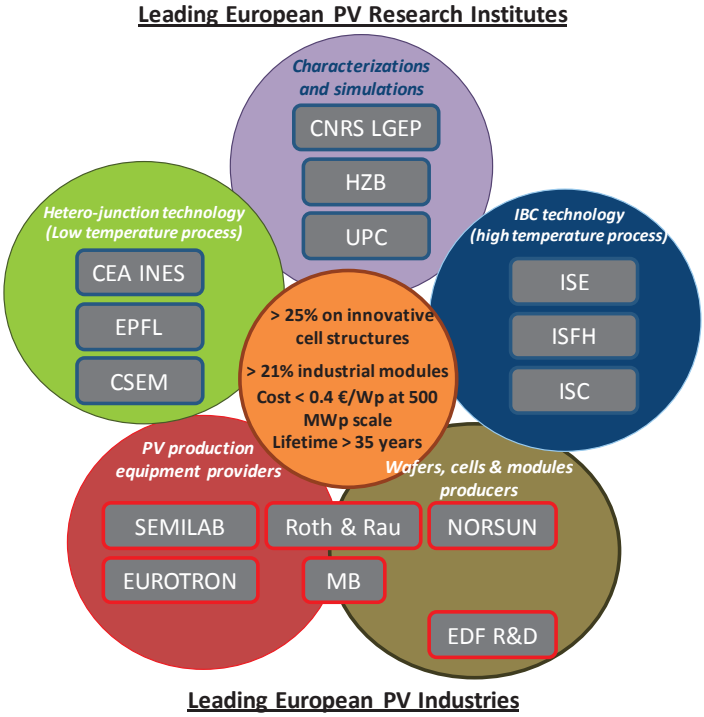

Fig. 1.11 HERCULES project partners [27].

The key objectives of the project are:

- To develop ultra-high efficiency modules at the pilot scale *i.e.* power conversion efficiency $\eta > 21\%$).
- To reduce production/investment complexity and demonstrate costs down to 0.7 €/Wp at pilot scale.
- To increase the durability of modules up to 35 years.
- To demonstrate ultra-high efficiency solar cells: $\eta > 25\%$.

* LGEP is the former name of GeePs

The leading concepts in the project objectives are:

- PERT (Passivated Emitter, Rear Totally diffused) cells:

  They have the advantage of being compatible with most of the usual equipment currently used in a p-type production line. Only two additional steps are required to switch from a p-type to an n-type wafer based process. PERT cells can have a bifacial design, leading to up to 30% higher power output as compared to single sided cells.

- IBC (interdigitated back contact) cells:

  If both electrical contacts are on the rear side of the cell, shading losses due the the front grid are absent and an independent front side optimization is possible. Furthermore, IBC cells open new opportunities for module interconnection.

- HET (Heterojunction) cells[*]:

  In amorphous/crystalline silicon heterojunctions, excellent passivation of the wafer's surfaces leads to solar cell Vocs exceeding 740 mV. Furthermore, all process steps are carried out at temperatures not exceeding 250°C, which makes the HET concept very attractive especially for very thin (100 µm and below) substrates.

Part of the characterization in this thesis is related to the HERCULES project.

1.5 Principle of photoluminescence

The term "photoluminescence" refers to the emission process where the radiation, that is the photon, is emitted due to excitation by means of light absorption.

All the objects absorb and re-emit electromagnetic radiation, no matter which kind of material they are composed of. Under thermal equilibrium condition, the thermal radiation is characterized by Plank's law and is only dependent on the temperature of the object. The object is called "black body" if all the incident radiations onto the object are absorbed. Incandescence is one example where the emission spectrum shifts to a visible range when an object is heated to over several thousand Kelvin as shown in Fig. 1.12.

In contrast, luminescence, first introduced by the German physicist Eilhard Wiedemann in 1888 [29], is a kind of emission that occurs when the system is out of thermal equilibrium. The radiation originates from electron transitions between energy levels in atoms or molecules, which are accompanied by the generation of photons, as it is addressed by Lasher et al. from the view of spontaneous transition [30]. When people tried to explain this

[*] In the context of the project, HET refers to SHJ (silicon heterojunction) in this thesis

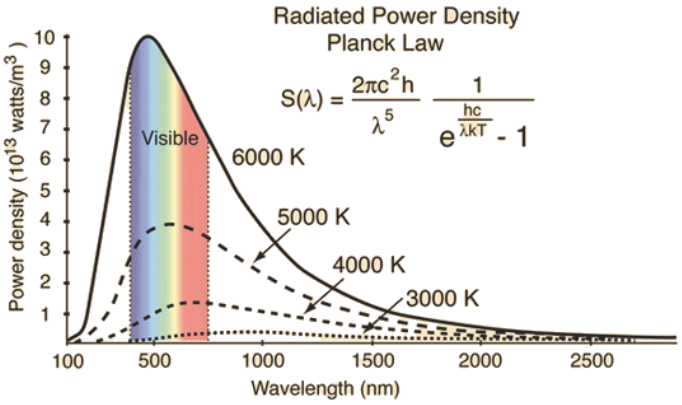

Fig. 1.12 Black body radiation at different temperature [28].

phenomenon with Planck's law, they ended with some effective temperature which is some impossible value compared with the real temperature of system [31].

Later this difficulty was overcome by P. Würfel by considering the split of chemical potential in the system. According to him, the principle is expressed as follows [32]:

$$n_\gamma = \frac{\kappa(\hbar\omega)^2}{\pi^2\hbar^3c^3}\left[\exp\left(\frac{\hbar\omega-(\mu_c-\mu_v)}{kT}\right)-1\right]^{-1} \tag{1.1}$$

where n_γ denotes the emission of photon current (number of photons per unit time per solid angle, per volume, per energy interval), c represents the vacuum light speed, κ is the material refractive index, and μ_c and μ_v are the chemical potential of electron and hole respectively. The photoluminescence is successfully interpreted by the generalized Plank's law.

If we consider the objects in reality as a grey body, the material absorption has to be taken into account. The photo current emitted from the surface of a slab of thickness d is described by the generalized Kirchhoff's law [32]:

$$j_r(\hbar\omega) = a(\hbar\omega)\frac{(\hbar\omega)^2}{4\pi^2\hbar^3c^2}\left[\exp\left(\frac{\hbar\omega-(\mu_c-\mu_v)}{kT}\right)-1\right]^{-1} \tag{1.2}$$

where j_r represents the number of photons emitted per unit time per unit area per unit energy interval per solid angle, and $a(\hbar\omega)$ is given by:

$$a(\hbar\omega) = [1-R(\hbar\omega)]\left[1-\exp(-\alpha(\hbar\omega)d)\right]\left[1-R(\hbar\omega)\exp(-\alpha(\hbar\omega)d)\right]^{-1} \tag{1.3}$$

where α is the absorption coefficient, R represents the reflectivity of the interface of the slab.

Würfel further extended this principle to indirect transitions to explain the crystalline silicon photoluminescence [33] as shown in Fig. 1.13.

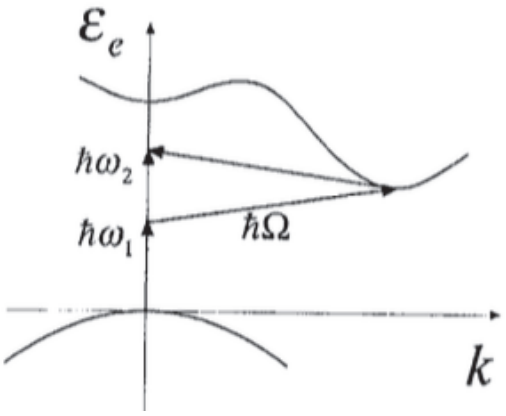

Fig. 1.13 c-Si bandgap transition is indirect and phonon-assisted. For the excitation process, an electron absorbs the photon energy $\hbar\omega_1$ and the phonon energy $\hbar\Omega$ to end up with energy $\hbar\omega_2$. For the emission process, an electron can either absorb the phonon energy $\hbar\Omega$ to emit a photon of energy $\hbar\omega_2$ or emit the phonon energy $\hbar\Omega$ and emit a photon of energy $\hbar\omega_1$ [33].

1.6 Previous work

1.6.1 Photoluminescence characterization

Photoluminescence has a long history as a characterization technique in semiconductor and photovotaics. In silicon solar cells, recombination mechanisms taking place in the material (Shockley-Read-Hall, Auger) are the dominant processes that are proportional to the electronic properties of the material. They can therefore be probed using luminescence techniques. A shematic of the three main recombination mechanism is shown in Fig. 1.14

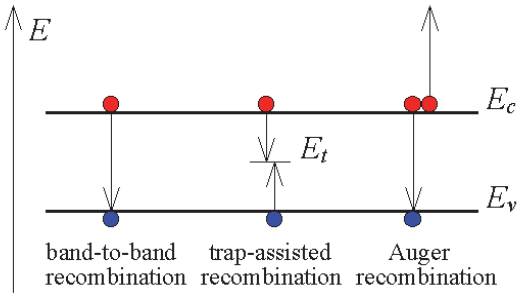

Fig. 1.14 Schematic of band-to-band radiative recombination, trap-assisted (SRH) recombination and Auger recombination [34].

PL is widely applied to determine wafer quality, passivation condition, excess minority carrier lifetime and impurities among other properties.

In 1981, Street investigated amorphous silicon using photoluminescence (PL) and recognized two emission bands which are related to defects and band tail states [35, 36].

In 1987 Colley and Lightowlers measured the concentration of impurities such as aluminum, phosphorus and boron in silicon by Fourier transform photoluminescence spectroscopy, as shown in Fig. 1.15.

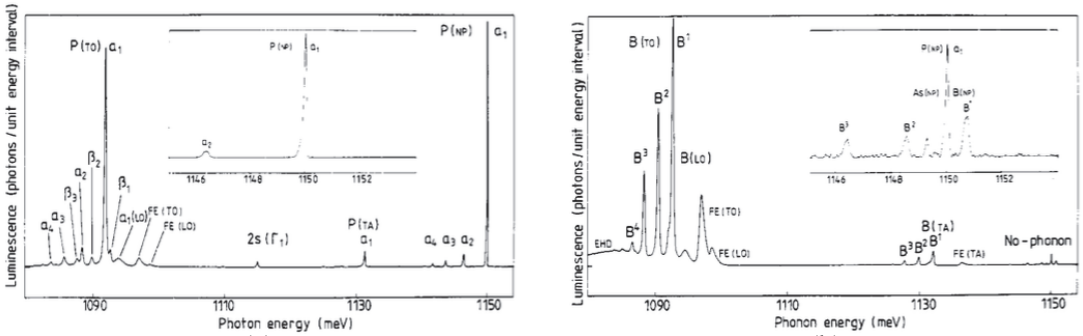

Fig. 1.15 PL spectrum obtained by 100 scans of samples containing (a) 3.2×10^{14} cm^{-3} phosphor and negligible boron, (b) 1.3×10^{13} cm^{-3} boron and negligible phosphorus [37].

Ahrenkiel applied time transient PL to determine minority carrier lifetime in GaAs in 1992 [38]. Time-resolved PL is applied to measure the sample lifetime and to investigate $Al_xGa_{1-x}As$/GaAs and GaInP/GaAs heterojunction devices.

Alex studied the temperature dependence of c-Si bandgap from 2 K to 750 K with PL spectrum as shown in Fig. 1.16. The analysis is based on indirect excitonic emission with 14.7 meV exciton binding energy. The shift of bandgap agrees with experiments better than some of others' theoretical predications.

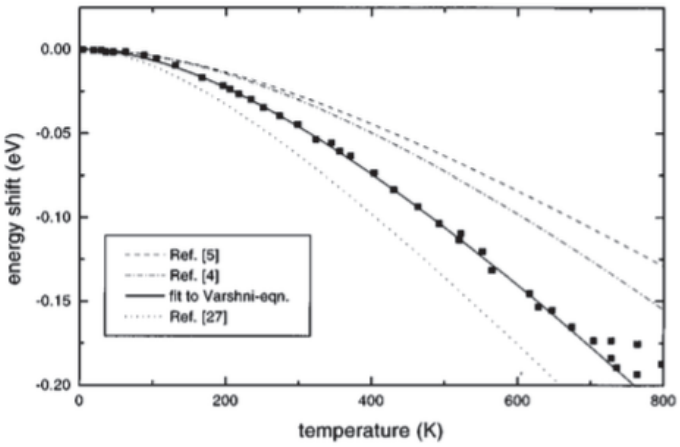

Fig. 1.16 Experimental data and Varshini equation fitting [39].

Trupke and his colleagues published a series of research work focused on the lifetime determination by quasi static state photoluminescence (QSSPL) [40, 41, 42, 43]. Here, PL

is measured while the excitation light varies slowly with respect to PL response and the sample can be considered as if in steady state. Trupke also reported the first lifetime imaging to estimate silicon wafer quality for photovoltaic application as shown in Fig. 1.17.

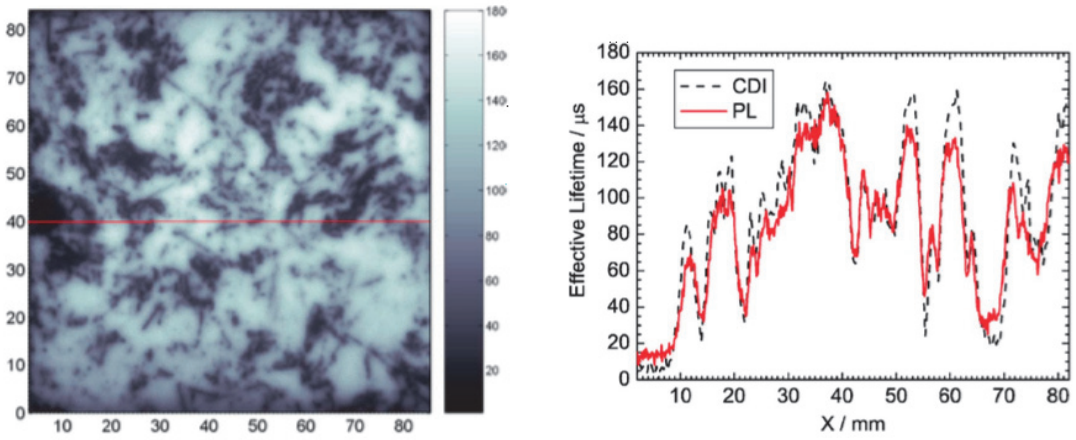

(a) (b)

Fig. 1.17 (a) Lifetime imaging obtained from PL decay of 8.5x8.5 cm2 area of a 302 µm thick, 1.2 Ωcm mc-Si p-type wafer. (b) Lifetime and carrier density profile of the image along the red line [44].

Tardon studied the a-Si:H/c-Si heterojunction and lifetime temperature dependence with PL (see Fig. 1.18). The dependence is explained by assuming that $E_c - E_{Fn}$ to be independent of temperature, and that the variation of effective density of states due to temperature dependence. We will discuss this in the modeling chapter. Courtois also investigated this question and explained the temperature dependence of lifetime by the decrease of radiative and Auger lifetime [45]. In fact, we have observed similar dependence even for low injection condition in which SRH recombination always dominates, as will be shown in the experiment chapter.

Bae developed the technique to determine the surface recombination velocity s_r by PL on silicon wafer. The commercial tool SiPHER has been utilized. This technique employs two different wavelengths, 532 nm and 827 nm to measure the PL intensity. The ratio of the two PL intensities R_{PL} contains the information on the surface recombination as shown in Fig. 1.19. The theoretical calculation of $R_{PL}(s_r)$ is made to for different minority carrier diffusion lengths. And from the experimental data and $R_{PL}(s_r)$ curves, s_r is obtained.

Photoluminescence has demonstrated its great flexibility in the characterization of silicon-based solar cell as it is contactless and nondestructive. No preparation, for example ITO or metal contacts, is required for the measurements. Furthermore, the principle of PL allows to investigate samples of both full size wafer and small size which is technically

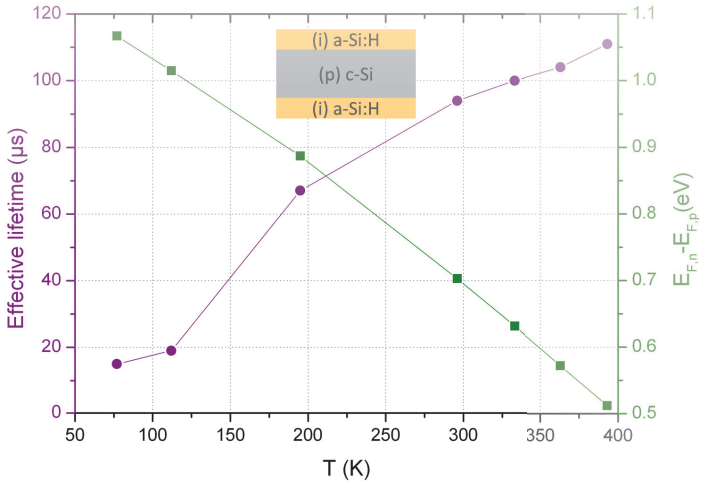

Fig. 1.18 Effective lifetime and quasi-Fermi level splitting of SHJ sample at various temperatures [45]. Data adapted by Courtois from [46].

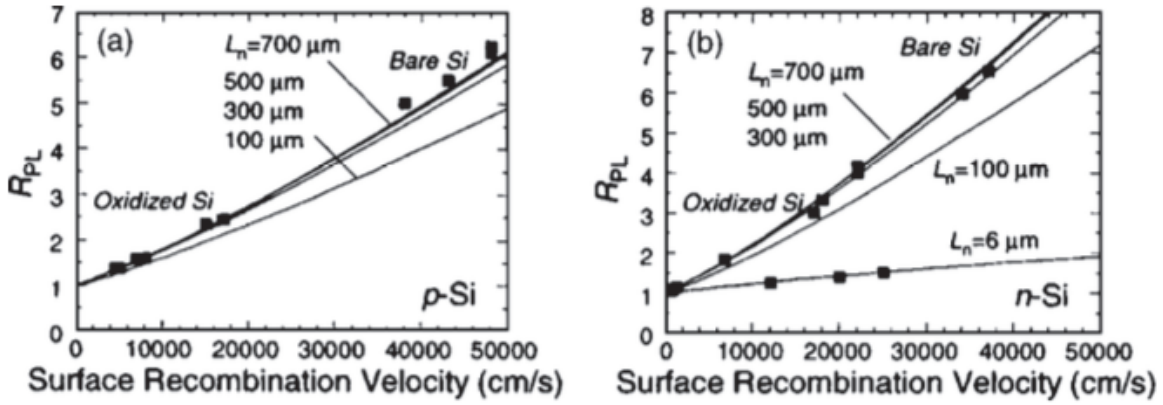

Fig. 1.19 Theoretical lines and experimental points PL intensity ratio R_{PL} vs front surface recombination velocity S_r as a function of diffusion length (a) p-type Si, (b) n-type Si. [47].

the most attractive advantage over photoconductance measurement. Most importantly, this technique is easily coupled to a cryostat for temperature dependent experiments.

In 2006 Brüggemann proposed the modulated photoluminescence (MPL) technique. He investigated the application of MPL in a-Si:H/c-Si heterojunction solar cells. Several kinds of passivations were examined with MPL technique as shown in Fig. 1.20. This technique is simple and straightforward, the determination of effective lifetime is independent of the absolute value of PL radiation. In 2009 he proposed that generalized Kirchhoff's law applies to a-Si:H/c-Si heterojunction [48].

Several studies on the characterization of a-Si:H/c-Si heterojunctions in recent years using PL such as: layer analysis during device deposition [50], carrier lifetime imaging by time-resolved PL (see Fig. 1.21) and by photoconductance decay method [51], DC-biased

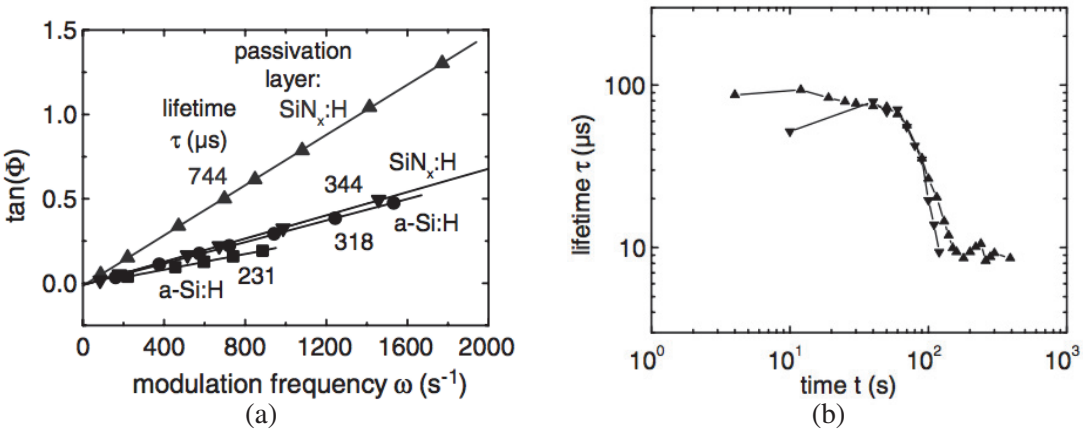

Fig. 1.20 Application of MPL. (a) Four different passivation layers deposited on p-type c-Si. The linear variation of tangent of phase shift in function of frequency is shown. (b) The passivation degradation of iodine/ethanol solution in air [49]. The lifetime drops with solution evaporation.

PL [52], valid range of commonly used PL relationship with respect to carrier profile and injection [53]. However, the research in a wide range of temperature has not been extensively reported particularly on PL applied to heterojunction solar cells.

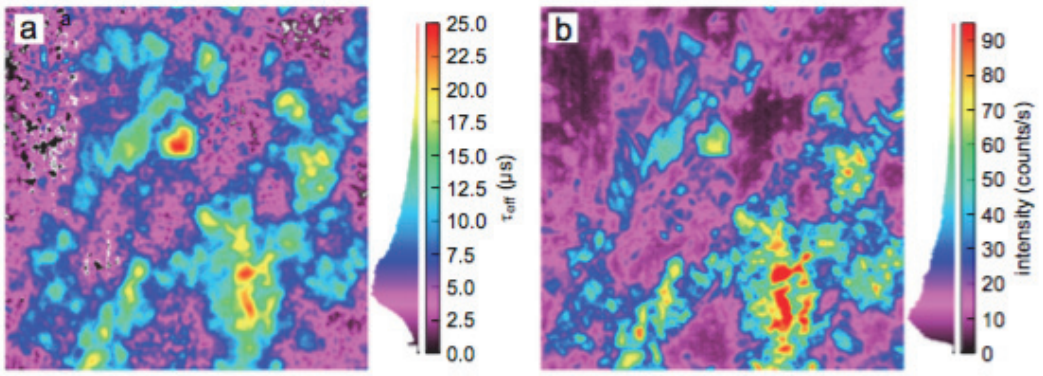

Fig. 1.21 (a) Lifetime and (b) PL imaging of SiNx passivated multi-crystalline Si wafer, extracted by time-resolved PL using fiber-coupled image intensifier unit from Hamamatsu Photonics [54].

J. Schmidt discussed the measurement of bulk "differential lifetime" $\tau_{b,d} = (\partial U(\Delta n)/\partial \Delta n)^{-1}$ and "actual lifetime" $\tau_b = \Delta n/U(\Delta n)$ [55].

He compared three techniques : microwave-detected photoconductance decay (μPCD), modulated free-carrier absorption (MFCA) and quasi-steady-state photoconductance (QSSPC). MW-PCD and MFCA are identified as differential measurements due to small signal modulation. QSSPC is considered to measure actual parameters. For high injection

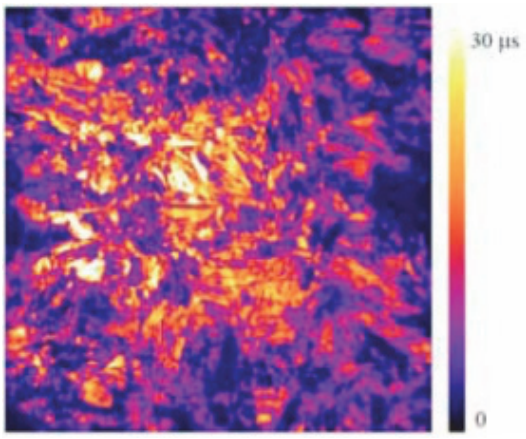

Fig. 1.22 Effective minority carrier lifetime from a PL image on a 6-inch SiN passivated multicrystalline silicon wafer. Calibration was achieved using a Sinton Instruments WCT120 QSSPC system integrated into the BT Imaging LIS-R1 PL imaging system [51].

measurements, QSSPC exhibits 3 times higher Auger lifetime than MFCA. For low injection measurements, they give similar results. He only investigated low lifetime samples in the QSSPC mode. He did not consider the transient mode although possible with his technique.

In [56], B. Halliop et al. deposited samples of a-Si:H/c-Si heterojunction by DC saddle-field PECVD and benchmarked the lifetime determined by MPL to alternative techniques. They compared the lifetime given by µPCD, QSSPC in different labs and MPL as shown in Tab. 1.2. The lifetime by the alternative techniques are generally twice larger than the MPL ones. However, they did not give detailed parameters about MPL measurement or about the QSSPC measurement.

Table 1.2 Progress of efficiency [56].

Sample	µPCD lifetime (µs)	WCT120 lifetime (µs) (Toronto/LGEP)	MPL lifetime (µs)
HC4	263	269/287	122
HC5	147	167/136	79
HC1	189	217/149	79
HC8	370	509/485	147
HC9	456	523/466	265

1.6.2 Temperature dependent characterization

Temperature is an important parameter as various mechanisms could be enhanced upon activation. Carrier recombination, especially non radiative recombination through defects, are

dependent on temperature. The behavior of a-Si:H/c-Si heterojunctions, however is still unclear at this time in terms of temperature dependence. It has been observed that PL emitted from c-Si wafer that is passivated with a-Si:H on both sides increases when the temperature decreases, which is coherent with the determination of band-to-band recombination coefficient by Trupke [57] and Nguyen [58] (see Fig. 1.23).

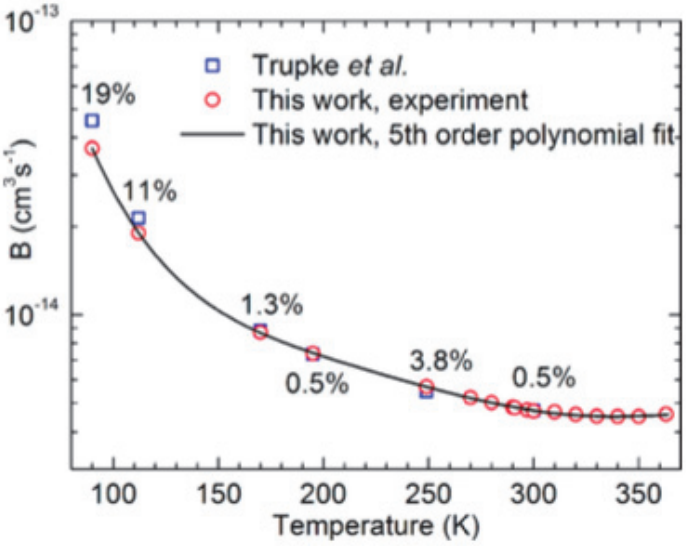

Fig. 1.23 Temperature dependent radiative recombination coefficient B determined using PL technique [58].

Rein analyzed the temperature-dependent lifetime spectroscopy (TDLS) for crystalline silicon and showed that the temperature dependence of the lifetime could be indicative of the presence of shallow defects. Analysis of Mo contamination is characterized with this method as shown in Fig. 1.24.

Tardon studied the a-Si:H/c-Si heterojunction and lifetime temperature dependence with PL (see Fig. 1.18). The dependence is explained by assuming the quasi-Fermi level to be independent of the temperature and the variation of the effective density of states due to its bandgap temperature dependence. This cannot be reproduced by simulations. We will discuss in detail in the modeling part of this thesis Courtois also investigated this point and explained the lifetime dependence by the decrease of radiative and Auger lifetime [45]. In fact, we have observed similar dependence even for low injection condition in which SRH recombination always dominates. This will be shown with the discussion of experimental results.

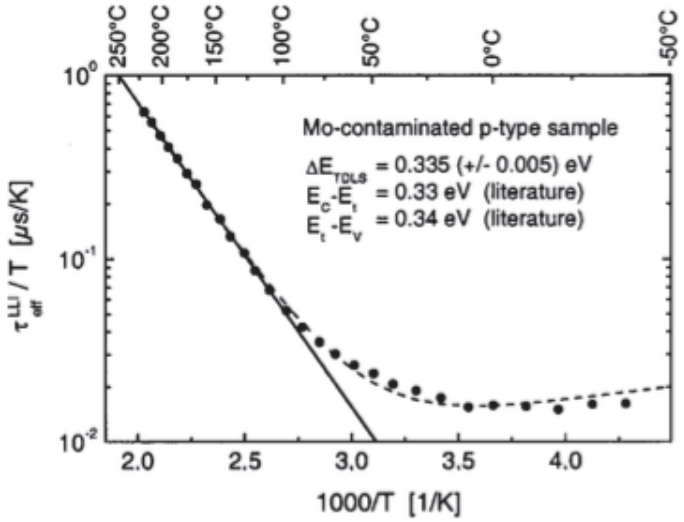

Fig. 1.24 3.7×10^{11} cm^{-3} Mo contamination p-type silicon sample, analyzed by TDLS [59].

1.7 Numerical simulation and guidelines

Although the physics of semiconductor material is well-established, it is often intricate and time consuming to analyze the parameters of a practical sample by analytical calculation. Technology computer aided design is an indispensibable too to solve complex structure and catch the underlined physics. There are already some well-known software to aide a-Si:H/c-Si heterojunctions solar cell design such as AFORS-HET* and many others developed by research groups, for example SC-Simul [60]. Silvaco is a commercial EDA software provider in the field of semiconductor device. They have a comprehensive set of products for a wide range of applications such as displays, power, reliability, optical, advanced process development, analog, high-speed I/O design, foundation library, memory design. Atlas, as the device simulation framework, performs 2D and 3D simulations from DC, AC, and transient analysis for silicon, binary, ternary, and quaternary material-based devices.

Numerical tool such as AFORS-HET is based on user-friendly graphical user interface. In contrary, ATLAS is text-based and the user need to input program commands. This leads to great freedom to define the work-flow of the simulation process. To benefit from this flexibility, in our work we utilized ATLAS as the numerical tool to investigate the a-Si:H/c-Si heterojunctions. An overview of the simulation is given by Fig. 1.25. ATLAS takes the structure files and command files as input and generates log files and solution files as output. Structure files describe the device structure to be simulated. Command files declare the

* **https://www.helmholtz-berlin.de/forschung/oe/ee/si-pv/projekte/asicsi/afors-het/index_en.html**.

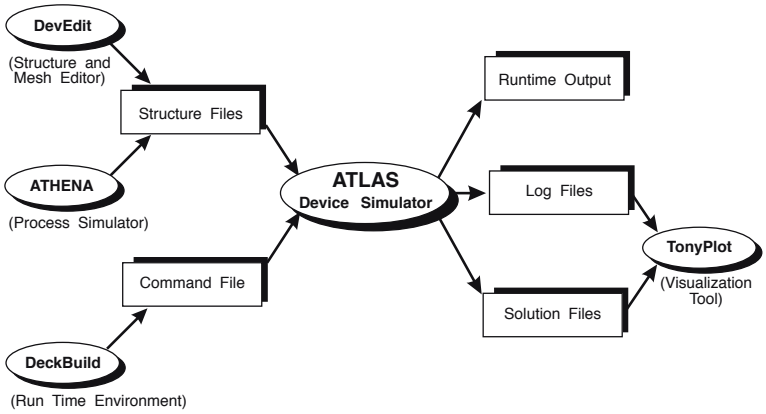

Fig. 1.25 Atlas input and output chart.

simulation parameters and work-flows. Log files store the terminal characteristics. Solution files contains the simulation results that we are interested in.

Usually, upstream steps generate device structure files that can be loaded directly into Atlas simulator. Often this is done with Athena, the process simulation tool. In our case, no precedent process simulation work exists, so the device structure is established by Deckbuild, the runtime environment. At the same time, we also pass to Deckbuild the simulation parameters such as illumination intensity, physical models to apply and characteristics to be extracted from simulation results. The simulation results can be visualized with Tonyplot.

1.8 Work in this thesis

Most of the research presented here relies on a new PL/MPL system that has been assembled to study heterointerfaces. We have developed a new version of the MPL system including mapping capabilities and temperature control(20-300K).

Few research on the temperature dependence of the electronic properties of a-Si:H/c-Si junction have been reported. In this range of temperature, another interesting fact is that we have observed a quite different temperature dependence on the samples that are doped using ion implantation. The PL response of a-Si:H/c-Si junction is complicated and the temperature dependence has not been covered by other researchers. As recombination at the heterointerfaces has to be reduced in order to enhance the performance of silicon heterojunction (HETs) solar cells, we will study various combinations of passivation as well as doping within the framework of the European project HERCULES.These experiments are supported by TCAD simulation in order to determine the dominant recombination mechanisms and the influence of shallow defects.

Particularly we will discuss the lifetime extraction from simulation and introduce the concept of differential and steady state lifetime.

The system developed is benchmarked to the Sinton Instruments, which is based on the quasi-steady-state photoconductance (QSSPC) and photoconductance decay. It is widely accepted as the industrial standard. However, the Sinton tester cannot be used at low temperature and on full cell. We will investigate the nature of the lifetime measured in both techniques and evaluate the discrepencies in terms of injection level.

At last, we introduce the application of micro-PL mapping at high injection in order to investigate III-V InAs quantum dot stacks separated by 10 nm GaAs. This structure is particularly interesting as it finds potential application in multijunction solar cells. we will see how the PL spectra evolve at nm scale resolution as well as with temperature and correlate the observation to the coupling of charge transfer across the stack.

Chapter 2

Experimental techniques

In this chapter, we will describe the main experimental techniques utilized in this work. particularly we focus on the PL/MPL system that has been assembled for the measurement of the lifetime . As the measurements have been benchmarked to photodecay we describe the Sinton tester. At last, the micro PL system utilized for the mapping of QDs stacks is introduced. The descriptions are given as a reference for future chapters.

2.1 Photoconductance measurement

Sinton commercialized a product based on the photoconductance decay as a method to measure the carrier lifetime.[61]. The lifetime tester shown in Fig. 2.1(a) is one of the products on the market and the principle is shown in Fig. 2.1(b). To measure the effective lifetime, a silicon sample is placed on top of the detection stage. A flash light illuminates the sample to generate electron-hole pairs that significantly increase the conductance of the sample. A coil located under the stage induces and measures Eddy currents to determine the conductance. After the light goes off, the carrier concentration drops exponentially due to recombination and so does the conductance. The effective carrier lifetime is determined from the decay signature of photo conductance. Such a measurement, only provides an average value of lifetime over an circular area of $\phi 4$ cm. This average does not translate the distribution of lifetime across the sample on one hand but also the dominant recombination centers e.g. surface, interface and bulk). The effective minority carrier lifetime is given by [62]:

$$\tau_{eff} = \frac{\Delta n(t)}{G(t) - \frac{\mathrm{d}\Delta n(t)}{\mathrm{d}t}} \tag{2.1}$$

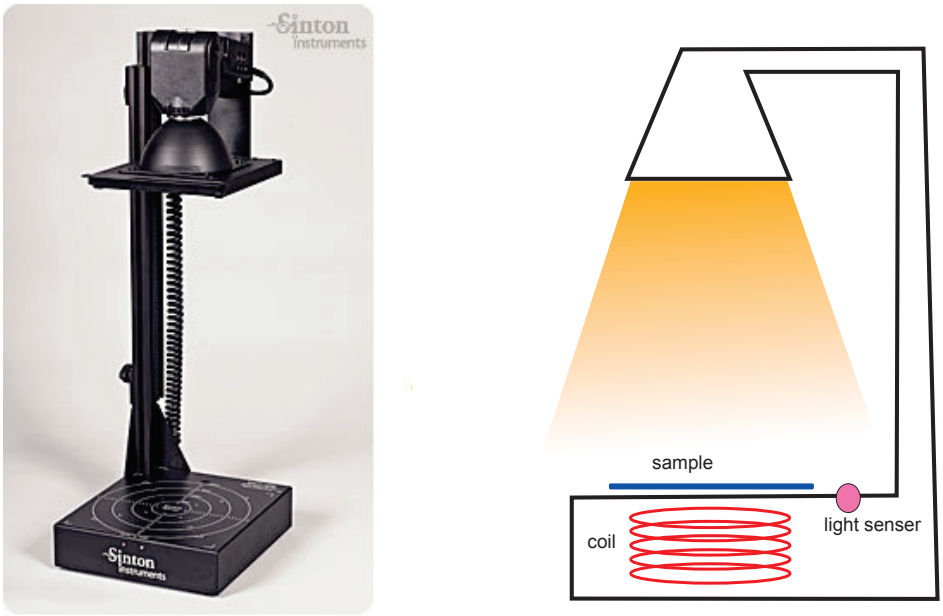

(a) (b)

Fig. 2.1 (a) Commercialized photo conductance decay instrument WCT-120 lifetime tester of Sinton Instruments (formerly Sinton Consulting). (b) The schematic of measurement.

with $\Delta n(t)$ the excess carrier concentration out of equilibrium and $G(t)$ the generation rate. There are three modes of measurement available with the Sinton lifetime tester as will be discussed below.

2.1.1 Transient mode

For samples with long carrier lifetime (>200 µs), the transient mode is recommended. A flash shorter than the sample lifetime generates excess carriers all over the sample. After the flash goes off, the carrier concentration starts to decay slowly. Assuming that the light pulse is much shorter than the carrier lifetime of the sample, the generation term $G(t)$ in Eq. 2.1 becomes negligible and the lifetime is deduced only from the decay fo the carrier concentration . This is the "transient mode":

$$\tau_{eff} = \frac{\Delta n(t)}{-\frac{d\Delta n(t)}{dt}} \tag{2.2}$$

2.1.2 QSSPC mode

However, for samples with short lifetime (<200 µs) *i.e.* shorter than the flash pulse width or with a conduction decay faster than the detector can measure, the QSSPC (Quasi Steady State Photo Conductance) method is used. The sample is illuminated with a long flash which decays slowly enough that the term $d\Delta n(t)/dt$ in Eq. 2.1 can be neglected and the sample is assumed to be in static state. The carrier lifetime is determined from the generation rate. This latest is measured using a light detector located on the stage, see Fig. 2.1(b), and the optical parameters of the sample.

$$\tau_{eff} = \frac{\Delta n(t)}{G(t)} \tag{2.3}$$

2.1.3 General mode

It is also possible to do the measurement using an intermediate method known as "generalized mode" that considers both the generation and decay terms in Eq. 2.1. One does not assume that the generation rate is zero or constant during the measurement. The real value of the intensity of the flash light as a function of time should be measured to determine an accurate generation rate.

2.2 Photoluminescence

Two PL setups are employed in this work, i.e. "macro-PL" and "micro-PL". Macro-PL is essentially used to investigate SHJ samples. Notably, this PL system has the peculiarity to perform PL measurements in the frequency regime and can therefore be extended to MPL. On the other hand, micro-PL setup used to investigate nanostructured materials is based on

a confocal microscope, allowing to investigate mappings with high spatial resolution at the sub-micro scale.

2.2.1 Macro-PL measurement

Fig. 2.2 shows our macro-PL system. It is equipped with a cryostat driven by helium circulation which allows cooling down to 20 K. The excitation is a laser diode beam projected onto the sample through the cryostat window using an optical fiber. The emitted luminescence is collected by a parabolic mirror and focused with optical lenses onto the monochromator. The optics part is a $4f$ system with a magnification of one. A high-pass optical filter is placed in front of the monochromator to filter the reflected or scattered excitation light. A photodiode measures the dispersed spectrum at a given wavelength. The photo-current is amplified and converted into voltage then captured by the multimeter. The monochromator is configured to measure the PL spectrum with a resolution of 25 nm (monochromator slit with of 2 mm).

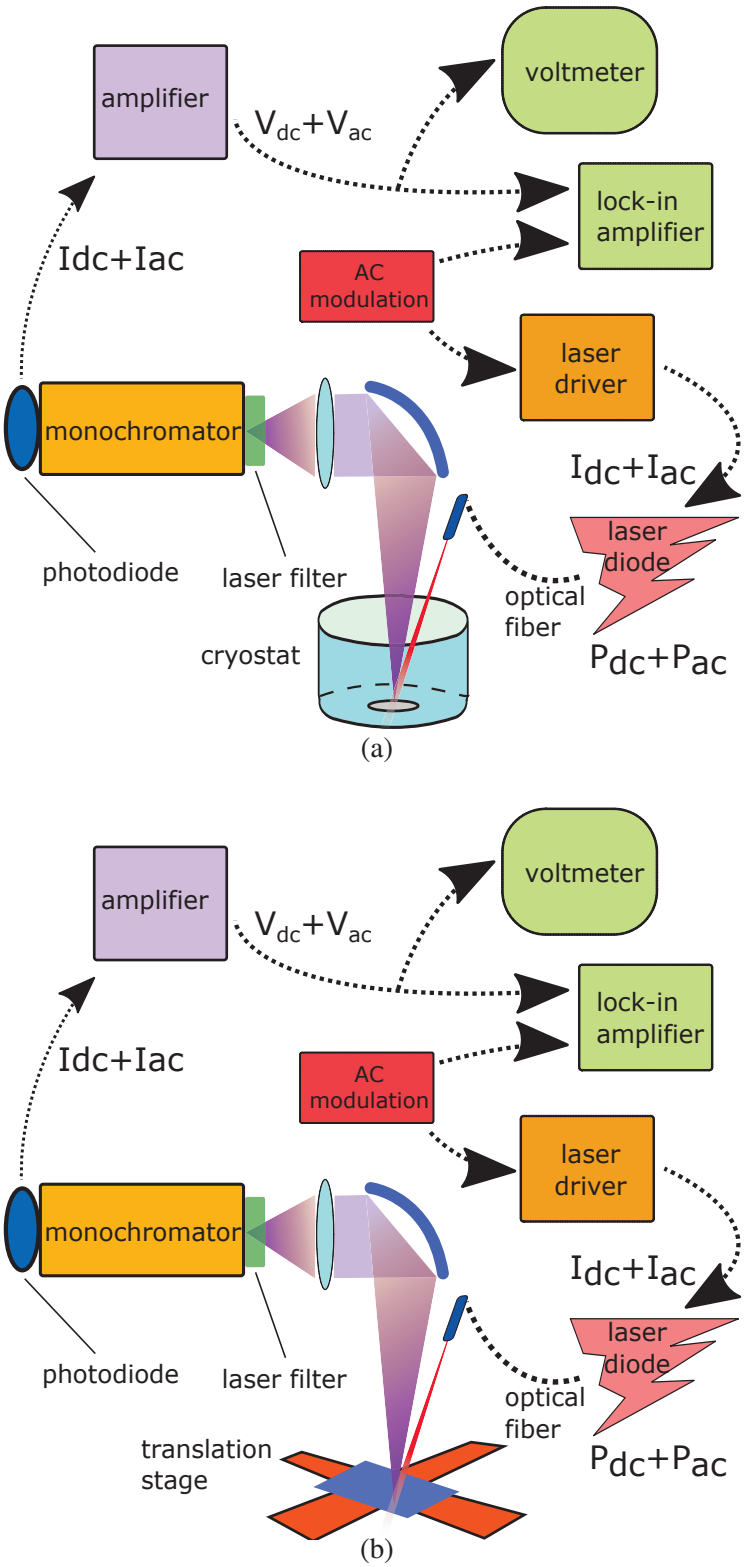

Fig. 2.2 Macro-PL setup schematic of (a) the configuration for temperature dependent measurement and (b) the configuration for room temperature mapping.

2.2.1.1 Steady state PL

This configuration allows the measurement of single point as a function of temperature or PL mappings at room temperature.

Single point Steady state PL spectrum is useful to investigate the defects. The signature of the defects is more pronounced at low temperature [63], so the temperature dependent measurement has been developped.

Mapping The word "imaging" refers to the capture of an image with a camera while "mapping" refers to the acquisition of an image pixel after pixel [64].

Moreover, PL imaging is widely used in photovoltaic industry to detect defects in silicon wafers and investigate the homogeneity of deposition. Si or InGaAs cameras are often used for PL imaging because Si camera can capture part of the Si peak spectrum whereas InGaAs can capture the whole Si spectrum. To capture a PL image, the whole sample is illuminated by an infrared laser source. A filter is mounted to the camera to block the excitation laser so only the PL is imaged.

In this work, PL mapping is assembled by mounting a translation stage to the existing single point measurement setup as shown in Fig. 2.2(b). The mapping is obtained by fixing the laser beam, moving the sample step by step and measuring point after point. Between the steps, the multimeter will record the PL signal that is already converted to voltage. The scanning follows a zigzag route (Fig. 2.3(a)) in order to reduce measurement time. The measured data are presented in the form of pixel images as shown in Fig. 2.3(b).

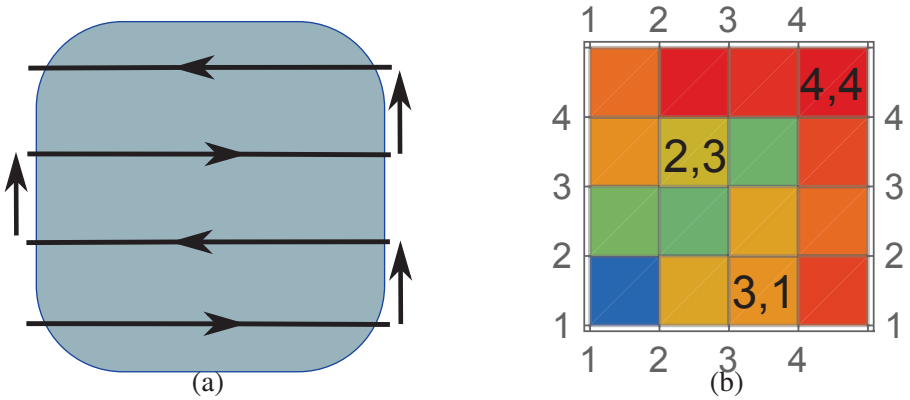

Fig. 2.3 (a) The zigzag scanning route on the sample. (b) Schematic of the coordinate of each pixel on the mapping is represented by the index on its left-bottom number. This index indicates the sequential number of the measured point instead of real spatial distance.

2.2.1.2 Modulated photoluminescence

Based on macro PL, the modulated PL measurement technique is developed to observe the distribution of the lifetime across large samples.

Theory When a material is irradiated with a modulated excitation, the generation rate of electron-hole pairs is subjected to the same modulation:

$$\widetilde{G}(t) = G_{DC} + G_{AC}\mathrm{e}^{i\omega t} \tag{2.4}$$

G_{DC} and G_{AC} are the DC and AC components of generation rate. ω is the modulation angular frequency. The variation of PL intensity as a function of time should take the same form except that due to relaxation a phase shift term ϕ is considered:

$$\widetilde{I}(t) = I_{DC} + I_{AC}\mathrm{e}^{i(\omega t+\phi)} \tag{2.5}$$

I_{DC} and I_{AC} are the DC and amplitude of the first order AC components of photoluminescence intensity.

From see Appendix A :

$$\phi(\omega) = -\arctan(\omega\tau_{eff}) \tag{2.6}$$

$$I_{AC}(\omega) \propto \frac{1}{\sqrt{1+(\omega\tau_{eff})^2}} \tag{2.7}$$

Eq. 2.6 enables us to extract the lifetime from the phase shift with lock-in measurements. Eq. 2.7 provides another method to extract lifetime from the amplitude.

Since photoluminescence is a bimolecular process, it also gives rise to second order response to modulation. However the signal is often too weak and beyond the detection limit.

It should be noted here that the MPL method measures the ”differential” lifetime instead of ”steady-state” lifetime. This will be discussed in a later chapter.

System frequency response Special attention should be paid to the frequency response of the measurement system. Because laser driver, laser diode, photo diode and amplifier are all low pass devices, they introduce system errors into the experimental results. The amplitude attenuation and phase shift with frequency are both affected by the setup and the sample. The former should be determined beforehand and then subtracted from the measured data.

Fig. 2.4 shows the frequency response of the system for four different gains of the amplifier. The response is measured by replacing the sample with a frosted glass to diffuse the incident laser beam. Part of the diffused light enters the monochromator and therefore only the system characteristics is measured. As is shown in the figure, the 10^8 gain is significantly dependent on frequency. The amplifier bandwidth is 220 kHz, 1.8, 3.5 and 14 MHz for the amplification gain of 10^8, 10^7, 10^6 and 10^5 respectively. Although the frequency range for our measurement is much smaller than the bandwidth limit, the 10^8 gain still affects the amplitude and the phase shift. For this reason, it is recommended to avoid using this gain channel despite higher amplification. It is also advised that the measured data should be calibrated. This can be done via simple calculations.

The system error of amplitude and phase shift can be interpolated with polynomials. Let $\Theta_{amp}(f)$ and $\Theta_{pha}(f)$ be the system introduced amplitude error and phase shift error. And let $I_{AC,raw}(f)$ and $\phi_{raw}(f)$ be the raw data of amplitude and phase shift of a sample. The calibrated amplitude $I_{AC,cor}(f)$ and phase shift $\phi_{cor}(f)$ are obtained by:

$$I_{AC,cor}(f) = \frac{I_{AC,raw}(f)}{\Theta_{amp}(f)} \tag{2.8}$$

$$\phi_{cor}(f) = \phi_{raw}(f) - \Theta_{pha}(f) \tag{2.9}$$

This is especially important for low lifetime where the error of the system is not negligible compared to the amplitude and phase shift introduced by the sample.

Measurement sensitivity To optimize the experiments, one must evaluate the sensitivity of the system. We define the sensitivity of MPL lifetime measurement as the variation of signal (phase) with respect to the variation of lifetime.

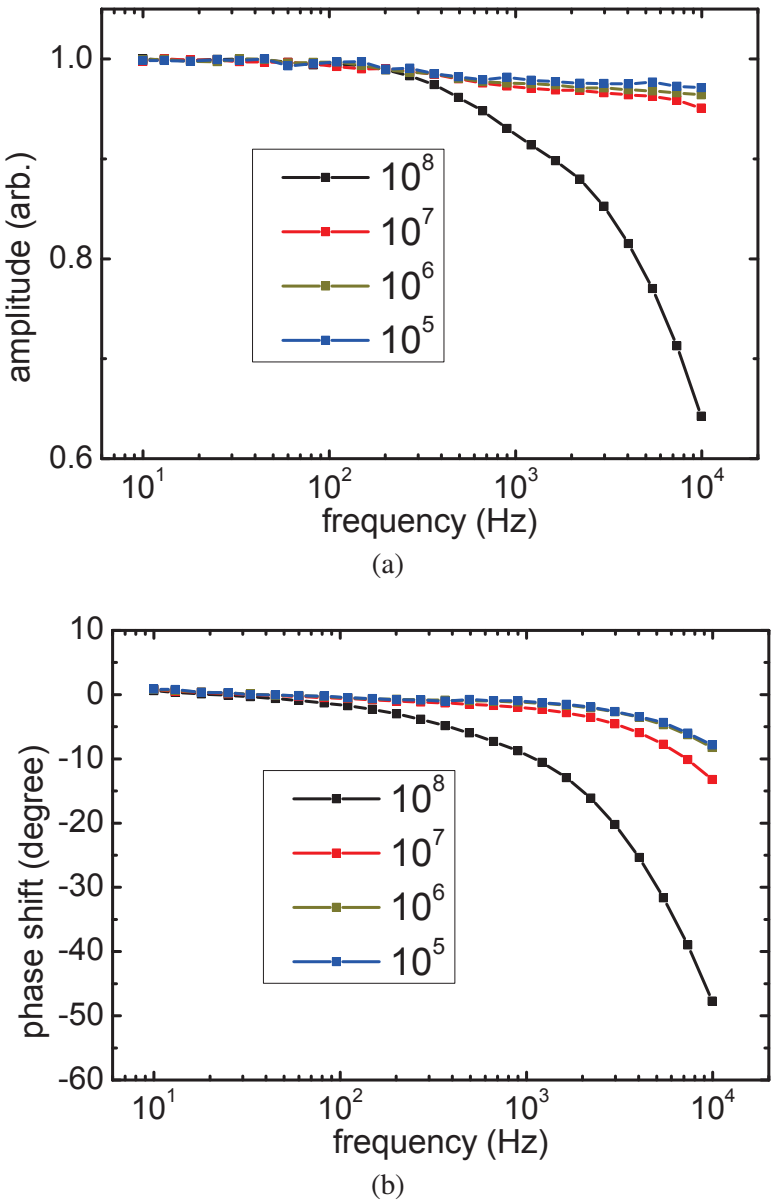

Fig. 2.4 Frequency response of the MPL measurement setup in the range of 10 to 10000 Hz for various gains of the amplifier. The amplitude response are normalized to the maximum of each curve. (a) Amplitude vs. frequency. (b) Phase shift vs. frequency.

The sensitivity of phase shift is given by:

$$SEN_{pha}(\omega) = \frac{\mathrm{d}\phi}{\mathrm{d}\tau_{eff}} = \frac{\omega}{1 + \left(\omega\tau_{eff}\right)^2} \tag{2.10}$$

The sensitivity of phase as a function of ω has a maximum when

$$\omega\tau_{eff} = 1$$

When this condition is satisfied, one should read a phase shift of -45 degrees from the lock-in amplifier.

Using

$$\tau_{eff,\mu s} \approx \frac{1.6 \times 10^5}{f_{Hz}} \tag{2.11}$$

we can quickly evaluate the lifetime with maximum sensitivity during experiments.

Lifetime extraction The lock-in amplifier measures the amplitude and phase shift as a function of frequency. Theoretically any of the two measurements at different frequencies are sufficient to calculate the lifetime from amplitude data according to Eq. 2.7 and even one measurement is enough to extract lifetime from phase shift data according to Eq. 2.6. In practice, it is recommended to do the measurements at many frequencies in a wide range and extract the lifetime by curve fitting in order to improve the accuracy.

Fig. 2.5 shows the amplitude and phase shift as a function of frequency. When the frequency increases, a decrease of the amplitude and a larger phase delay are observed. In the case of long lifetime, i.e. 1000 µs as shown in Fig. 2.5, when modulation frequency increases, the amplitude attenuates and a large phase shift approximates 90 degrees. For both cases, the measurements reach a plateau at very high frequency and it is no longer possible to determine the lifetime. As a result, more measurements at low frequency is a preferred approach. We need to match the measurement frequency range according to the sample lifetime and to the sensitivity given by Eq. 2.11.

One example of the MPL measurement result from our experiments is shown in Fig. 2.6. The sample is a silicon heterojunction with symmetrical layers of AlOx passivation (AlOx/(n)c-Si/AlOx). The amplitude and phase are fitted separately and the lifetimes thus evaluated are 613 and 616 µs respectively. The two results differ by 0.5%, so we can conclude that there is an excellent agreement between the lifetime extraction from the amplitude and from the phase shift.

The most efficient strategy is to do many measurements around the frequency that satisfies Eq. 2.11. However, as we can not predict the lifetime beforehand, several iterations should be carried out to reach the optimal frequency.

MPL mapping The excess carrier lifetime mapping provides an overview method of characterization of silicon wafer. It can be realized with microwave photoconductance decay

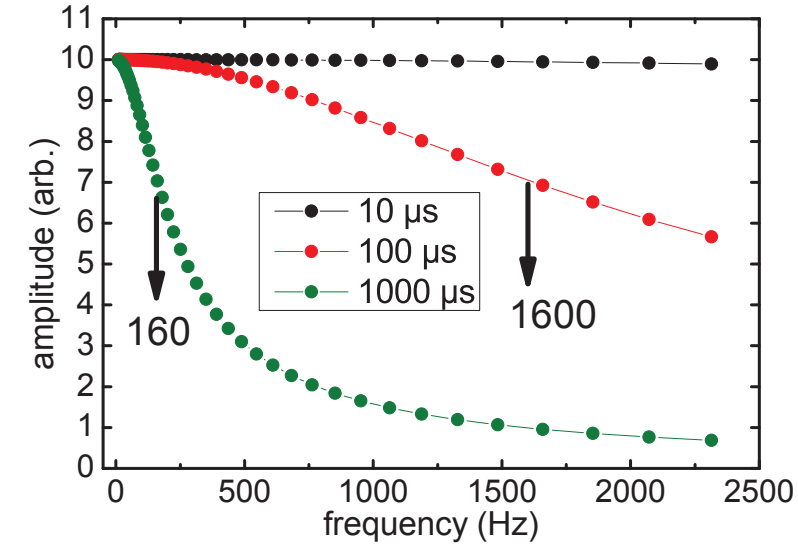

(a)

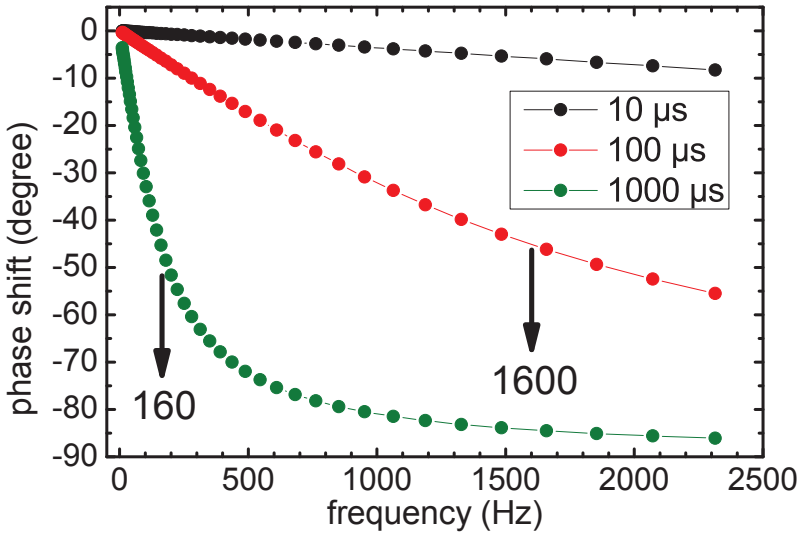

(b)

Fig. 2.5 Amplitude and phase shift as a function of frequency up to 2500 Hz for 10, 100 and 1000 µs lifetime. These curves are obtained by calculation with Eq. 2.7 and 2.6. The amplitude curves are normalized to 10 for clear view. Black arrows indicate most sensitive detection frequency. (a) Amplitude vs. frequency. (b) Phase shift vs. frequency.

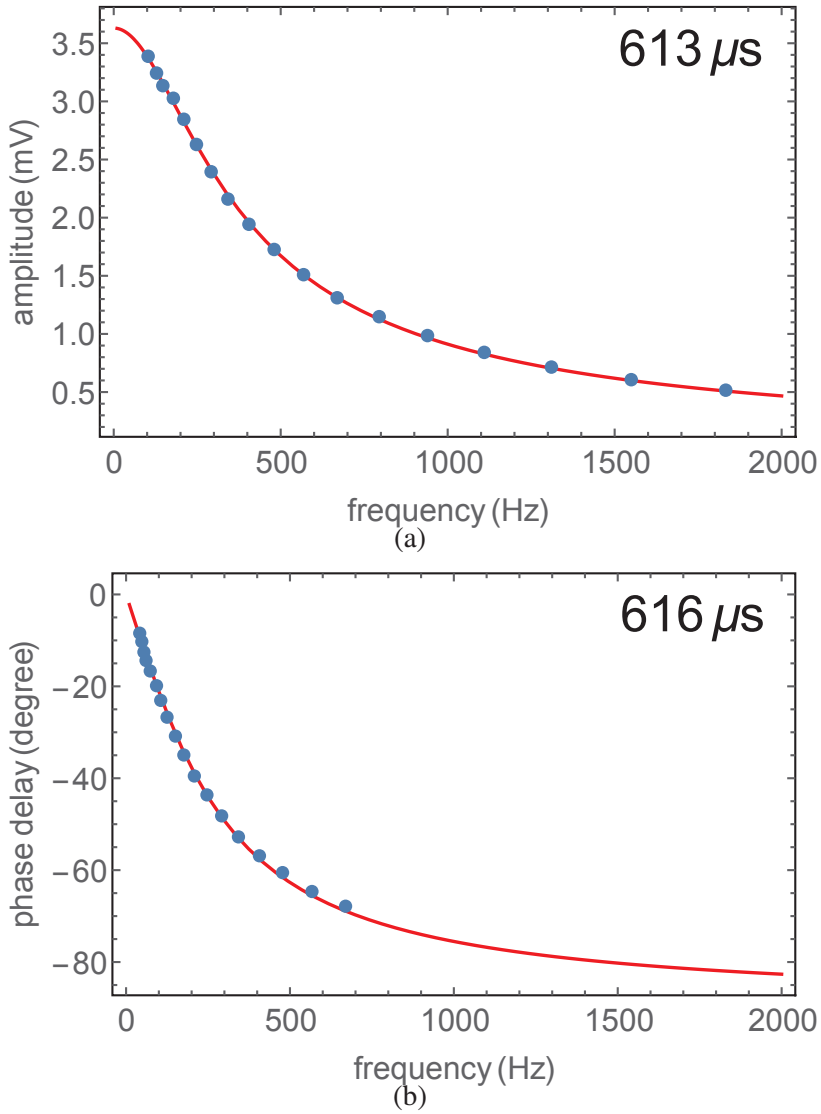

Fig. 2.6 Lifetime extraction by curve fitting from (a) amplitude vs. frequency and from (b) phase shift vs. frequency experimental data respectively.

(μPCD) [65]. When the photoconductance in the sample changes, its microwave reflection will also change. By scanning the excitation light over the sample, μPCD mapping can be obtained as shown in Fig. 1.22. However, there is no commercialized lifetime imaging technique based on PL. Theoretically if the Si or InGaAs camera is calibrated, it is possible to obtain lifetime image from PL image. But the calibration is very dependent on the absorption of the sample. One needs to know the optical absorption for each sample. Another possible method is to obtain lifetime image by PL decay measurement with camera as shown in Fig. 1.21.

In this work, we developed the lifetime mapping on the MPL platform Fig. 2.2(b). The mapping is obtained by fixing the laser beam, moving the sample step by step and measuring successive pixels. The scanning follows a zigzag route as shown in Fig. 2.3(a). The measured data are presented in the form of pixel image as shown in Fig. 2.3(b).

2.2.2 Micro PL measurement

The PL microscopy is based on a confocal microscope combined with piezo stepper. In this system the excitation as well as the PL signal is injected and extracted by means of an optical fiber.

The principle of confocal microscopy and the setup is shown in Fig. 2.7. In a confocal

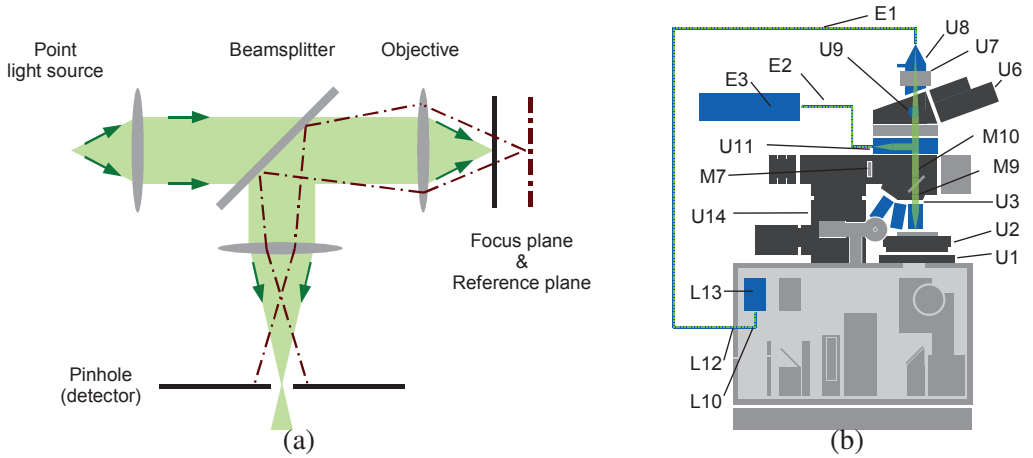

Fig. 2.7 (a) Schematic of confocal measurement and (b) WITec platform in reflection configuration [66].

system, the most important part is the pinhole which is placed at the image plane of the optics system. The pinhole image appears on the conjugate plane, that is, the object plane on which we focus on. The reference plane gives an example of the out-of-focus plane. The pinhole blocks the out-of-focus light and only the light on the focal point within the

pinhole image hits the detector. This process increases efficiently the spatial resolution and the contrast. Some of the important components in Fig. 2.7 include: U3, the objective; U8, the fiber coupling unit; E1, multi-modal optical fiber and L13 (PMT or APD), the single photon counting detector. The core of the fiber serves as the pinhole so smaller core size has better resolution but bigger core size collects more light. More details on the specifications can be found in Appendix B.2.

Furthermore, we also performed PL decay measurements with micro-PL to characterize the lifetime of silicon sample. Since the lifetime of silicon is very long compared to that of III-V materials, our time-resolved measurement is different from Time-Correlated Single Photon Counting (TCSPC) in the ultra fast measurement regime. It is simply a measurement of PL intensity as a function of time. Furthermore, the measurement is performed in high injection instead of low injection as required for single photon measurement.

Chapter 3

Theory and model

In this chapter, we discuss the differential nature of the MPL lifetime. This is a very important aspect to consider when we compare different techniques. The radiative, Auger and SRH lifetime will be discussed in the framework of MPL. Especially, the simulation of the MPL lifetime and the data extraction from calculated parameters should not be forgotten. Furthermore, temperature dependent lifetime spectroscopy will be reviewed. This method is adopted in this thesis to analyze the temperature dependence of SHJ samples and to extract parameters such as the defect energy level and capture coefficients.

3.1 Steady state vs. differential lifetime

In previous chapters we utilized the "effective lifetime" to refer to the lifetime value obtained in experiments. In fact, the values obtained with different characterization techniques can be very different. It is important to discuss and distinguish them.

Jan Schmidt first addressed the problem of small signal measurements and defined "differential bulk lifetime" from a comprehensive derivation of the diffusion equation [55]. He started from the ambipolar diffusion equation:

$$\frac{\partial \Delta n}{\partial t} = D_a \frac{\partial^2 \Delta n}{\partial x^2} - U(\Delta n) + G(x,t) \tag{3.1}$$

Then he introduces a generation rate with both the constant and dynamic part $G(x,t) = G_{ss}(x) + G_d(x,t)$ and the consequential excess carrier concentration $\Delta n(x,t) = \Delta n_{ss}(x) + \Delta n_d(x,t)$. Taylor expansion gives

$$U(\Delta n) = U(\Delta n_{ss}) + \frac{\partial \Delta U}{\partial \Delta n}|_{n_{ss}} \Delta n_d(x,t) \tag{3.2}$$

By substituting $G(x,t)$, $\Delta n(x,t)$ and $U(\Delta n)$ into Eq. 3.1 and eliminating the time independent terms, we have:

$$\frac{\partial \Delta n_d(x,t)}{\partial t} = D_a \frac{\partial^2 \Delta n_d(x,t)}{\partial x^2} - \frac{\partial U}{\partial \Delta n}|_{n_{ss}} \Delta n_d(x,t) + G_d(x,t) \tag{3.3}$$

Comparing Eq. 3.3 to Eq. 3.1, Schmidt defines differential bulk carrier lifetime:

$$\tau_{b,d} = \left[\frac{\partial U(\Delta n)}{\partial \Delta n}\right]^{-1} |_{\Delta n = n_{ss}} \tag{3.4}$$

The "actual bulk lifetime" can be retrieved from the integration of "differential bulk lifetime".

$$\tau_b = \left(\int_0^{n_{ss}} \tau_{b,d}(\Delta n)^{-1} \mathrm{d}\Delta n\right)^{-1} \tag{3.5}$$

Also in the high injection limit, the Auger lifetime is investigated in terms of "actual lifetime" and "differential lifetime".

In this section, we take a different approach and derive the "differential lifetime" directly from the physical significance of the "lifetime" and the nonlinearity of carrier concentration as a function of the recombination rate.

There are many examples in physics when the rate of increase or decrease of a quantity is proportional to its current value. In terms of time variation, this would result in an exponential form of evolution as a function of time. To describe this process, we can usually define a "time constant" to be the ratio of this quantity over its variation rate. Let G be the constant generation rate and R the constant recombination rate. The relation $G = R$ will hold for steady state measurements. Thus Eq. 2.1 will give:

$$\tau_{eff} = \frac{\Delta n}{G} = \frac{\Delta n}{R} \tag{3.6}$$

That is also the way minority carrier lifetime is defined in semiconductors.

In an ideal case τ_{eff} is a constant independent of Δn. However, this is not always true due to the non-linear dependence of recombination rate and excess carrier density in practice. Even considering the SRH recombination model alone, we find the lifetime to be independent of the injection level only when the injection is very low or very high as will be discussed later. In an intermediate injection regime, the lifetime is injection dependent.

Characterization techniques based on small signal modulation are actually giving the "differential lifetime":

$$\tau_{diff} = \frac{\mathrm{d}\Delta n}{\mathrm{d}R} \tag{3.7}$$

The explanation of their difference is shown in Fig. 3.1(a). Assuming that we are measuring at point P. Steady state measurement equals the recombination rate to the generation rate so the lifetime is given by Eq. 3.6. The small signal measurements, however, induce an oscillation of the system near point P and thus express information on the slope near that point.

On the contrary, the lifetime given by Eq. 3.6 is valid only in steady-state condition. Hence we use the term ”steady-state lifetime” from now on:

$$\tau_{ss} = \frac{\Delta n}{G} = \frac{\Delta n}{R} \tag{3.8}$$

In Appendix A, the formula of MPL lifetime is derived from the right side of Eq. A.5. However, from the left side of this equation we will obtain

$$\tau_{ss} = \frac{\Delta n_{DC}}{G_{DC}} \tag{3.9}$$

which is in accordance with Eq. 3.6. One may argue that the MPL lifetime is the effective lifetime but this is not true. Since MPL uses a small signal modulation method, it has the nature of differential lifetime given by Eq. 3.7.

Let us consider an extreme example to justify the differential nature of the MPL lifetime. It is demonstrated in Fig. 3.1(b). Imagine that we have some material with the recombination of excess carriers becomes extremely strong when the carrier concentration goes above a certain value. So Δn is clamped to this threshold value. No matter how we increase the carrier generation, Δn stays constant. The increase of carrier generation is balanced by the increase of carrier recombination. When we are measuring at point Q, the modulation of generation rate G_{AC} has no impact on Δn_{AC}. Thus $\Delta n_{AC} = 0$. According to Eq. A.6, we get $\tau_{eff} = 0$, which corresponds to τ_{diff} instead of τ_{eff} in the figure.

Now let us reconsider the derivation of the MPL lifetime using the definition of differential lifetime in Eq. 3.7 instead of Eq. 2.1. From the rate function

$$\frac{\mathrm{d}\Delta n}{\mathrm{d}t} = G - R \tag{3.10}$$

with G the generation rate and R the recombination rate. $\mathrm{d}\Delta n/\mathrm{d}t$ is the function of G and R. R is a function of Δn. We have

$$\frac{\mathrm{d}^2\Delta n}{\mathrm{d}t^2} = \frac{\mathrm{d}G}{\mathrm{d}t} - \frac{\mathrm{d}R}{\mathrm{d}\Delta n}\frac{\mathrm{d}\Delta n}{\mathrm{d}t} \tag{3.11}$$

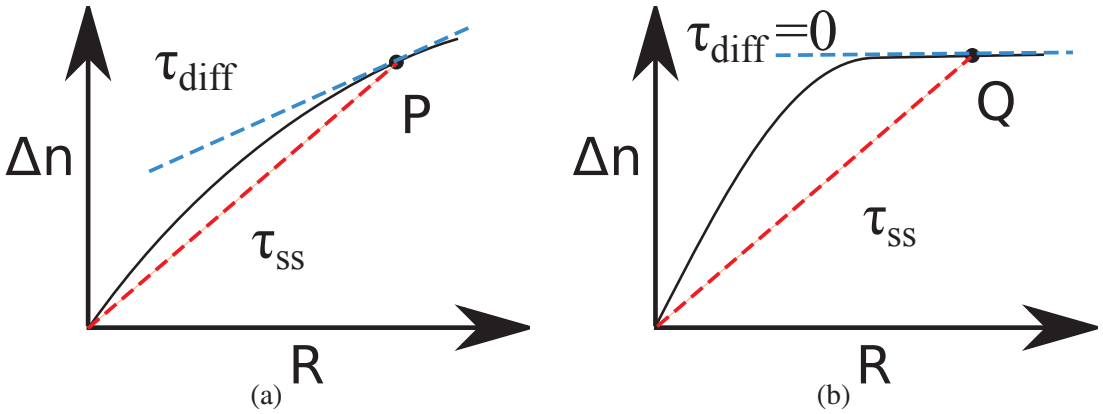

Fig. 3.1 (a) Schematic of the steady-state lifetime τ_{ss} and the differential lifetime τ_{diff}. (b) An extreme case illustrating the differential nature of the MPL lifetime.

With

$$\widetilde{G}(t) = G_{DC} + G_{AC}\mathrm{e}^{i\omega t} \tag{3.12}$$

and

$$\widetilde{\Delta n}(t) = \Delta n_{DC} + \Delta n_{AC}\mathrm{e}^{i(\omega t+\phi)} \tag{3.13}$$

being substitued into Eq. 3.11, we get

$$\begin{aligned} \Delta n_{AC}(i\omega)^2\mathrm{e}^{i(\omega t+\phi)} &= i\omega G_{AC}\mathrm{e}^{i\omega t} - \frac{1}{\tau_{diff}}\Delta n_{AC} i\omega \mathrm{e}^{i(\omega t+\phi)} \\ \Delta n_{AC} i\omega &= G_{AC}\mathrm{e}^{-i\phi} - \frac{1}{\tau_{diff}}\Delta n_{AC} \\ \Delta n_{AC} &= \tau_{diff} G_{AC}\frac{\mathrm{e}^{-i\phi}}{1+i\tau_{diff}\omega} \end{aligned} \tag{3.14}$$

Since Δn_{AC} is real, the right side of Eq. 3.14 must be real and the imaginary part is zero. Thus we arrive at exactly the same expression as Eq. A.6 except that τ_{diff} takes the place of τ_{eff}. From this equation we obtain the two expressions:

$$\Delta n_{AC} = \frac{\tau_{diff} G_{AC}}{\sqrt{1+(\omega\tau_{diff})^2}} \tag{3.15}$$

$$\phi = -\arctan(\omega\tau_{diff}) \tag{3.16}$$

They are also exactly Eq. A.8 and Eq. 2.6 with replacement of τ_{eff} by τ_{diff}.

3.2 Bulk recombination mechanism and related lifetime

3.2.1 Band to band radiative recombination

3.2.1.1 Steady state lifetime

Radiative recombination is the origin of luminescence. Its rate is described as:

$$R_{rad} = Bnp \tag{3.17}$$

where B is 4.7×10^{-15} cm^{-3}s^{-1} at 300 K in c-Si [58]. Assuming that $\Delta n = \Delta p$, steady state radiative recombination lifetime is defined as:

$$\tau_{ss,rad} = \frac{\Delta n}{R_{rad}} = \frac{\Delta n}{Bnp} \tag{3.18}$$

3.2.1.2 Differential lifetime

The differential lifetime of radiative recombination, according to Eq. 3.7, is given by

$$\begin{aligned} \frac{1}{\tau_{diff,rad}} &= \frac{\mathrm{d}R_{rad}}{\mathrm{d}\Delta n} = B\frac{\mathrm{d}np}{\mathrm{d}\Delta n} = B\frac{\mathrm{d}(n_0+\Delta n)(p_0+\Delta n)}{\mathrm{d}\Delta n} \\ &= B(n_0 + p_0 + 2\Delta n) \\ &= B(n+p) \end{aligned} \tag{3.19}$$

For an n-type sample, assuming $n_0 = N_d$ and $\Delta n = \Delta p$ the ratio of $\tau_{ss,rad}$ to $\tau_{diff,rad}$ can be expressed as

$$\frac{\tau_{ss,rad}}{\tau_{diff,rad}} = 1 + \frac{\Delta n}{N_d + \Delta n} \tag{3.20}$$

This ratio is between 1 and 2 and $\tau_{ss,rad}$ is always greater than $\tau_{diff,rad}$. The same rule also applies to p-type samples, N_d being replaced by N_a. As is shown in Fig. 3.2, the ratio of $\tau_{ss,rad}$ to $\tau_{diff,rad}$ increases from 1 to 2 as the injection level increases.

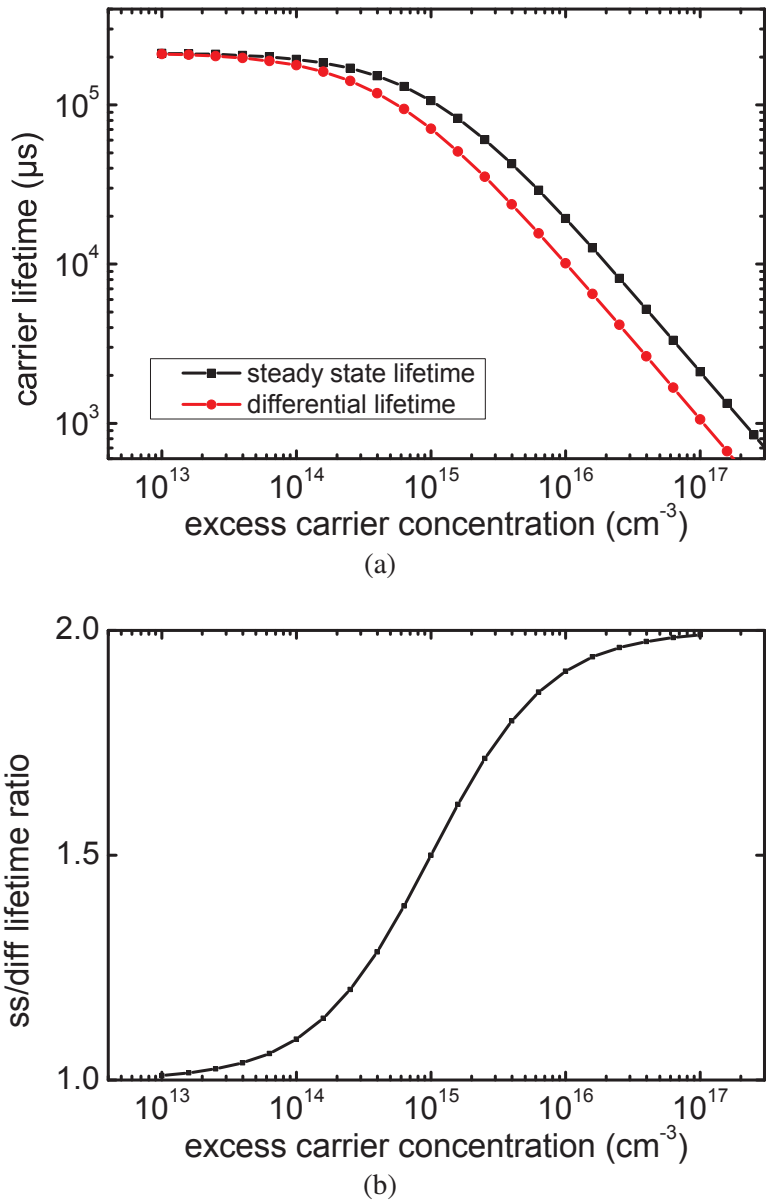

Fig. 3.2 (a) Comparison of steady-state and differential radiative lifetime. (b) Ratio of steady-state lifetime to differential lifetime. The steady-state and differential radiative lifetimes are calculated with with Eq. 3.18, 3.19 and 3.20. Following parameters are used: $T = 300$ K, $B = 4.7 \times 10^{-15}$ cm^{-3}s^{-1}, $N_d = 10^{15}$ cm^{-3}.

3.2.1.3 Temperature dependence

The temperature dependence of band-to-band radiative recombination has been much studied [57, 58]. The radiative recombination coefficient B is characterized as a function of

temperature and given in the temperature range of 90~363 K by:

$$\begin{aligned}\log_{10} B(T) = &-9.65614 - 8.05258\times10^{-2}\times T + 6.02695\times10^{-4}\times T^2 \\ &- 2.29844\times10^{-6}\times T^3 + 4.31934\times10^{-9}\times T^4 \\ &- 3.16154\times10^{-12}\times T^5\end{aligned} \tag{3.21}$$

Temperature dependent differential lifetime of radiative recombination is shown in Fig. 3.3, as a function of excess carrier concentration at various temperatures. Due to the in-

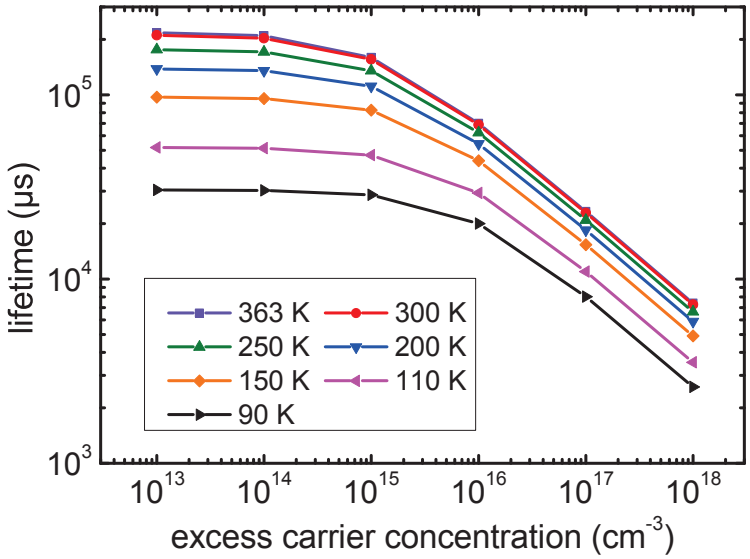

Fig. 3.3 Radiative recombination differential lifetime given by Eq. 3.19 in one sun illumination. $N_d = 10^{15}\text{cm}^{-3}$ is used.

crease of recombination coefficient, the carrier lifetime decreases rapidly with decreasing temperature.

3.2.2 Auger recombination

3.2.2.1 Steady state lifetime

Auger recombination dominates in high injection conditions. This process involves three particles. One pair of electron hole recombines while transferring their energy to a third particle (electron or hole). The third particle jumps to higher energy and returns to the band edge by releasing energy through phonon emission.

Auger recombination is often described as [67]

$$R_{Aug} = c_n n^2 p + c_p n p^2 \tag{3.22}$$

Assuming that $\Delta n = \Delta p$, steady state Auger lifetime is defined as:

$$\tau_{ss,Aug} = \frac{\Delta n}{R_{Aug}} = \frac{\Delta n}{c_n n^2 p + c_p n p^2} \tag{3.23}$$

For an n-type sample, assuming $n_0 = N_d$ and $p_0 \ll n_0$, the steady state Auger lifetime is defined as:

$$\frac{1}{\tau_{ss,Aug}} = \left(N_d + \Delta n\right)\left[c_n\left(N_d + \Delta n\right) + \Delta c_p n\right] \tag{3.24}$$

When injection is very high ($\Delta n \gg N_d$), which is usually the case when Auger recombination should be taken into consideration, we have

$$\frac{1}{\tau_{ss,Aug}} = (c_n + c_p)\Delta n^2 \tag{3.25}$$

3.2.2.2 Differential lifetime

For n-type samples, the differential lifetime of Auger recombination, as defined by Eq. 3.7, is

$$\begin{aligned}\frac{1}{\tau_{diff,Aug}} &= 1/\frac{\mathrm{d}\Delta n}{\mathrm{d}R_{Aug}} = \frac{\mathrm{d}R_{Aug}}{\mathrm{d}\Delta n} \\ &= c_p\left(\Delta n + p_0\right)\left(3\Delta n + 2n_0 + p_0\right) + c_n\left(\Delta n + n_0\right)\left(3\Delta n + n_0 + 2p_0\right) \\ &= c_p p(2n + p) + c_n n(2p + n) \\ &\approx \Delta c_p n\left(2N_d + 3\Delta n\right) + c_n\left(N_d + \Delta n\right)\left(N_d + 3\Delta n\right)\end{aligned} \tag{3.26}$$

When injection is high ($\Delta n \gg N_d$), we have

$$\frac{1}{\tau_{diff,Aug}} = 3(c_n + c_p)\Delta n^2 \tag{3.27}$$

Hence when $\Delta n \gg N_d$ is satisfied,

$$\tau_{diff,Aug} = \frac{1}{3}\tau_{ss,Aug} \tag{3.28}$$

For p-type samples we can draw the same conclusion. Under high injection, Auger recombination turns to be dominant and it is observed in experiments [55] that

$$\tau_{diff} = \frac{1}{3}\tau_{ss} \tag{3.29}$$

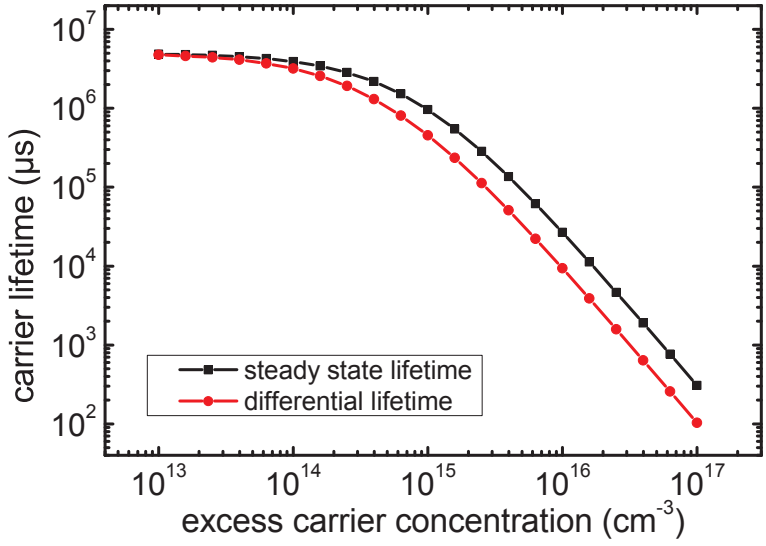

(a)

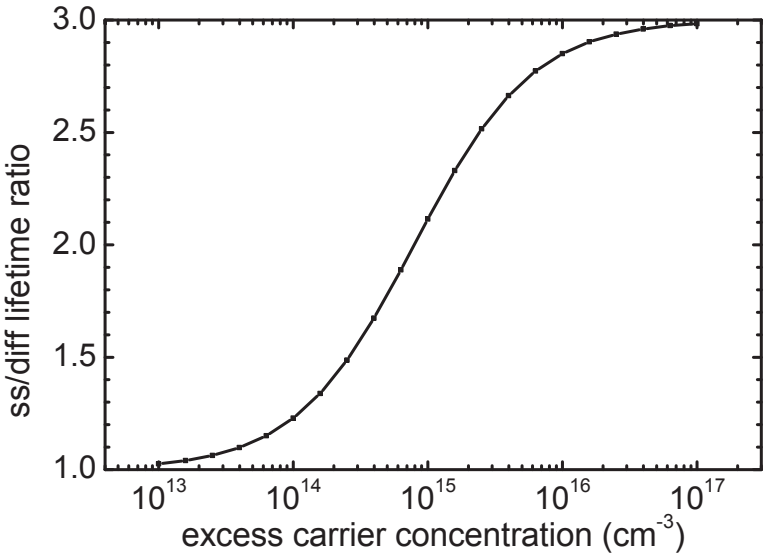

(b)

Fig. 3.4 (a) Comparison of steady-state and differential Auger lifetime. (b) Ratio of steady-state lifetime to differential lifetime. Steady state and differential Auger lifetimes are calculated with Eq. 3.23 and 3.26. Following parameters are used: $T = 300$ K, $N_d = 10^{15}$ cm^{-3}, $c_n = 2.8 \times 10^{-31}$ cm^{6}s^{-1}, $c_p = 9.9 \times 10^{-32}$ cm^{6}s^{-1} [68].

Some new models have taken into consideration the enhancement of Auger recombination due to the dopant density and the injection level [69]. The most recent models have been further improved by considering Coulomb-enhanced Auger recombination and Coulomb-enhanced radiative recombination [70, 71]. These new models are more accurate compared to classic models, but they are too complicated to give an intuitive derivation of differential lifetime. Thus the details are not discussed here.

3.2.2.3 Temperature dependence

In silicon the temperature dependence of Auger recombination is given by Klaassen's model [72]. Auger coefficients in Eq. 3.22 are described by

$$c_n = c_n^{300K} \left(\frac{T}{300}\right)^{\gamma_n} \tag{3.30}$$

$$c_p = c_p^{300K} \left(\frac{T}{300}\right)^{\gamma_p} \tag{3.31}$$

with $c_n^{300K} = 1.83{\times}10^{-31}\ \mathrm{cm^6 s^{-1}}$, $c_p^{300K} = 2.78{\times}10^{-31}\ \mathrm{cm^6 s^{-1}}$, $\gamma_n = 1.18$ and $\gamma_p = 0.72$. With this model, the temperature dependent differential lifetime of Auger recombination is calculated and shown in Fig. 3.5. For the sake of comparison, we do the calculation at the same

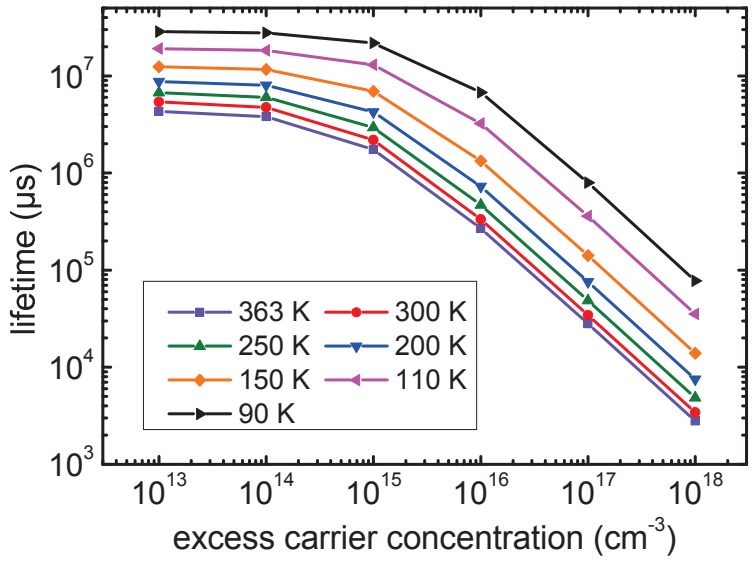

Fig. 3.5 Auger recombination differential lifetime given by Eq. 3.26 in one sun illumination. $N_d = 10^{15}\mathrm{cm^{-3}}$ is used.

temperatures as in Fig. 3.3. In contrast to radiative recombination, Auger recombination

decreases when temperature decreases. Hence at low temperature radiative recombinations should dominate for high carrier concentrations.

3.2.3 Defect-mediated non-radiative recombination

In this thesis we do not treat separately interface/surface defect and bulk defects. People often describe the recombination at the surface by introducing a surface recombination velocity. However recombinations through surface/interface defects follow the same defect mediated mechanism described by the Shockley-Read-Hall (SRH) theory as recombination through both defects, this is why we will not consider them separately.

3.2.3.1 Steady state lifetime

For a single type of defect at energy E_t, the net SRH recombination rate is given by:

$$R_{SRH} = \frac{np - n_i^2}{\tau_{p0}(n + n_1) + \tau_{n0}(p + p_1)} \tag{3.32}$$

$\tau_{p0} = 1/(\upsilon_{th,p} N_R \sigma_p)$, $\tau_{n0} = 1/(\upsilon_{th,n} N_R \sigma_n)$ where $\upsilon_{th,p}$ and $\upsilon_{th,n}$ are the thermal velocities of holes and electrons, σ_p and σ_n the capture cross sections for holes and electrons, and N_R the defect density. $n_1 = N_c \exp(-\frac{E_c - E_t}{k_B T})$, $p_1 = N_\upsilon \exp(-\frac{E_t - E_\upsilon}{k_B T})$ where N_c and N_υ are effective density of states of conduction and valence band, E_c and E_υ the conduction and valence band edge energy levels. Assuming that $\Delta n = \Delta p = n - n_0 = p - p_0$, the steady state carrier lifetime is given by Eq. 3.6. Thus we have:

$$\begin{aligned} \tau_{SS,SRH} &= \frac{\Delta n}{np - n_i^2} \left[\tau_{p0}(n + n_1) + \tau_{n0}(p + p_1)\right] \\ &= \frac{\tau_{p0}(n + n_1) + \tau_{n0}(p + p_1)}{\Delta n + n_0 + p_0} \end{aligned} \tag{3.33}$$

3.2.3.2 Differential lifetime

Assuming that $\Delta n = \Delta p = n - n_0 = p - p_0$, we obtain from Eq. 3.7:

$$\begin{aligned}\frac{1}{\tau_{diff,SRH}} &= \frac{(2\Delta n + n_0 + p_0)\left[\tau_{p0}(n+n_1)+\tau_{n0}(p+p_1)\right] - (np - n_i^2)(\tau_{p0}+\tau_{n0})}{\left[\tau_{p0}(n+n_1)+\tau_{n0}(p+p_1)\right]^2} \\ &= \frac{(2\Delta n + n_0 + p_0)\tau_{ss,SRH}(\Delta n + n_0 + p_0) - \Delta n(\Delta n + n_0 + p_0)(\tau_{p0}+\tau_{n0})}{[\tau_{ss,SRH}(\Delta n + n_0 + p_0)]^2} \\ &= \frac{(2\Delta n + n_0 + p_0)\tau_{ss,SRH} - \Delta n(\tau_{p0}+\tau_{n0})}{\tau_{ss,SRH}^2(\Delta n + n_0 + p_0)}\end{aligned} \tag{3.34}$$

The ratio between $\tau_{ss,SRH}$ and $\tau_{diff,SRH}$ is

$$\begin{aligned}\frac{\tau_{ss,SRH}}{\tau_{diff,SRH}} &= \frac{(2\Delta n + n_0 + p_0)\tau_{ss,SRH} - \Delta n(\tau_{p0}+\tau_{n0})}{\tau_{ss,SRH}(\Delta n + n_0 + p_0)} \\ &= \frac{\tau_{ss,SRH}(\Delta n + n_0 + p_0) + \Delta n(\tau_{ss,SRH} - \tau_{p0} - \tau_{n0})}{\tau_{ss,SRH}(\Delta n + n_0 + p_0)} \\ &= 1 + (1 - \frac{\tau_{p0}+\tau_{n0}}{\tau_{ss,SRH}})\frac{\Delta n}{\Delta n + n_0 + p_0}\end{aligned} \tag{3.35}$$

$\tau_{p0} + \tau_{n0}$ gives the possible maximum of $\tau_{ss,SRH}$, which means that the second addend is always negative and that $\tau_{ss,SRH}$ is always smaller than $\tau_{diff,SRH}$. In the limit of low injection ($\Delta n \ll p_0 + n_0$), Eq. 3.35 leads to

$$\tau_{diff,SRH} = \tau_{SS,SRH}$$

In the limit of high injection ($\Delta n \gg p_0 + n_0$), Eq. 3.35 leads to

$$\frac{\tau_{ss,SRH}}{\tau_{diff,SRH}} = 2 - \frac{\tau_{p0}+\tau_{n0}}{\tau_{ss,SRH}} \tag{3.36}$$

This equation can be further simplified since under high injection condition $\tau_{SS,SRH} = \tau_{p0} + \tau_{n0}$ we get

$$\tau_{diff,SRH} = \tau_{SS,SRH}$$

Steady state and differential SRH lifetimes coincide with each other in both low and high injection limit. Some typical parameters are used to illustrate the discrepancy between $\tau_{diff,SRH}$ and $\tau_{SS,SRH}$ in Fig. 3.6(a). It is found in Fig. 3.6(b) that the greatest discrepancy occurs when the carrier concentration approaches the doping level.

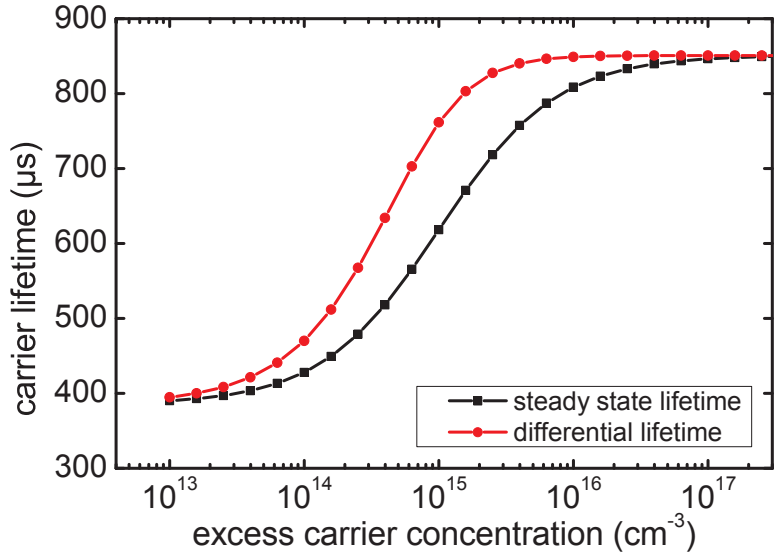

(a)

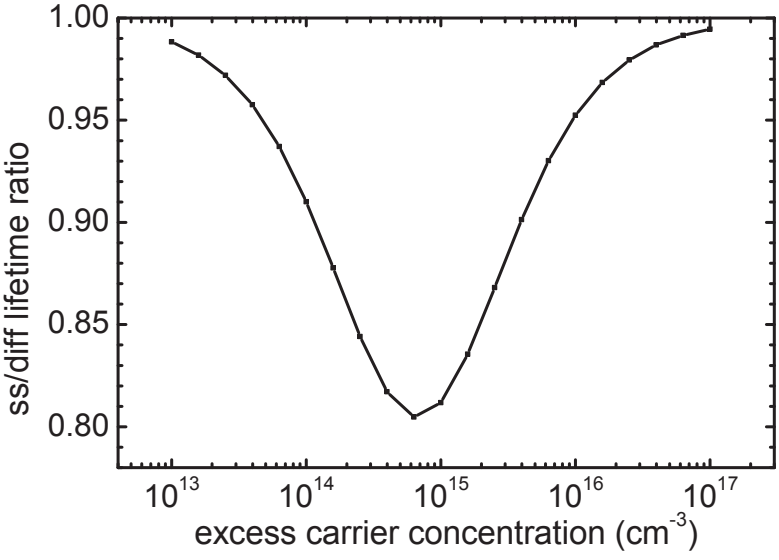

(b)

Fig. 3.6 (a) Comparison of steady state and differential lifetime. (b) Ratio of steady state lifetime to differential lifetime. The steady state and differential SRH lifetimes are calculated with Eq. 3.33, 3.34. Following parameters are used: $T = 300$ K, $N_d = 10^{15}$ cm^{-3}, $N_a = 0$ cm^{-3}, $\tau_{p0} = 385$ μs, $\tau_{n0} = 465$ μs, $E_c - E_t = 0.3$ eV.

3.2.3.3 Temperature dependence

Temperature dependence of SRH recombination has been developed into an analysis method by Rein, that is the temperature dependent lifetime spectroscopy (TDLS) [59]. It is based on the classical SRH recombination model. Steady state SRH lifetime is given by Eq. 3.33. By defining the symmetry factor

$$k = \sigma_n/\sigma_p = \tau_{p0}/\tau_{n0}{}^{*} \tag{3.37}$$

we can develop Eq. 3.33 as

$$\tau_{SS,SRH} = \tau_{n0}\frac{(\Delta n + p_0 + p_1) + k(\Delta n + n_0 + n_1)}{\Delta n + n_0 + p_0} \tag{3.38}$$

Under the high level injection limit ($\Delta n \gg p_0 + n_0$), the steady state SRH lifetime can be simplified as

$$\tau_{SS,SRH}^{HLI} = \tau_{n0} + \tau_{p0} = \tau_{n0}(1 + k) \tag{3.39}$$

Since $\tau_{n0} = 1/(\upsilon_{th} N_R \sigma_n)$, the temperature dependence of capture cross section σ_n can be found out from the temperature dependent τ_{n0}, if the symmetry factor k is constant. However, Auger and radiative recombination have great impact in high injection measurement, so it is often difficult to separate the SRH lifetime from the measured effective lifetime. High level injection analysis is seldom mentioned.

In contrary, at low level injection ($\Delta n \ll p_0 + n_0$), the steady state SRH lifetime for n-type wafer is given by

$$\tau_{SS,SRH}^{LLI} = \tau_{n0}\left[\frac{p_1}{n_0} + k(1 + \frac{n_1}{n_0})\right] \tag{3.40}$$

For a defect level in the upper half of the band gap, p_1 is negligible compared to n_0, so

$$\tau_{SS,SRH}^{LLI} = \tau_{p0}\left(1 + \frac{n_1}{n_0}\right) \tag{3.41}$$

we can further develop the temperature dependence of the expression by taking into account thermal velocity $\upsilon_{th} \propto T^{1/2}$, $N_c \propto T^{3/2}$ and assuming that the capture cross sections and dopant ionization are independent of temperature:

$$\tau_{SS,SRH}^{LLI} = c_1\left(\frac{T}{300}\right)^{-1/2} + c_2\left(\frac{T}{300}\right)\exp\left(-\frac{\Delta E_t}{k_B T}\right) \tag{3.42}$$

with $c_1 = \tau_{p0}^{300\mathrm{K}}$ and $c_2 = \tau_{p0}^{300K} N_c^{300K}/n_0$. τ_{p0}^{300K} and N_c^{300K} are τ_{p0} and N_c at 300 K. ΔE_t is the defect level energy with respect to the conduction band edge.

* We assume here that $\upsilon_{th,n}$=$\upsilon_{th,p}$=υ_{th}

For a defect level in the lower half of the band gap in n-type c-Si, $c_1 = \tau_{p0}^{300K}$ and $c_2 = \tau_{n0}^{300K} N_v^{300K}/n_0$. ΔE_t is the defect level energy with respect to the valence band edge. N_v^{300K} is N_v at 300 K.

For a defect level in the upper half of the band gap in p-type c-Si, $c_1 = \tau_{n0}^{300K}$ and $c_2 = \tau_{p0}^{300K} N_c^{300K}/p_0$. ΔE_t is the defect level energy with respect to the conduction band edge. τ_{n0} is τ_n at 300 K

For a defect level in the lower half of the band gap in p-type c-Si, $c_1 = \tau_{n0}^{300K}$ and $c_2 = \tau_{n0}^{300K} N_v^{300K}/p_0$. ΔE_t is the defect level energy with respect to the valence band edge.

Lifetime as a function of temperature in low injection condition can be fitted with Eq. 3.42 to extract the defect level either with respect to the conduction band or to the valence band. However it is not sufficient to provide more information on whether the defect level is in the upper or lower part of the band gap.

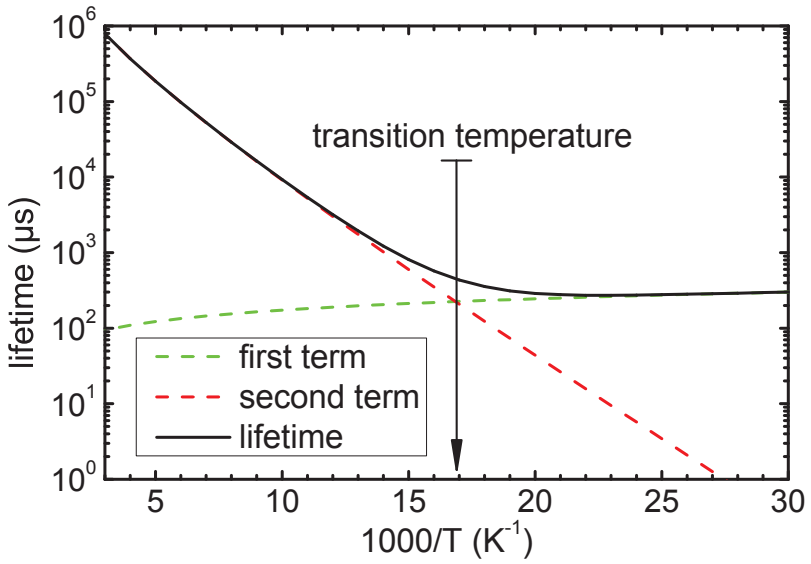

Fig. 3.7 An illustration of Eq. 3.42. The first term of the formula and the second term cross at transition temperature. $E_t = 40$ meV, $\tau_{p0}^{300K} = 100$ µs is used for the calculation.

As shown in Fig. 3.7, we can find in this equation that when the temperature decreases, the first term dominates whereas the impact of the second term fades out. The first term is related to the capture process of carriers while the second term is related to the emission process. When the temperature increases, the emission dominates the lifetime. When temperature is very low, emission is weak and thus the lifetime is dominated by the capture process.

If no temperature dependence of the capture cross section is considered, we find that the first term increases when the temperature decreases, and the second term decreases when

the temperature decreases. This can be seen in Fig. 3.7. However, it is possible that the first term decreases with decreasing temperature when a capture cross section temperature dependence interferes. For this reason, when we observe that the lifetime decreases when temperature decreases, it is necessary to determine whether we are dealing with an emission dominated recombination process or a capture dominated recombination process.

The discussions above also mean that there is a transition temperature T_t at which the capture and emission process are in equilibrium. It is also translate the dominating regime *i.e.* capture or emission. Above T_t the emission process dominates the lifetime while below T_t the capture process dominates. According to Eq. 3.42 the two terms are equal to each other at this temperature when

$$c_1 \left(\frac{T}{300}\right)^{-1/2} = c_2 \left(\frac{T}{300}\right) \exp\left(-\frac{\Delta E_t}{k_B T}\right) \tag{3.43}$$

so we have

$$T_t^{3/2} \exp(-\frac{\Delta E_t}{k_B T_t}) = \frac{c_1}{c_2}(300\text{K})^{3/2} \tag{3.44}$$

In n-type silicon, for a defect level in the upper half of the band gap, $c_1/c_2 = n_0/N_c^{300K}$. Fig. 3.8 shows the evolution of the transition energy as a function of the defect energy if it is located in the upper band gap of n-type c-Si with $n_0 = 10^{15}$ cm^{-3}. In experiments we have

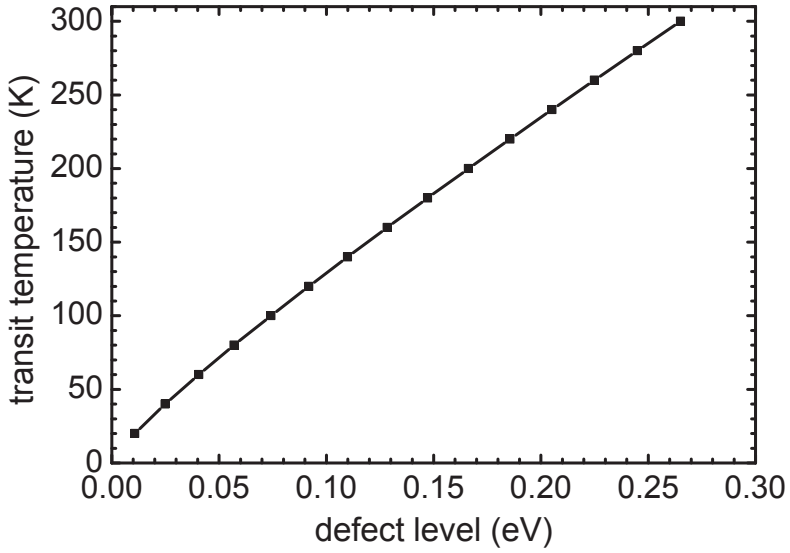

Fig. 3.8 The transition temperature as a function of defect energy below conduction band. Calculated by Eq. 3.44 with $n_0 = 10^{15}$ cm^{-3} and $N_c^{300K} = 2.84 \times 10^{19}$ cm^{-3}.

observed T_t above 100 K. However the extracted defect level is about 0.02 eV, which is not in agreement with Fig. 3.8. This discrepancy could be related to the temperature dependence

of n_0. That should be taken into account at low temperature where dopants are not fully ionized.

Since due to the domination of the Auger and radiative recombination at high level injection, the SRH recombination is often not able to be precisely determined. In contrast, the low level injection is dominated by SRH recombination and is able to extract important information as discussed in previous text. For this reason, we would mean low level injection measurements when referring to TDLS analysis in later discussions in this thesis.

3.3 Comparison of steady state and differential lifetime

Now we consider the "total lifetime" that accounts for all the recombinations. A for the steady-state lifetime:

$$\frac{1}{\tau_{ss,tot}} = \frac{1}{\tau_{ss,rad}} + \frac{1}{\tau_{ss,Aug}} + \frac{1}{\tau_{ss,SRH}} \tag{3.45}$$

the differential effective lifetime follows the same rule:

$$\begin{aligned} \frac{1}{\tau_{diff,tot}} &= \frac{\mathrm{d}R}{\mathrm{d}\Delta n} \\ &= \frac{\mathrm{d}}{\mathrm{d}\Delta n}(R_{rad} + R_{Aug} + R_{SRH}) \\ &= \frac{\mathrm{d}R_{rad}}{\mathrm{d}\Delta n} + \frac{\mathrm{d}R_{Aug}}{\mathrm{d}\Delta n} + \frac{\mathrm{d}R_{SRH}}{\mathrm{d}\Delta n} \\ &= \frac{1}{\tau_{diff,rad}} + \frac{1}{\tau_{diff,Aug}} + \frac{1}{\tau_{diff,SRH}} \end{aligned} \tag{3.46}$$

3.3.1 Auger and radiative recombination

We first neglect the SRH mechanism and look at the global effect of Auger and radiative recombination. The steady-state and differential lifetime is obtained from analytic calculation using Eq. 3.7 and 3.8. Eq. 3.46 is not directly used. As is shown in Fig. 3.9(a), the result quite resembles the behavior of Auger lifetime. For high lifetime sample Fig. 3.9(b) is practical for the estimation of differential lifetime from steady-state lifetime or vice versa.

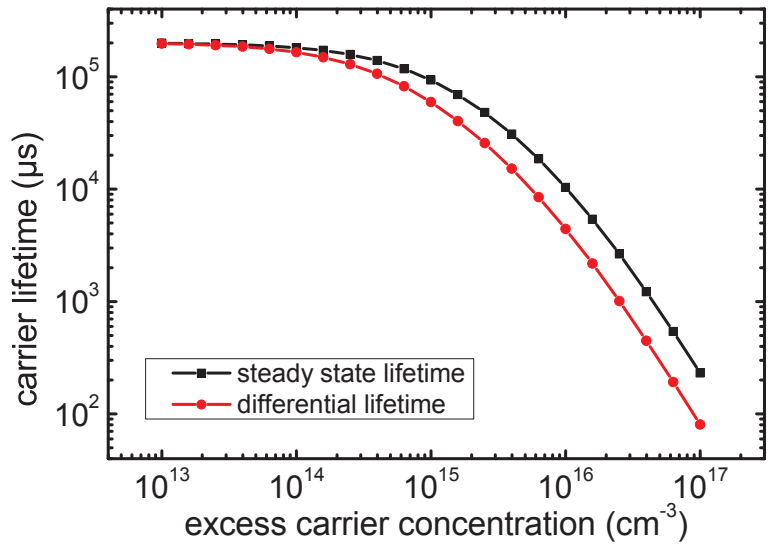

(a)

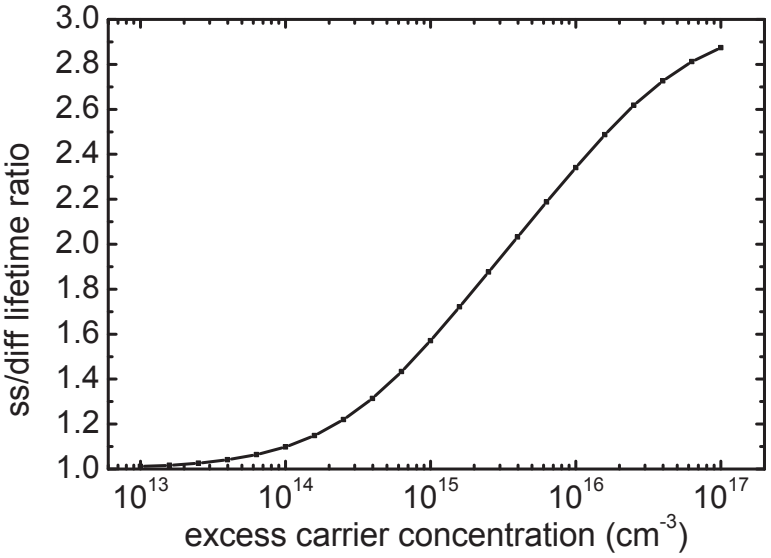

(b)

Fig. 3.9 (a) Comparison of steady-state and differential lifetime when both Auger and radiative recombination mechanism are taken into account. (b) The ratio of steady-state lifetime to differential lifetime.

3.3.2 Auger, radiative and SRH recombination

We evaluate the effective lifetime with Eq. 3.46 with the same parameters used in Fig. 3.2, 3.4 and 3.6. $\tau_{diff,tot}$ and $\tau_{SS,tot}$are shown in Fig. 3.10, along with separate recombination components (Auger, radiative and SRH).

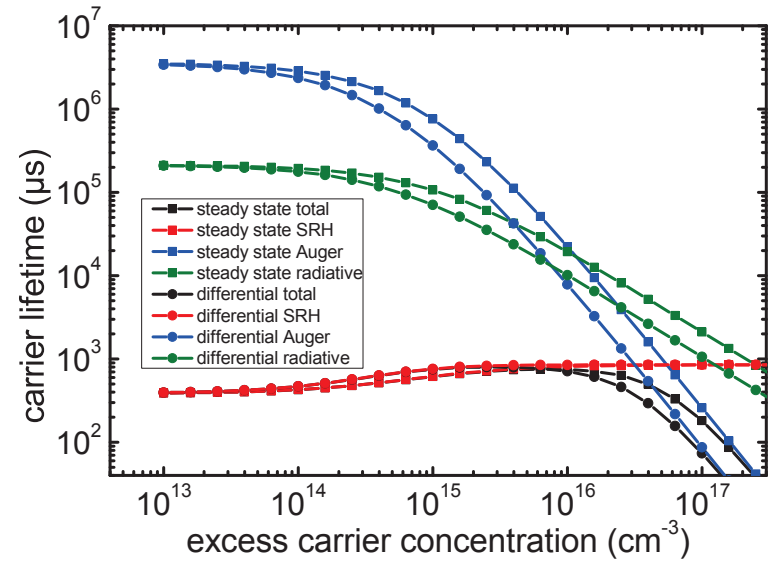

(a)

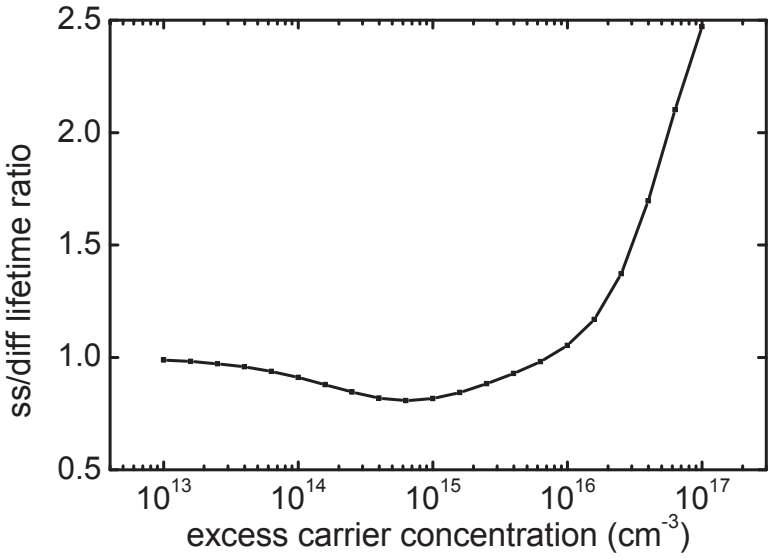

(b)

Fig. 3.10 (a) Comparison of steady-state and differential lifetime when SRH, Auger and radiative recombination mechanism are taken into account. (b) The ratio of steady-state lifetime to differential lifetime. The steady state and differential total lifetime summarized from Fig. 3.2, 3.4 and 3.6.

Note that neither Auger nor radiative recombination is dominant for low carrier concentration ($<10^{16}$ cm^{-3}). For high concentration Auger recombination dominates ($>10^{17}$ cm^{-3}). In the intermediate region ($>10^{16}$ cm^{-3}), all the three recombination mechanisms affect the lifetime together. This region depends on the sample parameters. Lower SRH recombination shifts the lifetime upwards and thus the onset region moves to lower concentration. This is the case for high quality and well passivated wafers.

In Fig. 3.10(b), we show the ratio of steady-state total lifetime to differential total lifetime. For low carrier concentration $\tau_{diff,tot}$ is lower than $\tau_{SS,tot}$ but not very large. For high carrier concentration, there is large difference between $\tau_{diff,tot}$ and $\tau_{ss,tot}$. When Auger recombination dominates, we have $\tau_{SS,tot}/\tau_{diff,tot} = 3$. In Fig. 3.10(a) the Auger recombination has not completely dominated the lifetime at 10^{17} cm^{-3}, thus we get 2.5 for the maximum value of this ratio in Fig. 3.10(b).

3.4 Simulation of the differential lifetime

It is interesting to reproduce MPL in simulation. It would be also interesting to know if the difference between the two definitions of lifetime would introduce a discrepancy. We simulate the heterojunction device using ATLAS and take into consideration the radiative, SRH and Auger recombination.

3.4.1 Investigated structure

First we describe the structure that will be used in all simulations in this work in Fig. 3.11. The layer stack is symmetrical, p-type a-Si:H on top of n-type c-Si:H. A very thin intrinsic c-Si layer (1 nm) with large quantity of defects is placed between a-Si:H and c-Si layer to simulate interface defects. To define the interface defect density, we first designate the bulk defect density in this layer and then integrate the defect density throughout the thin layer:

$$N_{inter} = \int_{x_{palic}}^{x_{ic/nc}} N_{bulk} \mathrm{d}x = N_{bulk}(x_{ic/nc} - x_{palic}) \tag{3.47}$$

The thickness of p-type a-Si:H layer is 20 nm and the thickness of n-type c-Si layer is 280 µm. 785 nm monochromatic laser excitation is injected from one side of the stack. The doping concentration of the c-Si substrate is $N_d = 1.8 \times 10^{15}$ cm^{-3}. The density of states in the bandgap of (p) a-Si:H is made of two band tails (acceptor g_{TA} and donor g_{TD}) and two

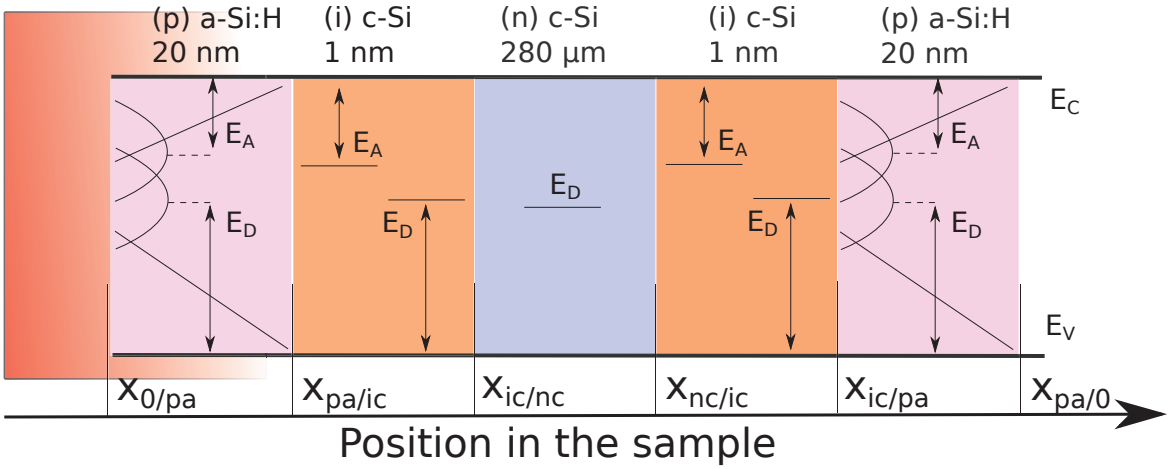

Fig. 3.11 The structure stack utilized in all simulations and defects in band gap. The structure is symmetrical. The thickness is not drawn to scale.Monochromatic 785 nm laser is incident from one side of the stack.

Gaussian distributions (acceptor g_{GA} and donor g_{GD}). In ATLAS it is defined as follows:

$$\begin{aligned} g_{TA}(E) &= NTA \exp\left(\frac{E - E_c}{WTA}\right) \\ g_{TD}(E) &= NTD \exp\left(\frac{E_v - E}{WTD}\right) \\ g_{GA}(E) &= NGA \exp\left[-\left(\frac{EGA - E}{WGA}\right)^2\right] \\ g_{GD}(E) &= NGD \exp\left[-\left(\frac{E - EGD}{WGD}\right)^2\right] \end{aligned} \tag{3.48}$$

The values of parameters in Eq. 3.48 are given in Tab. 3.1. Capture cross sections of all

Table 3.1 Parameters used in p-type a-Si:H for simulations

Total density	**NTA**	**NTD**	**NGA**	**NGD**
Value (cm^{-3}/eV)	2×10^{21}	2×10^{21}	4.66×10^{19}	4.66×10^{19}
Characteristic decay energy	**WTA**	**WTD**	**WGA**	**WGD**
Value (eV)	0.04	0.086	0.269	0.269
Capture cross section	**SIGTAE**	**SIGTAH**	**SIGGAE**	**SIGGAH**
Value (cm^2)	1×10^{-17}	1×10^{-16}	1×10^{-17}	1×10^{-16}
Capture cross section	**SIGTDE**	**SIGTDH**	**SIGGDE**	**SIGGDH**
Value (cm^2)	1×10^{-16}	1×10^{-17}	1×10^{-16}	1×10^{-17}

kinds of defects are also given in Tab. 3.1. The notation is explained as follows: SIG, capture cross section; T, band tail; G, Gaussian distribution; A, acceptor defect; D, donor defect; E, electron capture; H, hole capture.

In addition, we introduce a single acceptor doping level in a-Si:H with a density of $N_a = 2.45 \times 10^{19}$ cm^{-3}, which places the equilibrium Fermi level at 0.39 eV above the valence band edge. The $N_d = 1.8 \times 10^{15}$ cm^{-3} doping in c-Si layer fixes the Fermi level at 0.25 eV below conduction band. The bandgap of a-Si:H and c-Si were taken equal to 1.75 eV and 1.124 eV, and the electron affinity of a-Si:H and c-Si were taken equal to 3.90 eV and 4.05 eV, leading to a built-in potential of:

$$\begin{aligned} V_{bi} &= q\chi^{a-Si:H} + E_g^{a-Si:H} - (E_f - E_v^{a-Si:H}) - q\chi^{c-Si} - (E_c^{c-Si} - E_f) \\ &= 3.90 + 1.75 - 0.39 - 4.05 - 0.25 = 0.96 \text{ eV} \end{aligned} \tag{3.49}$$

The bandgap and carrier concentrations of the simulated structure in thermal equilibrium is shown in Fig. 3.12. As we can see in the figure, in the vicinity of the interface there

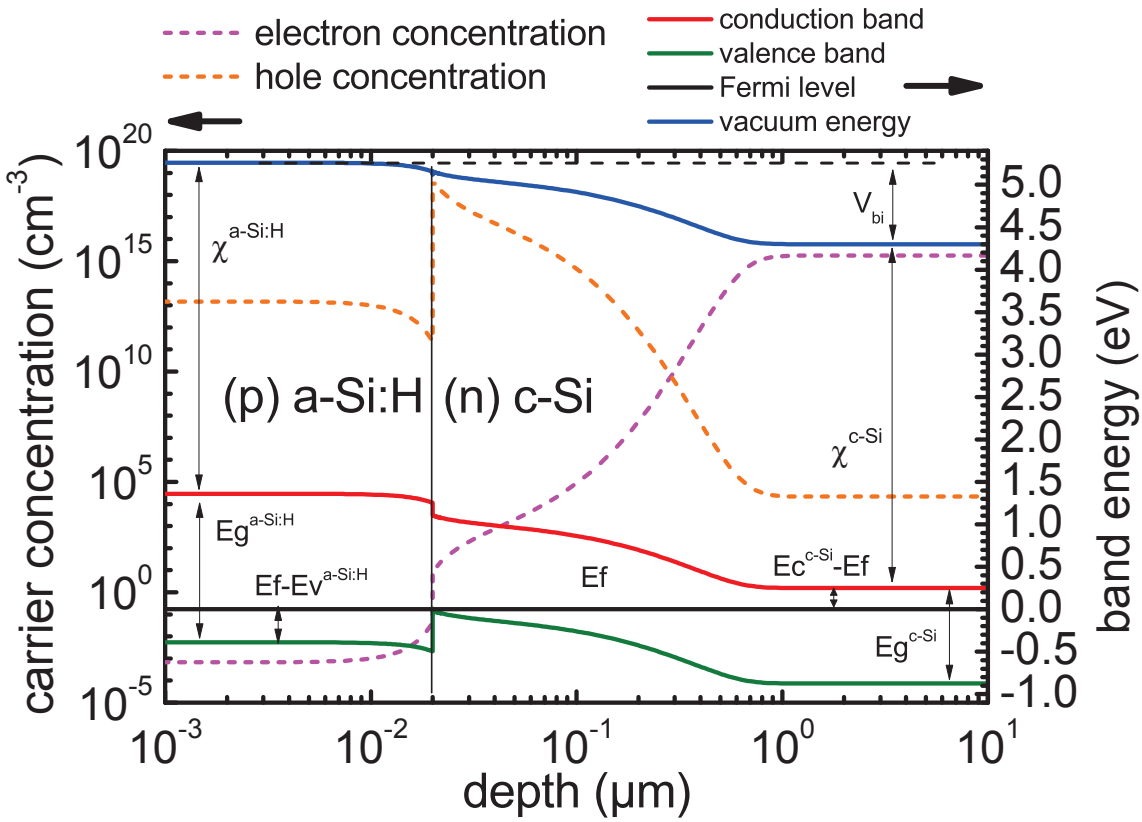

Fig. 3.12 Band diagram and carrier concentration of the simulated SHJ stack structure in thermal equilibrium. Values of all parameters are given in the text and in Tab. 3.1.

exists a charge depletion region in c-Si of about 1 µm thick where the majority and minority carrier concentrations are inversed. The concentration of minority carrier, in our case the hole, decreases from the a-Si:H/c-Si interface towards to the c-Si bulk by many orders of magnitude within this thin layer. The influence of this layer will be discussed in later sections.

3.4.2 Simulation method of the MPL lifetime

The simulation of MPL relies on the functionality of the simulation software. It can be best simulated if the software itself is capable of the simulation of modulated PL. However, this feature has not been implemented in existing simulation softwares. Even the carrier lifetime, although important, is not a direct output parameter in softwares, neither in steady state nor in modulated condition. After all, the steady state carrier lifetime can be obtained with $\tau_{ss}(G) = \Delta n(G)/G = \Delta n(R)/R$ (Eq. 3.6). The question is how do we get differential lifetime from a steady state simulation.

As is discussed in section 3.1, the differential lifetime is the slope of the steady state carrier concentration-generation $\Delta n(R)$ curve at the specified generation rate R. This fact allows us to calculate the differential lifetime from the steady state simulation by simply applying a finite difference method. It is thus described as below:

$$\tau_{diff}(G) = \frac{\Delta n(G + \Delta G) - \Delta n(G - \Delta G)}{2\Delta G} \tag{3.50}$$

This is a derivative by central difference. The slope at point G curve can be obtained by two simulations at point $G+\Delta G$ and $G-\Delta G$. In the future we will chose ΔG to be 2% of G value in the simulations. In this way the differential lifetime for generation rate G is obtained.

When we simulate a real structure instead of doing an analytical calculation, we can have a profile of carrier concentration meaning that the carrier concentration is not homogeneous throughout the structure. Since the measured PL or MPL is a global value that integrates photons being emitted throughout the structure, the definition of lifetime in Eq. 3.6 and Eq. 3.7 has to be extended to average values of Δn and G.

However, since PL is negligible in a-Si:H, one can restrict the averaging to the crystalline silicon part only (see Fig. 3.11):

$$\Delta n_{avg} = \frac{1}{d_{c-Si}} \int_{x_{pa/ic}}^{x_{ic/pa}} \Delta n(x)\mathrm{d}x \tag{3.51}$$

$$G_{avg} = \frac{1}{d_{c-Si}} \int_{x_{pa/ic}}^{x_{ic/pa}} G(x)\mathrm{d}x \tag{3.52}$$

where $d_{c-Si} = x_{ic/na} - x_{pa/ic}$ is the c-Si wafer thickness. For later simulations in this work, all Δn and G will refer to the averaged value Δn_{avg} and G_{avg} and thus the subscript will be omitted.

3.4.3 Lifetime extraction from different regions

According to the Fig. 3.12, the Fermi level alignment between (p) a-Si:H and (n) c-Si:H results in the band bending and the formation of the space charge region of about 1 µm that includes an inversion layer of about 0.3 µm. Although this region is only about 1 µm thick (from $x = x_{pa/ic}$ to $x \approx x_{pa/ic} + 1$ µm) in Fig. 3.12, the hole concentration gets many orders of magnitude higher close to the interface than in the bulk. When we extract the minority excess carrier concentration, the holes in this region may play an important role. Moreover, since interface recombination dominates in our simulations, we should make sure that the interface is properly modelled to extract a valid lifetime. We will show the difference between two cases: lifetime data extracted from region including inversion layer or without.

To simulate the interface defects, we introduce two types of defects in the 1 nm thick interface layers (see Fig. 3.11): acceptor defects with the density N_{acc} at 0.4 eV below the c-Si conduction band and donor defects with the density N_{don} at 0.6 eV above the valence band. These positions have been chosen to be compatible with the dangling bond states positions from the defect-pool model in a-Si:H. The simulation is conducted with defect densities of $N_{don,vol} = N_{acc,vol} = 10^{19}$ cm^{-3} and $N_{don} = N_{acc} = 10^{17}$ cm^{-3} to show the impact of different defect densities. This corresponds to interface defect densities of $N_{don} = N_{acc} = 10^{12}$ cm^{-2} and $N_{don} = N_{acc} = 10^{10}$ cm^{-2}, respectively. We put also mid gap donor-like defects with the density of 10^{10} cm^{-3} in the c-Si. Monochromatic illumination (785 nm) with intensity equivalent to one sun is applied.

3.4.3.1 Without space charge layer

We start by doing simulations and extracting the average excess carrier concentration in the region excluding the space charge region. To simplify, we choose a value of space charge layer thickness of 1 µm and calculate the average values of Δn from:

$$\Delta p_{avg} = \frac{1}{d_{c-Si} - 2\mu m} \int_{x_{pa/ic}+1\mu m}^{x_{ic/pa}-1\mu m} \Delta n(x) \mathrm{d}x \tag{3.53}$$

The steady-state Auger and radiative lifetime are obtained directly from Eq. 3.23 and 3.18. The total differential and steady-state lifetimes are obtained directly from Eq. 3.7 and 3.8. Since the steady-state SRH recombination rate is not an output parameter of ATLAS, we have

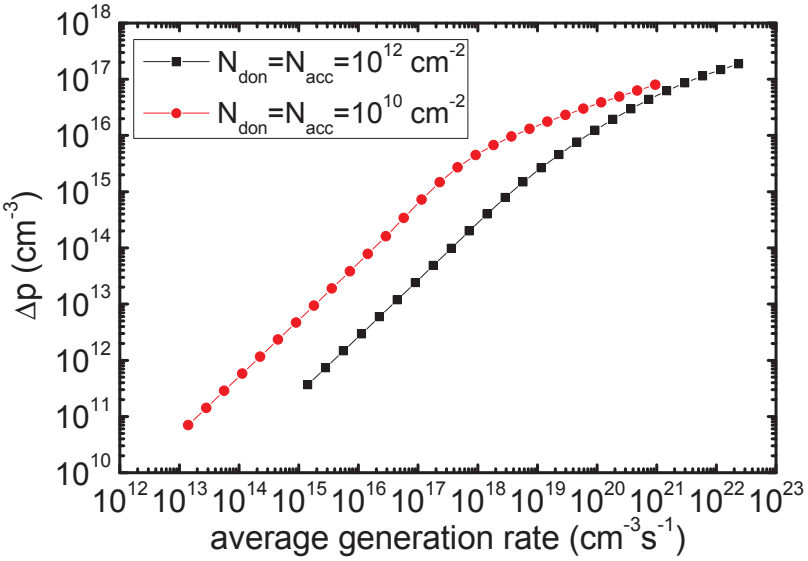

(a)

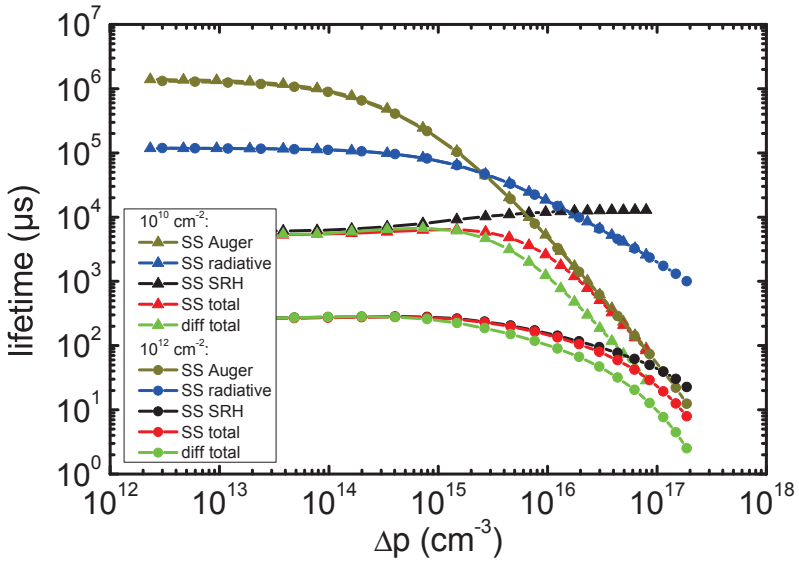

(b)

Fig. 3.13 (a) Excess carrier concentration dependent recombination rate and (b) the discrepancy between steady state lifetime and differential lifetime. The excess carrier concentration and the lifetime are extracted by averaging on the c-Si wafer including the inversion layer.

to calculate it from Eq. 3.45 with the available output parameters such as carrier concentration, Auger recombination rate, radiative recombination rate and total recombination rate. Note that only the carrier concentration is obtained without the space charge region whereas the recombination rate is always obtained taking into account the overall c-Si substrate.

First we check the minority carrier lifetime dependence on recombination rate. In Fig. 3.13(a), we can see that the Δp for surface defect density of 10^{10} cm^{-2} is higher than that of 10^{12} cm^{-2}. For lower generation rate, the slopes of the two $\Delta p(G)$ curve are the same. When generation increases, the slopes of the curves change and Δp tends to saturate ($\Delta p > 10^{15}$ cm^{-3}). This is where the Auger recombination becomes dominant.

In Fig. 3.13(b), we show the steady-state radiative, Auger and SRH lifetime and both total steady-state and differential lifetime. The total lifetime is given by Eq. 3.45 and 3.46. The lifetime is limited by bulk SRH recombination for low injection and by Auger recombination for high injection. It is noticeable that the differential lifetime is mostly lower than the steady state lifetime, whether the dominant recombination is SRH or Auger.

In Fig. 3.13(b), the radiative and Auger recombination are the same for both the surface defect densities of 10^{10} cm^{-2} and 10^{12} cm^{-2}. This is because we are plotting the data as a function of carrier concentration. When the carrier concentration is relatively low, we see that the SRH recombination of interface defects dominates. 10^{10} cm^{-2} interface defect density leads to 5204 µs SRH lifetime, and 10^{12} cm^{-2} the interface defect density leads to 262 µs SRH lifetime. This means that 100 times difference of interface defect density results in only 20 times difference of SRH lifetime. Or we say that when interface defect density increases by a factor of 100, the lifetime decreases only by a factor of 20. This means that for an interface defect density of 10^{10} cm^{-2}, it is not dominant and that the dominant SRH channel should be the 10^{10} cm^{-3} bulk defects.

Since the SRH lifetime of 10^{12} cm^{-2} interface defect density is 20 times lower than that of 10^{10} cm^{-2}, we can be sure that a density value of 10^{12} cm^{-2} assures the dominance of interface defects. Besides, the SRH lifetime dependence on carrier concentration of the 10^{10} cm^{-2} density correspond to Fig. 3.6(a). However, the carrier concentration dependence of SRH lifetime of the 10^{10} cm^{-2} density is quite different.

The differential lifetime coincide with steady-state lifetime when SRH recombination dominates and they begin to diverge when Auger recombination becomes dominant.

When the carrier concentration increases, Auger and radiative recombination dominate and the lifetimes of the two cases gradually approximate each other.

As is mentioned above, these lifetime is extracted by excluding the space charge layer. This may not reflect the true lifetime since the impact of the interface could be very strong. We should investigate the impact of the carrier concentration in the space charge region.

3.4.3.2 With inversion layer

We go back to the definition by Eq. 3.51 and consider the whole c-Si region and extract excess carrier concentration from all c-Si region. Again, the steady-state Auger and radiative lifetime are obtained directly from Eq. 3.23 and 3.18. The total differential and steady-state lifetimes are obtained directly from Eq. 3.7 and 3.8. Since the steady-state SRH recombination is not an output parameter of ATLAS, we have to calculate it from Eq. 3.45.

In Fig. 3.14(a) we find that for low injection the dependence is quite different from the previous case where the space charge region is not considered for Δp extraction. When Δp is very low, this results in an increase of lifetime for both steady-state and differential lifetime, and more for steady-state, as is shown in Fig. 3.14(b).

The SRH lifetime of the interface defect density of 10^{10} cm^{-2} is always much higher than that of the interface defect density of 10^{12} cm^{-2}. Again we can be sure that the interface defect recombination dominates. When the carrier concentration increases, the SRH lifetimes of interface defect density of 10^{10} cm^{-2} decreases, which is different from the case in previous section where the carrier concentration in the space charge region is not considered. As we have pointed out in previous discussions, the interface defect density of 10^{10} cm^{-2} has a limited impact and the bulk SRH recombination dominates. Thus we conclude that whether the interface or bulk defects dominate the SRH recombination, Δp in the space charge region has an evident impact on the lifetime.

Similar lifetime dependence on carrier concentration has been reported by Garín et al and attributed to depletion region modulation effect which is often found in photoconductance lifetime measurements. The space charge region induced by fixed charges within the dielectric layer on c-Si wafer is responsible for this effect [73].

For high injection, the Auger recombination is dominant for $\Delta p > 10^{17}$ cm^{-3}. The lifetime is the same as when space charge region is not considered.

To further investigate the discrepancy for low excess hole concentration, we plot Δp for various illumination intensity of $N_{don,sur} = N_{acc,sur} = 10^{12}$ cm^{-2} simulation result in Fig. 3.15(a). We can see that Δp increases with increasing illumination. At the same injection level, Δp at the front side of the sample is slightly higher than that of the back side because the incident light is absorbed at the front side and the carriers diffuse to the back side with certain loss through recombination on their way. One should pay attention to the fact that Fig. 3.15 depicts the excess carrier concentration instead of carrier concentration. In terms of carrier concentration in the dark, an strong inversion layer exists and results in a high hole concentration at the interface (see Fig. 3.12). However, now we also find a high concentration of excess carrier concentration at the interface under illumination.

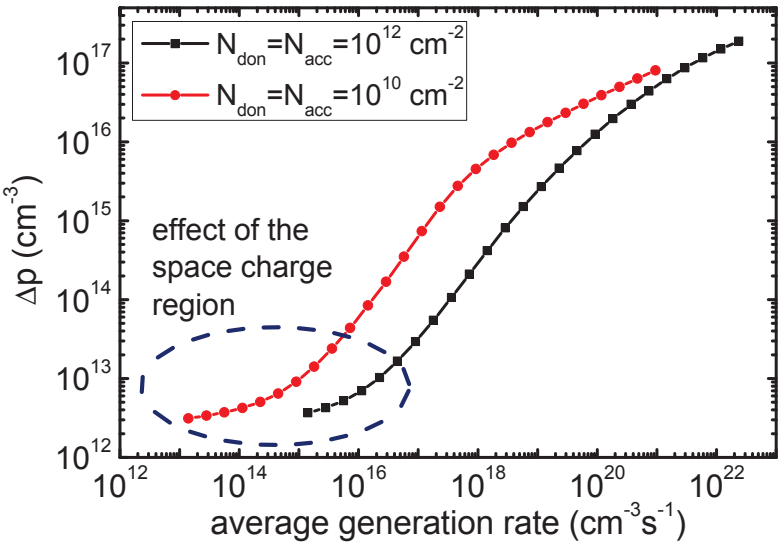

(a) Excess carrier concentration dependent recombination rate

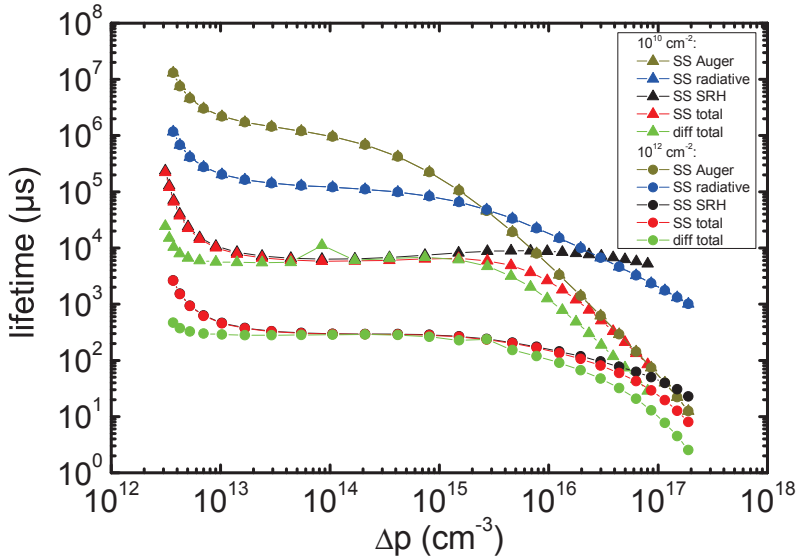

(b) Discrepancy between steady state lifetime and differential lifetime

Fig. 3.14 (a) Excess carrier concentration dependent recombination rate and (b) the discrepancy between steady-state lifetime and differential lifetime. The excess carrier concentration and the lifetime are extracted when averaging on the c-Si wafer including the space charge region.

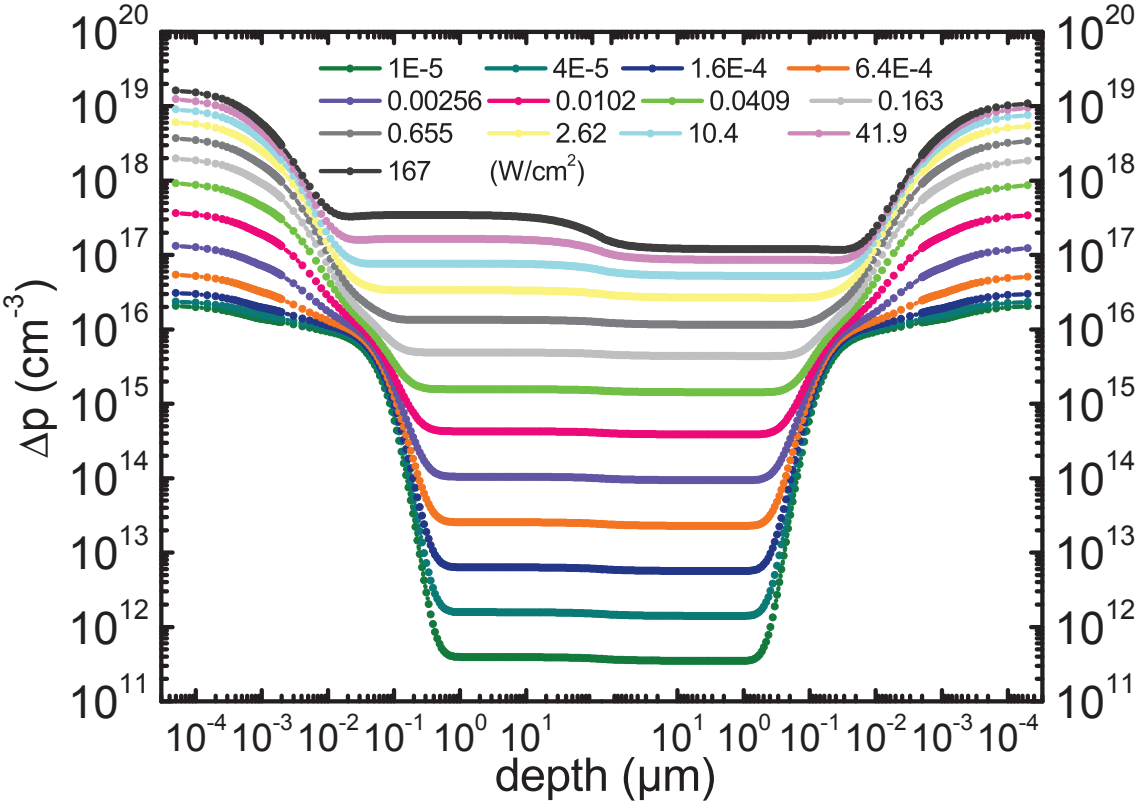

(a)

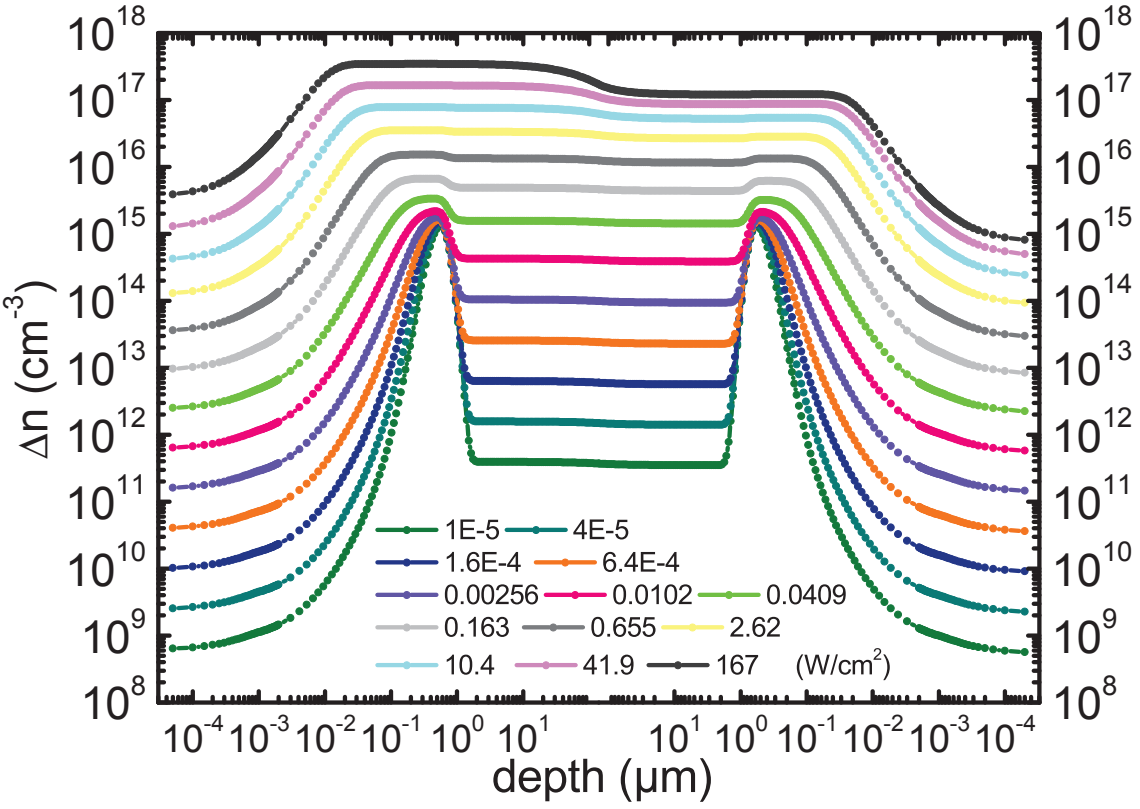

(b)

Fig. 3.15 Excess (a) hole and (b) electron concentration of $N_{don} = N_{acc} = 10^{12}$ cm^{-2} simulation result inside c-Si wafer ($x_{pa/ic} \sim x_{ic/na}$) for various illumination intensity.

The electron concentration in the c-Si layer is plotted in Fig. 3.15(b). Whether in dark or under illumination, Δn in bulk region is higher than in the space charge region. Thus Δn in the space charge region will not have any impact on the lifetime.

As is shown in Fig. 3.15, almost all Δp accumulate at the interfaces for very low injections. The Δp in the bulk region is 5 orders of magnitude lower than in the inversion layer. This means that low injection measurements could be much more sensitive to the SHJ interface.

If we compare Δp of the highest and lowest injection, we can see that there is 3 orders of magnitude of variation in the inversion layer, and in the bulk we find a variation of 6 orders of magnitude. This also implies that when the injection increases, recombination effects in the bulk are more significant and Auger effect may dominate because of the relatively low SRH recombination compared to interfaces. In Fig. 3.14(a), Auger dominates for $\Delta p > 10^{17}$ cm^{-3}. This Δp is an average value throughout the entire c-Si thickness of the simulated model. It corresponds to the injection level of 41.9432 W/cm^2 and above.

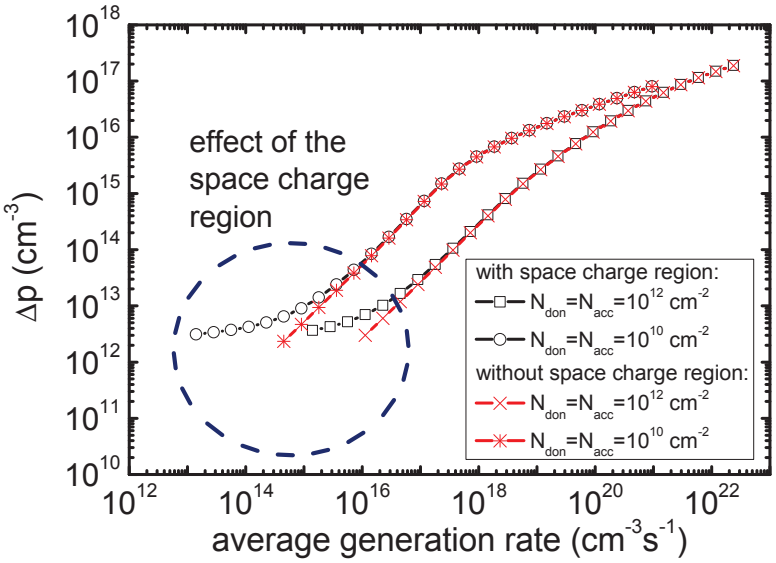

Fig. 3.16 Comparison of Δp versus generation rate. Data extracted from c-Si region including and excluding space charge region for different interface defect density.

We compare $\Delta p(G)$ in four conditions: interface recombination dominant, bulk dominant and different extraction method for both. Fig. 3.16 indicates that when we extract the parameters, the only discrepancy emerges for $\Delta p < 10^{13}$ cm^{-3}. For higher concentration, even if the interfaces recombination dominates, it is the excess carrier in the bulk that determines the lifetime. The band bending exhausts the minority carriers in the bulk, in our case

the holes, and attracts them to the interface for low injections. This is when the inversion layer carrier concentration is important to calculate lifetime.

To conclude, to extract the lifetime from simulation results, one need not pay extra attention to the space charge region. This is because for solar cell operations, the injection level (1000 W/m^2) which corresponds to about 4×10^{15} cm^{-3}, excess carrier lifetime extraction is independent of the inversion layer carrier concentration. Only the bulk concentration is important. However, for low level injection simulation, one should be careful about the impact of space charge region when extracting lifetime.

3.5 Conclusion

The differential nature of MPL lifetime has been discussed in detail. Radiative, Auger and SRH recombination lifetimes are presented in this context. For the former two, their differential lifetime is lower than the steady state lifetime by a factor of two and three, respectively. For SRH recombination, differential lifetime and steady state lifetime are the same for high and low injection. The TDLS analysis method is also presented. This is the characterization method utilized in this work to analyze temperature dependent lifetime measured by MPL. We have also demonstrated the guidelines of simulation. The method to extract lifetime from the carrier density, generation rate and recombination rate which have inhomogeneous profiles across the simulated stacks. The impact of space charge region on the extracted carrier is studied. The minority carriers are found to accumulate in the space charge region for low injections, and thus have influenced the extracted carrier lifetime at low level injection.

Chapter 4

Experimental results

In this chapter we first introduce the SHJ samples that are studied. The lifetime is measured using the PL and MPL system developed in previous chapters. The first data at room temperature consider various structural parameters such as passivation thickness, TCO, emitter and absorber. These data are benchmarked to the photodecay Sinton system. Moreover, we extended the capability of the systems to be able to map the PL and MPL accross the wafer SHJ. Temperature dependent PL spectrum has led to the discussion of PL quenching effect as well as the measurement of the radiative recombination coefficient. Furthermore, the defect energy levels that appear to be very shallow have been identified with temperature dependent lifetime spectroscopy (TDLS) analysis. In the end, we use numerical simulation to reproduce the temperature dependence of MPL lifetime.

4.1 Samples: sources and description

The SHJ samples investigated in this work are described in Tab. 4.1 to Tab. 4.4 with the various sources and specifications. The samples are referred in series as: A, B, C, D, E, F and G.

Series #A in Tab. 4.1 was fabricated by the Department of ECE at the University of Toronto. These samples are based on n-type c-Si wafer, symmetrically passivated with intrinsic a-Si:H and/or p-type a-Si:H. Here, the doping concentration of the p-type a-Si:H was varied. More details about the deposition process can be found in [56].

Tab. 4.2 describes the SHJ samples provided in the framework of the European project HERCULES*. Series #B and #C are composed of a n-type wafer passivated with intrinsic and n or p-type a-Si:H. Series #D is passivated by AlOx instead of a-Si:H and series #E is the emitter fabricated by ion implantation of boron atoms then passivated with different

* www.helmholtz-berlin.de/projects/hercules

thin films. Various institutes are taking part and multiple techniques have been employed to optimize the fabrication process.

Series #F in Tab. 4.3 was provided in the framework of the ANR project SMASH-IBC[2] (Solar Modules with Advanced Silicon Heterojunction - Interdigitated Back Contact Cells). The purpose of this series is to study the degradation of the passivation after deposition of the TCO by sputtering. These samples were benchmarked to standard ITO samples.

Series #G in Tab. 4.4 was fabricated by the CEA-INES (Institut National de l'Énergie Solaire) and LPICM (Laboratoire de Physique des Interfaces et des Couches Minces). These samples consist of n-type c-Si wafer symmetrically passivated with intrinsic a-Si:H layer of different thicknesses but without any doped a-Si:H.

The stacks are labeled as follows: p/i/n-c-Si/i/p refers to a n-type wafer with intrinsic material on both sides and p-type material on top of the intrinsic material.

Table 4.1 Sample series #A

Source/Project	Department of Electrical & Computer Engineering and Department of Materials Science Engineering, University of Toronto	
Wafer description	Double-side polished 1–5 Ωcm n-type FZ wafers with <100> orientation and 280 µm thickness	
Stack description	20nm thick p-type a-Si:H layer deposited using PECVD (Plasma Enhanced Chemical Vapor Deposition) with different concentration ratios of B_2H_6/SiH_4 gas mixture. Symmetric layer deposition on two sides.	
Reference	**Detailed description**	**RT MPL lifetime (µs)**
#A1	$B_2H_6/(B_2H_6+SiH_4)$=0.75%, p/n-c-Si/p	138
#A2	$B_2H_6/(B_2H_6+SiH_4)$=0.5%, p/n-c-Si/p	184
#A3	$B_2H_6/(B_2H_6+SiH_4)$=1%, p/n-c-Si/p	118
#A4	$B_2H_6/(B_2H_6+SiH_4)$=0.75%, 4 nm intrinsic layer, p/i/n-c-Si/i/p	291
#A5	$B_2H_6/(B_2H_6+SiH_4)$=0.75%, 10 nm intrinsic layer, p/i/n-c-Si/i/p	407

A overview of the samples and their lifetime measured by MPL is given in Fig. 4.1.

Table 4.2 Sample series #B, #C, #D, #E

Source/Project	High Efficiency Rear Contact solar cells and Ultra powerful modULES (HERCULES)	
Wafer description	Double-side textured 1–3 Ωcm n-type CZ wafers with <100> orientation and 130 µm thickness	
Stack description	Symmetric layer deposition on two sides. n/i/n-c-Si/i/n	
Reference	**Detailed description**	**RT MPL lifetime (µs)**
#B1	From CSEM. 10 nm (n) a-Si:H , 12 nm (i) a-Si:H.	270
#B2	From ISFH. 12.5 nm (n) a-Si:H , 8.5 nm (i) a-Si:H.	269
#B3	From CEA. 5 nm (n) a-Si:H , 4 nm (i) a-Si:H.	180
#B4	From ISE. 10 nm (n) a-Si:H , 10 nm (i) a-Si:H.	257
Stack description	Symmetric layer deposition on two sides. p/i/n-c-Si/i/p	
Reference	**Detailed description**	**RT MPL lifetime (µs)**
#C1	From CSEM. 12 nm (p) a-Si:H , 10 nm (i) a-Si:H.	260
#C2	From ISFH. 12 nm (p) a-Si:H , 8.5 nm (i) a-Si:H.	255
#C3	From CEA. 4 nm (p) a-Si:H , 6 nm (i) a-Si:H.	254
#C4	From ISE. 10 nm (p) a-Si:H , 10 nm (i) a-Si:H.	248
Stack description	AlOx deposited by atomic layer deposition (ALD) in ISE and UPC, by PECVD in INES. Symmetric layer deposition on two sides.	
Reference	**Detailed description**	
#D1	From ISE. 5nm AlOx with SiC:B. SiC:B/AlOx/n-c-Si/AlOx/SiC:B	
#D2	From UPC. 50nm AlOx with SiC. SiC/AlOx/n-c-Si/AlOx/SiC	
#D3	From INES. 8nm AlOx with SiO:B on one side. SiO:B/AlOx/n-c-Si/AlOx	
#D4	From INES. Laser treated in UPC. 8nm AlOx with SiO:B on one side which is treated by laser to diffuse dopant into wafer. SiO:B/AlOx/n-c-Si/AlOx	
Stack description	Doped by ion implantation using at 5×10^{14} cm^{-2} to 5×10^{15} cm^{-2} and 2 keV on both sides then passivated by various materials in different labs.	
Reference	**Detailed description**	
#E1	From CSEM. 10 nm intrinsic a-Si:H. i/n-c-Si/i	
#E2	From ISE. 105 nm SiOx. SiOx/n-c-Si/SiOx	
#E3	From ISE. 20 nm AlOx. AlOx/n-c-Si/AlOx	

Table 4.3 Sample series #F

Source/Project	Solar Modules with Advanced Silicon Heterojunction - Interdigitated Back Contact Cells (SMASH-IBC^2)
Wafer description	Double-side polished 1–5 Ωcm n-type FZ wafers with <100> orientation and 100 µm thickness
Stack description	Symmetric stack deposition of 36 nm n-type a-Si:H on both sides. All samples have the same structure n/n-c-Si/n. Contact deposited on one side.
Reference	**Detailed description**
#F1	reference sample with ITO contact.
#F2	70 nm ZnO doped with Al
#F3	350 nm ZnO doped with Al
#F4	70 nm intrinsic ZnO and 70 nm Al-doped ZnO

Table 4.4 Sample series #G

Source/Project	Institut National de l'Énergie Solaire (INES) & Laboratoire de Physique des Interfaces et des Couches Minces (LPICM)	
Wafer description	Double-side polished 3 Ωcm n-type FZ wafers with <100> orientation and 280 µm thickness	
Stack description	Symmetric stack deposition of n-type a-Si:H on both sides. All samples have the same structure. Contact deposited on one side.	
Reference	**Detailed description**	**RT MPL lifetime (µs)**
#G1	From INES. 5 nm (i). i/n-c-Si/i	114
#G2	From INES. 8 nm (i). i/n-c-Si/i	326
#G3	From INES. 10 nm (i). i/n-c-Si/i	364
#G4	From INES. 50 nm (i). i/n-c-Si/i	741
#G5	From INES. 10 nm (n) a-Si:H, no intrinsic. n/n-c-Si/n	519
#G6	From INES. 10 nm (n) a-Si:H , 8 nm (i) a-Si:H. n/i/n-c-Si/i/n	728
#G7	From LPICM. 10 nm (i). i/n-c-Si/i	689
#G8	From LPICM. 50 nm (i). i/n-c-Si/i	722

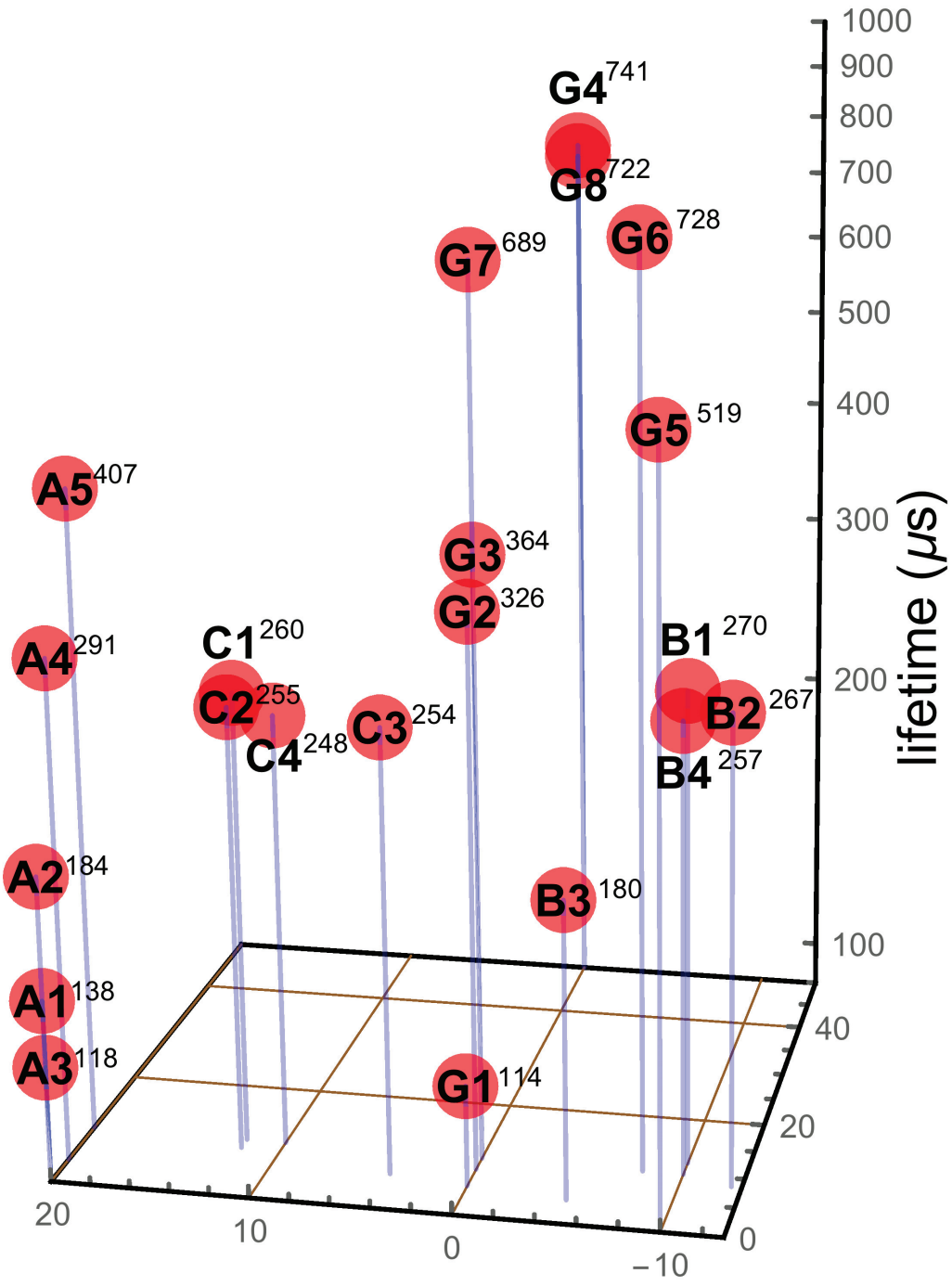

Fig. 4.1 Overview of samples. The MPL lifetime is given as a superscript of the reference name. The thickness of the doped a-Si:H is labeled with a positive number for p-type and a negative number for n-type.

4.2 Measurement of the lifetime at room temperature by PL and MPL

This section focuses on PL/MPL measurements carried out at room temperature. The effective lifetime extracted by MPL is the main criterion for assessing the quality of the passivation. In addition, we will also illustrate the potential of mapping the full SHJ wafer both by PL intensity and MPL lifetime.

4.2.1 Comparison of the photoconductance decay QSSPC and transient modes

In chapter 2, we introduced a brief descrption of the Sinton lifetime tester and the measurement modes involved. Transient mode is suitable for long lifetime sample typically >200 µs whereas the QSSPC mode for samples of low lifetime <200 µs.

We introduced in chapter 3, section 3.1 a distinction between steady state and differential lifetime. Indeed, the lifetime determined with "transient mode" should be classified as differential lifetime whereas the lifetime determined by QSSPC mode is classified as steady state according to Eq. 2.3. Due to the different natures of the measurements, we believe *a priori* that these measurements should not coincide.

Limited by the pulse width of the flashlight of the Sinton tester $[1/64 - 1ms]$, it is not possible to compare QSSPC and transient modes when the sample presents a long lifetime. However, this comparison is possible for short-lifetime samples. We measured the sample #G1 with these two modes. The Results are presented in Fig. 4.2. The two curves superpose very well in the carrier concentration range of 10^{14} cm^{-3} $\sim 5\times10^{14}$ cm^{-3}. Below 10^{14} cm^{-3} however the poor S/N ratio prevents any comparison. Above 5×10^{14} cm^{-3}, the discrepancy emerges. When the carrier concentration is higher than 5×10^{15} cm^{-3} the two traces diverge dramatically. This abrupt increase in the transient mode is due to the detection limit of the system.

Eq. 3.34 leads to $\tau_{diff,SRH} = \tau_{SS,SRH}$ in low injection condition ($\Delta n \ll N_a$ or $\Delta p \ll N_d$). The typical doping level for a solar cell wafer is above 10^{15} cm^{-3}. If the carrier concentration in the sample is below this value, the low injection regime is satisfied. Therefore the QSSPC lifetime corresponds to the transient lifetime as predicted by Eq. 3.35.

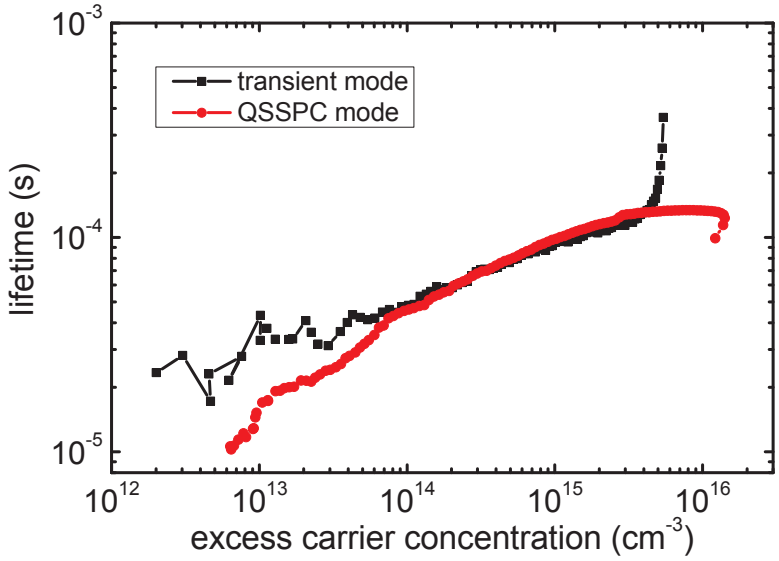

Fig. 4.2 Lifetime of sample #G1 given by the Sinton tester with QSSPC and transient modes.

4.2.2 Comparison between the photoconductance decay and MPL

As discussed above, $\tau_{diff,SRH} = \tau_{SS,SRH}$ in low injection condition ($\Delta n \ll N_a$ or $\Delta p \ll N_d$). This means that although MPL is a differential measurement method and QSSPC is a steady-state method, they should yield the same result in low injection regime. Moreover, both MPL and transient modes of the Sinton are differential methods, as a result both should yield similar lifetime.

To support this statement, we investigated with the Sinton and the MPL two samples, one with a large lifetime and the other one with a low lifetime at room temperature : sample #G6 has a large lifetime of ~10 ms by transient mode at an excess carrier concentration of 10^{15} cm^{-3}, sample #G1 has a low lifetime ~100 µs with QSSPC at an excess carrier concentration of 10^{15} cm^{-3}. The results are displayed in Fig. 4.3.

For sample #G1, the QSSPC mode exhibits similar result as the MPL despite that they are based on different principles as explained above. Note that the MPL detection limit for this sample corresponds to an excess carrier concentration of about 10^{15} cm^{-3}.

For sample #G6, the transient mode, however, shows significant discrepancy with the MPL lifetime. The variation of the lifetime indicates that the two MPL measurements at ~ 3×10^{15} cm^{-3} and ~ 10^{16} cm^{-3} become limited by Auger and radiative recombination instead of SRH. The lifetime determined by Auger and radiative recombination can be determined from Fig. 3.9. At $\Delta n = 10^{16}$ cm^{-3} *i.e* 4428 µs. The SRH lifetime is determined from Fig. 4.3 in the plateau region at $\Delta n \approx 10^{14}$ cm^{-3} *i.e* ~ 9000 µs. Therefore the total lifetime is calculated using Eq. 3.46 *i.e* 2967 µs, which approximates the Sinton result of 3000 µs

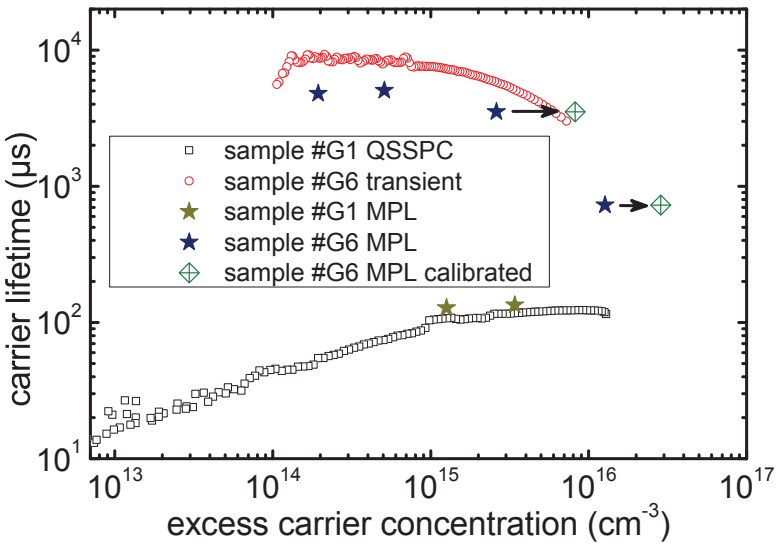

Fig. 4.3 Comparison of the lifetimes measured by WTC-120 and MPL. The lifetime of sample #G1 is measured with WTC-120 in QSSPC mode and by MPL. The lifetime of sample #G6 is measured with WTC-120 in transient mode and by MPL. The MPL lifetime of sample #G6 after calibration is close to the one measured with WTC-120 in transient mode.

corresponding to the largest excess carrier concentration obtained from the transient mode. Nevertheless it is still very different than the MPL lifetime of 728 µs obtained at 1.1×10^{15} cm^{-3}.

This observation is opposite to our initial statement *i.e* the two methods measure the differential lifetime. In fact, knowing that the MPL does not provide directly the carrier concentration, the validity of the established Δn is questionable. We address this issue in the following.

To extract the carrier concentration, the incident laser power is measured with a power meter and calibrated using:

$$G = \frac{PA}{Sd} \tag{4.1}$$

where G is the averaged generation rate, P the laser power, A the absorption fraction of laser power, S the laser spot size and d the thickness of the sample. Eventually, Δn is extracted from the measured lifetime with Eq. 3.9 and the photo generation rate. Eq. 3.9 yields the steady state lifetime. However, to evaluate Δn, this is the differential lifetime that is used. Therefore the data must be calibrated.

When $\Delta n < 10^{15}$ cm^{-3}, the transient trace of sample #G6 exhibits a plateau region. Here, we consider in this region that the dominant recombination mechanism is SRH i.e. 9381 µs for the SRH lifetime.

In Fig. 4.3, the decrease of the MPL lifetime as a function of the carrier concentration implies that the two measurements at $\Delta n = 2.6 \times 10^{15}$ cm^{-3} and $\Delta n = 1.3 \times 10^{16}$ cm^{-3} are dominated by Auger and radiative recombination. To preclude the effect of SRH lifetime, we subtract the SRH lifetime *i.e.* 9381 µs from the total lifetime to determine only the contributions of Auger and radiative recombination, 5646 µs and 789 µs respectively. From Fig. 3.9 one can determine with the total lifetime values, the corresponding carrier concentration. The calibrated Δn is shown in Fig. 4.3.

We have previously demonstrated that under given conditions, the MPL lifetime is comparable to the photodecay modes. The difference in the MPL and transient Sinton lifetimes reported in [56] may be due to the difference in carrier concentrations. Since the measurement conditions are not mentioned in this reference, we assume that the experiment was carried out for $\Delta n = 10^{15}$ cm^{-3} for the Sinton whereas it was done under one sun illumination for MPL. As a result, the two measures cannot be compared.

4.2.3 MPL lifetime measurements on SHJ

The study of thinner a-Si:H layer is important for the optimization of solar cell in production. Note that the a-Si:H does absorb in certain amount of light and a thinner layer would be beneficial.

4.2.3.1 Impact of the intrinsic layer

The intrinsic a-Si:H passivation is mandatory in SHJ to reduce the interface defects and recombination. We present the impact of the intrinsic layer on the lifetime for series #G.Their MPL lifetime at room temperature is measured under one sun illumination. We take the profile of Fig. 4.1 along the plane where the doped a-Si:H thickness is zero, the result is displayed in Fig. 4.4.

We observe that the increase in i-layer thickness leads to the increase of measured lifetime. However, sample #G7 has only 10 nm intrinsic a-Si:H layer and it has an MPL lifetime almost as high as that of samples #G4 and #G8 that have 50 nm intrinsic a-Si:H layer, and significantly than that of sample #G3 that has the same intrinsic a-Si:H layer thickness. For thin (i) a-Si:H layer, the passivation is very sensitive to the actual thickness and to the deposition condition. Thus the relatively low and large lifetimes of samples #G3 and #G7 (that should have the same (i) a-Si:H thickness) might be due to differences between techniques. The technique for sample #G7 may have introduced fewer defects.

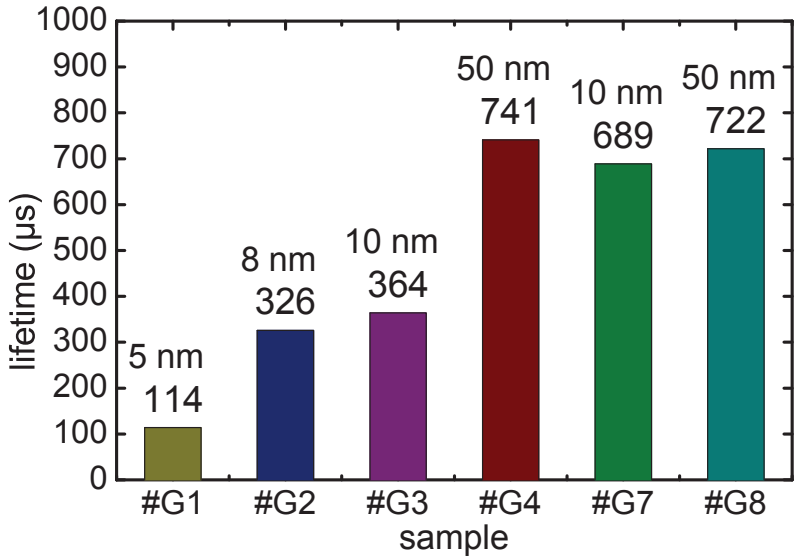

Fig. 4.4 Comparison of the MPL lifetime with only the intrinsic a-Si:H passivation.

4.2.3.2 Impact of the emitter and the doping

We present the impact of the doping of the emitter on the lifetime for the series #A (no (i) a-Si:H buffer). Their MPL lifetimes at room temperature are measured under one sun illumination. The result are shown in Fig. 4.5. Three samples, #A1, #A2 and #A3 have

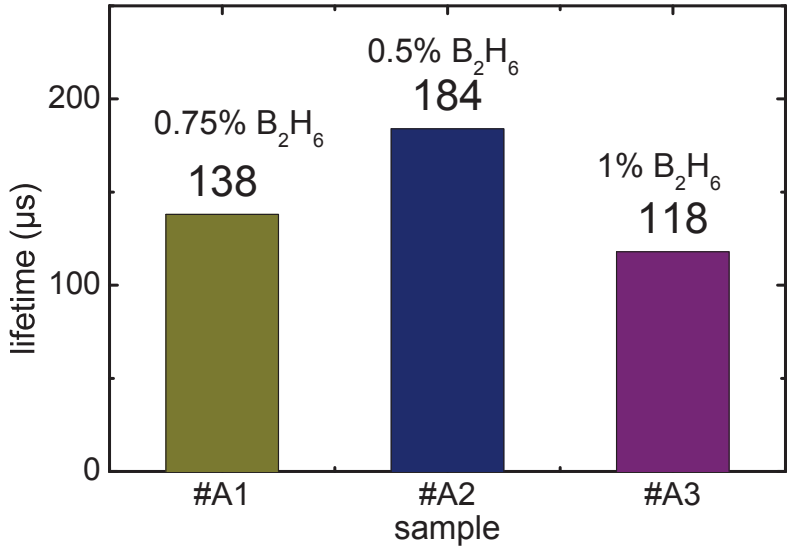

Fig. 4.5 Comparison of the MPL lifetime with only intrinsic a-Si:H passivation.

the same stack configuration. Sample #A3 has the highest doping level and #A2 the lowest, with #A1 in between. Their corresponding lifetimes decrease from high to low doping. This

indicates that the higher doping in the emitter introduces more defects and therefore increases interface recombination.

4.2.3.3 Emitters versus BSF

The Sample series #B and #C are composed of BSF and emitter SHJ that come from four different labs. These latest, provided samples fabricated according to their optimized BSF and emitter parameters. This allows us to compare the quality of different type of BSF and emitter passivations.

Fig. 4.6 present the MPL lifetime at room temperature and under one sun illumination for the BSF passivation. We find the same lifetime about 270 µs for sample #B1, #B2 and #B4 and only 180 µs for #B3.

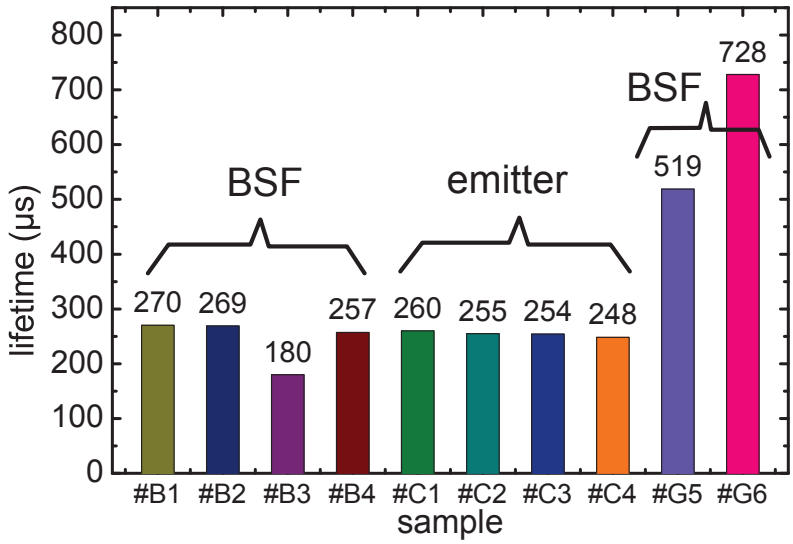

Fig. 4.6 Comparison of the MPL lifetime for various BSF and emitter SHJ.

This degradation originates from the relatively thinner intrinsic and doped a-Si:H layer implemented in this sample.

On the opposite, samples #G5 and #G6 have significantly larger lifetimes. It is worth noting that #G5 has no intrinsic layer and exhibits a larger lifetime than the sample series #B. This means that n-type a-Si:H alone can also perform as a good passivation layer for n-type c-Si. The passivation is strongly dependent on the process parameters *i.e.* dopant concentration, hydrogen concentration, temperature. Sample #G5 are relatively lowly doped. Fig. 4.6 also shows that the MPL lifetime of the emitter samples (series #C, with (p) a-Si:H/(i) a-Si:H stacks). These are slightly lower than that of the BSF samples.

P-type a-Si:H present more defects than n-type a-Si:H when the Fermi level is at the same level with respect to valence band and conduction band. For this reason the p-type a-Si:H passivation is usually less efficient than the n-type a-Si:H, as a result an intrinsic layer is mandatory for the emitter.

4.2.3.4 Impact of the TCO

Contacts are an important feature of a solar cells. Their optimization and the interface with the a-Si:H are indispensable to properly extract the photo-generated excess carriers. However, the sputtering deposition of ITO may damage the passivation of the wafer and increase the interface recombination. To decrease the degradation as well as to reduce the cost of fabrication of a solar cell (ITO contact), we investigate a new TCO based on ZnO and ZnO:Al. The impact on the passivation is studied by the the lifetime characterization. The corresponding series is #F in Tab. 4.3. The contact is deposited by sputtering in a 6 mm diameter circle on top of the structures. The MPL measurement is performed within and ou of the contact region as shown in Fig. 4.7. All the samples in the series are measured before and after annealing to investigate the impact. All measurements are carried out under one sun illumination.

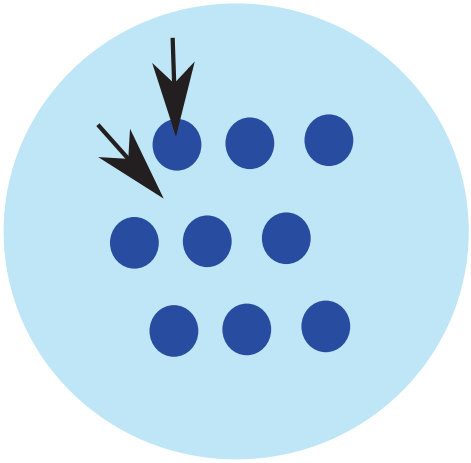

Fig. 4.7 TCO contacts on the investigated wafer. Black arrows indicate the measured area.

Sample #F1 represents the conventional ITO contact. Samples #F2 and #F3 are Al-doped ZnO of different thickness. Sample #F4 is doped ZnO on top of the intrinsic ZnO.

The lifetimes are measured before the annealing as shown in Fig. 4.8(a). The lifetimes outside the contact are almost the same for every sample. With ITO as for the reference sample #F1, the lifetime slightly decreases from 595 µs to 576 µs. All the ZnO or doped ZnO contacts show 13%∼33% more degradation than the ITO contact. Intrinsic ZnO is

worse than doped ZnO. Comparing with the ITO, we observe that the sputtered ZnO implies the degradation of hte passivation by damaging the underlying layer. However, we observe an increase with the thickness of ZnO. Tab. 4.3 shows that the thickness of ZnO is such that $d_{\#F2} < d_{\#F4} < d_{\#F3}$. The measured lifetime shown in Fig. 4.8(a) does not follow exactly the same trend. One possible explanation would be the presence of a band bending at the contact interface caused by the mismatch of the work functions between ZnO and SHJ Fermi level.

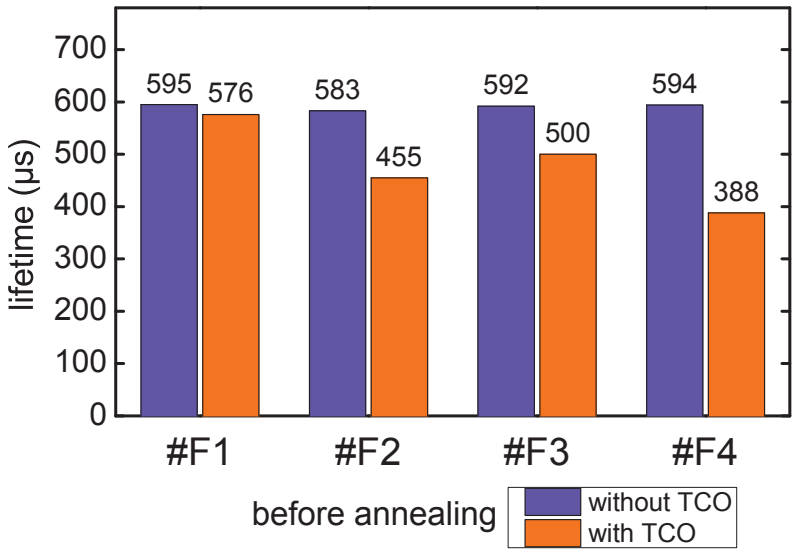

(a)

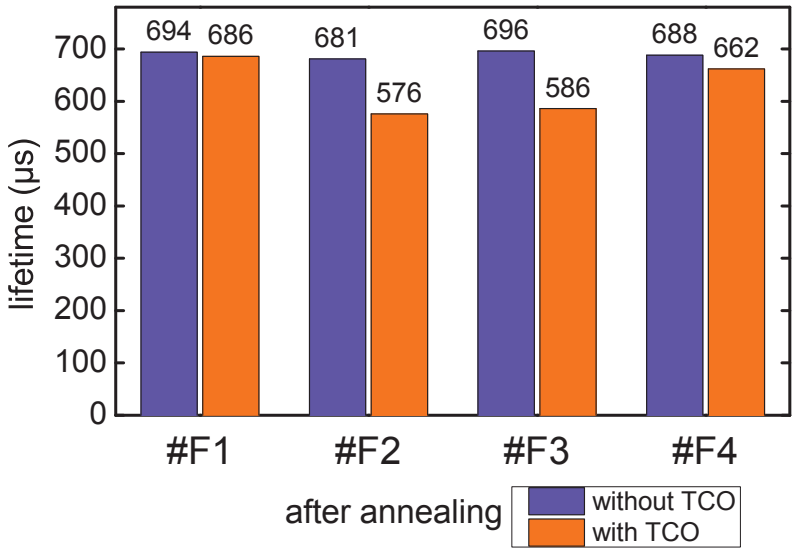

(b)

Fig. 4.8 The MPL lifetime of sample series #F (a) before and (b) after 200 °C annealing for 5 minutes.

After annealing, the lifetime increases for the various types of contacts. We observe the same trend for the region without contact. The annealing heals the damage caused during the sputtering process. Sample #F4 has both intrinsic and doped ZnO. The annealing treatment yields to a significant improvement about 96% of its lifetime larger thant the other ZnO contacts and close to the sample #F1 (the reference ITO contact).

4.2.4 PL and MPL mapping

PL mapping is widely used to investigate wafer quality and deposition uniformity. As shown in chapter 2, our setup can be configured as Fig. 2.2(b) for the acquisition of the PL and MPL lifetime mapping.

4.2.4.1 PL mapping

Fig. 4.9 shows the result of the PL mapping of samples.

As observed in Fig. 4.9(a), the mapping shows some scratches in the bottom-left corner which cannot be seen with naked eye but it is measurable by PL mapping. These patterns result from bulk imperfections or the damage of the surface passivation. The most significant feature in this mapping would be the square region of high PL intensity. The size of this square coincides with the polished aluminum sample stage which is much smaller than the wafer. In Fig. 4.9(b), however, after the sample stage is covered by an absorptive material, the square shape disappears. As a result, PL imaging is prone to the surface optical reflection. On the other hand, one can also take advantage from this reflection using a reflective sample stage to enhance the PL signal for a better detection.

In Fig. 4.9(c) the PL is stronger on the corner of the wafer than in other locations. In this figure we find some traces in the middle of wafer from top to bottom. These traces could be the result of contact or contamination from the conveyor belt in the automated manufacturing line.

In Fig. 4.9(d), note that the color bar is in logarithmic scale, the cyan region is as dark as the purple region in linear scale and only the red region is visible. So the PL from sample #C4 is delimited by the square region which is much smaller than the wafer size. In fact the wafer of this sample is larger than the deposited material. This region is in the center part of the wafer and PL decreases rapidly towards the border. This discrepancy relates to the inhomogeneity of the deposition process.

Fig. 4.9(e) and Fig. 4.9(f) show the front and back side PL of the same wafer. We can see three dark square regions in both figures. This sample was first covered with a dielectric layer doped with boron on one side. After a laser treatment, the dopant atoms diffuse into the

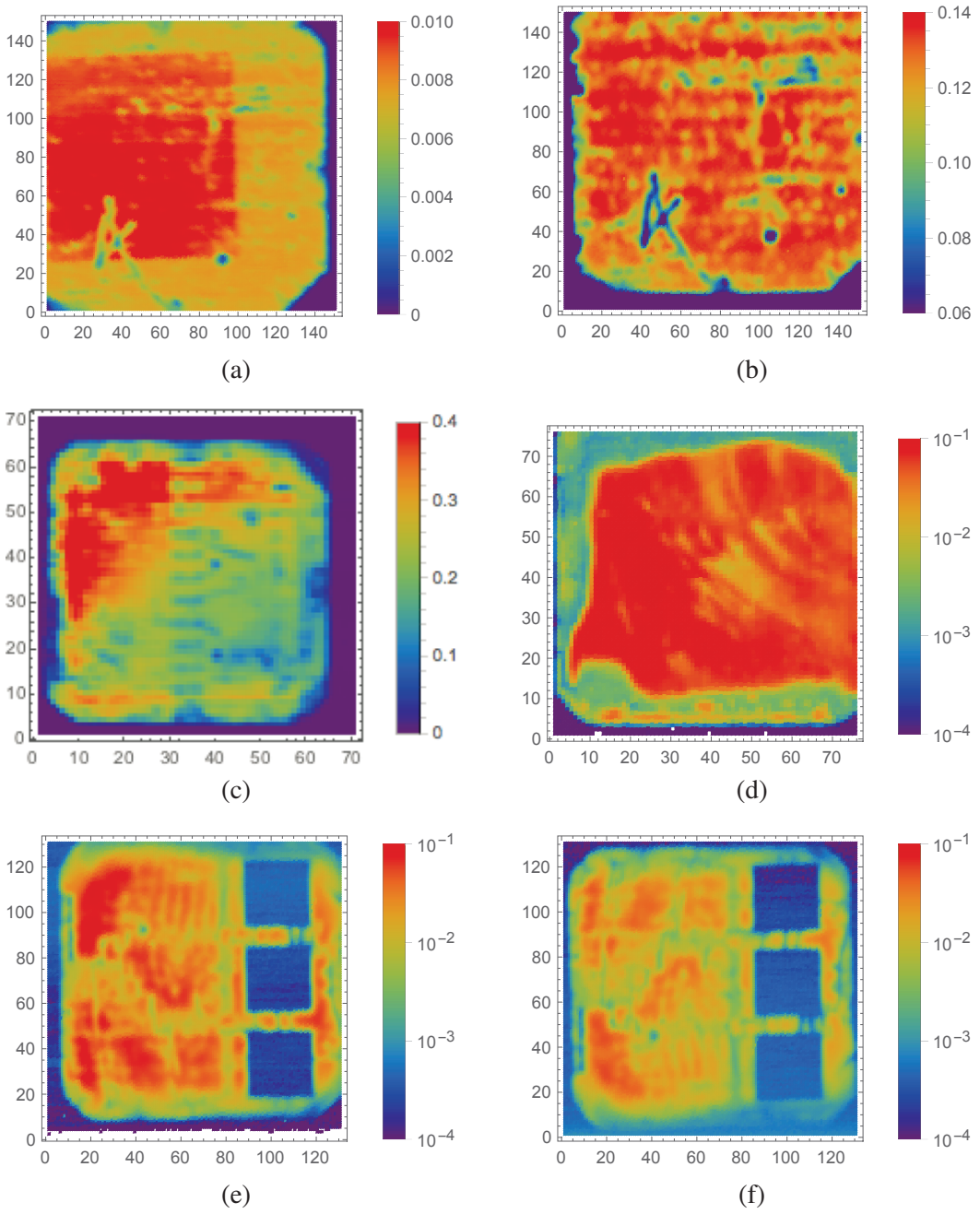

Fig. 4.9 PL intensity mapping of sample #C1 (a) with back reflection and (b) without back reflection, (c) sample #D2 (d) sample #C4 and (e)(f) for #D4. (c)(d)(e) are colored in logarithm scale. Sample #D4 is treated by laser in three square regions on one side to diffuse the dopants from the dielectric layer into wafer. (e) corresponds to front side and (f) to back side. XY coordinate refers to the pixel.

substrate to form highly doped regions that become contacts after metalizationn. Although treated on one side only, the wafer shows low PL intensity from both sides. The passivation on the fired side is damaged and yields to high surface recombination. Therefore, the carrier concentration in the bulk is significantly reduced and the PL is weak even from the back side.

4.2.4.2 MPL mapping

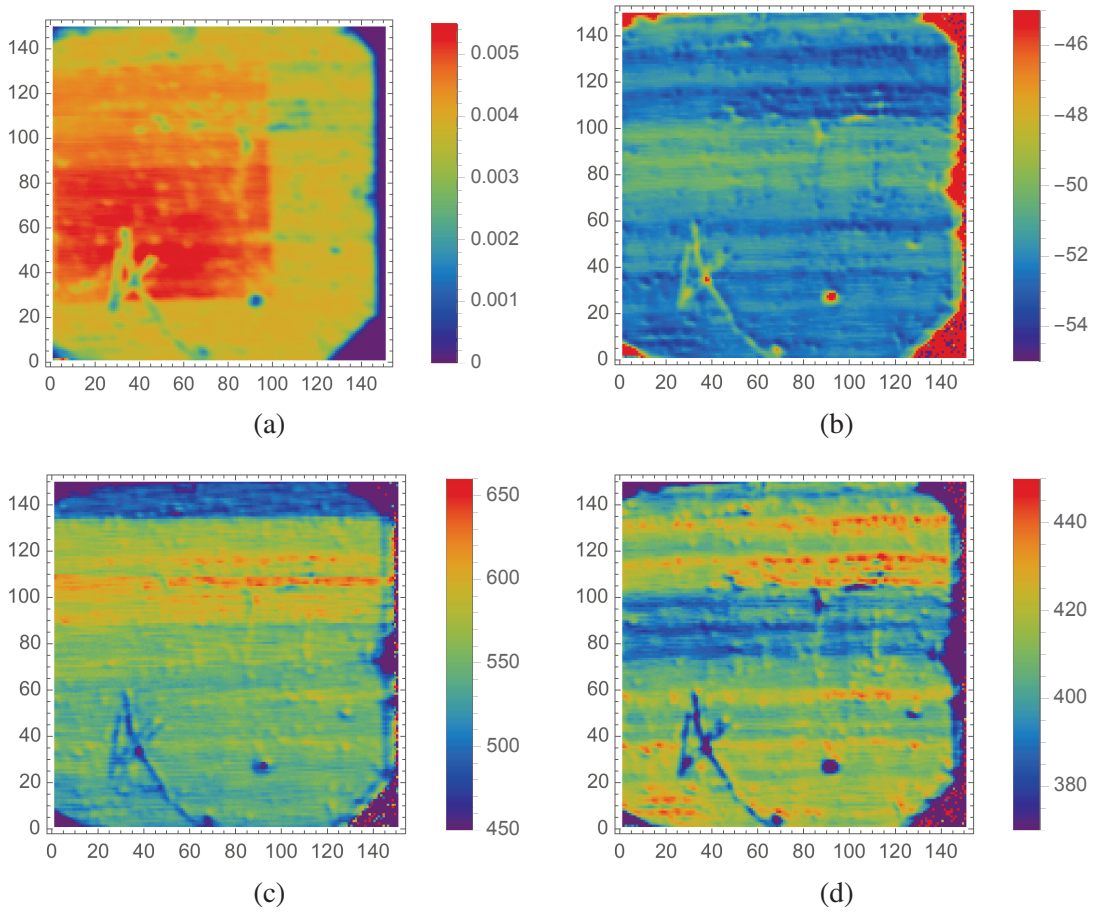

Fig. 4.10 MPL mapping of sample #C1 at 500 Hz. (a) amplitude (b) phase shift (degree) (c) lifetime (µs) extracted from amplitude (d) lifetime (µs) extracted from phase shift. XY coordinate refers to the pixel.

We also investigated the possibility of MPL mapping. While scanning over the surface of the sample for PL mapping, small signal modulation is applied to the laser diode injection current. Since the AC component of PL is negligible compared to the DC component (AC/DC$\ll$ 0.1), there is little impact of MPL mapping on PL mapping. Both the amplitude and phase shift of the AC component are recorded by the lock-in amplifier and for each we

extract an MPL mapping. Recall that the lifetime mappings can be built from either the amplitude or the phase shift.

The same sample in Fig. 4.9(a) is taken as an example of MPL mapping. As shown in Fig. 4.10(a), the amplitude imaging of the MPL quite reproduces the PL imaging. It is reasonable since the small signal modulation of the laser intensity does not change the light-matter interaction. So the intensity of the PL should be the only difference of AC and DC components of PL.

However, the phase delay imaging is quite different as is shown in Fig. 4.10(b). It is worth pointing out that the back reflection at the sample stage has no impact on the phase shift mapping as opposed to Fig. 4.9(a) and Fig. 4.10(a) for the DC PL. The horizontal traces on the samples are very clear in phase imaging. We can confirm that these strips do not originate from the movements of translation stage by rotating the sample and doing the mapping again as shown in Fig. 4.11. Knowing that we observed strip-like traces all over the samples surface which may be the result of damage during ingot slicing, this type of defect was not resolved in PL mapping. This emphasizes the added value of MPL as a diagnosis tool.

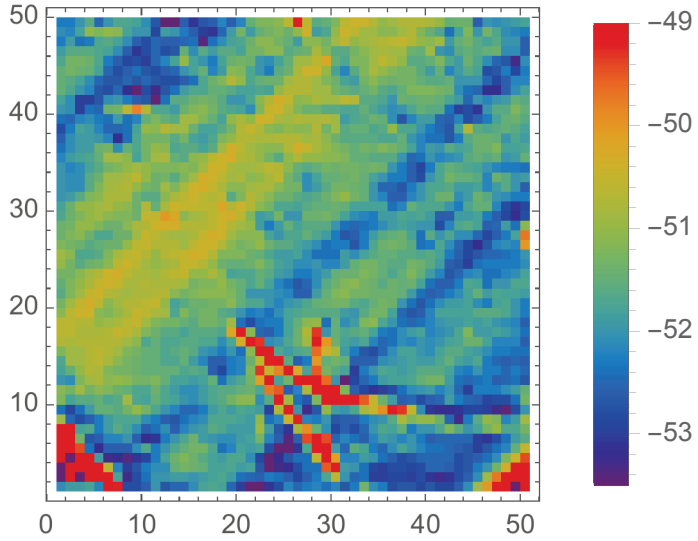

Fig. 4.11 100×100 mm^2 phase shift (degree) mapping of sample #C1 at 500 Hz after rotation of 45° counterclockwise. The step is 2 mm. XY coordinate refers to the pixel.

We perform two MPL mappings at 45 Hz and 500 Hz separately, and with the amplitude and phase shift data the carrier effective lifetime can be extracted with Eqs. 2.6 and 2.7. We notice that the reflection of the stage has no impact on the lifetime as shown in Fig.4.10(c) and Fig.4.10(d). The lifetime mapping extracted from the phase shift is exactly a reproduction of the phase shift mapping.

Only two frequencies are used in the mapping to reduce the duration of the experiment. Consequently the lifetime extracted is subjected to some error and as shown in Fig.4.10(c) and Fig.4.10(d), the mappings obtained from amplitude and phase shift are not identical.

The time used to build 1, 2, 3 and 4 mm steps mappings is 81, 21, 10 and 6 hours, respectively. Each contains 22801, 5625, 2601 and 1444 points, respectively in the image. The major time consumption is attributed to the point by point lock-in measurement. A camera that works at high frame rates can be implemented to substantially reduce the acquisition time. For example, the PI-MAX4 cameras of Princeton Instruments [74] can work at a repetition rate of 10 MHz.

4.3 Temperature dependent PL/MPL measurements

Because Boltzmann statistics which describes the state occupation is a function of temperature, the defect activation, and the dopant ionization are temperature dependent. When temperature changes, the emission of electrons will be impacted and thus the recombination rate changes. This can have significant influence on the PL spectrum and the carrier lifetime.

Moreover, the PL is also temperature dependent. The photon flux of PL is given by

$$j_r(\hbar\omega) = A(\hbar\omega, T)\frac{(\hbar\omega)^2}{4\pi^2\hbar^3c^2}\left[\exp\left(\frac{\hbar\omega - \Delta E_f}{kT}\right) - 1\right]^{-1} \tag{4.2}$$

where j_r represents the number of photons emitted per unit time per unit area per unit energy interval per solid angle, c represents the vacuum light speed, and ΔE_f refers to the quasi Fermi level splitting in the material. $A(\hbar\omega, T)$ is given by:

$$A(\hbar\omega, T) = \frac{[1 - R(\hbar\omega)]\left(1 - \mathrm{e}^{-\alpha(\hbar\omega,T)d}\right)}{1 - R(\hbar\omega)\mathrm{e}^{-\alpha(\hbar\omega,T)d}} \tag{4.3}$$

where α is the absorption coefficient, R represents the reflectivity of slab interface. $A(\hbar\omega, T)$ is the optical term that considers the material re-absorption of the PL, as well as the multi-reflection inside the wafer. The optical absorption coefficient α is temperature dependent.

Moreover, in our experiments, the excess carrier concentration can be determined from the generation rate according to Eq. 3.6. At room temperature this is straightforward since the absorption coefficient of silicon is very high, $\alpha = 1030\ \mathrm{cm}^{-1}$ for 780 nm light [75]. This yields an absorption depth of about 10 µm. Considering that the thickness of our wafers varies between 100 and 300 µm, all the light entering the wafer is absorbed. To precisely estimate the generation rate within the SHJ samples, one should also determine the low temperature absorption. Since the absorption coefficient of silicon decreases monotonically

with decreasing temperature, we only need to investigate the lowest temperature (20 K) our cryostat can reach. We refer to the absorption data in [76]. Because the data available in this reference are limited to 1.3 eV, we extrapolate the 4.2 & 20 K curve to 1.58 eV (785 nm) and find 24.5 $cm^{-\frac{1}{2}}eV^{-\frac{1}{2}}$. This quantity corresponds to an optical absorption coefficient $\alpha = 381$ cm^{-1} and an absorption depth of 26 µm, that remains thinner than the wafer.

Now we are sure that all the illumination that enters the sample is absorbed. a polished c-Si wafer absorbs about 70% of the incident light and a textured wafer absorbs about 90%. If the incident laser power is measured, the power absorbed can be calculated.

4.3.1 Steady state photoluminescence

In this section we focus on the PL measurements carried out under continuous wave as a function of temperature and the intensity of the excitation. The different SHJ samples respond differently, their PL spectra are classified into two groups as displayed in Figs. 4.12 and 4.13.

4.3.1.1 Regular temperature dependence of the photoluminescence

In Fig. 4.12, regardless of the SHJ structure or the intensity of the excitation, we observe a similar temperature dependence: when the temperature decreases, the PL maximum intensity keeps increasing until 30∼50 K, then slightly decreases beyond.

In Fig. 4.12, the samples tested are: BSF sample (#B1), emitter sample (#C2), intrinsic layer sample (#G7 , #G8) and an AlOx passivated sample (#D2). All these different SHJ exhibit the same temperature dependance, we can conclude that they perform identically on the c-Si interface. Furthermore, only the silicon band to band radiative recombination peak at 1.0 and 1.1 eV is visible. Fig. 4.12(e) and Fig. 4.12(f) show the spectrum of the same sample under different illuminations. We observe that the temperature dependence is not related to the injection level.

The dependence observed is a the result of the convolution between an increasing band-to-band radiative recombination coefficient and a decreasing carrier lifetime. This point will be further discussed in the next section.

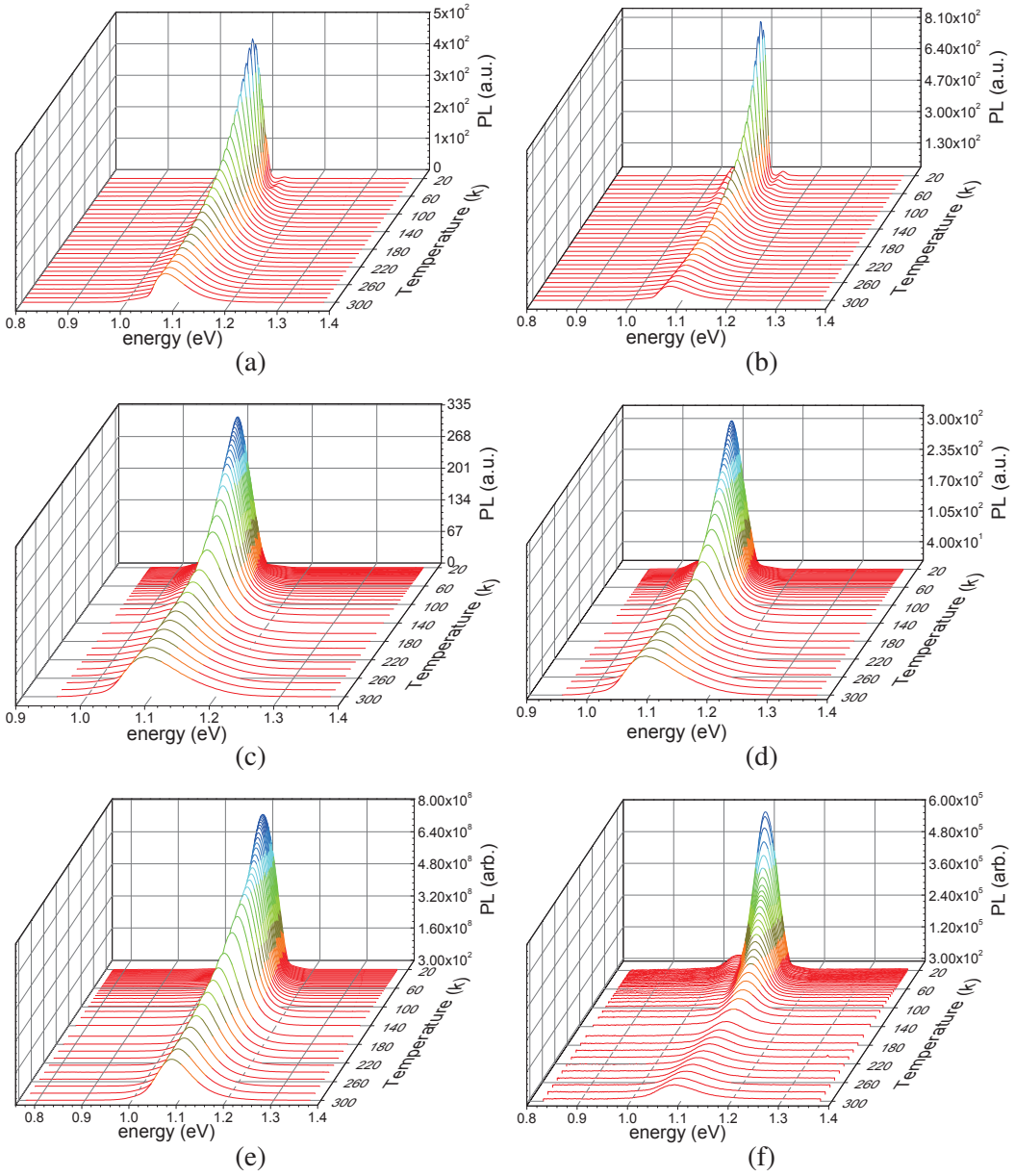

Fig. 4.12 Temperature dependent PL spectra of various SHJ samples. (a) #B1 under 36.5 mW illumination. (b) #C2 under 36.5 mW illumination. (c) #G7 under 36.5 mW illumination. (d) #G8 under 36.5 mW illumination. (e) #D2 under 34.8 mW illumination. (f) #D2 under 0.26 mW illumination.

4.3.1.2 Irregular temperature dependence of the Photoluminescence

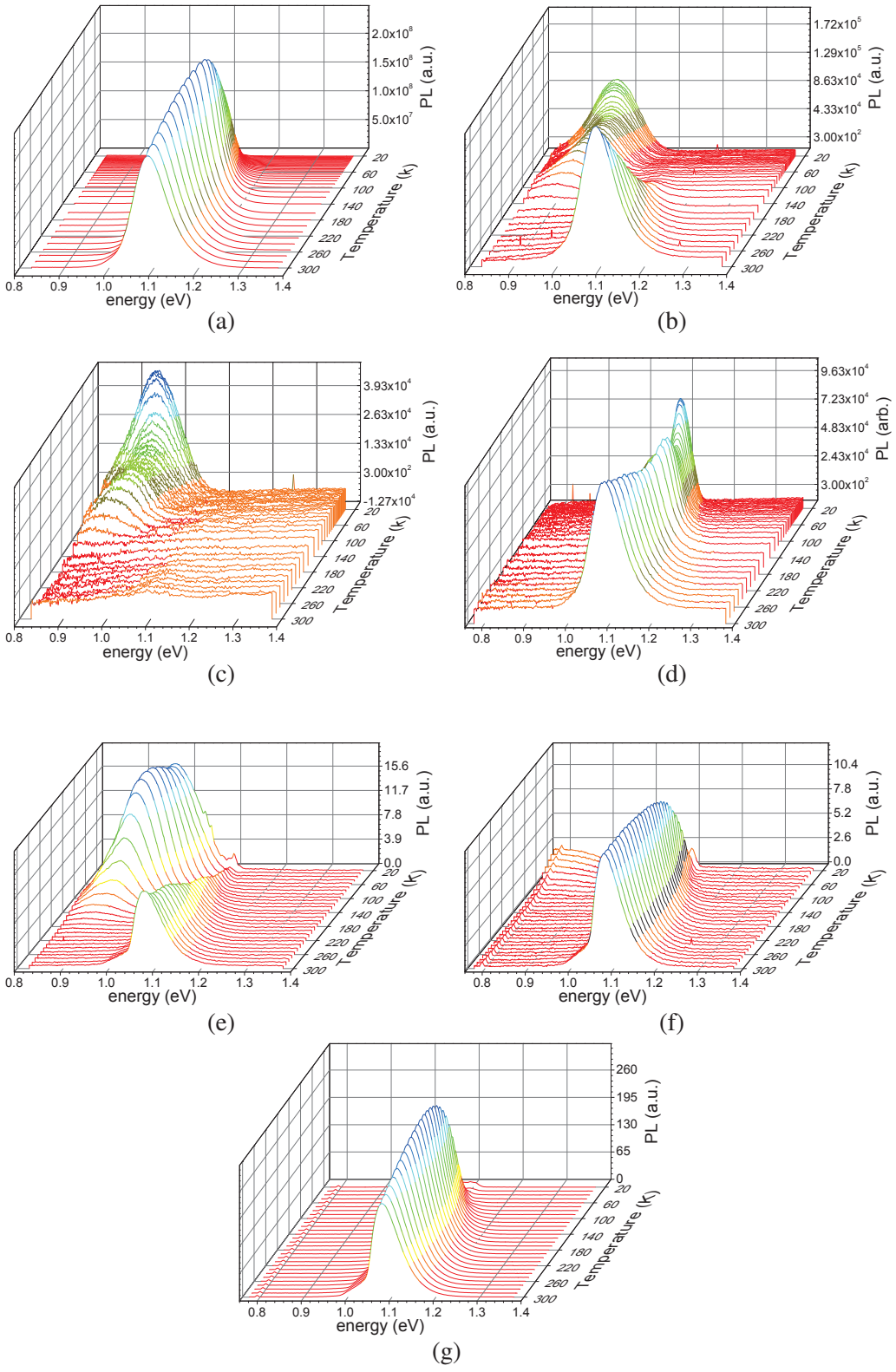

Fig. 4.13 Temperature dependent PL spectra of various SHJ samples. (a) #D1 under 37 mW illumination. (b) #D1 under 0.69 mW illumination. (c) #D1 under 0.26 mW illumination. (d) #D3 under 0.65 mW illumination. (e) #E1 under 37 mW illumination. (f) #E2 under 37 mW illumination. (g) #E3 under 37 mW illumination.

In Fig. 4.13, we observe more complex PL spectra as a function of temperature for AlOx passivated samples and implanted samples. The patterns are very different from Fig. 4.12. These signatures appear to be excitation dependent as well.

Observation of the photoluminescence quenching figs. 4.13(a) to 4.13(c) are the PL spectra of the same sample for different illumination. In Fig. 4.13(a), the PL intensity does not vary in a wide temperature range then decreases smoothly below 100 K. When the illumination decreases, we observe that the silicon band-to-band peak decreases rapidly in Fig. 4.13(b) whereas a low energy peak starting at 0.86 eV emerges. In Fig. 4.13(c), the silicon band-to-band peak vanished and only remains a peak at 0.95 eV. This latest is assigned to a defect to band or defect to defect recombination center.

Fig. 4.13(b) shows clearly the balance between band-to-band radiative recombination and defect-to-band or defect-to-defect recombination. When the temperature decreases, the defect captures the carriers and therefore limits the band-to-band radiative recombination. The PL intensity dependence of the smaller energy peak (0.97 eV at 20 K)is plotted in Fig. 4.14(a). We employ the subsequent model in an attempt to understand the temperature dependence of this defect energy peak:

1. $\frac{I_0}{I(T)} = 1 + c\exp\left(-E^*/kT\right)$

   This model describes band-to-band radiative recombination mediated by defects. The defect induces a deformation of the band structure and thus the recombination center is surrounded by an energy barrier E^*. The carriers must overcome this barrier to be captured by the recombination center. A temperature increase will favor the transfer of the carrier from the band edge to the recombination center and will recombine non-radiatively. Hence the PL decreases with increasing temperature as discussed in [77] and referred by [78, 79, 77].

2. $\frac{I_0}{I(T)} = 1 + cT^{3/2}\exp\left(-E_T/kT\right)$

   This model describes the defect-to-band radiative recombination. A shallow recombination center close to the band edge at an energy E_T, below the conduction band for instance dominates. The radiative recombination through this defect is dominated by the reemission process. When the temperature increases, fewer carriers occupy the defect level and the PL decreases. It is discussed in [80] and referred by [79].

3. $\frac{I_0}{I(T)} = 1 + c_1\exp\left(-E_{T1}/kT\right) + c_2\exp\left(-E_{T2}/kT\right)$

   The most accepted theory is the donor-acceptor pair (DAP) radiative recombination [78] where E_{T1} and E_{T2} correspond to the donor and acceptor energy levels. The

auhors observed a perfect fitting of the 1.4 eV emission peak of a CdTe sample, however the magnitude of one of the two fitting parameters either E_{T1} or E_{T2} is far below kT, hard to justify .

4. $\frac{I_0}{I(T)} = 1 + c_1 T^{3/2} + c_2 T^{3/2} \exp\left(-E_T/kT\right)$

   This model discusses also the donor-acceptor pair (DAP) radiative recombination and help to overcome the drawback of the previous model 3. In the DAP recombination process, the two impurity ions have different binding energies, for example $E_{T1} > E_{T2}$. The shallow impurity is dominated by emission (the exponential term) whereas the deep one by the capture. At high temperature, the DAP recombination is limited by the thermal ionization that breaks the pairs. When the temperature decreases the emission is weakened and the recombination is limited by the capture rate. [78, 81].

In these models, $I(T)$ the PL peak maximum, I_0 the $I(T)$ extrapolation to 0 K, E_T, E_{T1} and E_{T2} is the defect energy level, c, c_1 and c_2 are coefficients.

The fitting result is shown in Fig. 4.14(b). One can see, only model 3 gives a good agreement between measurement and theory. The fitting parameters are: $E_{T1} = 0.008 \pm 0.007$ eV, $E_{T2} = 0.064 \pm 0.013$ eV, $c_1 = 3.3 \pm 0.6$, $c_2 = 1927 \pm 2764$. The very low value of $E_{T1} = 8$ meV has no physical significance, and the fitting of c_2 has large error range. Models 1 and 2 are applied to translate the PL peak introduced by dislocation in mc-Si. Models 4 and 3 are applied to II-VI materials. Only the 3 model can fit the experimental data however the energies extracted have no physical meaning.

Besides, the temperature range in [79] is limited to 80 - 300 K. Furthermore, we have investigated various injection levels and find that for low injection level even model 3 does not fit anymore. A comparison between the PL spectra of sample series #D indicates that this PL quenching has only to do with the AlOx layer thickness. Further study is required to clarify the underlying mechanism, we believe that there might be a more complex temperature dependance particularly on the capture cross section.

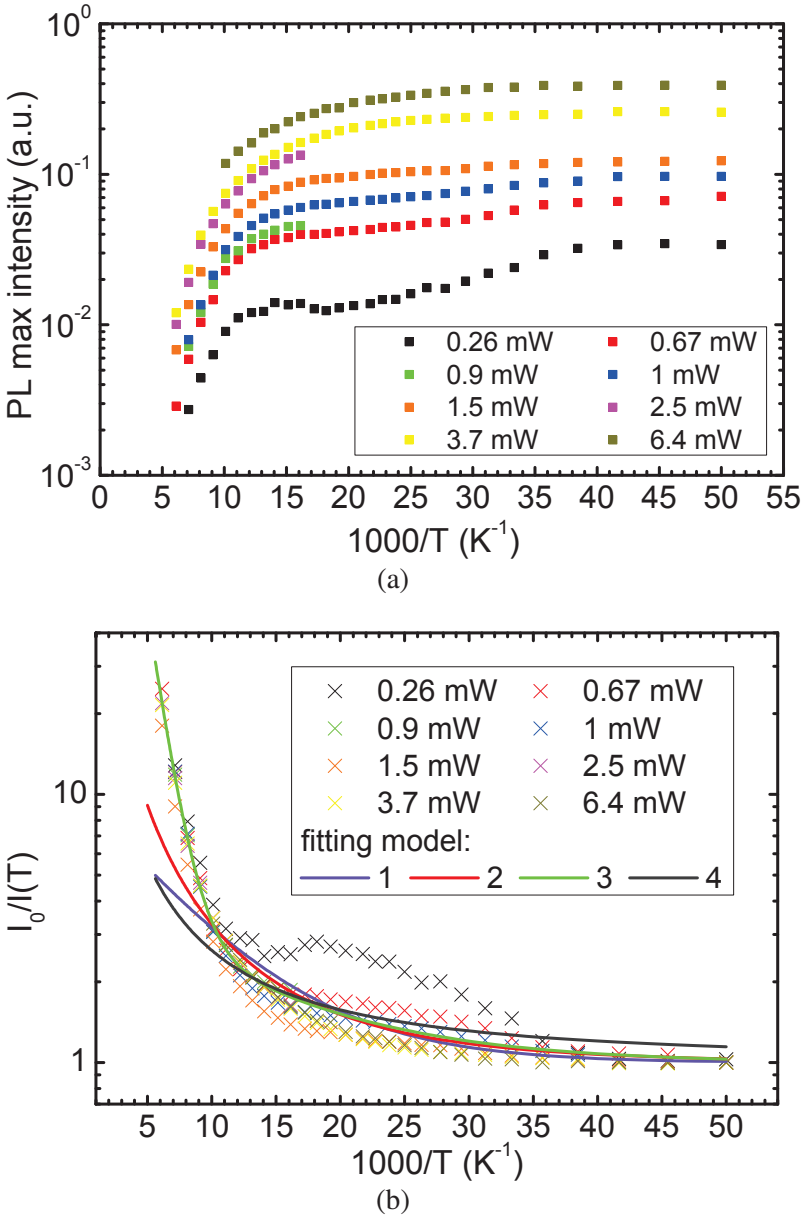

Fig. 4.14 (a) PL dependence as a function of the temperature for the radiative recombination through defect level. (b) Inversed PL intensity normalized to $T \rightarrow 0$ K value.

4.3.2 Temperature dependence of the modulated photoluminescence

In this section we present the MPL lifetime measurement as a function of temperature.

4.3.2.1 High injection

These measurements are performed under one sun illumination, the result is shown in Fig. 4.15. We find that all the samples investigated have the same overall behavior. The MPL

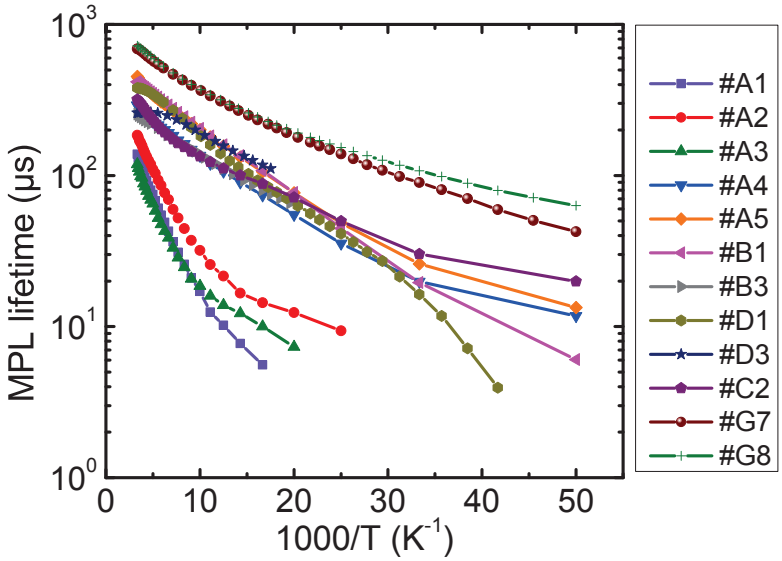

Fig. 4.15 The MPL lifetime of various samples under one sun (36.5 mW) illumination.

lifetime decreases as the temperature decreases. This overall behavior does not depend on the SHJ structure nor the passivation. We can also observe that samples #A1, #A2 and #A3 present lower lifetime than all the remaining samples. Moreover, these three samples exhibit the same temperature dependance beyond 100 K. However, the dependance is steeper compare to all the other SHJ. Note that these three samples are the only ones without intrinsic a-Si:H layer passivation.

In the previous section, we showed, Fig. 4.13, that decreasing the illumination reveals different temperature dependences. Following this observation, we proceeded to low injection measurements.

4.3.2.2 Low injection temperature dependent lifetime spectroscopy

The Low injection regime allow us to use TDLS analysis to study temperature dependence of the lifetime. Eq. 3.42 discusses this method [59].

Emitter with an intrinsic a-Si:H layer The temperature dependence of MPL lifetime of sample #A5 for various intensities is shown in Fig. 4.16(a). When the intensity decreases, the slope of the curve at high temperature increases. We define the ”apparent activation

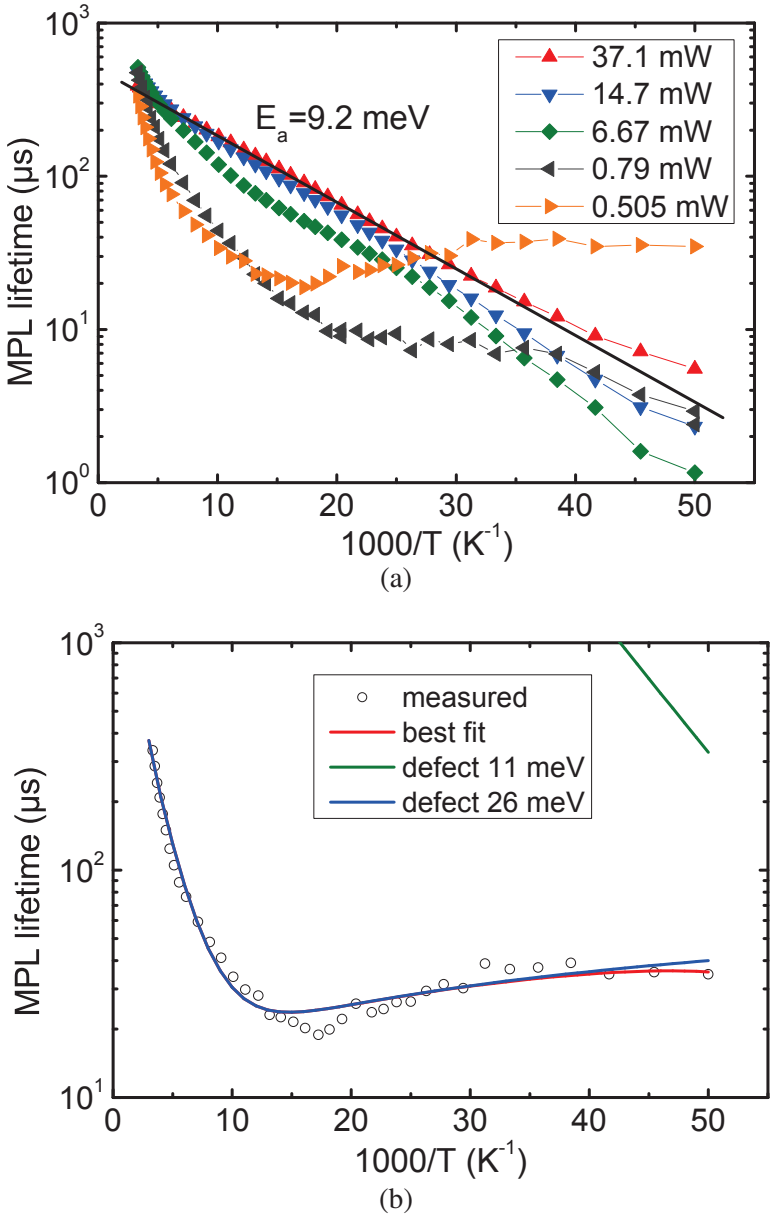

Fig. 4.16 (a) The MPL lifetime of sample #A5 ((p) a-Si:H passivation with intrinsic buffer layer) for various intensities. (b) TDLS analysis of sample #A5 at low injection of 0.505 mW.

energy" as the slope of the plot for this temperature range. For 37.1 mW illumination, we evaluate an apparent activation energy of 9.2 meV, while for 0.505 mW illlumination the apparent activation energy above 200 K is about 40 meV.

The TDLS analysis requires a very low injection so that the excess carrier concentration becomes negligible compared to equilibrium carrier concentration. The PL signal detected

is therefore relatively weak. As a result, only the samples presenting long lifetime are investigated to ensure a detectable signal and a low excess carrier concentration at the same time. The sample#A5 Fig. 4.16(b), exhibits the typical signature of a defect and SRH recombination. However a very shallow defect with an activation energy of 26 meV is fitted.

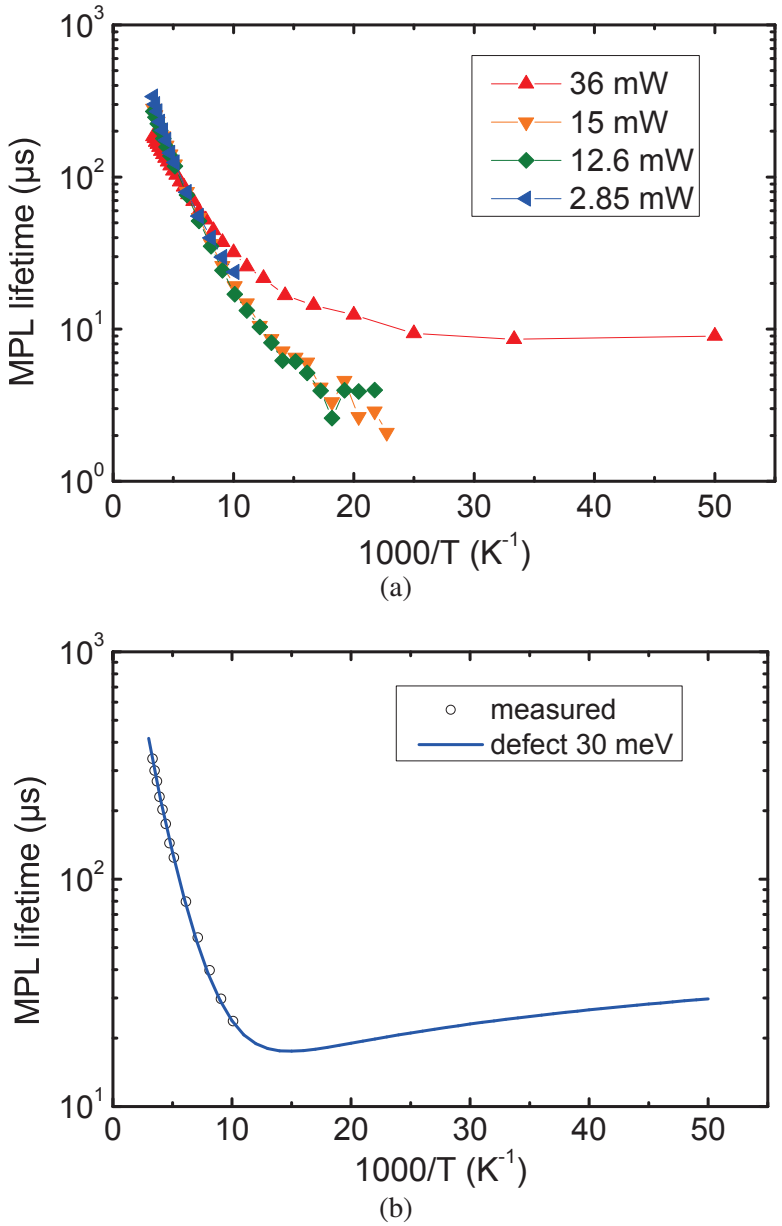

Fig. 4.17 (a) The MPL lifetime of sample #A2 ((p) a-Si:H passivation without the intrinsic buffer layer) for various intensities. (b) The TDLS analysis of sample #A2 at low injection of 2.85 mW.

Emitter without the intrinsic a-Si:H layer The temperature dependence of MPL lifetime of sample #A2 for various illumination intensity is displayed in Fig. 4.17(a). When the illumination decreases, the slope of the curve at high temperature increases. However, below 15 mW, the change of slope is no longer obvious, that is different from the sample #A5. This trend maybe explained by the poorer passivation of sample #A2 as opposed to sample #A5, in order words this sample is readily in the low injection regime for relatively low illumination intensity.

Sample #A2 is analyzed at 2.85 mW illumination. We observe in Fig. 4.16(b), a typical signature of defect and SRH recombination. By fitting the high temperature range, we determine a very shallow defect activation energy of 30 meV. This value is close to what we have found for #A5. The low S/N ratio does not permit to fit the low temperature range.

Intrinsic a-Si:H layer only We studied the samples #G7 and #G8 with only the intrinsic a-Si:H as a passivation layer. Their lifetime temperature dependence is shown in Fig. 4.18(a) at both high and low injection. We observe that the 10 nm and 50 nm intrinsic layer have the same passivation efficiency at room temperature. This means that 10 nm is enough to passivate and extra thickness does not provide any advantage to increase the lifetime. From TDLS it is not possible to reproduce the data for the whole temperature range. A fit with two defect levels is possible but yields defect level energies of 13.8 and 7.6 meV, respectively.

BSF We investigated BSF sample #B1. In Fig. 4.19, the lifetime is measured as a function of temperature for two different injection (high and low). Under one sun illumination (36 mW), the apparent activation energy is 9 meV. TDLS again yields to two shallow defect levels of 13.8 meV and 10 meV in Fig. 4.19(b). The existence of a protrusion between 20 and 25 K^{-1} makes the curve fitting by two simple defects inappropriate. We are unable at this stage to explain this observation.

AlOx The sample #D2 is passivated with AlOx. The lifetime temperature dependence is shown Fig. 4.20.

Under high injection, 35 mW and for a temperature range >200 K, we again determine a very shallow apparent activation energy 1.9 meV. At low injection, 0.265 mW for the same temperature range, we estimate an energy of 35 meV at 0.265 mW. TDLS yields to defect energies of 21.8 meV and 15.6 meV.

Summary of the temperature dependence of the MPL lifeitme All the SHJ samples investigated exhibit a similar temperature dependence *i.e.* the lifetime decreases when the

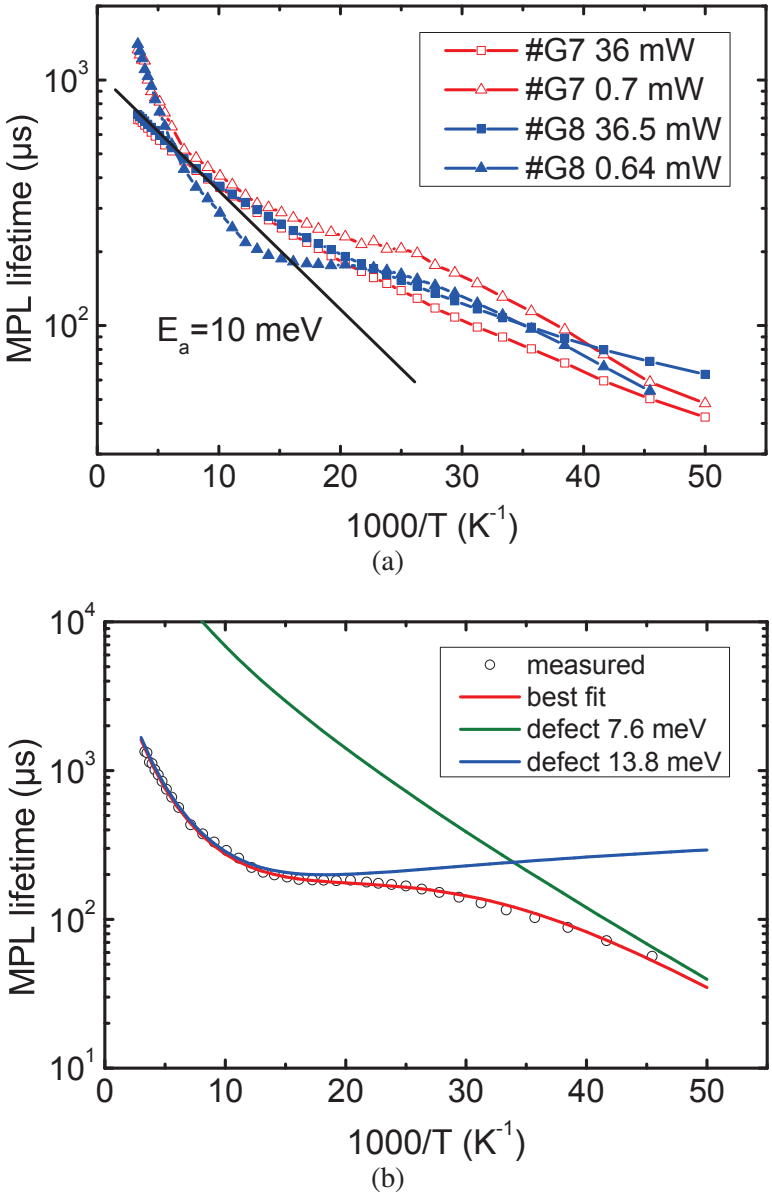

Fig. 4.18 (a) The MPL lifetime of samples #G7 and #G8 (intrinsic a-Si:H layer passivation only) for both high and low injection. (b) TDLS of sample #G8 for 0.64 mW low injection.

temperature decreases no matter the type of passivation (a-Si:H or AlOx). This temperature dependence is at the same time dependent on the injection. Higher injection always results in lower apparent activation energy as opposed to lower injection. For very low injection, TDLS generally yields to two shallow defect energy levels less than 30 meV and dependent on the passivation. This feature appears for good and poorly passivated samples. However, these energies are too shallow ($\ll kT$) to be assigned to a known impurity species. The

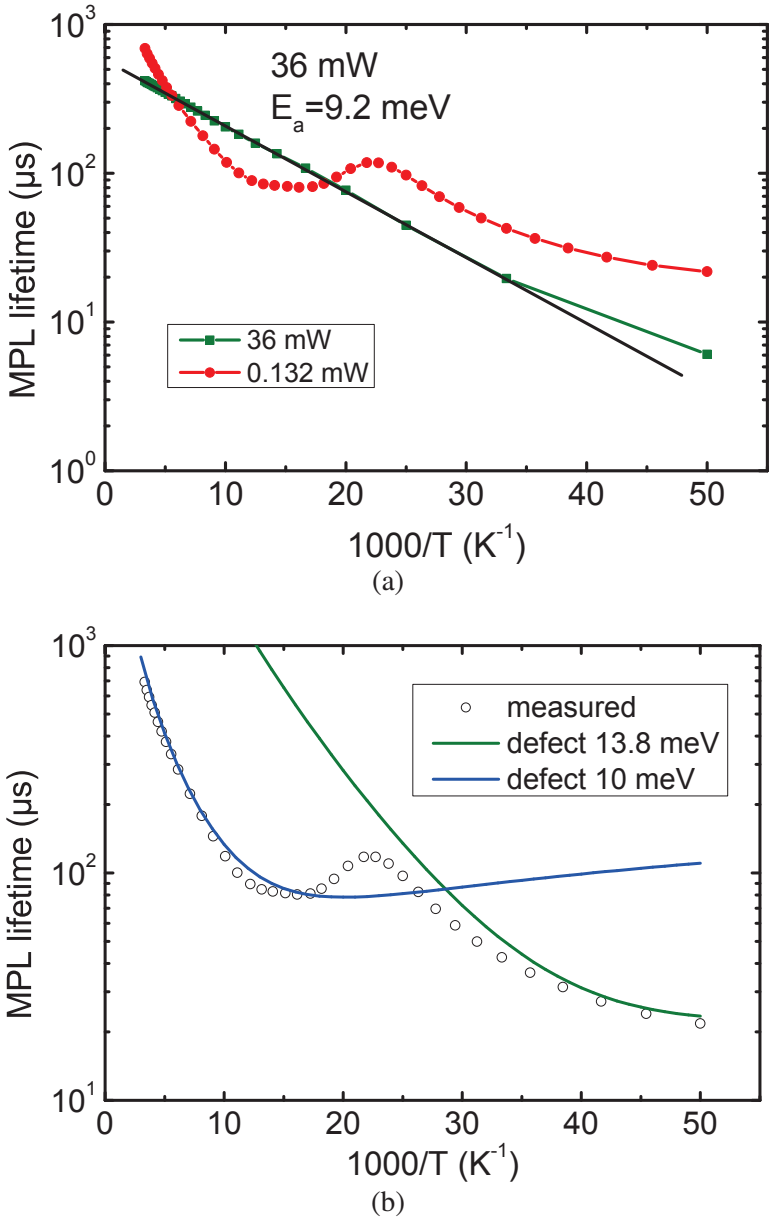

Fig. 4.19 (a) The MPL lifetime of sample #B1 (BSF type: (n) a-Si:H with intrinsic buffer layer) for both high and low injection. (b) TDLS of sample #B1 for 0.64 mW low injection.

lifetime of poorly passivated samples is determined by SHJ interface. We assume here that the mechanism involved is inherent to the c-Si interface.

In an attempt to elucidate this peculiar behavior and the extremely low activation energies observed, we built the simulation model described in section 4.4. Note that, the calculations do not converge for temperatures below 100 K (for $1000/T > 10$).

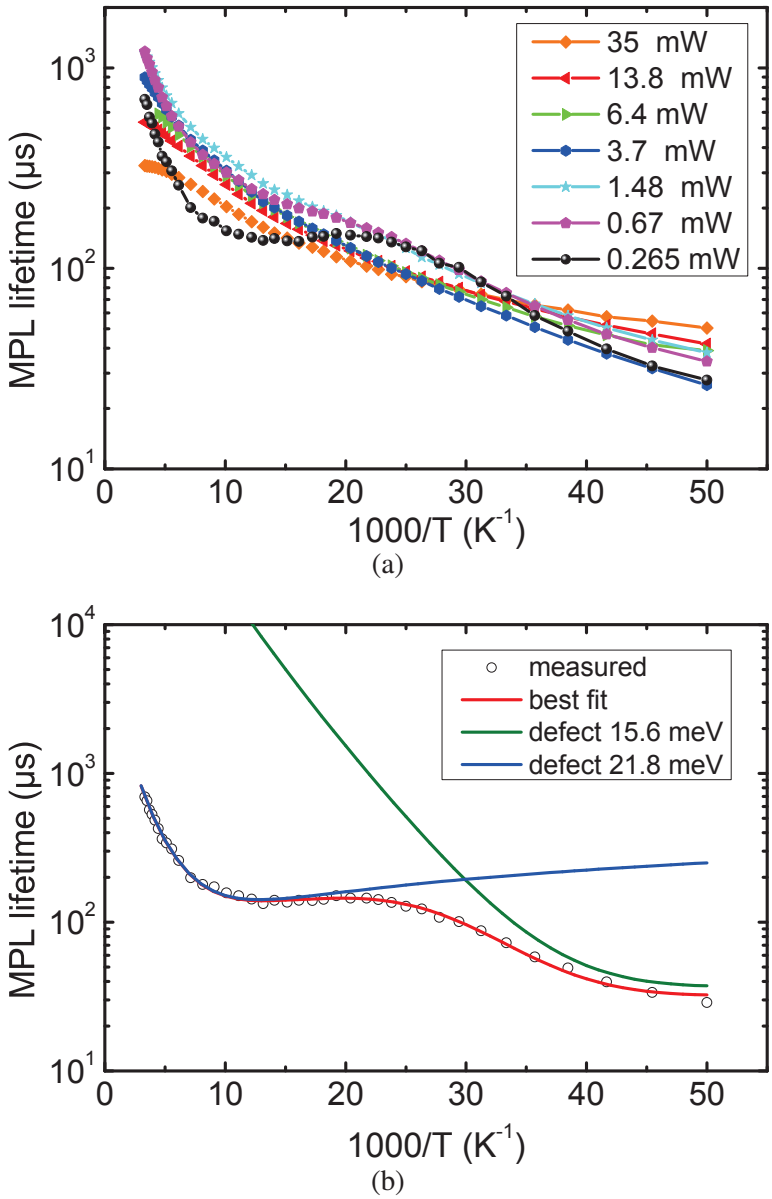

Fig. 4.20 (a) The MPL lifetime of sample #D2 (AlOx passivation) for high and low injection. (b) TDLS of sample #D2 for 0.265 mW low injection.

4.3.2.3 Temperature dependence of the integrated PL spectrum

In section 4.3.1.1 we have shown in Fig. 4.12 the ”regular” temperature dependence of the PL spectra of SHJ samples. Now we look into the spectral dependence considering the temperature dependence of the band-to-band radiative recombination coefficient and the carrier lifetime.

The measurement should be performed under very low intensity to ensure that the carrier lifetime is indeed dominated by SRH recombination and that Eq. 3.8 applies to evaluate the carrier concentration from the lifetime. For this reason, the measured spectrum of sample #D2 in Fig. 4.12(f) (power density~0.9 mW/cm^2, photon flux~3.6×10^{15} cm^{-2}s^{-1}) is chosen.

First, to calculate the equilibrium electron concentration $n_0(T)$, the temperature dependence of the dopant ionization is taken into consideration. We calculate the $n_0(T)$ from the charge neutrality equation [82, section 4.4]:

$$\begin{aligned} n_0 &\approx N_d^+ \\ n_0 &= N_c \exp\left(-\frac{E_c - E_f}{kT}\right) \\ \frac{N_d^+}{N_d} &= \frac{1}{1 + 2e^{(E_f - E_d)/kT}} \end{aligned} \tag{4.4}$$

where E_f is the Fermi level, E_c the conduction band energy, E_d the donor activation energy, N_d the donor concentration, N_d^+ the ionized donor concentration and N_c the effective density of states of the conduction band. We take E_d at 45 meV as reported for phosphorus in silicon [83, page 23], and $N_d = 1.8 \times 10^{15}$ cm^{-3} for the phosphorus doped c-Si wafers.

The calculation yields $n_0(T)$ as shown in Fig. 4.21(a). The hole concentration $p_0(T)$ at equilibrium is negligible in this n-type wafer. In addition, being in the low injection regime allows to estimate the excess carrier concentration $\Delta n(T) = \Delta p(T)$ from the lifetime using Eq. 3.8 as follows:

$$\Delta n(T) = \Delta p(T) = \tau(T)G = \tau(T) j_{laser}/d_{wafer} \tag{4.5}$$

where G is the average generation rate in the wafer, $\tau(T)$ the temperature dependent MPL lifetime, j_{laser} the laser photon flux, d_{wafer} the thickness of the wafer. The lifetime of the sample is taken from Fig. 4.20(b). $\Delta n(T)$, $\Delta p(T)$ and $n_0(T)$ are shown in Fig. 4.21(a). Then the integrated PL intensity as a function of temperature is calculated :

$$j(T) = B(T)n(T)p(T) = B(T)\left[\Delta n(T) + n_0(T)\right]\Delta p(T) \tag{4.6}$$

$B(T)$ is the temperature dependent band-to-band recombination coefficient. Using the temperature dependent B values of Eq. 3.21 given by Nguyen et al [58] for $T > 90$ K, we can calculate the integrated PL intensity from our MPL lifetime as shown in Fig. 4.21(b).

Now we can compare this calculated plot and the measured integrated PL. For that purpose we rescale it so that it coincides with the calculated PL at 300 K. The data after calibration are shown in Fig. 4.21(b).

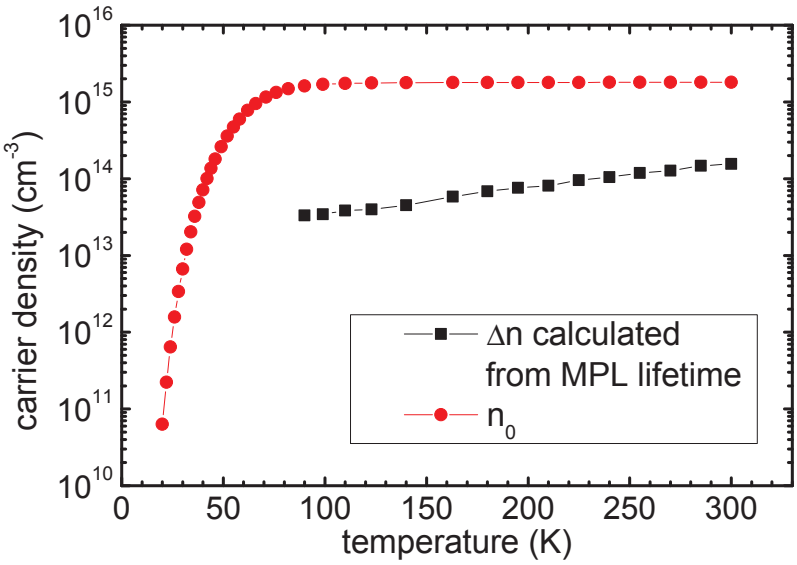

(a)

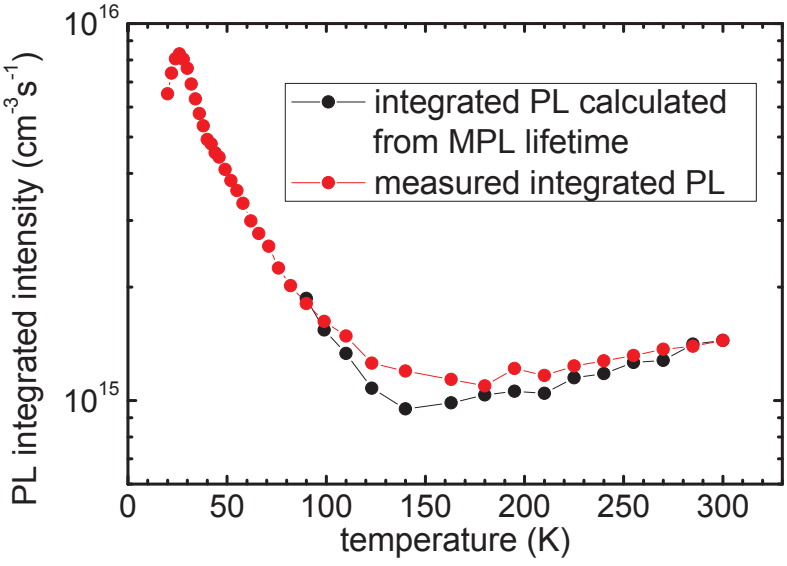

(b)

Fig. 4.21 (a) Electron concentration at equilibrium and the excess carrier concentration estimated from the MPL lifetime as a function of temperature using Nguyen's $B(T)$ data [58]. (b) Experimental result of the integrated PL intensity of sample #D2 under 0.26 mW illumination. The PL intensity is also calculated using the experimental MPL lifetime.

We observe that the calculated integrated PL intensity is in good agreement with the experimental data.

As a result, using Eq. 4.6, we establish the radiative recombination coefficient $B(T)$ from our measured data in Fig. 4.21(b) using

$$B(T) = \frac{j(T)}{\left[\Delta n(T) + n_0(T)\right] \Delta p(T)} \tag{4.7}$$

and propose values for B below 77 K, which are not available in the literature. We can give a 5^{th} order polynomial approximation from fitting:

$$\begin{aligned} \log_{10} B(T) = &- 5.92914 - 0.230597T + 0.00271769T^2 \\ &- 1.57055 \times 10^{-5}T^3 + 4.356627 \times 10^{-8}T^4 - 4.6377 \times 10^{-11}T^5 \end{aligned} \tag{4.8}$$

where $B(T)$ is expressed in $\mathrm{cm^3 s^{-1}}$.

Fig. 4.22 displays the benchmark of our work with the data reported in the literature notably Nguyen's and Trupke's results. As expected from Fig. 4.21(b), the $B(T)$ curves are

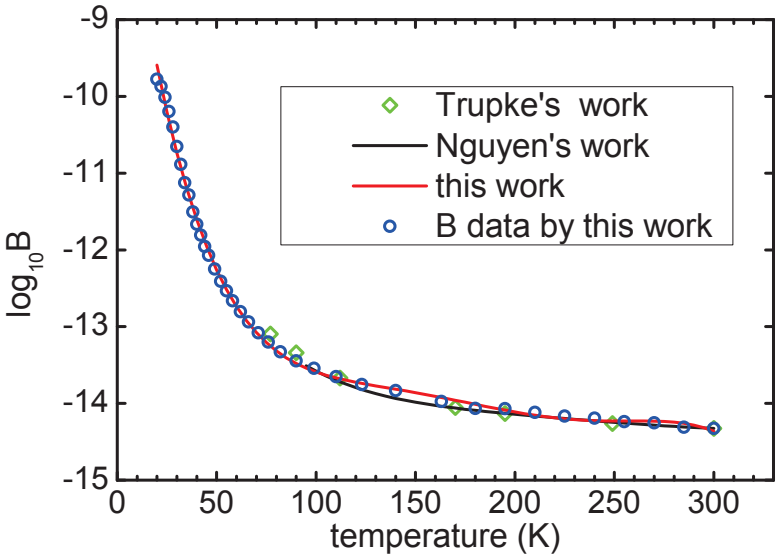

Fig. 4.22 Radiative recombination coefficient $\log_{10} B$ cited from [58], Trupke's work [57] and fitting from the experimental data in this work. The integrated PL is directly deduced from the experiments in Fig. 4.21(b) is used for the fitting.

in good agreement above 77 K. Note that there were no data available below 77 K in the literature and our work contributed to extended the range of B available for the community down to 20 K. A 5^{th} order polynomial may be used as an approximation.

4.4 Simulation

In the aforementioned experiments, we extracted a shallow defect level around 20 meV (see section 4.3.2) by TDLS. Such a low value is highly questionable as there is no evidence of such shallow defect reported in the literature *e.g.* the phosphorus energy level is 45 meV below E_c. In the following we consider the phosphorus level in combination with either bulk and/or interface defects and we calculate the effective lifetime using ATLAS/Silvaco and the full device structure of Fig. 3.11. Auger and radiative are accounted for in the simulations. The temperature dependent effective density of states of conduction and valence band $N_c = 2.84 \times 10^{19}(T/300)^{3/2}$ cm^{-3}, $N_v = 1.04 \times 10^{19}(T/300)^{3/2}$ cm^{-3} and the thermal velocities of electron and hole $v_{th,n} = 1.07 \times 10^7(T/300)^{1/2}$ cm/s, $v_{th,p} = 1.30 \times 10^7(T/300)^{1/2}$ cm/s are introduced in the simulations.

4.4.1 Without SRH recombination from doping

First, we consider the situation where the phosphorus level is not an SRH recombination center. This means the electron from the ionized phosphorus level only contributes to the conduction band, without capture or emission of holes. The temperature dependent ionization of the phosphorus level has been taken into account. We introduced an additional shallow defect at 20 meV *i.e.* the energy evaluated from previous experiments.

4.4.1.1 Low level illumination intensity

The parameters used in the simulation are shown in Tab. 4.5. the defects are positionned

Table 4.5 Simultion parameters of low intensity

Parameter	Value
Illumination	1.12 mW/cm^2
Defect type	Donor
Defect level	E_c−0.02/0.4 eV
Defect density	variable
Capture cross section σ_n	10^{-14} cm^2
Capture cross section σ_p	10^{-14} cm^2

either in the bulk or at the interface. The simulation result is shown in Fig. 4.23.

We find that a deep defect (0.4 eV below conduction band) exhibits an opposite temperature dependence compared to the experiments, that is when the temperature decreases the lifetime increases. On the other hand, both shallow defects (0.02 eV below conduction band)

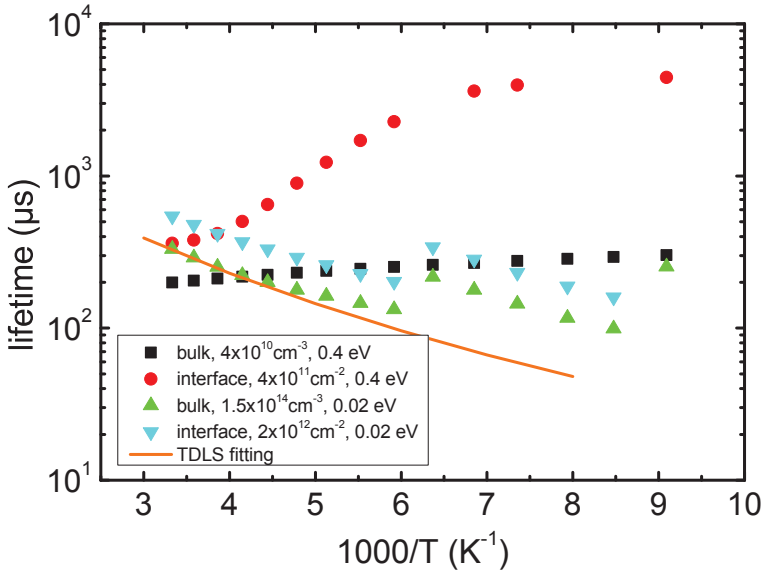

Fig. 4.23 Low injection simulation with the parameters in Tab. 4.5.

in the bulk and at the interface present a temperature dependence similar to the experimental trend. Note that the abrupt change of lifetime in the range of $6 < 1000/T < 7$ is due the non convergence of the numerical calculation.

Nevertheless, one can use TDLS to extract the defect parameters in the range of $1000/T < 6$. 0.02 eV is so shallow that the capture term is negligible compared to the emission term in Eq. 3.42, only the c_2 term can be reliably retrieved by curve fitting. Note that from the analysis of the SRH recombination mechanism described in chapter 3, the expected value of $\tau_{p0}^{300K} N_c^{300K}/n_0$ is 810 µs. The fitting gives $\tau_{p0}^{300K} N_c^{300K}/n_0 = 773 \pm 45$ µs, $\Delta E_t = 23 \pm 2$ meV, in fair agreement with $E_c - E_d$. However, we also see that when the temperature decreases there is some discrepancy between the data and the fitting. This could be related to the band bending at the interface or less reliable simulation results.

4.4.1.2 High level illumination intensity

The parameters used in simulation are shown in Tab. 4.6. The defects are positionned either in the bulk or at the interface.

The simulation result is shown in Fig. 4.24. Again, the deep defects at 0.4 eV below E_c does not follow the temperature dependence as for the experiments. With a defect density of 1.5×10^{14} cm^{-3} and a defect level of 0.02 eV below the conduction band, we found a similar temperature dependence as measured by MPL. Note that again we suffer from poor convergence in some temperature ranges.

Table 4.6 Simultion parameters of high intensity

Parameter	Value
Illumination	112 mW/cm^2
Defect type	Donor
Defect level	E_c−0.02/0.4 eV
Defect density	variable
Capture cross section σ_n	10^{-14} cm^2
Capture cross section σ_p	10^{-14} cm^2

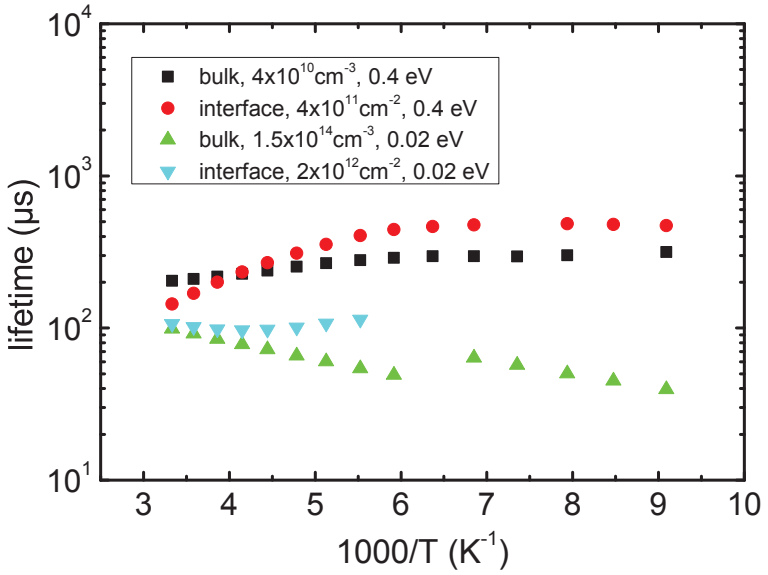

Fig. 4.24 High injection simulation with the parameters in Tab. 4.6.

We implemented TDLS to extract the defect parameters in the range of $1000/T < 6$. $\tau_{p0}^{300K} N_c^{300K}/n_0 = 206 \pm 18$ µs, $\Delta E_t = 7 \pm 3$ meV. This energy level ΔE_t should correspond to the 20 meV defect energy level. However, we found 7 meV. We already know that TDLS does not apply to high injection and this limitation is hereby confirmed.

4.4.2 With SRH recombination from doping

Next, we consider the situation where the phosphorus level is an SRH recombination center. The donor concentration is fixed to $N_d = 1.8 \times 10^{15}$ cm^{-3}. Its energy level is also fixed to $E_D = 45$ meV below the conduction band. Various capture cross sections are considered in the simulations. In these simulations, no other defects are considered.

4.4.2.1 Low level illumination intensity

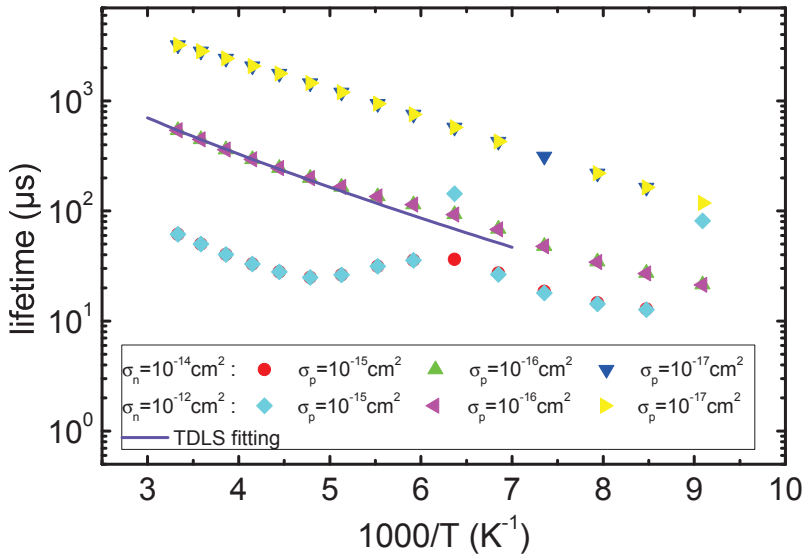

Fig. 4.25 Low injection simulation with different σn and σp.

We observe in Fig. 4.25 that the lifetime is dominated by σ_p. The value of σ_p has a large impact on the lifetime whereas the value of σ_n has minor impact. Furthermore, since we are in low injection regime, the σ_p has no evident impact on the slope, *i.e.* the apparent activation energy of the curves at high temperatures for $\sigma_p = 10^{-15}$ and $\sigma_p = 10^{-16}$.

With TDLS, we extracted the defect parameters from the two curves corresponding to $\sigma_p = 10^{-16}$ cm^2. For the same reason discussed previously we fit only the term related to c_2 in Eq. 3.42. Also, due to non convergence of the simulation at low temperature, we only fit in the high temperature range. The result gives $\tau_{p0}^{300K} N_c^{300K}/n_0 = 2179 \pm 557$ µs, $\Delta E_t = 41 \pm 5$ meV. Due to great fitting errors, we should look only at ΔE_t that is in fair agreement with the phosphorus level position.

4.4.2.2 High level illumination intensity

Fig. 4.26 shows tha the lifetime is dominated by σ_p. When σ_p increases the lifetime decreases, which means that the excess carrier concentration decreases and the result approaches what has been observed in low injection. When the σ_p increases we observe a change of the slope which corresponds to larger apparent activation energies.

We applied the TDLS for $\sigma_p = 10^{-15}$ cm^2 and we obtained $\Delta E_t = 22 \pm 3$ meV. This is much lower than the 45 meV expected for the phosphorus energy level. However, we know that TDLS should be applied only in low injection, again the simulation confirms that

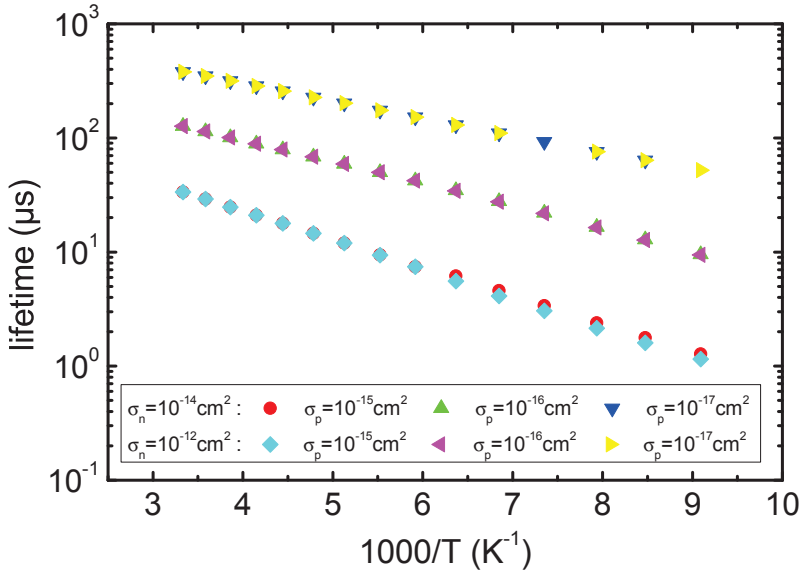

Fig. 4.26 High injection simulation with different σ_n and σ_p.

high injection leads to a lower extracted ΔE_t (and thus lower apparent activation energy). Overall, this is coherent with the experimental result of the MPL lifetime as a function of temperature.

4.4.2.3 Surface defects and phosphorus defect at the same time

A more complicated but more realistic situation can be considered when taking into account the interface defects. We investigate this situation in low injection (1.12 mW/cm^2) and $\sigma_n = 10^{-14}$ cm^2 for the phosphorus defect.

We add deep surface defects ($\sigma_n = \sigma_p = 10^{-14}$ cm^2) to simulate a more realistic heterojunction. The density of interface defects and σ_p of phosphorus defects are variables. The result is shown in Fig. 4.27(a). The MPL lifetime for (#A5, #A2, #G8, #B1 and #D2) can be found in Fig. 4.27(b).

As expected, we find that when the interface defect density increases, the lifetime decreases. However, this trend is only evident at high temperature *i.e.* the interface deep defects are dominant only at high temperature. Despite the fact, at high temperatures when the interface defect densities are the same, smaller σ_p of the phosphorus defect leads to much higher lifetime. So the recombination through phosphorus defect still has evident impact on the lifetime. The comparison between Fig. 4.25 and Fig. 4.27(a) confirms that at low temperature, the recombination through the phosphorus defect level dominates. Thus we see only two branches at low temperature in Fig. 4.27(a) that correspond to $\sigma_p = 10^{-16}$ cm^2 and $\sigma_p = 10^{-17}$ cm^2, respectively.

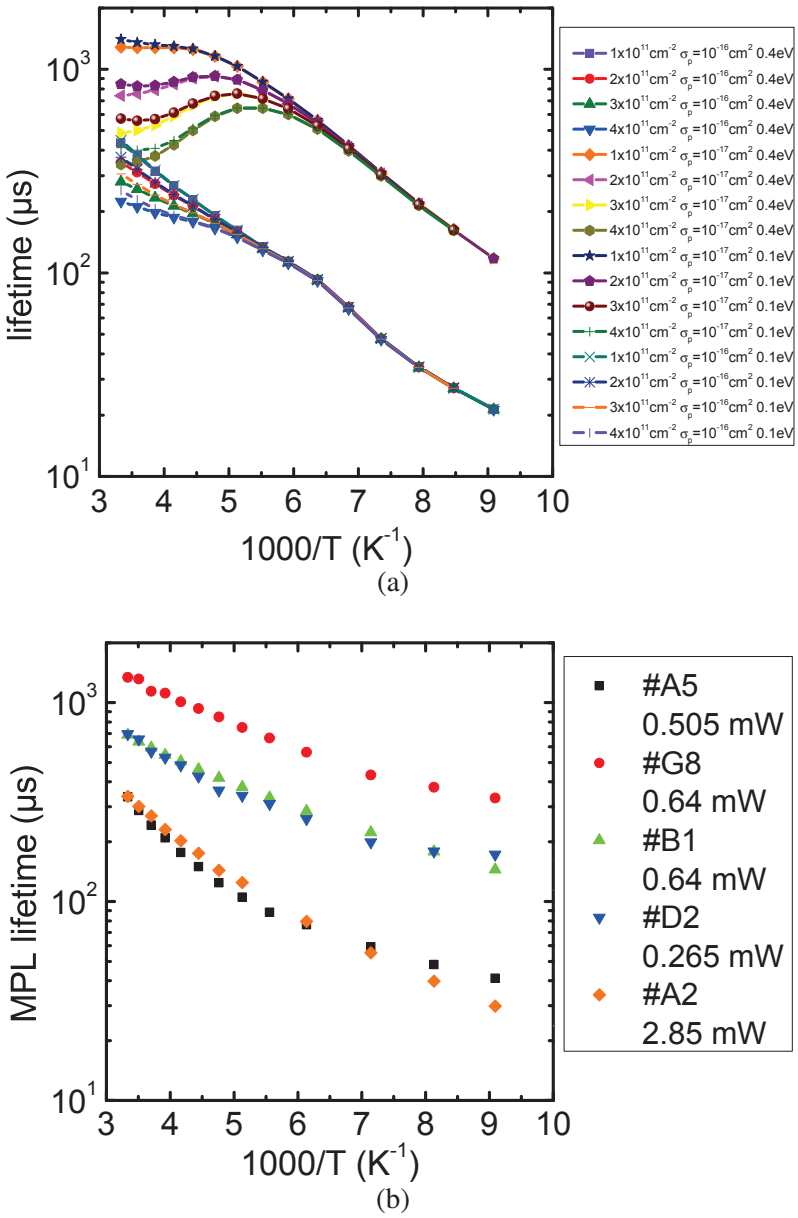

Fig. 4.27 (a) Simulations at low injection (1.12 mW/cm^2) with phosphorus level in the bulk and interface defects at 0.4 eV or 0.1 eV below the conduction band. Various interface defect densities and σ_p of the phosphorus defect are investigated. (b) Experimental MPL lifetimes of the samples investigated at low injection in section 4.3.2.

4.4.2.4 Conclusion of the simulation

To conclude, we have shown that TDLS can extract a reasonable activation energy from the simulation result in low injection conditions. The donor defect as an SRH recombination center could be a possible explanation to support the temperature dependence of the lifetime

found in section 4.3.2. However, the experimental MPL lifetime of samples with different passivations (but the same wafer) do not exhibit the same lifetime and the temperature dependence as shown in Fig. 4.27(a). The interface passivation has an impact on both high and low temperature dependence. The shallow defect energy level extracted in Figs. 4.16(b), 4.18(b), 4.19(b) and 4.20(b) remain another possibility but further investigation is necessary to clarify this point.

4.5 Conclusion

In this chapter we demonstrated that our system is able to perform PL and MPL mapping to characterize the sample homogeneity. PL mapping is impacted by optical properties whereas the MPL mode, especially when using the phase is optical parameters independent and provide a clear image of the sample properties.

In the literature, it is reported that photoconductance decay lifetime and the MPL lifetime are distinct. The discrepency originates from the uncertainty in the excess carrier concentration. In this work, we have demonstrated experimetally that under certain conditions these lifetime are equal should the excess carrier concentration be calibrated. In addition, we have compared the SHJ samples using TRPL (see Appendix C) and MPL. We observed that both techniques yield to a lifetime that decreases when the temperature decreases.

By investigating the integrated PL spectra, we reached very good agreement with the literature in the high temperature range for the radiative recombination coefficient $B(T)$. Moreover, we have extended with original data of B in the low temperature range ($20 \sim 77$ K) thanks to our MPL experiments. We proposed a 5th order polynomial function that fits our experimental data and extended the range of validity down to 20 K.

For samples passivated by an AlOx layer we found a peculiar temperature dependence of PL. The band-to-band peak decreases with decreasing temperature, while a lower energy peak appears. This lower energy peak dominates at low level illumination intensity. We investigated various models proposed in the literature. One model is able to correctly fit our experimental data. However this model introduces two shallow energies, (our fitting values are 8 and 64 meV), these values do not present any physical significance and therefore we assume that a more complex temperature dependence of the properties *e.g.* σ should be investigated.

We have tried to reproduce the overall lifetime dependence by simulation with ATLAS. Deep,as well as shallow defects in the bulk and at the interface have been considered. The donor energy level has been considered as an SRH recombination center. So far, the simula-

tion succeeds in explaining the decrease of the apparent activation energy with the increase the injection, but it fails to reproduce the experiments.

Chapter 5

Observation of the Excitation transfer in stacked quantum dot chains by micro PL

This work is a collaborative research between SDRL (Semiconductor Device Research Laboratory) in Chulalongkorn University and UPMC (Université Pierre et Marie CURIE) in the framework of ICT-ASIA programme funded by MAEE (Ministère des affaires étrangères et européennes) (MAEE) and CNRS (Centre National de la Recherche Scientifique).

5.1 Introduction

Stacked InAs quantum dot chains (QDCs) on InGaAs/GaAs cross-hatch pattern (CHP) templates yield a rich emission spectrum with an unusual carrier transfer characteristic compared to conventional quantum dot (QD) stacks. The photoluminescent spectra of the controlled, single QDC layer comprise multiple peaks from the orthogonal QDCs, the free-standing QDs, the CHP, the wetting layers and the GaAs substrate. When the QDC layers are stacked, employing a 10 nm GaAs spacer between adjacent QDC layers, the PL spectra are dominated by the top-most stack, indicating that the QDC layers are nominally uncoupled. Under high excitation power densities when the high-energy peaks of the top stack are saturated, however, low-energy PL peaks from the bottom stacks emerge as a result of carrier transfers across the GaAs spacers. These unique PL signatures contrast with the state-filling effects in conventional, coupled QD stacks and serve as a means to quickly assess the presence of electronic coupling in stacks of dissimilar-sized nanostructures.

On the other hand, the temperature dependent measurements also help identify the energy peaks because the PL spectrum is quite dependent on temperature. Spectroscopy by sweep of temperature can demonstrate the peaks that are not visible at other temperatures. Moreover,

the PL peak energetic positions correspond to specific size and shape of QDs. The inter-dot carrier coupling effect is observed and translated as a red shift of 120 mV on the [1$\bar{1}$0] direction peak is observed at 30 K on 1-stack with regards to 3-stack samples, which is assigned to lateral coupling.

Semiconductor quantum dots (QDs) grown by molecular beam epitaxy (MBE) are often stacked in order to increase the active optical volume and to tune the emission or detection wavelength and polarization of the QD ensembles [84, 85]. Stacking QDs is achieved through thin spacer layers which physically separate but often electronically couple adjacent QD layers [86]. Understanding the coupling nature of vertically stacked QD structures is of fundamental importance to the operation and optimization of QD-based devices such as memory [87], lasers [88] and solar cells [89, 90]. Though useful, coupling is not always necessary or desired, particularly for broadband applications which benefit from the superposition of different wavelengths from individual QD layers [91]. If present, electronic coupling results in the lowering of the excitonic ground-state (GS) energy, and consequently a red-shift of photoluminescent peak [86, 92]. The degree of coupling is thus usually inferred from the magnitude of the energetic red-shift relative to those emitted from a single QD layer structure [86]. This approach can be misleading in stacked QDs as the strain profile at the growth front is affected by the underlying nanostructures: subsequent QD layers usually nucleate at a lower deposition amount [92, 93]. If grown at the same two-dimensional (2D) equivalent thickness throughout, upper QD layers would be bigger than those of the lower QD layers, with a concomitant red-shift due to size—not coupling. One way to unambiguously identify the presence and evaluate the strength of coupling is to vary the spacer thickness and observe the changes in PL signals as a result of excitation transfer of carriers. This approach has been adopted to study coupling between, for examples, stacked QDs [94] and stacked quantum dots and wells [95]. Alternatively, one can fix the spacer thickness, vary the size of each stack, perform PL measurements and simply count the number of GS peaks: a single (multiple) GS peak indicates the presence (absence) of coupling [94]. This chapter adopts the latter approach to study an unusual coupling property of stacked quantum dot chains (QDCs) on cross-hatch pattern (CHP) templates as shown in Fig. 5.1.

QDCs or laterally-coupled QDs have garnered significant interests in the past decade [97] and have recently gained renewed interests due to their unique geometry suitable for fundamental transport studies [98] and polarization-sensitive optoelectronic devices [99]. However, QDCs are rarely studied in stacked forms due to their complex optical characteristics [100], paticularly when coupling can simultaneously occur laterally and vertically as is the case here. Here, stacked InAs QDCs on InGaAs/GaAs CHP templates grown by molecular beam epitaxy (MBE) are characterized by micro-photoluminescence (μ-PL) and a

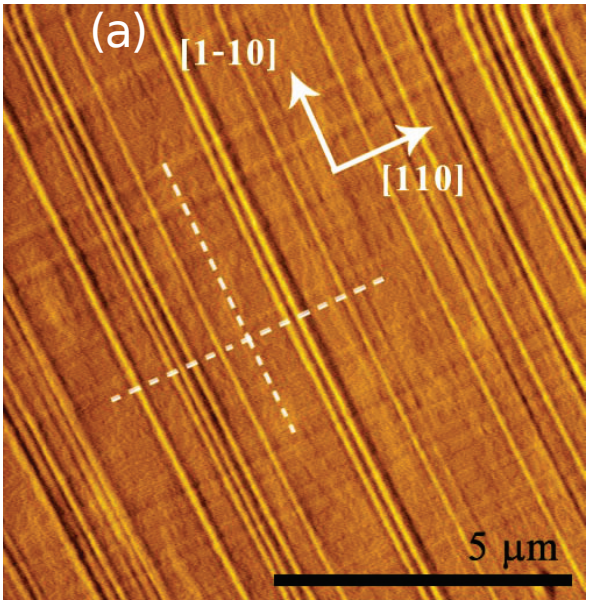

Fig. 5.1 (a) AFM image of $In_{0.2}Ga_{0.8}As$ on GaAs cross-hatch pattern. (b) Surface undulation along dashed lines in (b) [110] and (c) [1$\bar{1}$0] directions. [96]

complete PL fingerprint of QDCs/CHP structures is reported. We observed that under high excitation power densities, stacked QDCs do not exhibit state-filling effects as would be observed in stacked QDs. The otherwise excited-state carriers are instead transferred toward the lower QDC layer, an effect attributed to the combination of extended wavefunctions, resonant tunelling and thermalization.

5.2 Experimental

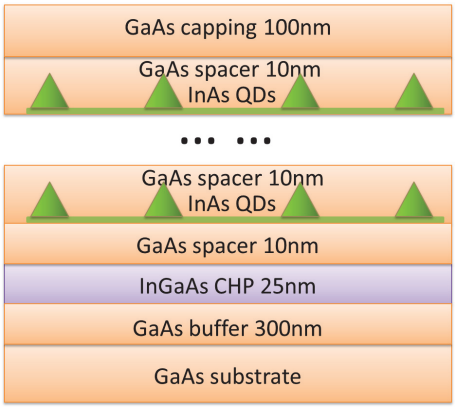

Fig. 5.2 Schematic of investigated QDCs stacks structure.

The QDs samples are fabricated by Dr. Songphol Kanjanachuchai and his research team in Semiconductor Device Research Laboratory of Chulalongkorn University. The structures investigated as is shown in Fig. 5.2 comprise multiple stacks of InAs QDCs grown on partially-relaxed InGaAs film on GaAs by solid-source MBE Using Riber's 32P MBE system, and after in situ thermal cleaning of GaAs (001) surface, growth starts from 300 nm GaAs buffer layer, followed by 25 nm $In_{0.2}Ga_{0.8}As$, 10 nm GaAs spacer, and 1, 3, or 5 stacks of InAs QDC/10 nm GaAs spacer pairs. The cross-hatch pattern surface of the InGaAs layer serves as a template on which chains of QDs form along the orthogonal [110] and [1$\bar{1}$0] directions. The smoothness of the growth fronts and the formation of QDs are monitored in situ via streaky and spotty reflection high-energy electron diffraction (RHEED) patterns, respectively. Each QD layer is grown until the RHEED pattern changes from streaks to spots, i.e., at the onset of QD formation. The 2D equivalent thicknesses of the bottom-most stack are 1.7 monolayer (ML) and the remaining stacks are 1.3 ML. Finally, all samples are capped with 100 nm GaAs for PL measurements. Two PL set-ups are employed. For free-space, macro-PL setup, the samples are fixed in a cryostat, excited by a broad beam (2.39 mm spot size), 514.5 nm Ar+ laser, and emission detected by a liquid nitrogen-cooled InGaAs point detector (Hamamatsu's G7754) using standard lock-in techniques. For confocal, micro-PL setup, the sample is mounted on a piezoelectric-driven platform (Witec's alpha300), excited by a narrow beam ($\sim$ 1 µm spot size) frequency-doubled 532nm Nd:YAG laser operating in continuous mode, and emission detected by a thermoelectrically-cooled InGaAs array detector (Andor's DU491A). Spatial and energy-resolved PL maps are acquired from the micro-PL setup by raster scanning and simultaneously collecting point spectra. All maps shown represent PL intensities integrated over a 10 meV bandwidth around energies of interest.

5.3 QDCs stacks morphology

For morphology measurement, one extra series of sample is fabricated at the same time, but these samples are not capped with GaAs layer to allow for AFM imaging. The final structure of these samples is the same as the passivated samples shown in Fig. 5.2 except that they have no GaAs layer on top.

The surface profile is obtained by AFM in tapping mode in air [100]. Fig. 5.3 displays 10×10 μm^2 AFM image showing the QDs geometry and distribution on the topmost layer in . As is shown in Fig. 5.3(a), for 1-stack the QDs are aligned along [1$\bar{1}$0] and [110] dislocation lines of the underlying CHP layer and some of them distribute randomly. For 3 and 5 stacks, however, free-standing QDs are not seen as almost all of the QDs align themselves along dislocation lines but on 5-stack even the [110] dots are not distinguishable. It is also evident

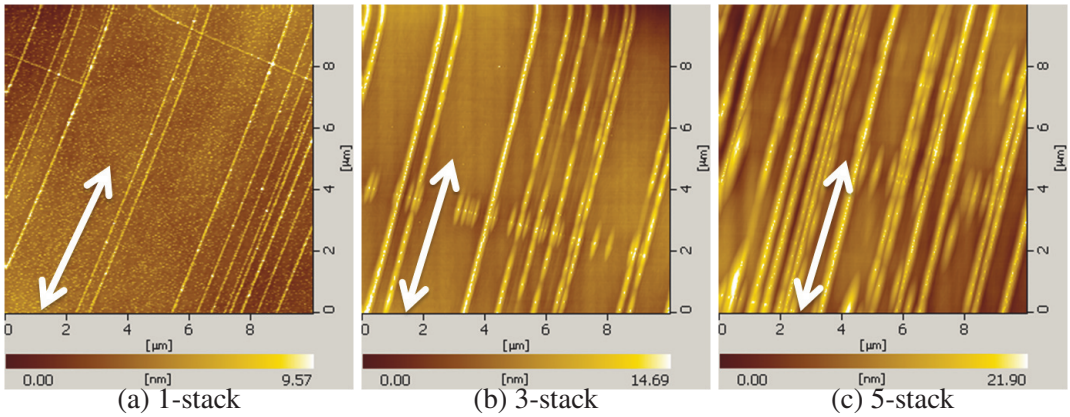

(a) 1-stack (b) 3-stack (c) 5-stack

Fig. 5.3 AFM imaging of a 10×10 µm^2 area on 1, 3 and 5 stacks QDs (white arrow indicates [1$\bar{1}$0]) direction.

in Fig. 5.3(c) that the surface density of 5-stack QDs is much larger than the other two, which has some impact on the spectroscopy.

Generally speaking, we observe much more QDCs along [1$\bar{1}$0] direction. This reflects the asymmetry of the underlying CHP layer. There exist more dislocation lines in [1$\bar{1}$0] direction than in [110] dislocation. As is explained in the reference [96], the [1$\bar{1}$0] stripes nucleate earlier than the other direction, thus have greater dot density.

Fig. 5.4 zooms in on Fig. 5.3 to give a closer look at the QDs of the three samples on the scale of 1×1 µm^2. In Fig. 5.4(a) the shape of the 1-stack QDs is circular while 3-stack and 5-stack are eclipse. Their morphology depends on the growth direction. QDs of 3-stack and 5-stack are prolonged along [1$\bar{1}$0] direction, see Fig. 5.4(b) and Fig. 5.4(c).

The size of QDs varies between stack numbers. The diameter of QDs for the 1-stack sample is about 30nm. In contrast, the size of 3-stack and 5-stack are 35nm along [110] and 60nm along [1$\bar{1}$0]. In addition, in Fig. 5.4(a), as the [1$\bar{1}$0] QDs began to grow prior to the [110], and to free-standing ones, their sizes are a little different, that is, $QD_{[1\bar{1}0]}$>$QD_{[110]}$>$QD_{free-standing}$ [96], whereas in Fig. 5.4(b) and Fig. 5.4(c), the dot size on both directions are similar for multiple stack samples.

The distance between QDs also varies with stack number. This inter-dot distance is a key parameter that affects coupling between QDs ensembles [100]. In Fig. 5.4(a) the 1-stack QDs are much closer to each other than on 3-stack and 5-stack, which means the lateral coupling is more likely for 1-stack. This is revealed by the PL spectrum in coming sections. As the lateral coupling rapidly decreases as the distance increases, the other two samples are not in favor of this effect.

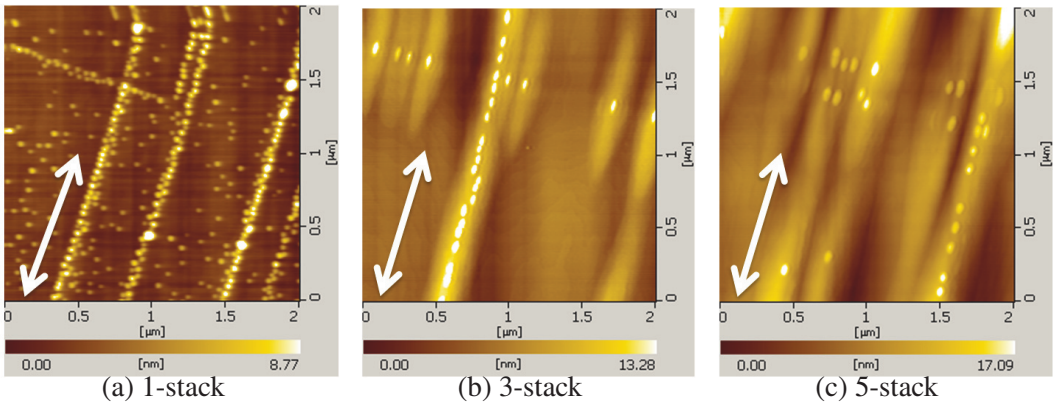

(a) 1-stack (b) 3-stack (c) 5-stack

Fig. 5.4 Zoom in on a 2×2 µm^2 area of AFM imaging of 1, 3 and 5 stacks QDs.

5.4 Results and discussion

Conventional InAs Stranski-Krastanow QDs grown on flat GaAs (001) are randomly distributed and typically emit a single PL peak at around 1 µm with a full width at half maximum (FWHM) of a few 10s meV [101]. Certain growth conditions can extend the wavelength to the 1.3–1.55 µm telecom window [102] or lead to bimodal or multimodal size distributions with multiple PL peaks [103, 104, 105], while random distribution remains. In contrast, InAs QDs grown on CHPs are guided, forming chains along the orthogonal [110] and [1$\bar{1}$0] directions, each direction with its own size, size distribution, and wettling layer (WL) due to the asymmetry of the underlying dislocations [106]. The formation of QDs along the orthogonal dislocation chains has been established by planview transmission electron microscopy (TEM) [107], whereas vertical correlation of QDs with 10 nm GaAs spacer has been confirmed by cross-sectional TEM [108]. The 60° dislocations at the lower InGaAs/GaAs interface, typical in zincblende heteroepitaxy, cause surface strain fields that affect adatoms motion during growth [109], but do not affect the intrinsic emission efficiency of the overlying QDs [110]. The PL spectrum of a QDC layer would thus contain many more PL peaks than those of conventional SK QDs due to the co- existence of many optically active structures.

We will show and discuss the results in three parts. The first part describes the PL maps and spectra of the 1-stack QDC layer, showing all the possible luminescent peaks. The second part shows that luminescence is dominated by the uppermost QDC layer which is nominally uncoupled to the underlying QDC layers. The third part shows that the luminescence from the bottom QDC layers emerges at high excitation level, and provides a qualitative explanation of the underlying mechanism.

5.4.1 Single QDC layer: basic emission peaks

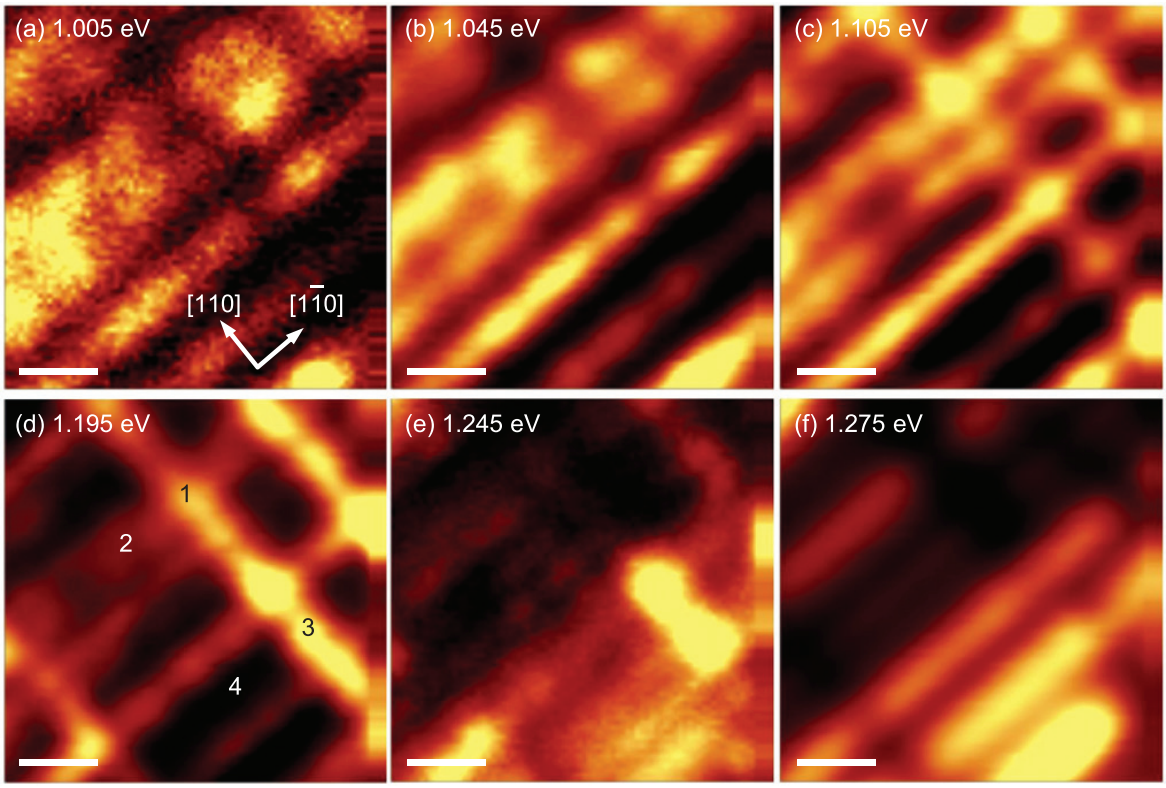

Fig. 5.5 PL of a single InAs QD chain layer on an InGaAs/GaAs cross-hatch pattern. Same-area, 20×20 μm^2 micro-PL maps at increasing integrated intensity from (a) 1.005 to (b) 1.045, (c) 1.105, (d) 1.195, (e) 1.245 and (f) 1.275 eV. The scale bars in (a)-(f) are 4 μm.

The 1-stack QDC sample emits in the 1-1.4 eV range similar to conventional SK QDs, but with a much richer optical feature. Fig. 5.5(a)-(f) show spatial- and energy-resolved spectral maps on the same 20×20 μm^2 area of the sample at 80 K. The PL maps, integrated over increasing energies from 1.005 in Fig. 5.5(a) to 1.275 eV in Fig. 5.5(f), show spatially non-uniform emissions with a cross-hatch pattern resembling the surface undulation of the underlying InGaAs/GaAs template. Fig. 5.5(a) shows that at 1 eV, the lower energetic end of the spectra, emissions emerge from bright patches which look like stripes along the [1$\bar{1}$0] direction. The stripes become clearer and better resolved as the energy increases to 1.045 eV in Fig. 5.5(b). The dottiness of the lines making up the stripes is simply a reflection of the variation in local QD density, in good agreement with the morphology of uncapped samples shown in Fig. 5.3. When the energy increases to 1.105 eV in Fig. 5.5(c), emissions from the existing [1$\bar{1}$0] direction begin to fade while those from the orthogonal, [110] direction emerge. The emissions from the [110] and [1$\bar{1}$0] stripes overlap and yield the characteristic CHP luminescence observed in Fig. 5.5(c). As the energy continues to increase to 1.195

eV in Fig. 5.5(d), the [1$\bar{1}$0] emission peters out whereas the [110] emission intensifies. And as the energy keeps on increasing to 1.245 eV in Fig. 5.5(e) and 1.275 eV in Fig. 5.5(f), the [110] and [1$\bar{1}$0] emissions are extinguished, replaced by bright patches emerging in the previously dark areas—i.e. the bright/dark regions in Fig. 5.5(a) and 5.5(f) are reversed.

The QDs can be categorized, in evolution sequence [111] and with corresponding labels shown in Fig. 5.5(d), into four distinct groups:

1. At the intersection of the orthogonal [110] and [1$\bar{1}$0] dislocations.
2. On the [1$\bar{1}$0] dislocation lines.
3. On the [110] dislocation lines.
4. On the remaining areas.

The four QD ensembles emit slightly differently. Fig. 5.6(a) shows point spectra at pixels 1-4 in Fig. 5.5(d), corresponding to the four QD ensembles above. Emissions from pixels 1-3 comprise two principal peaks: a broad peak centered at around 1.15 eV and a narrow peak at 1.27 eV. In contrast, emission from pixel 4 comprises only one narrow peak, also centered at 1.27 eV.

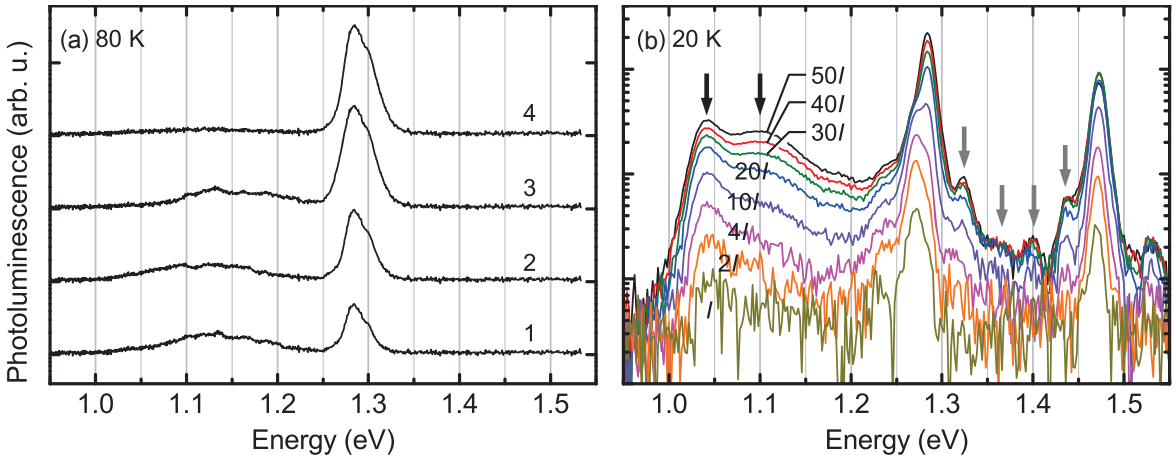

Fig. 5.6 Spectra at pixels 1-4 in Fig. 5.5(d) are shown in (a): pixel 1 is taken at an intersection between [1$\bar{1}$0] and [110] dislocation lines, 2 on a [1$\bar{1}$0] dislocation line, 3 on a [110] dislocation line, and 4 on a dislocations-free area. (b) Macro-PL spectra measured at increasing excitation power density from, bottom to top, I=0.11 W/cm^2 to 2, 4, 10, 20, 30, 40 and 50 times I. Spectra in (a) are offset for clarity.

The broad peaks result from QD chains along the [1$\bar{1}$0] and [110] directions as unequivocally proven by microscopy and spectroscopy. The micro-PL maps in Fig. 5.5(a)-5.5(f) provide the microscopic proof whereas the macro-PL spectra in Fig. 5.6(b) provides the

spectroscopic confirmation. It has long been known that the underlying InGaAs/GaAs CHP are asymmetric: the [1$\bar{1}$0] stripes nucleate earlier, have greater density, and result in surface steps which are taller than the [110] stripes [96]. The asymmetry is transferred to the overgrown layers, resulting in QDs along the [1$\bar{1}$0] direction forming slightly earlier and are thus taller and emit at a lower energy than those along the orthogonal [110] direction [106, 111, 112]. The microscopic images in Fig. 5.5(c)-(d) provide a clear visual evidence of QD luminescence decorating the [1$\bar{1}$0] and [110] stripes, at slightly different energies. This small energy difference however cannot be resolved in the corresponding point spectra: Fig. 5.6(a) shows that pixel 2, taken along the [1$\bar{1}$0] direction, emits at a slightly lower peak energy than pixel 3, taken along the orthogonal [110] direction. Though these two peaks are spatially resolved in microscopy, they are spectrally unresolved as a result of micro-PL setup's fast integration time. The macro-PL setup, in contrast, has a much longer integration time and can provide complementary spectra with greater signal-to-noise ratios.

Fig. 5.6(b) shows excitation power-dependent macro-PL spectra of the same sample (but on a different area) at 20 K. The lowest two energetic peaks—1.04 eV for the [1$\bar{1}$0]-aligned QDs and 1.10 eV for the [110] aligned QDs highlighted by the black arrows—can now be clearly resolved at high excitation powers.

The narrow 1.27 eV peak is asymmetric: the left and right sides of the 1.27 eV peak in Fig. 5.6(a) tail off slightly differently—a characteristic of two unresolved Gaussian peaks with different FWHM. The closely-spaced emissions arise from the superposition or spectral overlap of the small free-standing QDs and the underlying InGaAs CHP template. The PL map in Fig. 5.5(f) shows that the areas that give off this luminescence are those between the cross hatches which happen to be the nucleation sites for free-standing QDs, too.

The four small peaks between 1.3 and 1.47 eV (observed only in the macro-PL setup as indicated by the grey arrows in Fig. 5.6(b)) are most likely associated with multiple wetting layers, some of which were previously identified [106]. For conventional InAs/GaAs SK QDs, a single WL exists and emits at around 1.44 eV. This is true even if bimodal size distributions are present [105], as long as the growth front is flat. For InAs QDs on InGaAs CHPs, the growth front is not flat. In fact, the surface steps in the [1$\bar{1}$0] and [110] directions are different [96]. The WL underneath the QD chains along the [1$\bar{1}$0] and [110] directions can thus be expected to be different—for example, they could form one-dimensional wetting wires [113]—but similar structures investigated so far reported just a single WL energy [106].

The multiple WL peaks above are only observed close to the carbon impurity, 1.49 eV peak and the bulk GaAs, 1.52 eV peak. Measurements taken at different areas where the 1.49 and 1.52 eV peaks are absent do not reveal the multiple WL peaks. This indicates the

possibility that bulk C centers render ineffectual the carrier capture by QDs from the GaAs matrix and the WLs and explains the elusiveness of the multiple WL luminescence. It is a normal practice for those carrying out PL measurements to shine the exciting laser on a spot that yields the best signal and in so doing moving away from areas with large local concentrations of C, and hence missing the WL peaks.

It is worth pointing out that the multimodal size distribution of the 1-stack layer which gives rise to multiple emission peaks has not been optimized for broadband applications. If desired, one can increase the inhomogeneity of the spectrum by, for instance, growing the QDs at a higher rate or subjecting them to rapid thermal annealing [114]. In addition, one can also increase the luminous efficacy of real devices by soft-annealing under hydrogen so that most defects are neutralized and do not adversely affect long-term reliability [106].

5.4.2 Multi-Stack QDCs: dominant emission from top-most layers

In reflection-based PL set-ups, the 1-stack QDC layer enjoys an unobstructed output window but the 3- and 5-stack QDC layers may not. This depends on electronic coupling. If the stacked layers are coupled, they behave as a single ensemble and should enjoy an unobstructed output window as is the case for the 1-stack sample. But if the stacked layers are uncoupled, luminescence from all the layers should be detectable, unless some are obstructed—reabsorbed, scattered, or reflected—in which case the emissions are dominated by the overlying structures due to geometrical advantage. Such behavior in stacks of randomly distributed QDs cannot be proven through spectroscopy alone. But if the random distribution is reduced, as is the case for QDCs, and with μ-PL mapping to show this, it is possible to draw such a conclusion as shown below.

Fig. 5.7(a)–(d) show the PL maps of the 3-stack QDC sample at increasing integrated energy from 1.075 eV in Fig. 5.7(a) to 1.235 eV in Fig. 5.7(d). Similarly, Fig. 5.7(e)–(h) show the PL maps of the 5-stack QDC sample from 1.075 eV in Fig. 5.7(e) to 1.235 eV in Fig. 5.7(h) (see animated videos in the supplementary data for the complete ranges). The maps show luminescence which is CHP-like for the 3-stack sample, but stripes-like for the 5-stack sample. Since adjacent stacks are separated by a 10 nm GaAs spacer which is sufficiently thin to allow coupling in conventional SK QD stacks [94], a question emerges as to why CHP-like luminescence similar to the 1-stack sample described above is not observed in the 5-stack case, or is not more clearly observed in the 3-stack case because the bottom-most QDC layer for the three samples is identically grown, has the biggest dot size and the lowest GS energies, and should thus provide the same optical features (CHP-like) as observed in the previous section. The maps shown in Fig. 5.7 instead more closely match the AFM morphologies of the top-most QDC layer where the number density of QDs along

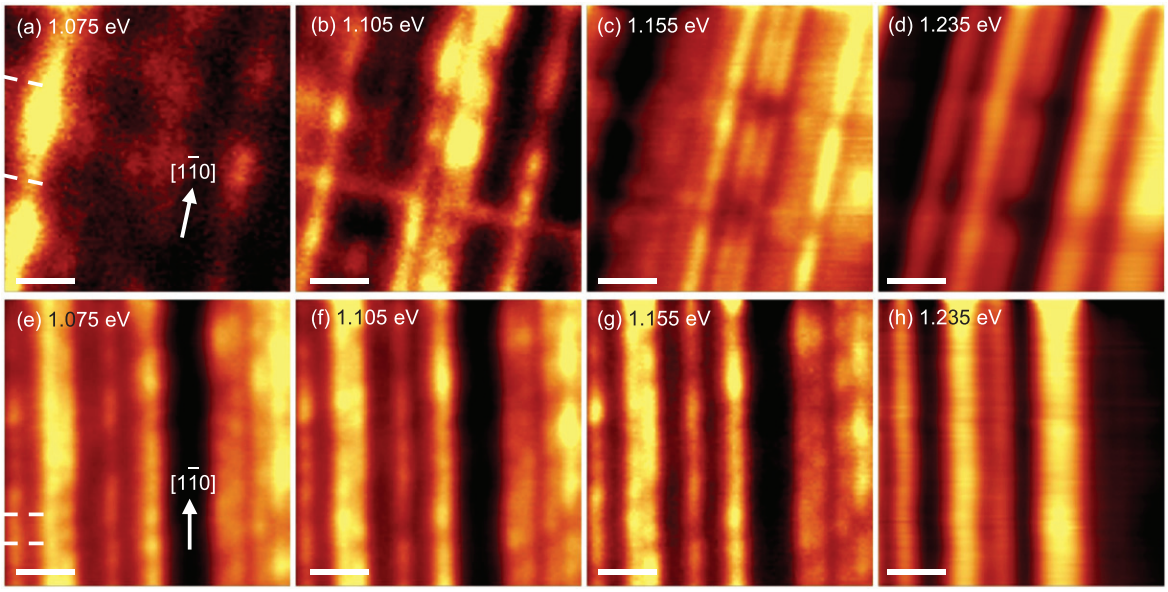

Fig. 5.7 Same-area, room-temperature, 10×10 μm^2 micro-PL maps of (upper panels) the 3-stack QD chain sample at increasing integrated intensity from (a) 1.075 to (b) 1.105, (c) 1.155 and (d) 1.235 eV, and (lower panels) the 5-stack QD chain sample from (e) 1.075 to (f) 1.105, (g) 1.155 and (h) 1.235 eV. The scale bars are 2 μm. The broken lines are guide to the eye and indicate some of the buried [110] dislocation lines.

the [110] direction is significantly reduced as shown in Fig. 5.3, implying that the emission is dominated by the top-most layer. The bottom-most QDC layer buried along the [110] direction is almost undetectable; it can be barely distinguished by the collinearity of bright or dark spots, as indicated by broken lines in Fig. 5.7.

One possible explanation for the much reduced [110] emission is carrier tunnelling from the bottom to the top QDC layer as has been observed in the QD bi-layer reported by Heitz et al [94]. However, this mechanism cannot explain the missing CHP-like emissions because carriers always tunnel towards the lower energetic state, i.e., the bottom-most QDC layer (1.1 eV active), not the top-most QDC layer (1.2 eV). If inter-stack tunnelling were present, the CHP-like emissions would have been enhanced, not suppressed.

Another possible explanation is that the top QDC layer has the highest quantum efficiency, thus dominating the weaker emission from the low quantum efficiency bottom stacks. The QDC stack is strained throughout as it is sandwiched between the top GaAs capping layer and the bottom partially-relaxed InGaAs CHP layer which in turn rests on a GaAs buffer. Since the top stack is in contact with the dislocations-free GaAs cap layer, whereas the bottom stack is in close proximity to the dislocations-prone CHP layer, the top stack would have a greater optical quality. Unless the strain profile surrounding each QD layer is

carefully compensated [115], increasing the number of QD layers would in general result in accumulated strain that ultimately degrades the optical quality of the whole QD stack [116].

5.4.3 Multi-Stack QDCs: excitation transfer

After many trials to uncover the bottom layer emissions—mostly by varying the optical path from normal to edge—it was found that the elusive emissions are not entirely missing, only significantly diminished since they are partially retrieved simply by increasing the excitation power density. This approach is however against a normal PL practice of using minimum excitation to study the true ground-state energies of QDs [92] and also to avoid sample heating.

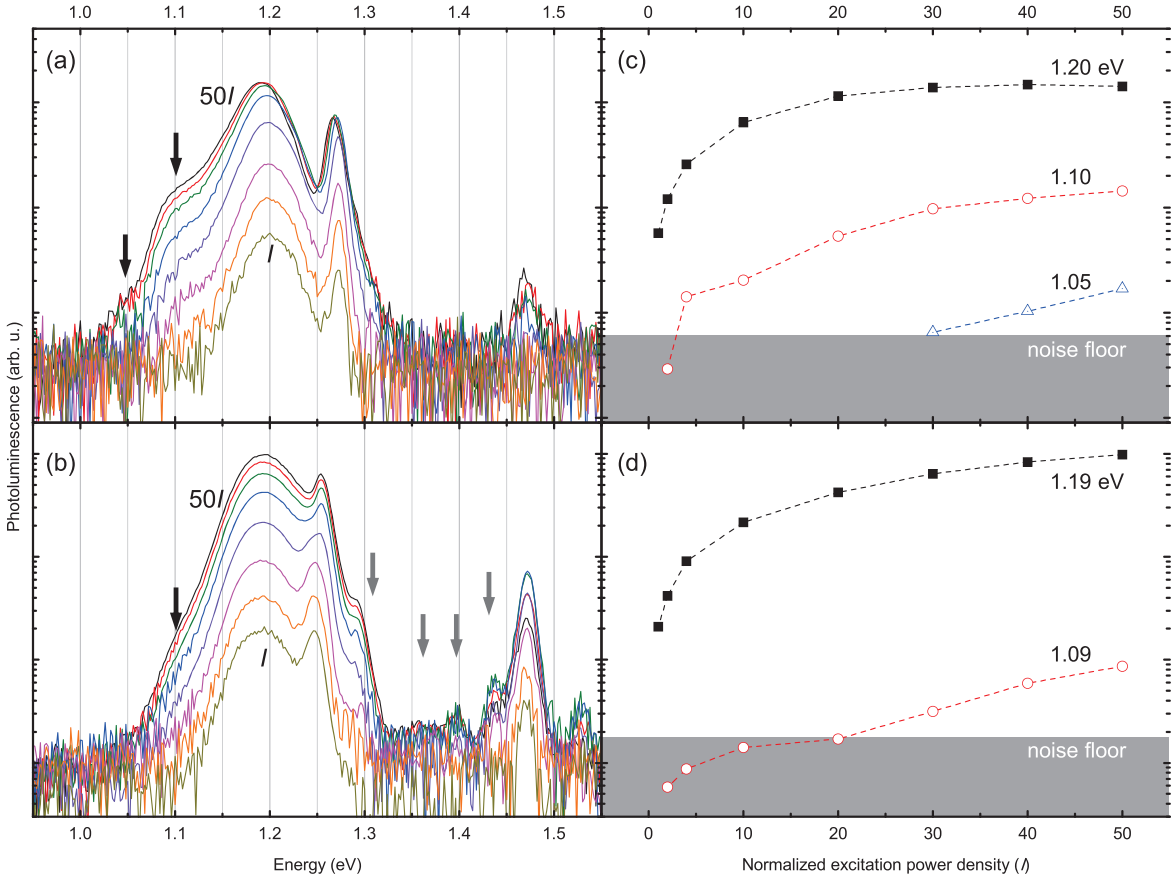

Fig. 5.8 Macro-PL spectra of the (a) 3- and (b) 5-stack QDC sample measured at increasing excitation power density from, bottom to top, I=0.11 W/cm^2 to 2, 4, 10, 20, 30, 40 and 50 times I. The solid arrows indicate peaks that appear only at high excitation levels. The grey arrows point to WL-related peaks. The increase in PL intensity as a function of excitation power density (normalized to I) for the (c) 3- and (d) 5-stack QDC samples at selected energies.

Fig. 5.8(a) and (b) show the macro-PL spectra of the 3- and 5-stack QDC samples, respectively. The spectra are measured from a low excitation power density I_0 of 0.11 W/cm^2 to $50I_0$. For the 3-stack sample, increasing excitation results in intensity saturation of the 1.2 eV peak emissions from the top-most layer. Such saturation in conventional SK QDs would coincide with the appearance of one or more higher energy peaks as a result of state filling [117, 118], and this is true for both single-layered and stacked QDs [95]. The spectra in Fig. 5.8(a) are however the opposite: as the 1.2 eV peak saturates, a lower energy peak emerges at around 1.1 eV, and at $40I_0$ excitation, another peak at an even lower energy of around 1.05 eV can be seen to be emerging. The sequential appearance of the 1.1 and 1.05 eV peaks upon saturation of the 1.2 eV peak is evident in the excitation-dependent PL intensity plots at the three energies shown in Fig. 5.8(c). The two additional peaks—1.1 and 1.05 eV—coincide with those of the 1-stack layer described earlier, strongly indicating that they arise from the bottom-most QDC layer.

The partial recovery of the bottom-most QDC emissions could be a direct or an indirect result of increased excitation, or a combination of both. The direct result is simply due to the greater availability of photons reaching the bottom-most stack. The indirect result is due to excitation transfer of carriers from the top- (high energy) to the bottom (low energy) layer, which is energetically favorable but ineffective at low-level excitations. The inefficiency is a result of suppressed tunnelling. At 10nm ($\sim$ 36 ML), the GaAs spacer is sufficiently thin that tunnelling readily occur among stacks of conventional SK QDs [94]. But this is not the case for stacks of QDCs here. The tunnelling between stacks of QDCs must have been suppressed by the presence of the underlying misfit dislocations—the sole differentiating factor between the QDC and QD stacks. Often associated with dislocations are strain fields known to cause local inhomogeneities in various physical properties [119]. The strain fields can be so strong that they affect surface atom motion and guide the nucleation of nanoscale QDs [120, 121] or the running direction of micron scale droplets [122]. Their effects on coupling are thus not surprising. External strains applied via piezoelectric crystal, for example, have been shown to affect fundamental QD excitonic properties [123], particularly to tune the excitonic binding energies [124]. Internal strains caused by interfacial misfit dislocations should likewise affect excitonic GS wavefunctions as a result of electric field induced by piezoelectric effects and/or strain gradients. Electric fields, built-in or externally applied, increase the effective distance between carriers confined in vertically-stacked quantum structures, and thus decrease coupling. The decrease is offset at high-level optical excitation. As the GS becomes saturated from the increased excitation, the first excited state (ES) would normally emerge in uncoupled nanostructures. For the multi-stack QDC structures, however, the ES wavefunctions extend further in space (are less localized) than those

of the GS, penetrating further into the GaAs spacer and subsequently falling into the lower GS of the bottom stack. The extra carriers that would normally give rise to the higher-energy ES peaks thus avail themselves of the lower-energy GS of another stack which explains the successive emergence of the lower-energy PL peaks and the absence of state-filling effects in Fig. 5.8(a). Excitation transfer between an ES of one nanostructure and a GS of another in resonant has been reported in many systems [94, 95].

For the 5-stack sample, increasing excitation also results in intensity saturation of the 1.19 eV peak of the top-most QD layer and the appearance of the 1.09 eV peak as shown in the spectra in Fig. 5.8(b) and the excitation-dependent PL intensity plots of the two peaks in Fig. 5.8(d). The saturation of the 1.19 eV peak and the emergence of the 1.09 eV peak seen in Fig. 5.8(d) are, however, more gradual than those of their equivalence in the 3-stack sample—the 1.2 and 1.1 eV peaks—in Fig. 5.8(c). This possibly results from the greater saturated intensity due simply to the 5-stack sample's greater QD areal density—approximately by 5/3 times. The state-filling effects are also absent; the high energy peaks between 1.3 and 1.47 eV are WLs as described while discussing the 1-stack sample earlier. These WL peaks cannot be observed in Fig. 5.8(a) since this is a low C-impurity area evidenced by the 3-stack sample's lowest 1.47 eV peak among the three samples.

5.5 Temperature dependent PL of QDs

The PL is measured under various temperatures between 30 K and 300 K, with a step of 10 K. The sample is clamped onto the cryostat and illuminated under a power density of 120 mW/cm^2. This power density permits only the ground state emissions. We performed several rounds of temperature measurements, from high to low as well as from low to high, to make sure that the measurement is stable and no hysteresis appears.

The macro PL spectra are shown in Fig. 5.9. We observe that at room temperature PL intensity is as weak as noise level, which is negligible compared to those at low temperatures. When temperature is lowered to, ie. 240 K, emission peaks begin to emerge.

Firstly, four emission peaks are observed on 1-stack. At low temperatures the spectral components are much more sharper than at high temperatures. These components correspond to [1$\bar{1}$0], [110], free-standing and CHP layer. Although not so evident, the peak positions are also temperature-dependent.

For 3-stack sample, the PL spectroscopy is quite different from 1-stack sample. Only a high peak and a very small peak are observable. As will be discussed below, the first one corresponds to [1$\bar{1}$0] and [110] dots and second one correspond to the CHP layer in Fig. 5.3(b).

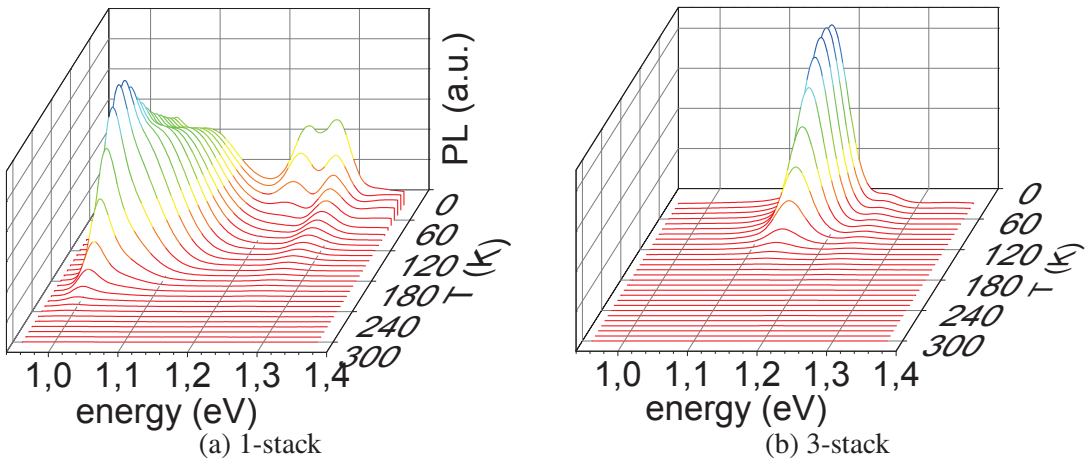

(a) 1-stack (b) 3-stack

Fig. 5.9 Temperature dependence of PL spectrum of 1 and 3 stack QDs.

The main difference between 1-stack and 3 stack is the evidence that QDs of 1-stack are close enough, as is shown in Fig. 5.4(a) to produce lateral coupling effect which results in red shift of spectrum of 120 mV [125].

Strong emissions minimize weaker ones when plotted in the same scale as in Fig. 5.9. We select some PL spectra under various temperatures and rescaled them as shown in Fig. 5.10 to give a clearer view of the emission peaks and the variation with temperature.

We select several temperatures to demonstrate the dependence in Fig. 5.10. For 1-stack, Fig. 5.10(a) shows that four emission peaks are identified by deconvolution. From low to high energy they are supposed to correspond to $[1\bar{1}0]$, [110], free-standing QDs and CHP layer as is found from the mapping result in Fig. 5.5. However, the peak energies don't match. We should be aware that the emission energy is temperature dependent, since the bandgap is also a temperature dependent. As a result, four peaks at 1.05, 1.10, 1.24, 1.29 eV correspond to the four different emissions that we observed in PL mapping, as shown in Fig. 5.6.

In the same way, from Fig. 5.10(b) two peaks at 1.17, 1.25 eV are identified. The first peak actually comprises two components from $[1\bar{1}0]$ and [110] QDCs which can be identified from the cross hatch pattern in Fig. 5.7(b). The second peak corresponds to the CHP layer. At 130 K, we notice there are actually two Gaussian curves in the first peak. The low energy peak is rather wide while the high energy peak is narrow, i.e. can be observed in a much smaller energy range. This corresponds to Fig. 5.7.

The $[1\bar{1}0]$ and [110] QDCs are slightly different in emission energy, because they are slightly different in size. As is mentioned in previous text, there is an asymmetry in the CHP layer that $[1\bar{1}0]$ surface steps are taller than those along [110] direction. This asymmetry is

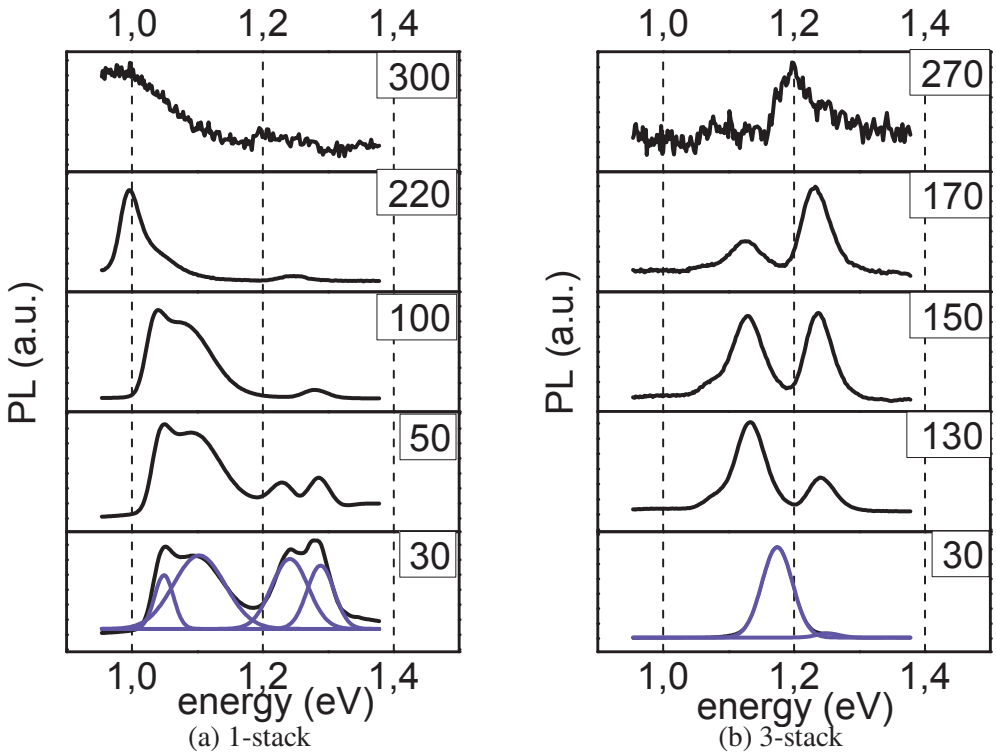

(a) 1-stack (b) 3-stack

Fig. 5.10 Temperature dependence of PL spectrum of 1 and 3 stack QDs. All the curves are rescaled to give a clear view.

transfered to following QDCs stacks during growth. $[1\bar{1}0]$ dots form earlier and are taller than the other direction, thus emit at lower energy.

5.6 Conclusion

MBE-grown InAs QD chains on InGaAs/GaAs CHPs are optically active and rich with luminescent signatures from QD ensembles, CHP template, and multiple wetting layers. The latter have so far evaded detection and can only be observed around areas with relatively high concentrations of C-impurity evidenced from their co-occurrence with the 1.49 eV peak. Based on this observation, we recommend that PL signals should be optimized around a known impurity peak in order to obtain a fuller picture of physics—albeit at the expense of signal strength. When these InAs QD chains are stacked and separated by GaAs spacers, the top-most QDC layer dominates the emissions. The bottom-stack emissions are however missing—an unexpected result from energetic consideration since the bottom-stack QDs are the biggest and thus have the lowest energetic states. The missing emissions are likely due to degraded bottom layer with increasing number of QDC layers and the non-coupling nature of the QDC stacks. Only by increasing excitation power density until the top-most QDC layer is saturated do PL signatures from the bottom layers appear—without state-filling effects in the top-most QDC layer. The extended wave functions of the ES are responsible for enhanced carrier tunnelling from the high-energy top layer to the low-energy bottom layer. This unique evolution of spectral changes with increased excitation power can be used to identify carrier transfer among stacks of dissimilar-sized nanostructures.

Moreover, we observed the temperature dependence of photoluminescence. The emission peaks are characteristic of the various QDs patterns present in the multi stack. Using micro PL mapping, it is possible to resolve the emission peak along the crystallographic orientations and therefore identify the different QDs patterns. A red shift of 120 meV is observed on the $[1\bar{1}0]$ direction peak at 30 K between the 3-stack and 5-stack sample, this is assigned to the lateral coupling between dots.

Chapter 6

Conclusions and perspectives

6.1 The road so far

In this work, we have reviewed the state of the art of silicon heterojunction solar cell and the application of the photoluminescence technique. The PL technique is applied to investigate a-Si:H/c-Si heterojunctions at room temperature as well as a function of temperature in the range of 20 $\sim$ 300 K. Based upon PL techniques, modulated PL is reviewed in detail. Detailed derivations of the principle and the differential nature of this technique are presented. We give an insight into the extraction of the carrier lifetime from experimental and simulation data. Most importantly, a major part is devoted to the temperature dependent lifetime spectroscopy using the MPL technique.

We have illustrated the discrepancy between steady-state lifetime and differential lifetime. The former refers to measurements performed in steady or quasi-steady-state mode, for example QSSPC and QSSPL. The latter refers to the measurements which investigate the changes in conductance or PL induced by a time dependent illumination conditions. We demonstrated that the MPL relates to the differential lifetime.

Considering the nature of the lifetime and the temperature dependence, the most important recombination mechanisms, i.e. radiative, Auger and SRH recombinations are discussed.

MPL is compared to the widely-used QSSPC and photoconductance decay techniques. We have proven that MPL measurements give similar lifetimes as photoconductance decay measurement because they are both time dependent measurements. We also show that the MPL lifetime should be similar to that derived from QSSPC at low level injection, because the SRH steady-state and differential lifetimes are equal at low injection and after the calibration of the carrier concentration.

We also demonstrate the PL and MPL *mapping*. Both of them can characterize the sample homogeneity. Dark regions and defects points are observed on the sample wafer. Although the two mapping techniques produce similar pattern, PL mapping is very dependent on the optical parameter of the sample stage. MPL mapping gives a clear image of the sample regardless of the optical properties of the stage.

With regard to the simulation, we have carried out the simulations of a-Si:H/c-Si junctions (SHJ) with SILVACO ATLAS. Since the carrier concentration differs by orders of magnitude at the interface and in the bulk of the SHJ, the extraction of the carrier lifetime is carefully studied. The carrier concentration at the interface has a large impact on the lifetime determination for very low injection whereas for high injection the impact is negligible.

We have investigated SHJ structures with MPL and found that the defect energy can only be determined under the low injection regime using the SRH model. However the very low defect energy evaluated have no physical meaning and some more investigation on the modelling aspect is still necessary. The MPL measurements are also compared to TRPL measurements as a function of temperature. Their corresponding lifetimes are comparable and follow the same pattern taking into account the temperature variation of the capture cross section. Both decrease when the temperature decreases.

A low energy PL peak is found in the AlOx passivated samples when we investigated the temperature dependent PL. The PL of this peak exhibits quenching as a function of temperature. We have tried four models to fit the PL maximum intensity of the peak as a function of temperature. One model has good agreement with the experimental data but it introduces a very shallow defect energy that is difficult to interpret.

We have also investigated the integrated PL intensity as a function of temperature. From the experimental data we reproduce the radiative recombination coefficient $B(T)$. For $T >$ 77 K our results are in good agreement with the previous work of the literature. However, the most striking advance is that we have extended the range of data down to 20 K and have proposed a fifth order polynomial that fits the experimental data in the whole T range (20 to 300 K).

Numerical simulations have shown that by introducing shallow defects into the bulk or at the interface, it is possible to obtain quite similar temperature dependence of the lifetime as found in the MPL experiments. We have confirmed that using TDLS it is possible to determine the correct energy level from the simulation under the low injection regime. We also considered the phosphorus donor level in the wafer as an SRH recombination center. Although we introduced additional interface defects into the simulation, this does not fully explain the experimentally observed temperature dependence of the MPL lifetime.

Finally, a last part of the thesis was dedicated to the study of the MBE-grown InAs QD chains on InGaAs/GaAs CHPs using the micro-PL technique. When these InAs QD chains are stacked and separated by GaAs spacers, the top-most QDC layer dominates the emissions. The bottom-stack emissions are however missing—an unexpected result from energetic consideration since the bottom-stack QDs are the biggest and thus have the lowest energetic states. The missing emissions are likely due to a degraded bottom layer with increasing number of QDC layers and the non-coupling nature of the QDC stacks. Only by increasing the excitation power density until the top-most QDC layer is saturated do PL signatures from the bottom layers appear—without state-filling effects in the top-most QDC layer. This unique evolution of spectral changes with increased excitation power can be used to identify carrier transfer among stacks of dissimilar-sized nanostructures.

Furthermore we have observed the temperature dependence of photoluminescence. The emission peaks are characteristic of the various QDs patterns present in the multi stack. Using micro PL mapping, it is possible to resolve the emission peak along the crystallographic orientations and therefore identify the different QDs patterns. A red shift of 120 meV is observed on the $[1\bar{1}0]$ direction peak at 30 K between the 3-stack and 5-stack sample, this is assigned to the lateral coupling between dots.

6.2 A look into the future

There are several aspects of this work that should be further investigated:

From the experimental point of view The experimental conditions could be improved.

1. By using a larger laser spot size to obtain a more homogeneous illumination profile, the sample will produce more homogeneous response to the excitation and the incident power density can be determined more precisely.

2. It would be interesting to be able to apply excitation sources of different wavelengths. This would help improving the separation between bulk and interface recombination from the PL measurements. This has been applied recently to discuss the influence of the CdS buffer layer in CIGS solar cells [126].

3. The low level injection measurement is essentially limited by the poor S/N ratio. A more sensitive detector (perhaps PMT) and a redesign of the optics are possible solutions.

4. At present, the MPL mapping takes hours even days to scan a full wafer. This time-consuming mapping has great potential to be improved by a CCD camera, if the camera is fast enough to capture a PL image at double or even higher frequency than the modulation frequency. The possible bottleneck would be high speed data transmission and storage.

From the analysis and simulation point of view Regarding the a-Si:H/c-Si heterojunction, further work is required to better understand several features that were observed in my studies.

1. The origin of the lower energy peak detected at very low temperature for AlOx passivation samples. The occurrence of this peak should be investigated systematically with respect to the deposition parameters.

2. The origin of the low energy and wide peak detected in ion-implanted samples could be further studied with regards to the creation of dislocations and to the possible amorphization of some areas.

3. Most importantly, there is a possibility that the temperature dependence of the MPL lifetime could be explained by models other than SRH recombination through very shallow defects. The cascade recombination [127] leads to temperature dependent capture cross section. Increasing the capture cross sections with decreasing temperature may explain the observed temperature dependence.

4. The overall low temperature dependence with the shoulder or protrusion in the MPL lifetime requires special attentions.

5. The TDLS analysis has not been combined with the injection dependent lifetime spectroscopy (IDLS) analysis, essentially because of the uncertainty over the carrier concentration. The aforementioned proposed improvements of the excitation and the detection would make the combination of the two analyses possible.

6. In this work, the temperature dependent simulation is limited to discrete defect levels. The next step would be to consider a distribution of defect levels in the bandgap at the SHJ interface. Uniform, Gaussian, and band tail profiles of defect should be investigated. In particular, it should be investigated to what extent the exponential band tails may lead to small apparent activation energies as experimentally observed.

References

[1] *Smog persists in Beijing turning it into one of the dirtiest city worldwide.* Jan. 25, 2013. URL: http://beijing.tianqi.com/news/11234.html.

[2] National Renewable Energy Laboratory. *2013 Renewable Energy Data Book*. National Renewable Energy Laboratory, 2014.

[3] *Photovoltaics Report*. Fraunhofer Institute for Solar Energy Systems, Mar. 11, 2016.

[4] Tatsuo Saga. "Advances in crystalline silicon solar cell technology for industrial mass production". In: *NPG Asia Materials* 2.3 (July 22, 2010), pp. 96–102. ISSN: 1884-4049. DOI: 10.1038/asiamat.2010.82.

[5] Andrew W. Blakers, Aihua Wang, Adele M. Milne, Jianhua Zhao, and Martin A. Green. "22.8% efficient silicon solar cell". In: *Applied Physics Letters* 55.13 (Sept. 25, 1989), pp. 1363–1365. ISSN: 0003-6951, 1077-3118. DOI: 10.1063/1.101596.

[6] J. Zhao, A. Wang, and M.A. Green. "24% efficient PERL structure silicon solar cells". In: *, Conference Record of the Twenty First IEEE Photovoltaic Specialists Conference, 1990.* , Conference Record of the Twenty First IEEE Photovoltaic Specialists Conference, 1990. May 1990, 333–335 vol.1. DOI: 10.1109/PVSC.1990.111642.

[7] Jianhua Zhao, Aihua Wang, and Martin A. Green. "24.5% efficiency PERT silicon solar cells on SEH MCZ substrates and cell performance on other SEH CZ and FZ substrates". In: *Solar Energy Materials and Solar Cells*. PVSEC 11 - Part II 66.1–4 (Feb. 2001), pp. 27–36. ISSN: 0927-0248. DOI: 10.1016/S0927-0248(00)00155-0.

[8] *How To Push Conventional 2-Sided Contacted Solar Cells To The Max*. URL: http://www.photonicsonline.com/doc/how-to-push-conventional-sided-contacted-solar-cells-to-the-max-0001.

[9] Frank Feldmann, Martin Bivour, Christian Reichel, Martin Hermle, and Stefan W. Glunz. "Passivated rear contacts for high-efficiency n-type Si solar cells providing high interface passivation quality and excellent transport characteristics". In: *Solar Energy Materials and Solar Cells* 120, Part A (Jan. 2014), pp. 270–274. ISSN: 0927-0248. DOI: 10.1016/j.solmat.2013.09.017.

[10] Stefaan De Wolf and B. Demaurex. *a-Si/c-Si Heterojunction Solar Cells | PV-LAB*. a-Si/c-Si Heterojunction Solar Cells. URL: http://pvlab.epfl.ch/heterojunction_solar_cells.

[11] Yoshihiro Hamakawa, Kouha Fujimoto, Kouji Okuda, Yoshio Kashima, Shuichi Nonomura, and Hiroaki Okamoto. "New types of high efficiency solar cells based on a-Si". In: *Applied Physics Letters* 43.7 (Oct. 1, 1983), pp. 644–646. ISSN: 0003-6951, 1077-3118. DOI: 10.1063/1.94462.

[12] Koji Okuda, Hiroaki Okamoto, and Yoshihiro Hamakawa. "Amorphous Si / Polycrystalline Si Stacked Solar Cell Having More Than 12% Conversion Efficiency". In: *Japanese Journal of Applied Physics* 22.9A (Sept. 1, 1983), p. L605. ISSN: 1347-4065. DOI: 10.1143/JJAP.22.L605.

[13] K. Wakisaka et al. "More than 16% solar cells with a new 'HIT' (doped a-Si/nondoped a-Si/crystalline Si) structure". In: *, Conference Record of the Twenty Second IEEE Photovoltaic Specialists Conference, 1991.* , Conference Record of the Twenty Second IEEE Photovoltaic Specialists Conference, 1991. Oct. 1991, 887–892 vol.2. DOI: 10.1109/PVSC.1991.169337.

[14] *Panasonic HIT(R) Solar Cell Achieves World's Highest Energy Conversion Efficiency of 25.6% at Research Level | Headquarters News | Panasonic Newsroom Global*. URL: http://news.panasonic.com/press/news/official.data/data.dir/2014/04/en140410-4/en140410-4.html.

[15] M. Taguchi, A. Yano, S. Tohoda, K. Matsuyama, Y. Nakamura, T. Nishiwaki, K. Fujita, and E. Maruyama. "24.7 Record Efficiency HIT Solar Cell on Thin Silicon Wafer". In: *IEEE Journal of Photovoltaics* 4.1 (Jan. 2014), pp. 96–99. ISSN: 2156-3381. DOI: 10.1109/JPHOTOV.2013.2282737.

[16] K. Masuko et al. "Achievement of More Than 25 % Conversion Efficiency With Crystalline Silicon Heterojunction Solar Cell". In: *IEEE Journal of Photovoltaics* 4.6 (Nov. 2014), pp. 1433–1435. ISSN: 2156-3381. DOI: 10.1109/JPHOTOV.2014.2352151.

[17] Ming Xu. "Temperature dependent photoluminescence in silicon based heterojunction solar cell". Amsterdam, Netherlands. 2014.

[18] R. Grigorovici, N. Croitoru, Marina M., and Nastase L. "Heterojunctions between amorphous Si and Si single crystals". In: *Rev. Roum. Phys.* 13 (1968), pp. 317–325.

[19] R. C. Chittick, J. H. Alexander, and H. F. Sterling. "The Preparation and Properties of Amorphous Silicon". In: *Journal of The Electrochemical Society* 116.1 (Jan. 1, 1969), pp. 77–81. ISSN: 0013-4651, 1945-7111. DOI: 10.1149/1.2411779.

[20] M. H. Brodsky, Manuel Cardona, and J. J. Cuomo. "Infrared and Raman spectra of the silicon-hydrogen bonds in amorphous silicon prepared by glow discharge and sputtering". In: *Physical Review B* 16.8 (Oct. 15, 1977), pp. 3556–3571. DOI: 10.1103/PhysRevB.16.3556.

[21] J. I. Pankove and M. L. Tarng. "Amorphous silicon as a passivant for crystalline silicon". In: *Applied Physics Letters* 34.2 (Jan. 15, 1979), pp. 156–157. ISSN: 0003-6951, 1077-3118. DOI: 10.1063/1.90711.

[22] M. Stutzmann, D. K. Biegelsen, and R. A. Street. "Detailed investigation of doping in hydrogenated amorphous silicon and germanium". In: *Physical Review B* 35.11 (Apr. 15, 1987), pp. 5666–5701. DOI: 10.1103/PhysRevB.35.5666.

[23] B. E. Pieters. “Characterization of thin-film silicon materials and solar cells through numerical modeling”. Dissertation. TU Delft, Delft University of Technology, Nov. 11, 2008. URL: http://repository.tudelft.nl/view/ir/uuid%3A83bc5ff4-8e33-4962-9014-68cfbad8226f/.

[24] M. J. Powell and S. C. Deane. “Improved defect-pool model for charged defects in amorphous silicon”. In: *Physical Review B* 48.15 (Oct. 15, 1993), pp. 10815–10827. DOI: 10.1103/PhysRevB.48.10815.

[25] M. J. Powell and S. C. Deane. “Defect-pool model and the hydrogen density of states in hydrogenated amorphous silicon”. In: *Physical Review B* 53.15 (Apr. 15, 1996), pp. 10121–10132. DOI: 10.1103/PhysRevB.53.10121.

[26] David Reaux, José Alvarez, Marie-Estelle Gueunier-Farret, and Jean-Paul Kleider. “Impact of Defect-pool Model Parameters on the Lifetime in c-Si/a-Si:H Heterojunction Solar Cells”. In: *Energy Procedia*. 5th International Conference on Silicon Photovoltaics, SiliconPV 2015 77 (Aug. 2015), pp. 153–158. ISSN: 1876-6102. DOI: 10.1016/j.egypro.2015.07.023.

[27] Delfina Muñoz. “HIGH EFFICIENCY REAR CONTACT SOLAR CELLS AND ULTRA POWERFUL MODULES”. 5th Silicon PV – HERCULES project Workshop. Konstanz, Mar. 26, 2015.

[28] *Blackbody Radiation*. URL: http://hyperphysics.phy-astr.gsu.edu/hbase/bbrc.html.

[29] Bernard Valeur and Mário N. Berberan-Santos. “A Brief History of Fluorescence and Phosphorescence before the Emergence of Quantum Theory”. In: *Journal of Chemical Education* 88.6 (2011), pp. 731–738. ISSN: 0021-9584. DOI: 10.1021/ed100182h.

[30] Gordon Lasher and Frank Stern. “Spontaneous and Stimulated Recombination Radiation in Semiconductors”. In: *Physical Review* 133.2A (Jan. 20, 1964), A553–A563. DOI: 10.1103/PhysRev.133.A553.

[31] P. T. Landsberg and G. Tonge. “Thermodynamic energy conversion efficiencies”. In: *Journal of Applied Physics* 51.7 (July 1, 1980), R1–R20. ISSN: 0021-8979, 1089-7550. DOI: 10.1063/1.328187.

[32] P. Würfel. “The chemical potential of radiation”. In: *Journal of Physics C: Solid State Physics* 15.18 (1982), p. 3967. URL: http://iopscience.iop.org/0022-3719/15/18/012.

[33] P. Würfel, S. Finkbeiner, and E. Daub. “Generalized Planck’s radiation law for luminescence via indirect transitions”. In: *Applied Physics A* 60.1 (1995), pp. 67–70. URL: http://link.springer.com/article/10.1007/BF01577615.

[34] *Carrier recombination and generation*. URL: http://ecee.colorado.edu/~bart/book/book/chapter2/ch2_8.htm.

[35] R.A. Street. “Luminescence and recombination in hydrogenated amorphous silicon”. In: *Advances in Physics* 30.5 (Oct. 1, 1981), pp. 593–676. ISSN: 0001-8732. DOI: 10.1080/00018738100101417.

[36] D. J. Dunstan and F. Boulitrop. “Photoluminescence in hydrogenated amorphous silicon”. In: *Physical Review B* 30.10 (Nov. 15, 1984), pp. 5945–5957. DOI: 10.1103/PhysRevB.30.5945.

[37] P. McL Colley and E. C. Lightowlers. “Calibration of the photoluminescence technique for measuring B, P and Al concentrations in Si in the range 10^{12} to 10^{15} cm^{-3} using Fourier transform spectroscopy”. In: *Semiconductor Science and Technology* 2.3 (Mar. 1, 1987), p. 157. ISSN: 0268-1242. DOI: 10.1088/0268-1242/2/3/005.

[38] R. K. Ahrenkiel. “Measurement of minority-carrier lifetime by time-resolved photoluminescence”. In: *Solid-State Electronics* 35.3 (Mar. 1992), pp. 239–250. ISSN: 0038-1101. DOI: 10.1016/0038-1101(92)90228-5.

[39] V. Alex, S. Finkbeiner, and J. Weber. “Temperature dependence of the indirect energy gap in crystalline silicon”. In: *Journal of Applied Physics* 79.9 (May 1, 1996), pp. 6943–6946. ISSN: 0021-8979, 1089-7550. DOI: 10.1063/1.362447.

[40] T. Trupke, R.A. Bardos, F. Hudert, P. Würfel, A. Wang, J. Zhao, and M.A. Green. “Effective excess carrier lifetimes exceeding 100ms in float zone silicon determined from photoluminescence”. In: *19h European Photovoltaic Solar Energy Conference*. June 2004, pp. 758–761.

[41] T. Trupke, R. A. Bardos, and M. D. Abbott. “Self-consistent calibration of photoluminescence and photoconductance lifetime measurements”. In: *Applied Physics Letters* 87.18 (2005), p. 184102. ISSN: 00036951. DOI: 10.1063/1.2119411.

[42] R. A. Bardos and T. Trupke. “Self-consistent determination of the generation rate in photoluminescence and photoconductance lifetime measurements”. In: *Photovoltaic Specialists Conference, 2005. Conference Record of the Thirty-first IEEE*. IEEE, 2005, pp. 899–902. URL: http://ieeexplore.ieee.org/xpls/abs_all.jsp?arnumber=1488276.

[43] T. Trupke and R.A. Bardos. “Photoluminescence: a surprisingly sensitive lifetime technique”. In: *Conference Record of the Thirty-first IEEE Photovoltaic Specialists Conference, 2005*. Conference Record of the Thirty-first IEEE Photovoltaic Specialists Conference, 2005. Jan. 2005, pp. 903–906. DOI: 10.1109/PVSC.2005.1488277.

[44] T. Trupke, R. A. Bardos, M. C. Schubert, and W. Warta. “Photoluminescence imaging of silicon wafers”. In: *Applied Physics Letters* 89.4 (July 24, 2006), p. 044107. ISSN: 0003-6951, 1077-3118. DOI: 10.1063/1.2234747.

[45] Guillaume Courtois. “Material and device characterisation through luminescence studies on crystalline and amorphous silicon based devices”. Dec. 20, 2013.

[46] Saioa Tardon. “Quantitative photoluminescence studies in a-Si: H/c-Si solar cells”. Universität Oldenburg, 2007. URL: http://oops.uni-oldenburg.de/54/.

[47] D. Baek, S. Rouvimov, B. Kim, T.-C. Jo, and D. K. Schroder. “Surface recombination velocity of silicon wafers by photoluminescence”. In: *Applied Physics Letters* 86.11 (Mar. 14, 2005), p. 112110. ISSN: 0003-6951, 1077-3118. DOI: 10.1063/1.1884258.

[48] R. Brüggemann. “Kirchhoff’s generalised law applied to amorphous silicon/crystalline silicon heterostructures”. In: *Philosophical Magazine* 89.28-30 (Oct. 1, 2009), pp. 2519–2529. ISSN: 1478-6435. DOI: 10 . 1080 / 14786430903074805.

[49] R. Brüggemann and S. Reynolds. “Modulated photoluminescence studies for lifetime determination in amorphous-silicon passivated crystalline-silicon wafers”. In: *Journal of Non-Crystalline Solids* 352.9-20 (June 2006), pp. 1888–1891. ISSN: 00223093. DOI: 10.1016/j.jnoncrysol.2005.11.092.

[50] S. Tardon and R. Brüggemann. “Characterization of the interface properties in a-Si : H/c-Si heterostructures by photoluminescence”. In: *Journal of Physics D: Applied Physics* 43.11 (Mar. 24, 2010), p. 115102. ISSN: 0022-3727. DOI: 10.1088/0022-3727/43/11/115102.

[51] T. Trupke, B. Mitchell, J. W. Weber, W. McMillan, R. A. Bardos, and R. Kroeze. “Photoluminescence Imaging for Photovoltaic Applications”. In: *Energy Procedia*. International Conference on Materials for Advanced Technologies 2011, Symposium O 15 (2012), pp. 135–146. ISSN: 1876-6102. DOI: 10.1016/j.egypro.2012.02.016.

[52] Guillaume Courtois, Parsathi Chatterjee, Veinardi Suendo, Antoine Salomon, and Pere Roca i Cabarrocas. “Investigation of silicon heterojunction solar cells by photoluminescence under DC-bias”. In: *EPJ Photovoltaics* 4 (Sept. 27, 2013), p. 45106. ISSN: 2105-0716. DOI: 10.1051/epjpv/2013022.

[53] Sandra Herlufsen, David Hinken, Matthias Offer, Jan Schmidt, and Karsten Bothe. “Validity of Calibrated Photoluminescence Lifetime Measurements of Crystalline Silicon Wafers for Arbitrary Lifetime and Injection Ranges”. In: *IEEE Journal of Photovoltaics* 3.1 (Jan. 2013), pp. 381–386. ISSN: 2156-3381, 2156-3403. DOI: 10.1109/JPHOTOV.2012.2218794.

[54] David Kiliani, Axel Herguth, Gabriel Micard, Jan Ebser, and Giso Hahn. “Time-resolved photoluminescence imaging with electronic shuttering using an image intensifier unit”. In: *Solar Energy Materials and Solar Cells*. SiliconPV 106 (Nov. 2012), pp. 55–59. ISSN: 0927-0248. DOI: 10.1016/j.solmat.2012.05.042.

[55] J. Schmidt. “Measurement of differential and actual recombination parameters on crystalline silicon wafers”. In: *IEEE Transactions on Electron Devices* 46.10 (Oct. 1999), pp. 2018–2025. ISSN: 0018-9383. DOI: 10.1109/16.791991.

[56] B. Halliop, M.F. Salaun, W. Favre, R. Varache, M.E. Gueunier-Farret, J.P. Kleider, and N.P. Kherani. “Interface properties of amorphous-crystalline silicon heterojunctions prepared using DC saddle-field PECVD”. In: *Journal of Non-Crystalline Solids* 358.17 (Sept. 2012), pp. 2227–2231. ISSN: 00223093. DOI: 10.1016/j.jnoncrysol.2012.01.048.

[57] T. Trupke, M. A. Green, P. Würfel, P. P. Altermatt, A. Wang, J. Zhao, and R. Corkish. “Temperature dependence of the radiative recombination coefficient of intrinsic crystalline silicon”. In: *Journal of Applied Physics* 94.8 (2003), p. 4930. ISSN: 00218979. DOI: 10.1063/1.1610231.

[58] Hieu T. Nguyen, Simeon C. Baker-Finch, and Daniel Macdonald. “Temperature dependence of the radiative recombination coefficient in crystalline silicon from spectral photoluminescence”. In: *Applied Physics Letters* 104.11 (Mar. 17, 2014), p. 112105. ISSN: 0003-6951, 1077-3118. DOI: 10.1063/1.4869295.

[59] S. Rein, T. Rehrl, W. Warta, and S. W. Glunz. “Lifetime spectroscopy for defect characterization: Systematic analysis of the possibilities and restrictions”. In: *Journal of Applied Physics* 91.4 (Feb. 15, 2002), pp. 2059–2070. ISSN: 0021-8979, 1089-7550. DOI: 10.1063/1.1428095.

[60] R. Brüggemann, M. Rösch, S. Tardon, and G.h. Bauer. "Application of SC-Simul for Numerical Modeling of the Opto-Electronic Properties of Heterojunction Diodes". In: *Symposium A – Amorphous and Nanocrystalline Silicon Science and Technology–2005*. Vol. 862. MRS Online Proceedings Library Archive. 2005. DOI: 10.1557/PROC-862-A9.3.

[61] Ronald A. Sinton, A. Cuevas, and Michael Stuckings. "Quasi-steady-state photoconductance, a new method for solar cell material and device characterization". In: *, Conference Record of the Twenty Fifth IEEE Photovoltaic Specialists Conference, 1996*. , Conference Record of the Twenty Fifth IEEE Photovoltaic Specialists Conference, 1996. May 1996, pp. 457–460. DOI: 10.1109/PVSC.1996.564042.

[62] Henning Nagel, Christopher Berge, and Armin G. Aberle. "Generalized analysis of quasi-steady-state and quasi-transient measurements of carrier lifetimes in semiconductors". In: *Journal of Applied Physics* 86.11 (Dec. 1, 1999), pp. 6218–6221. ISSN: 0021-8979, 1089-7550. DOI: 10.1063/1.371633.

[63] Ming Xu. "Temperature dependent photoluminescence and micro-mapping of multiple stacks InAs quantum dots". INTERNATIONAL WORKSHOP ON ON NANOSTRUCTURES CHARACTERIZATION AND NANOMATERIALS. Bangkok, Thailand, Aug. 2015.

[64] Heinz W. Siesler, ed. *Infrared and Raman Spectroscopic Imaging*. 2 edition. Wiley-VCH, Aug. 7, 2014. 464 pp.

[65] K. Lauer, A. Laades, H. Übensee, H. Metzner, and A. Lawerenz. "Detailed analysis of the microwave-detected photoconductance decay in crystalline silicon". In: *Journal of Applied Physics* 104.10 (Nov. 15, 2008), p. 104503. ISSN: 0021-8979, 1089-7550. DOI: 10.1063/1.3021459.

[66] WITec. *CONFOCAL MICROSCOPY, Alpha300 User Manual*.

[67] Peter T. Landsberg. "The band-band Auger effect in semiconductors". In: *Solid-State Electronics* 30.11 (Nov. 1987), pp. 1107–1115. ISSN: 0038-1101. DOI: 10.1016/0038-1101(87)90074-8.

[68] J. Dziewior and W. Schmid. "Auger coefficients for highly doped and highly excited silicon". In: *Applied Physics Letters* 31.5 (Sept. 1, 1977), pp. 346–348. ISSN: 0003-6951, 1077-3118. DOI: 10.1063/1.89694.

[69] Mark J. Kerr and Andres Cuevas. "General parameterization of Auger recombination in crystalline silicon". In: *Journal of Applied Physics* 91.4 (Feb. 15, 2002), pp. 2473–2480. ISSN: 0021-8979, 1089-7550. DOI: 10.1063/1.1432476.

[70] A. Richter, F. Werner, A. Cuevas, J. Schmidt, and S. W. Glunz. "Improved Parameterization of Auger Recombination in Silicon". In: *Energy Procedia*. Proceedings of the 2nd International Conference on Crystalline Silicon Photovoltaics SiliconPV 2012 27 (2012), pp. 88–94. ISSN: 1876-6102. DOI: 10.1016/j.egypro.2012.07.034.

[71] Armin Richter, Stefan W. Glunz, Florian Werner, Jan Schmidt, and Andres Cuevas. "Improved quantitative description of Auger recombination in crystalline silicon". In: *Physical Review B* 86.16 (Oct. 9, 2012), p. 165202. DOI: 10.1103/PhysRevB.86.165202.

[72] D. B. M. Klaassen. “A unified mobility model for device simulation—II. Temperature dependence of carrier mobility and lifetime”. In: *Solid-State Electronics* 35.7 (1992), pp. 961–967. URL: http://www.sciencedirect.com/science/article/pii/0038110192903268.

[73] M. Garín, I. Martín, S. Bermejo, and R. Alcubilla. “Fixed charge density in dielectrics deposited on c-Si using space charge region dominated lifetime measurements”. In: *Journal of Applied Physics* 101.12 (June 15, 2007), p. 123716. ISSN: 0021-8979, 1089-7550. DOI: 10.1063/1.2748355.

[74] *Princeton Instruments - PI-MAX 4 ICCD Camera*. URL: http://www.princetoninstruments.com/products/imcam/pimax/.

[75] Martin A. Green. “Self-consistent optical parameters of intrinsic silicon at 300 K including temperature coefficients”. In: *Solar Energy Materials and Solar Cells* 92.11 (Nov. 2008), pp. 1305–1310. ISSN: 0927-0248. DOI: 10.1016/j.solmat.2008.06.009.

[76] G. G. Macfarlane, T. P. McLean, J. E. Quarrington, and V. Roberts. “Fine structure in the absorption-edge spectrum of Si”. In: *Physical Review* 111.5 (1958), p. 1245. URL: http://prola.aps.org/abstract/PR/v111/i5/p1245_1.

[77] Jacques I. Pankove. *Optical Processes in Semiconductors*. Courier Corporation, Dec. 19, 2012. 454 pp. ISBN: 978-0-486-13870-1.

[78] Jüri Krustok, Heikki Collan, and Kari Hjelt. “Does the low-temperature Arrhenius plot of the photoluminescence intensity in CdTe point towards an erroneous activation energy?” In: *Journal of Applied Physics* 81.3 (Feb. 1, 1997), pp. 1442–1445. ISSN: 0021-8979, 1089-7550. DOI: 10.1063/1.363903.

[79] T. Arguirov, S. Ostapenko, M. J. Romero, W. Warta, M. The, P. Gundel, and M. C. Schubert. “Spatially Resolved Luminescence Spectroscopy on Multicrystalline Silicon”. In: *23rd European Photovoltaic Solar Energy Conference and Exhibition, 1-5 September 2008, Valencia, Spain* (Nov. 1, 2008), pp. 17–23. DOI: 10.4229/23rdEUPVSEC2008-1AP.1.5.

[80] M. Suezawa, Y. Sasaki, and K. Sumino. “Dependence of Photoluminescence on Temperature in Dislocated Silicon Crystals”. In: *physica status solidi (a)* 79.1 (Sept. 16, 1983), pp. 173–181. ISSN: 1521-396X. DOI: 10.1002/pssa.2210790119.

[81] J. Krustok, A. Jagomägi, M. Grossberg, J. Raudoja, and M. Danilson. “Photoluminescence properties of polycrystalline AgGaTe2”. In: *Solar Energy Materials and Solar Cells* 90.13 (Aug. 15, 2006), pp. 1973–1982. ISSN: 0927-0248. DOI: 10.1016/j.solmat.2006.02.003.

[82] Robert F. Pierret. *Advanced Semiconductor Fundamentals*. Prentice Hall, 2003. 221 pp. ISBN: 978-0-13-061792-7.

[83] Simon M. Sze and Kwok K. Ng. *Physics of Semiconductor Devices*. John Wiley & Sons, Nov. 3, 2006. 828 pp. ISBN: 978-0-470-06830-4.

[84] Z. R. Wasilewski, S. Fafard, and J. P. McCaffrey. “Size and shape engineering of vertically stacked self-assembled quantum dots”. In: *Journal of Crystal Growth* 201–202 (May 1999), pp. 1131–1135. ISSN: 0022-0248. DOI: 10.1016/S0022-0248(98)01539-5.

[85] Tomoya Inoue, Masaki Asada, Nami Yasuoka, Osamu Kojima, Takashi Kita, and Osamu Wada. "Polarization control of electroluminescence from vertically stacked InAs/GaAs quantum dots". In: *Applied Physics Letters* 96.21 (May 24, 2010), p. 211906. ISSN: 0003-6951, 1077-3118. DOI: 10.1063/1.3441403.

[86] G. S. Solomon, J. A. Trezza, A. F. Marshall, and Jr. Harris J. S. "Vertically Aligned and Electronically Coupled Growth Induced InAs Islands in GaAs". In: *Physical Review Letters* 76.6 (Feb. 5, 1996), pp. 952–955. DOI: 10.1103/PhysRevLett.76.952.

[87] S. Cortez et al. "Optically Driven Spin Memory in n-Doped InAs-GaAs Quantum Dots". In: *Physical Review Letters* 89.20 (Oct. 28, 2002), p. 207401. DOI: 10.1103/PhysRevLett.89.207401.

[88] Y. Arakawa and H. Sakaki. "Multidimensional quantum well laser and temperature dependence of its threshold current". In: *Applied Physics Letters* 40.11 (June 1, 1982), pp. 939–941. ISSN: 0003-6951, 1077-3118. DOI: 10.1063/1.92959.

[89] Antonio Luque and Antonio Martí. "Increasing the Efficiency of Ideal Solar Cells by Photon Induced Transitions at Intermediate Levels". In: *Physical Review Letters* 78.26 (June 30, 1997), pp. 5014–5017. DOI: 10.1103/PhysRevLett.78.5014.

[90] A. J. Nozik, M. C. Beard, J. M. Luther, M. Law, R. J. Ellingson, and J. C. Johnson. "Semiconductor Quantum Dots and Quantum Dot Arrays and Applications of Multiple Exciton Generation to Third-Generation Photovoltaic Solar Cells". In: *Chemical Reviews* 110.11 (Nov. 10, 2010), pp. 6873–6890. ISSN: 0009-2665. DOI: 10.1021/cr900289f.

[91] Nirat Patanasemakul, Somsak Panyakeow, and Songphol Kanjanachuchai. "Chirped InGaAs quantum dot molecules for broadband applications". In: *Nanoscale Research Letters* 7.1 (Apr. 6, 2012), p. 207. ISSN: 1556-276X. DOI: 10.1186/1556-276X-7-207. pmid: 22480323.

[92] E. C. Le Ru, P. Howe, T. S. Jones, and R. Murray. "Strain-engineered InAs/GaAs quantum dots for long-wavelength emission". In: *Physical Review B* 67.16 (Apr. 3, 2003), p. 165303. DOI: 10.1103/PhysRevB.67.165303.

[93] P. B. Joyce, E. C. Le Ru, T. J. Krzyzewski, G. R. Bell, R. Murray, and T. S. Jones. "Optical properties of bilayer InAs/GaAs quantum dot structures: Influence of strain and surface morphology". In: *Physical Review B* 66.7 (Aug. 7, 2002), p. 075316. DOI: 10.1103/PhysRevB.66.075316.

[94] T. Heitz, B. Drévillon, C. Godet, and J. E. Bourée. "Quantitative study of C-H bonding in polymerlike amorphous carbon films using in situ infrared ellipsometry". In: *Physical Review B* 58.20 (Nov. 15, 1998), pp. 13957–13973. DOI: 10.1103/PhysRevB.58.13957.

[95] Yu I. Mazur et al. "Tunneling-barrier controlled excitation transfer in hybrid quantum dot-quantum well nanostructures". In: *Journal of Applied Physics* 108.7 (Oct. 1, 2010), p. 074316. ISSN: 0021-8979, 1089-7550. DOI: 10.1063/1.3493240.

[96] T. Limwongse, S. Panyakeow, and S. Kanjanachuchai. "Evolution of InAs quantum dots grown on cross-hatch substrates". In: *physica status solidi (c)* 6.4 (Apr. 1, 2009), pp. 806–809. ISSN: 1610-1642. DOI: 10.1002/pssc.200880620.

[97] Oliver Schmidt. *Lateral Alignment of Epitaxial Quantum Dots*. 2007 edition. Berlin ; London: Springer, Sept. 14, 2007. 707 pp. ISBN: 978-3-540-46935-3.

[98] Vas P. Kunets, M. Rebello Sousa Dias, T. Rembert, M. E. Ware, Yu I. Mazur, V. Lopez-Richard, H. A. Mantooth, G. E. Marques, and G. J. Salamo. "Electron transport in quantum dot chains: Dimensionality effects and hopping conductance". In: *Journal of Applied Physics* 113.18 (May 14, 2013), p. 183709. ISSN: 0021-8979, 1089-7550. DOI: 10.1063/1.4804324.

[99] Yu I. Mazur, V. G. Dorogan, M. E. Ware, E. Marega Jr, P. M. Lytvyn, Z. Ya Zhuchenko, G. G. Tarasov, and G. J. Salamo. "Effect of dimensionality and morphology on polarized photoluminescence in quantum dot-chain structures". In: *Journal of Applied Physics* 112.8 (Oct. 15, 2012), p. 084314. ISSN: 0021-8979, 1089-7550. DOI: 10.1063/1.4759318.

[100] T. Chokamnuai, P. Rattanadon, S. Thainoi, S. Panyakeow, and S. Kanjanachuchai. "Polarization anisotropy of stacked InAs quantum dots on InGaAs/GaAs cross-hatch patterns". In: *Journal of Crystal Growth*. The 17th International Conference on Molecular Beam Epitaxy 378 (Sept. 1, 2013), pp. 524–528. ISSN: 0022-0248. DOI: 10.1016/j.jcrysgro.2012.12.092.

[101] J. -Y. Marzin, J. -M. Gérard, A. Izraël, D. Barrier, and G. Bastard. "Photoluminescence of Single InAs Quantum Dots Obtained by Self-Organized Growth on GaAs". In: *Physical Review Letters* 73.5 (Aug. 1, 1994), pp. 716–719. DOI: 10.1103/PhysRevLett.73.716.

[102] Luca Seravalli, Giovanna Trevisi, and Paola Frigeri. "Design and growth of metamorphic InAs/InGaAs quantum dots for single photon emission in the telecom window". In: *CrystEngComm* 14.20 (Sept. 17, 2012), pp. 6833–6838. ISSN: 1466-8033. DOI: 10.1039/C2CE25860A.

[103] N. Thongkamkoon, N. Patanasemakul, N. Siripitakchai, S. Thainoi, S. Panyakeow, and S. Kanjanachuchai. "Bimodal optical characteristics of lateral InGaAs quantum dot molecules". In: *Journal of Crystal Growth*. Proceedings of the 16th International Conference on Molecular Beam Epitaxy (ICMBE) 323.1 (May 15, 2011), pp. 206–210. ISSN: 0022-0248. DOI: 10.1016/j.jcrysgro.2010.11.104.

[104] S. J Lee, S. K Noh, J. W Choe, and E. K Kim. "Evolution of bimodal size-distribution on InAs coverage variation in as-grown InAs/GaAs quantum-dot heterostructures". In: *Journal of Crystal Growth* 267.3–4 (July 1, 2004), pp. 405–411. ISSN: 0022-0248. DOI: 10.1016/j.jcrysgro.2004.04.014.

[105] Hao Lee, Roger Lowe-Webb, Thomas J. Johnson, Weidong Yang, and Peter C. Sercel. "Photoluminescence study of in situ annealed InAs quantum dots: Double-peak emission associated with bimodal size distribution". In: *Applied Physics Letters* 73.24 (Dec. 14, 1998), pp. 3556–3558. ISSN: 0003-6951, 1077-3118. DOI: 10.1063/1.122805.

[106] Chalermchai Himwas, Somsak Panyakeow, and Songphol Kanjanachuchai. "Optical properties of as-grown and annealed InAs quantum dots on InGaAs cross-hatch patterns". In: *Nanoscale Research Letters* 6.1 (Aug. 17, 2011), pp. 1–7. ISSN: 1931-7573, 1556-276X. DOI: 10.1186/1556-276X-6-496.

[107] C. L. Zhang, Z. G. Wang, F. A. Zhao, B. Xu, and P. Jin. "Ordering growth of InAs quantum dots on ultra-thin InGaAs strained layer". In: *Journal of Crystal Growth* 265.1–2 (Apr. 15, 2004), pp. 60–64. ISSN: 0022-0248. DOI: 10.1016/j.jcrysgro.2004.01.039.

[108] Qianghua Xie, Anupam Madhukar, Ping Chen, and Nobuhiko P. Kobayashi. "Vertically Self-Organized InAs Quantum Box Islands on GaAs(100)". In: *Physical Review Letters* 75.13 (Sept. 25, 1995), pp. 2542–2545. DOI: 10.1103/PhysRevLett.75.2542.

[109] A. M. Andrews, R. LeSar, M. A. Kerner, J. S. Speck, A. E. Romanov, A. L. Kolesnikova, M. Bobeth, and W. Pompe. "Modeling crosshatch surface morphology in growing mismatched layers. Part II: Periodic boundary conditions and dislocation groups". In: *Journal of Applied Physics* 95.11 (June 1, 2004), pp. 6032–6047. ISSN: 0021-8979, 1089-7550. DOI: 10.1063/1.1707208.

[110] Dong Pan, Jian Xu, Elias Towe, Qin Xu, and J. W. Hsu. "Self-organization of (In,Ga)As / GaAs quantum dots on relaxed (In,Ga)As films". In: *Applied Physics Letters* 73.15 (Oct. 12, 1998), pp. 2164–2166. ISSN: 0003-6951, 1077-3118. DOI: 10.1063/1.122410.

[111] Songphol Kanjanachuchai and Teeravat Limwongse. "Nucleation Sequence of InAs Quantum Dots on Cross-Hatch Patterns". In: *Journal of Nanoscience and Nanotechnology* 11.12 (Dec. 1, 2011), pp. 10787–10791. DOI: 10.1166/jnn.2011.3976.

[112] H. Welsch, T. Kipp, T. Köppen, Ch Heyn, and W. Hansen. "Spatially and energetically resolved optical mapping of self-aligned InAs quantum dots". In: *Semiconductor Science and Technology* 23.4 (2008), p. 045016. ISSN: 0268-1242. DOI: 10.1088/0268-1242/23/4/045016.

[113] Xiaoyong Wang, Zhiming M. Wang, Baolai Liang, Gregory J. Salamo, and Chih-Kang Shih. "Direct Spectroscopic Evidence for the Formation of One-Dimensional Wetting Wires During the Growth of InGaAs/GaAs Quantum Dot Chains". In: *Nano Letters* 6.9 (Sept. 1, 2006), pp. 1847–1851. ISSN: 1530-6984. DOI: 10.1021/nl060271t.

[114] Tao Yang, Jun Tatebayashi, Kanna Aoki, Masao Nishioka, and Yasuhiko Arakawa. "Effects of rapid thermal annealing on the emission properties of highly uniform self-assembled InAs/GaAs quantum dots emitting at 1.3μm". In: *Applied Physics Letters* 90.11 (Mar. 12, 2007), p. 111912. ISSN: 0003-6951, 1077-3118. DOI: 10.1063/1.2713135.

[115] Kouichi Akahane and Naokatsu Yamamoto. "Wide-band emissions from highly stacked quantum dot structure grown using the strain-compensation technique". In: *Journal of Crystal Growth*. Proceedings of the 16th International Conference on Molecular Beam Epitaxy (ICMBE) 323.1 (May 15, 2011), pp. 154–157. ISSN: 0022-0248. DOI: 10.1016/j.jcrysgro.2010.12.037.

[116] K. Laouthaiwattana, O. Tangmattajittakul, S. Suraprapapich, S. Thainoi, P. Changmuang, S. Kanjanachuchai, S. Ratanathamaphan, and S. Panyakeow. "Optimization of stacking high-density quantum dot molecules for photovoltaic effect". In: *Solar Energy Materials and Solar Cells*. 17th International Photovoltaic Science and Engineering Conference 93.6–7 (June 2009), pp. 746–749. ISSN: 0927-0248. DOI: 10.1016/j.solmat.2008.09.020.

[117] L.M. Herz, L.V. Dao, M.B. Johnston, M. Gal, and C. Jagadish. "Observation of state filling effects in the carrier dynamics of self-assembled quantum dots". In: *1998 Conference on Optoelectronic and Microelectronic Materials Devices, 1998. Proceedings*. 1998 Conference on Optoelectronic and Microelectronic Materials Devices, 1998. Proceedings. 1998, pp. 344–347. DOI: 10.1109/COMMAD.1998.791658.

[118] X. M. Wen, L. V. Dao, P. Hannaford, S. Mokkapati, H. H. Tan, and C. Jagadish. "The state filling effect in p-doped InGaAs/GaAs quantum dots". In: *Journal of Physics: Condensed Matter* 19.38 (2007), p. 386213. ISSN: 0953-8984. DOI: 10.1088/0953-8984/19/38/386213.

[119] L. B Freund and Subra Suresh. *Thin film materials: stress, defect formation and surface evolution*. Cambridge [u.a.: Cambridge Univ. Press, 2006. ISBN: 978-0-521-82281-7.

[120] S. Yu. Shiryaev, F. Jensen, J. Lundsgaard Hansen, J. Wulff Petersen, and A. Nylandsted Larsen. "Nanoscale Structuring by Misfit Dislocations in Si1-xGex/Si Epitaxial Systems". In: *Physical Review Letters* 78.3 (Jan. 20, 1997), pp. 503–506. DOI: 10.1103/PhysRevLett.78.503.

[121] Y. H. Xie, S. B. Samavedam, M. Bulsara, T. A. Langdo, and E. A. Fitzgerald. "Relaxed template for fabricating regularly distributed quantum dot arrays". In: *Applied Physics Letters* 71.24 (Dec. 15, 1997), pp. 3567–3568. ISSN: 0003-6951, 1077-3118. DOI: 10.1063/1.120393.

[122] Songphol Kanjanachuchai and Pat Photongkam. "Dislocation-Guided Self-Running Droplets". In: *Crystal Growth & Design* 15.1 (Jan. 7, 2015), pp. 14–19. ISSN: 1528-7483. DOI: 10.1021/cg5013704.

[123] Y. H. Huo et al. "A light-hole exciton in a quantum dot". In: *Nature Physics* 10.1 (Jan. 2014), pp. 46–51. ISSN: 1745-2473. DOI: 10.1038/nphys2799.

[124] F. Ding et al. "Tuning the Exciton Binding Energies in Single Self-Assembled InGaAs/GaAs Quantum Dots by Piezoelectric-Induced Biaxial Stress". In: *Physical Review Letters* 104.6 (Feb. 12, 2010), p. 067405. DOI: 10.1103/PhysRevLett.104.067405.

[125] P. Yu et al. "Optical anisotropy in vertically coupled quantum dots". In: *Physical Review B* 60.24 (Dec. 15, 1999), pp. 16680–16685. DOI: 10.1103/PhysRevB.60.16680.

[126] G. El-Hajje, D. Ory, M. Paire, J. -F. Guillemoles, and L. Lombez. "Contactless characterization of metastable defects in Cu(In,Ga)Se2 solar cells using time-resolved photoluminescence". In: *Solar Energy Materials and Solar Cells* 145, Part 3 (Feb. 2016), pp. 462–467. ISSN: 0927-0248. DOI: 10.1016/j.solmat.2015.11.016.

[127] Melvin Lax. "Cascade Capture of Electrons in Solids". In: *Physical Review* 119.5 (Sept. 1, 1960), pp. 1502–1523. DOI: 10.1103/PhysRev.119.1502.

[128] Songphol Kanjanachuchai, Ming Xu, Alexandre Jaffré, Apichart Jittrong, Thitipong Chokamnuai, Somsak Panyakeow, and Mohamed Boutchich. "Excitation transfer in stacked quantum dot chains". In: *Semiconductor Science and Technology* 30.5 (May 1, 2015), p. 055005. ISSN: 0268-1242. DOI: 10.1088/0268-1242/30/5/055005.

[129] Ming Xu, Mohamed Boutchich, Alexandre Jaffre, Jose Alvarez, Marie-Estelle Gueunier-Farret, Jean-Paul Kleider, and Nazir P. Kherani. "Temperature dependent photoluminescence in silicon based heterojunction solar cell". In: *EU PVSEC Conference Proceedings*. European Photovoltaic Solar Energy Conference and Exhibition. Amsterdam, Netherlands, 2014, pp. 1214–1217. DOI: 10 . 4229 / EUPVSEC20142014-2BV.8.34.

[130] Ming Xu, Alexandre Jaffré, José Alvarez, Jean-Paul Kleider, Apichat Jittrong, Thitipong Chokamnuai, Somsak Panyakeow, Mohamed Boutchich, and Songphol Kanjanachuchai. "Temperature dependent photoluminescence and micromapping of multiple stacks InAs quantum dots". In: *AIP Conference Proceedings*. THE IRAGO CONFERENCE 2014. Vol. 1649. Ibaraki, Japan: AIP Publishing, Feb. 27, 2015, pp. 3–7. DOI: 10.1063/1.4913536.

[131] Ming Xu. "Photoluminescence techniques for heterojunction solar cell characterization". Journées Nationales du PhotoVoltaïque. 2013.

[132] Ming Xu. "Characterization of a-Si:H/c-Si heterojunction by temperature dependent modulated photoluminescence". International Conference on Amorphous and Nanocrystalline Semiconductors. Aachen, Germany, Sept. 2015.

Appendix A

Derivation of MPL theory

A.1 Modulated carrier concentration

We assume that when the material is illuminated by a beam of incident light of which the intensity is modulated by small signal:

$$\widetilde{P}(t) = P_{DC} + P_{AC}\mathrm{e}^{i\omega t} \tag{A.1}$$

where the real quantities P_{DC} and P_{AC} are the continuous part of the incident light power and the amplitude of the modulation part of the incident light power respectively, the generation rate of electron hole pairs also follows the same rule:

$$\widetilde{G}(t) = G_{DC} + G_{AC}\mathrm{e}^{i\omega t} \tag{A.2}$$

where the real quantities G_{DC} and G_{AC} are the continuous part of generation rate and the amplitude of the modulation part of generation rate respectively. The variation of excess carrier concentration as a function of time should take the same form except that due to relaxation a phase shift term ϕ should be considered:

$$\widetilde{\Delta n}(t) = \Delta n_{DC} + \Delta n_{AC}\mathrm{e}^{i(\omega t+\phi)} \tag{A.3}$$

where the real quantities Δn_{DC} and Δn_{AC} are the continuous part of excess carrier concentration and the amplitude of the modulated part of excess carrier concentration respectively. Substituting Eq. A.2 and A.3 into the definition of carrier lifetime (Eq. 2.1)

$$\tau_{eff} = \frac{\Delta n(t)}{G(t) - \frac{\mathrm{d}\Delta n(t)}{\mathrm{d}t}} \tag{A.4}$$

with $\Delta n(t)$ the excess carrier concentration out of equilibrium and $G(t)$ the generation rate, we have

$$\tau_{eff} G_{DC} - \Delta n_{DC} = \left[\Delta n_{AC} + i\tau_{eff}\omega\Delta n_{AC} - \tau_{eff} G_{AC} e^{-i\phi}\right] e^{i(\omega t+\phi)} \tag{A.5}$$

of which the left side is static and the right side is dynamic. By equating both sides to zero, from the coefficient of the exponential term on the right-hand side of the equation, we obtain

$$\begin{aligned} \Delta n_{AC} &= \tau_{eff} G_{AC} \frac{e^{-i\phi}}{1 + i\tau_{eff}\omega} \\ &= \frac{\tau_{eff} G_{AC}}{\sqrt{1 + (\omega\tau_{eff})^2}} e^{-i(\phi+\arctan(\tau_{eff}\omega))} \end{aligned} \tag{A.6}$$

and since Δn_{AC} is real, the right-hand side of Eq. A.6 must be real. By separating the imaginary part and equating it to zero, we get:

$$\phi = -\arctan(\omega\tau_{eff}) \tag{A.7}$$

and the real amplitude part:

$$\Delta n_{AC} = \frac{\tau_{eff} G_{AC}}{\sqrt{1 + (\omega\tau_{eff})^2}} \tag{A.8}$$

Eq. A.7 enables us to extract the lifetime from the phase shift in the experiments.

Eq. A.8 also provides information of lifetime. However, the carrier concentration cannot be directly measured. We should take advantage of its correlation with PL. This is discussed in next section.

A.2 Modulated PL

Following the previous discussions, note that the radiative recombination rate of the excess carriers can be given as:

$$U_{rad} = Bnp - Bn_0p_0 \tag{A.9}$$

where B is the radiative recombination coefficient, n and p the electron and the hole concentration respectively under illumination. We extend this equation to time dependent PL

by introducing the time dependent n and p given by Eq. A.3. Assuming $\widetilde{\Delta n} = \widetilde{\Delta p}$,

$$\begin{aligned} U_{rad}/B &= \left(\mathrm{Re}[\widetilde{\Delta n}(t)] + n_0\right)\left(\mathrm{Re}[\widetilde{\Delta n}(t)] + p_0\right) - n_0 p_0 \\ &= \left(\mathrm{Re}[\widetilde{\Delta n}(t)]\right)^2 + (n_0 + p_0)\mathrm{Re}[\widetilde{\Delta n}(t)] \\ &= \Delta n_{DC}^2 + (n_0 + p_0)\Delta n_{DC} + \\ &\quad 2\Delta n_{DC}\Delta n_{AC}\mathrm{Re}[e^{i(\omega t+\phi)}] + (n_0 + p_0)\Delta n_{AC}\mathrm{Re}[e^{i(\omega t+\phi)}] + \\ &\quad \Delta n_{AC}^2\left(\mathrm{Re}[e^{i(\omega t+\phi)}]\right)^2 \end{aligned} \tag{A.10}$$

using $[\mathrm{Re}(e^{ix})]^2 = \frac{1}{2}[1 + \mathrm{Re}(e^{i2x})]$ we get

$$U_{rad}/B = C_0 + C_1\mathrm{Re}[e^{i(\omega t+\phi)}] + C_2\mathrm{Re}[e^{i2(\omega t+\phi)}] \tag{A.11}$$

with

$$\begin{aligned} C_0 &= \Delta n_{DC}^2 + \frac{1}{2}\Delta n_{AC}^2 + (n_0 + p_0)\Delta n_{DC} \\ C_1 &= (2\Delta n_{DC} + n_0 + p_0)\Delta n_{AC} \\ C_2 &= \frac{1}{2}\Delta n_{AC}^2 \end{aligned} \tag{A.12}$$

C_0, C_1 and C_2 are the amplitude of continuous, first order and second order response of PL to carrier concentration modulation.

Eq. A.11 shows that the radiative recombination rate is also modulated. All the components C_0, C_1, C_2 contain information of Δn_{AC} given by Eq. A.8 and the first and second order C_1, C_2 contain information of phase shift ϕ defined in Eq. A.7. This fact enables us to obtain the differential lifetime from the modulated photoluminescence.

Firstly, although Δn_{AC} is comprised in the zeroth order C_0, the DC measurement is usually not sensitive enough to detect the impact of $\frac{1}{2}\Delta n_{AC}^2$. That is why we turn to lock-in measurement. Secondly, the second order C_2 is often weak and difficult to be measured. So the best choice is to utilize the first order C_1.

The phase shift of the first order can be directly measured by lock-in amplifier. The amplitude of the rate of the modulated excess carrier radiative recombination $U_{rad,AC}$ is given by C_1. Substituting Eq. A.8 into C_1 leads to

$$U_{rad,AC} = \frac{B(2\Delta n_{DC} + n_0 + p_0)\tau_{eff}G_{AC}}{\sqrt{1 + (\omega\tau_{eff})^2}} \tag{A.13}$$

In experiments we measure PL intensity which is proportional to U_{rad}. Since the PL intensity is measured as a function of ω, by omitting the terms independent of ω, we have

$$I_{AC}(\omega) \propto \frac{1}{\sqrt{1+(\omega\tau_{eff})^2}} \tag{A.14}$$

I_{AC} is the amplitude of the AC component of the PL intensity. It is proportional to Δn_{AC} by a constant that reduces all quantities independent of ω as well as the transfer function of the experimental system. This is the equation that we use in experiments to extract the lifetime from the PL amplitude.

Note that the first order modulated PL also contains information of phase shift according to Eq. A.11. The quantity ϕ originates to Eq. A.7. So Eq. A.7 also gives the phase shift of the modulated PL.

Appendix B

Setup specifications

B.1 Macro PL

- Laser diode: THORLABS L785P090
- Longpass filter: Edmund #86-071
  - Optical density: ≥4.0
  - Cut-on wavelength: 875 nm
  - Transmission wavelength: 890-1650 nm
- Monochromator: Newport 74000
  - Blaze grating: model 74028, 600 line/mm
  - Reciprocal linear dispersion: 13 nm/mm
- Photodiode
  - THORLABS SM05PD5A: InGaAs photodiode
    * Measurement range: 800-1800 nm
    * Active area diameter: $\phi = 2.0$ mm
  - HAMAMATSU G8605-25: InGaAs PIN photodiode,
    * Active area diameter: $\phi = 5.0$ mm
- Laser diode mount: THORLABS TCLDM9
- Amplifier: FEMTO DHPCA-100

- Multimeter: KEITHLEY 195 SYSTEM DMM
- Lock-in amplifier: STANFORD RESEARCH SYSTEMS SR830 DSP
- Motorized linear translation stage: Physik Instrumente (PI) M403.62S
  - Translation distance: 150 mm

B.2 Micro PL

For PL measurements, the available configurations are:

- Excitation Lasers: 532, 785 nm and 355 nm soon
- Spectral analysis range:
- From 530 to 1000 nm, Resolution: 0.2nm (600 gr/mm grating)
- From 800 nm to 1700 nm, Resolution: 0.5 and 1 nm (300 and 150 gr/mm gratings)
- Confocal pinhole: fiber core diameter of 50 µm (also 200 µm)
- Surface cartography and depth profiling resolution depend on the photoluminescence wavelength

Appendix C

PL transient decay

In a limited window of experiment time, we were able to mount the control unit onto Witec station and performed time resolved photoluminescence (TRPL) measurements as a function of temperature. Only one sample referenced #B1 has been investigated in the temperature range 80∼425 K. The TRPL technique often relies on a pulsed laser source coupled to a gated detection system allowing ultra fast measurements in the order of magnitude of ns. However in our context where the PL decay time is in the ms range the TRPL gated approach remains inappropriate. Accordingly, a burst mode laser excitation coupled to a counting detection was employed.

It should be noted that the Witec system based on a microscope station does not favor low laser injection levels. In particular, the laser power density can reach thousands of suns. In our experiment the laser power was 2 kW/cm^2, the duration of pulse excitation was 2.5 ms and repeated every 7.5 ms corresponding to a duty cycle of 1/3. The PL signal was then accumulated in hundreds of periods. An example of PL decay is illustrated in Fig. C.1(a). We zoom in to show more details in Fig. C.1(b). It can been seen in the figure that when the temperature decreases, the PL decays faster. This implies that the lifetime is shorter at lower temperature.

It should be stressed that although the injection level is extremely high, our measurement does not necessarily correspond to the high level injection. Because our measurement is only sensitive to the long time decay in the range of ms, the Auger and radiative recombination do not dominate any more. They are mostly negligible. For this reason, the PL decay in Fig. C.1(a) that we have observed in a time range of about milliseconds is dominated by SRH recombination. The linearity in Fig. C.1(b) also implies that the dominating recombination mechanism is neither Auger nor radiative.

The decay time parameter τ as a function of temperature is extracted by fitting the curves with PL intensity $\propto \exp(-t/\tau)$ and the result is shown in Fig. C.2. An apparent activation

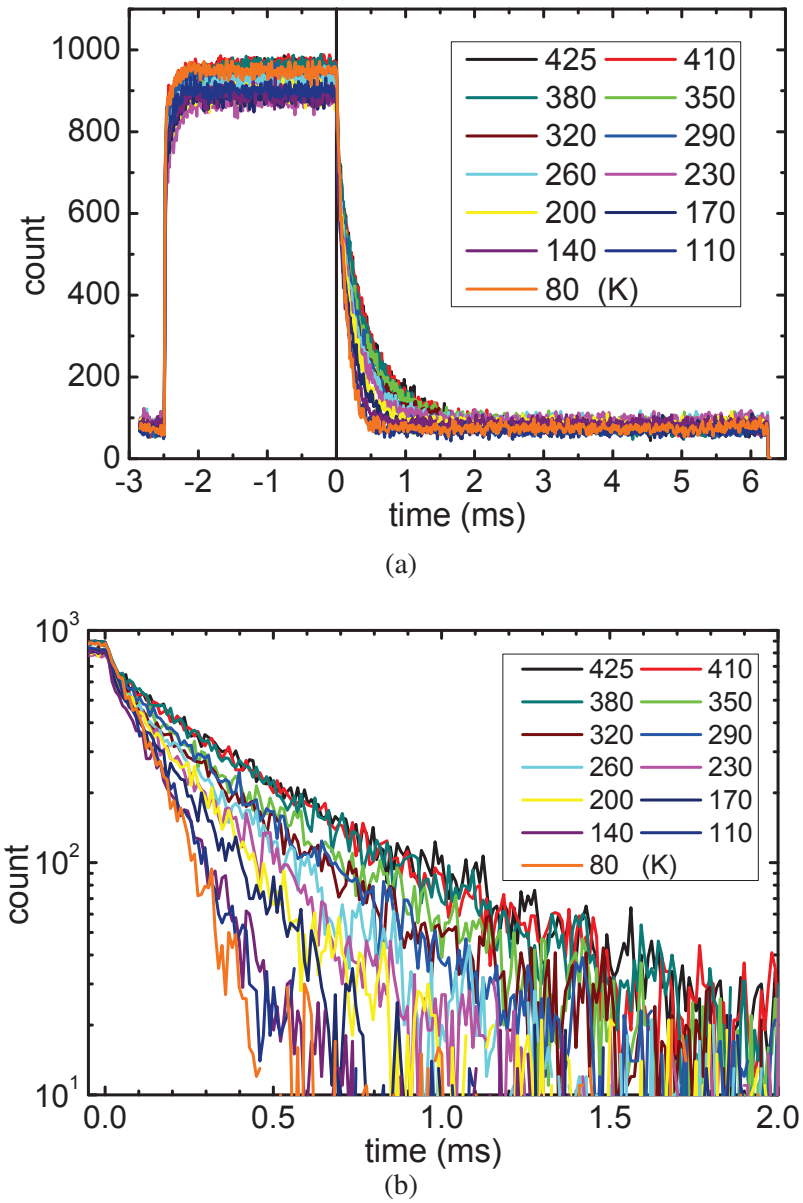

Fig. C.1 (a) PL evolution measured as a function of time from 80 K to 425 K. (b) Details of the exponential decay of PL signal following the cut-off of injection.

energy of 38 meV is obtained in the high temperature range.

The temperature dependence of lifetime found in TRPL is quite similar to that of the MPL lifetime described in chapter4 section 4.3.2. Both lifetime values decrease with decreasing temperature with some flattening at relatively lower temperature.

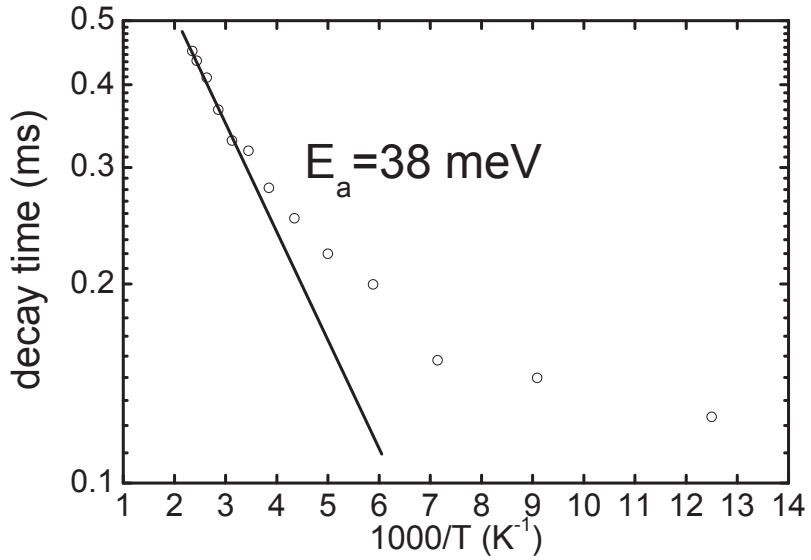

Fig. C.2 Lifetime extracted from PL decay. 38 meV activation energy is found.

Appendix D

Abbreviations table

a-Si:H	hydrogenated amorphous silicon
BSF	back surface field
c-Si	crystalline silicon
CZ	Czochralski
EDA	electronic design automation
FZ	float zone
HLI	high level injection
ITO	indium tin oxide
G	generation rate
INES	Institut National de l'Énergie Solaire
HIT	heterojunction with intrinsic thin layer
LLI	low level injection
LPICM	Laboratoire de Physique des Interfaces et des Couches Minces
μPCD	microwave photoconductance decay
MPL	modulated photoluminescence
PECVD	plasma enhanced chemical vapor deposition

PERC	passivated emitter, rear contact
PERL	passivated emitter, rear locally diffused
PERT	passivated emitter, rear totally diffused
PL	photoluminescence
QSSPC	quasi-steady-state photoconductance
R	recombination rate
SHJ	silicon heterojunction
SRH	Shockley-Read-Hall
τ_{diff}	differential lifetime
τ_{eff}	effective lifetime
τ_{ss}	steady-state lifetime
$\tau_{diff,tot}$	total (global) differential lifetime
$\tau_{ss,tot}$	total (global) steady-state lifetime
$\tau_{diff,rad}$	differential radiative lifetime
$\tau_{ss,rad}$	steady-state radiative lifetime
$\tau_{diff,Aug}$	differential Auger lifetime
$\tau_{ss,Aug}$	steady-state Auger lifetime
$\tau_{diff,SRH}$	differential SRH lifetime
$\tau_{ss,SRH}$	steady-state SRH lifetime
TCO	transparent conducting film
TDLS	temperature dependent lifetime spectroscopy
TRPL	time-resolved photoluminescence

Appendix E

Publications

- Peer reviewed paper
  - Songphol Kanjanachuchai, Ming Xu, Alexandre Jaffré, Apichart Jittrong, Thitipong Chokamnuai, Somsak Panyakeow, and Mohamed Boutchich. "Excitation transfer in stacked quantum dot chains". In: *Semiconductor Science and Technology* 30.5 (May 1, 2015), p. 055005. ISSN: 0268-1242. DOI: 10.1088/0268-1242/30/5/055005
- Conference papers
  - Ming Xu, Mohamed Boutchich, Alexandre Jaffre, Jose Alvarez, Marie-Estelle Gueunier-Farret, Jean-Paul Kleider, and Nazir P. Kherani. "Temperature dependent photoluminescence in silicon based heterojunction solar cell". In: *EU PVSEC Conference Proceedings*. European Photovoltaic Solar Energy Conference and Exhibition. Amsterdam, Netherlands, 2014, pp. 1214–1217. DOI: 10.4229/EUPVSEC20142014-2BV.8.34
  - Ming Xu, Alexandre Jaffré, José Alvarez, Jean-Paul Kleider, Apichat Jittrong, Thitipong Chokamnuai, Somsak Panyakeow, Mohamed Boutchich, and Songphol Kanjanachuchai. "Temperature dependent photoluminescence and micromapping of multiple stacks InAs quantum dots". In: *AIP Conference Proceedings*. THE IRAGO CONFERENCE 2014. Vol. 1649. Ibaraki, Japan: AIP Publishing, Feb. 27, 2015, pp. 3–7. DOI: 10.1063/1.4913536
- Oral presentations
  - Ming Xu. "Photoluminescence techniques for heterojunction solar cell characterization". Journées Nationales du PhotoVoltaïque. 2013

- Ming Xu. “Temperature dependent photoluminescence and micro-mapping of multiple stacks InAs quantum dots”. INTERNATIONAL WORKSHOP ON ON NANOSTRUCTURES CHARACTERIZATION AND NANOMATERIALS. Bangkok, Thailand, Aug. 2015
- Ming Xu. “Characterization of a-Si:H/c-Si heterojunction by temperature dependent modulated photoluminescence”. International Conference on Amorphous and Nanocrystalline Semiconductors. Aachen, Germany, Sept. 2015